UC Santa Barbara

UC Santa Barbara Electronic Theses and Dissertations

Title

Understanding the rainfall triggering post-fire debris flows in California

Permalink

https://escholarship.org/uc/item/8gc109rc

ISBN

9798186385943

Author

Castillo Guerra, Silvana

Publication Date

2026-06-10

Supplemental Material

https://escholarship.org/uc/item/8gc109rc#supplemental

Peer reviewed|Thesis/dissertation

eScholarship.org Powered by the California Digital Library
University of California

UNIVERSITY OF CALIFORNIA

Santa Barbara

Understanding the rainfall triggering post-fire debris flows in California

A dissertation submitted in partial satisfaction of the

requirements for the degree Doctor of Philosophy

in Geography

by

Silvana Castillo Guerra

Committee in charge:

Professor Charles Jones, Chair

Professor Leila M.V. Carvalho

Professor Vamsi Ganti

June 2026

The dissertation of Silvana Castillo Guerra is approved

_____

Leila M.V. Carvalho

_____

Vamsi Ganti

_____

Charles Jones, Committee Chair

May 2026

ACKNOWLEDGEMENTS

Over the years, I read multiple dissertations and always found myself drawn to read the acknowledgments. I found comfort in seeing, again and again, that no one reaches this point entirely alone. One acknowledgment particularly stayed with me because the author described how the thought of writing this section brought them hope during difficult times, a feeling that became familiar to me throughout my own journey. Now that I finally get to write my own, and since I do not plan to write a book anytime soon, I will allow myself to take a few more pages than usual to honor and immortalize, in a public document, some of the people who helped make this achievement possible.

First, I want to thank my family: my mom, my dad, Salu, and my Tía Isa, who have always been by my side in every quest I have decided to pursue. Thank you for picking up the phone every time I called and for patiently listening to every story (whether wild, boring, or funny), crisis, and complaint I had during these five years. I would not be who I am today without your love and support. I also want to thank my partner, Juan Daniel, who has completely outperformed as the newest member of my always-on-demand support network, all while working on his own Ph.D. studies. Thanks for being my emergency contact, when an analysis did not make sense, writing needed a second look, or an ellipse refused to be plotted. Finally, I want to thank my faith and God. It would be unfair not to acknowledge that, when I doubted the outcome of this Ph.D., religion was one of the places where I found some hope to keep moving forward.

None of the work described in these pages, nor my time at UCSB, would have been possible without my advisor, Professor Charles Jones. Thank you for giving me this academic

opportunity and ride the rollercoaster that post-fire debris flows (and research) turned out to be. To Charles and to my committee members, Professors Leila and Vamsi, I will always be grateful for your encouragement to learn new things, even when the unknown felt intimidating. Thank you for guiding me through methods, datasets, funding, and all the many pieces that made this dissertation possible, as well as for the helpful conversations and valuable input that improved this work.

Among the great gifts this Ph.D. gave me were the people I met along the way, who made these years far more meaningful than I thought they could be. To the people in my research lab: Kevin, the ever-positives Marian and Ayodeji, the "postdocs" who are no longer postdocs, Callum, and Gert-Jan, thank you for all the conversations, whether they were about research, life, or everything in between. I always left those chats with something good: hope, laughter, wisdom, or at least a much-needed distraction. Special thanks and appreciation to Dais, Ye and Emma with whom I shared many dinners and hopefully improved my tennis skills along the way. I will always treasure our doubles matches and remember our time together with great affection.

To my fellow grad students: Katie, Madison, Caitlyn, Rob, Jesse, Feifei, Yanni, Debsmita, Bri and Yifei, I always enjoyed running into you in the lounge, halls, or at social gatherings and hearing about your new adventures in life. Thank you for your kindness and for making these years feel warmer and lighter. Gabrielle and Derek, words feel too small to express my gratitude to you. You felt like family away from family. Thank you for opening your doors to me, for adopting me every Thanksgiving, and for the walks and long conversations that ranged from English vocabulary to the more serious topics in life. For all of that, and for your friendship, I will always be grateful.

I also want to thank the professors I had the privilege of working with or learning from, including Professors Anna, Qinghua, Dar, Joe, Susan, Jennifer, Dan and Ian. Because of you, I now know more about demography, economic geography, climate modeling, plant traits, Rossby waves and teleconnections, rivers and sediment, remote sensing, the Roman Empire, and soils than I ever imagined I would. Thank you for being generous teachers, mentors, and bosses, and for making your knowledge feel both rigorous and accessible.

Last but not least, I want to thank the staff. Thank you for your kindness, patience, and help, for every letter and document provided; for opening doors when I locked myself out of my office or when a classroom door refused to cooperate; for rescuing me from copier issues, and even saving my research after I deleted an entire folder from my home directory. Thanks to all of you, life felt easier at times, and during a Ph.D., that is no small thing.

CURRICULUM VITAE
SILVANA CASTILLO GUERRA

EDUCATION

2026 Ph.D. in Geography, University of California Santa Barbara

2020 M.Sc. in Geological Science, The University of British Columbia

2017 B. Sc. in Geology, Universidad EAFIT

PROFESSIONAL EXPERIENCE

2021- 2026 *Graduate Student Researcher - University of California Santa Barbara, California*

Research on rainfall triggering post-fire debris flows in California

2025 *Intern GIS Data & Documentation Support Consultant - Inter-American Development Bank, Washington D.C.*

Geographic Information Systems support for risk assessments of infrastructure and economic development projects

2019 - 2020 *Graduate Student Researcher - The University of British Columbia, Vancouver*

Landslide susceptibility in Canada and Colombia using statistical and heuristic methods

2016 - 2017 *Undergraduate Student Research - Universidad EAFIT, Medellin, Colombia*

Paleo-environmental and sedimentology of geological formations in the North Coast of Colombia

2015 - 2016 *Intern Geology – SERVIMINAS, Medellin, Colombia*

Support with geological and map visualization to a geological mapping in Colombia

TEACHING EXPERIENCE

2021 - 2025 *Teaching Assistant - Department of Geography, University of California Santa Barbara*

- GEOG 6: Sex, Drugs and Geography
- GEOG 13: Introduction to GIS programming
- GEOG 5: People, Place and the Environment
- GEOG 8: Global Warming
- GEOG 140: Historical Geography

2018 - 2019 *Teaching Assistant - Department of Earth, Ocean and Atmospheric Sciences, The University of British Columbia*

- EOAS 110: The solid Earth: A dynamic planet
- EOAS 326: Earth and life through time

AWARDS

2025	UC Santa Barbara Doctoral Student Travel Grant
2025	Schmidt Family Foundation Research Fellowship
2024	UC Santa Barbara Department of Geography Research Funding
2024	Geological Society of America (Environmental & Engineering Geology Division) Landslide Conference Funding
2021	Fulbright Scholarship
2018	COLFUTURO Scholarship
2014	Universidad EAFIT Honors Tuition Scholarship

PUBLICATIONS

Castillo, S., & Jones, C. (2026). Sequential Occurrence of Fire Weather and Debris Flow Triggering Rainfall in California: Implications for Post-Fire Debris-Flow Hazard under Future Climate. *(in preparation).*

Castillo, S., Jones, C., & Carvalho, L. M. V. (2026). Integrating Atmospheric and Surficial Controls to Predict Post-Fire Debris Flows in California. *(in preparation).*

Castillo, S., Jones, C., & Carvalho, L. M. V. (2025). Structural Properties and Reflectivity Patterns of Precipitation Systems Linked to Post-Fire Debris Flows in California. *Manuscript under review, Meteorological Applications.*

Castillo, S., & Jones, C. (2025). Rainfall conditions of post-fire debris flows between 2012–2023 across regions in California. *SSRN Working Paper*. Available at http://dx.doi.org/10.2139/ssrn.5138368.

Castillo Guerra, S., & Soto López, L. (2017). Reconstrucción paleoambiental de la Formación El Floral–Ciénaga de Oro a partir de una sección estratigráfica entre los municipios de Montería y Planeta Rica (Bachelor's thesis, Universidad EAFIT).

PRESENTATIONS

Castillo, S. (2026). Structural properties and reflectivity patterns of precipitation systems linked to post-fire debris flows in California [Talk]. *CW3E Friday Science Talks*.

Castillo, S., Jones, C., & Carvalho, L. (2025). Storm Structure Properties and Reflectivity Patterns in Post-Fire Debris Flow-Triggering Events Using Radar Composites [Oral]. *AGU2025 Fall Meeting*, New Orleans, LA, 15-19 Dec.

Castillo, S., & Jones, C. (2024). Meteorological conditions associated with post-fire debris flows in California [Poster]. *Establishing Directions in Postfire Debris-Flow Science Conference*, South Lake Tahoe, CA 20–22 May.

Castillo, S., & Jones, C. (2023). Rainfall conditions of post-fire debris flows between 2013–2023 across ecoregions in California [Poster]. *AGU2023 Fall Meeting*, San Francisco, CA, 11–15 Dec.

Castillo, S., & Jones, C. (2022). The generation of landslides after wildfire: A case study of 286 occurrences after a rainstorm in January 2019 in the San Gabriel Mountains, Southern California [Oral]. *AGU2022 Fall Meeting*, Chicago, IL, 12–16 Dec.

Castillo, S., & Jakob, M. (2021). Methods comparison to predict debris avalanche and debris flow susceptibility in the Capilano Watershed, BC, Canada [Oral]. *XIII International Symposium on Landslides*, Cartagena, Colombia, 22–26 Feb. https://www.issmge.org/uploads/publications/105/106/ISL2020-57.pdf

SERVICE

Mentored Undergraduate Research Project (2025) - Universidad Nacional de Colombia

Reviewer Graduate Application Materials Assistance (GAMA) Program (2024-2025) - University of California Santa Barbara, Department of Geography

ABSTRACT

Understanding the rainfall triggering post-fire debris flows in California

by

Silvana Castillo Guerra

Post-fire debris flows (PFDFs) are a cascading hazard resulting from the interaction between intense rainfall and susceptible terrain altered by wildfire. These events have proven devastating in the past, damaging infrastructure and communities, particularly in California, where fire season in the warm months is closely followed by rainfall during the cool season. The expansion of wildfire occurrence, along with pronounced variability in terrain and climate across California, highlights the need to better understand the rainfall conditions associated with this hazard under both current and future climates. Consequently, this dissertation integrates multiple datasets and methods to characterize rainfall and atmospheric conditions associated with storms triggering post-fire debris flows, providing new insight into the rainfall environments, precipitation-system structure, predictive controls, and future changes in PFDF hazard across California. First, an inventory of PFDF is compiled and used to characterize rainfall conditions associated with event occurrence using nearby rain gauges, including storm duration, rainfall accumulation, antecedent rainfall, and short-duration peak intensity. Results show that rainfall triggering PFDFs in California occurs within diverse storm environments, from long, persistent, and wet cool-season storms to shorter and intense warm-season storms.

However, short-duration peak rainfall intensities capable of triggering PFDFs occur across seasons, suggesting that similar triggering bursts may arise within very different broader storm environments. The following research chapter uses a radar-based tracking approach to characterize the structural properties of precipitation systems and reflectivity affecting burned areas during storms known to have triggered PFDFs. This analysis further demonstrates clear seasonal contrasts in area, speed and eccentricity of precipitation systems and shows that maximum reflectivity within burned areas provides useful temporal context for hazardous rainfall conditions identified by rain gauges. The third study evaluates the importance of rainfall, atmospheric, and surface variables for PFDF occurrence, and whether the inclusion of atmospheric conditions improves hazard predictability compared to traditional approaches. Predictive modeling using random forest indicates that radar reflectivity, peak short-duration rainfall intensity, atmospheric moisture, and low-level wind are among the most important predictors of PFDF occurrence, although surface characteristics remain relevant for interpreting where hazard is greatest within burned areas. Finally, PFDF hazard was assessed under future climate conditions using a temporally compound-event framework based on the successive occurrence of extreme fire weather and rainfall exceedances relevant to debris flow triggering within time windows of up to 1 year. Future climate analyses suggest that conditions conducive to PFDF hazard, particularly under high emissions, may become more frequent, and more closely timed, as the seasonal interval between extreme fire weather and triggering rainfall narrows. These findings provide an integrated perspective on the rainfall triggering post-fire debris flow hazard in California and offer information directly relevant to support the improvement of mitigation, preparedness, and climate adaptation of debris flow hazard in fire-prone landscapes.

TABLE OF CONTENTS

1. Introduction *1*

1.1. Controls on post-fire debris flow occurrence 2

1.2. Rainfall conditions associated with post-fire debris flows in California..... 4

1.3. Radar-based characterization of precipitation systems associated with post-fire debris flows..... 5

1.4. Atmospheric drivers of post-fire debris-flow occurrence and prediction..... 7

1.5. Post-fire debris flow hazard under future climate conditions..... 8

1.6. Research questions..... 9

1.7. References..... 10

2. Rainfall conditions of post-fire debris flows between 2014 – 2022 across regions in California..... 15

2.1. Introduction..... 16

2.2. Data and methods 18

2.2.1. Post-fire debris-flow inventory and spatial grouping 18

2.2.2. Rain gauge selection and rainfall metrics 20

2.3. Results..... 22

2.3.1. Storm duration 25

2.3.2. Cumulative rainfall and average intensity 27

2.3.3. Peak 15-min intensity 29

2.3.4. Antecedent precipitation clustering 33

2.4. Discussion and conclusions 36

2.5. References..... 40

3. Structural properties and reflectivity patterns of precipitation systems linked to post-fire debris flows in California..... 45

3.1. Introduction..... 46

3.2. Data and methods 50

3.2.1. Radar reflectivity data and post-fire debris flow inventory..... 50

3.2.2. Modified tracking algorithm..... 53

3.2.3. Reflectivity metrics..... 59

3.3. Results..... 61

3.3.1. Structural properties and reflectivity patterns of precipitation systems 61

3.3.2. Application to short- and long-duration storms..... 72

3.4. Discussion and conclusions 81
3.5. References 88
4. Integrating atmospheric and surficial controls to predict post-fire debris flows in California 96
4.1. Introduction 97
4.2. Data and methods 101
4.2.1. Event database 102
4.2.2. Predictor variables 104
4.3. Model development 113
4.3.1. Model training 113
4.3.2. Model evaluation 114
4.4. Results 116
4.4.1. Atmospheric and storm rainfall variables 116
4.4.2. Structural properties of precipitation systems 128
4.4.4. Model performance 133
4.4.5. Model validation 137
4.5. Discussion 143
4.6. Conclusions 147
4.7. References 148
5. Sequential occurrence of fire weather and debris flow triggering rainfall in California: Implications for post-fire debris flow hazard under future climate. 157
5.1. Introduction 158
5.2. Data and methods 161
5.3. Results 166
5.4. Discussion 177
5.5. Conclusions 181
5.6. References 182
6. Conclusions 188
6.1. Key results 189
6.2. Limitations and future work 193
Appendix A 196

LIST OF FIGURES

Figure 2.1. Post-fire debris-flow events and associated fire perimeters across California. 23

Figure 2.2. Relationship between storm duration and average storm intensity for post-fire debris flow events in California.....25

Figure 2.3. Distribution of storm duration for post-fire debris flow events across California 26

Figure 2.4. Distribution of storm cumulative rainfall (a–c) and average storm intensity (d–f) for post-fire debrisflow events across California.....28

Figure 2.5. Distribution of peak rainfall intensity measured over 15-min (a–c), 30-min (d–f), and 60-min (g–i) intervals for post-fire debris flow events across California.....31

Figure 2.6. Rainfall time series depicting high peak-15 min intensity events.....33

Figure 2.7. Precipitation clusters preceding post-fire debris flow events in the cool-season months in California. 35

Figure 3.1. Locations of documented post-fire debris flows (2014–2022; red triangles) and associated wildfire perimeters (2013–2021; black outlines) across California ...53

Figure 3.2. Flowchart of the modified tracking algorithm 55

Figure 3.3. Structural properties and radar reflectivity of a precipitation system over the Springs Fire.....62

Figure 3.4. Distribution of values by seasonal groups for precipitation systems at the time of peak 15-minute rainfall intensity 65

Figure 3.5. Radar reflectivity (dBZ) statistics at the time of peak 15-min rainfall intensity 69

Figure 3.6. Lag times between reflectivity metrics. 72

Figure 3.7. Reflectivity metrics tracked and rainfall recorded by nearest rain gauge during storm in Butte Fire in March 2016. 75
Figure 3.8. Precipitation system and reflectivity within the Butte fire perimeter during a storm in March 2016. 77
Figure 3.9. Reflectivity metrics tracked and rainfall recorded by nearest rain gauge during storm in Tamarack Fire on August 3, 2022. 79
Figure 3.10. Precipitation system and reflectivity within the Tamarack fire perimeter during a storm on August 3, 2022. 81
Figure 4.1. Workflow schematic showing the data pipeline from input datasets (surficial and rainfall, ERA5, and NEXRAD mosaics) through feature extraction, model training, and model evaluation. 102
Figure 4.2. Map of post-fire debris flow locations (2014–2022) and associated wildfire perimeters (2013–2021) across California. 104
Figure 4.3. Atmospheric and rainfall predictors considered for modeling post-fire debris flow occurrence in California. 120
Figure 4.4. Wind rose diagrams of 925-hPa wind direction and speed for post-fire debris flow events 123
Figure 4.5. Stability index predictors considered for modeling post-fire debris flow (PFDF) occurrence in California 125
Figure 4.6. Precipitation system characteristics at the time of peak 15-minute rainfall intensity associated with post-fire debris flow (PFDF) and non-PFDF storms in California 129

Figure 4.7. Distribution by PFDF response of a. Slope, b. Burn severity, c. Soil erodibility, and d. Vegetation type. 132
Figure 4.8. Model performance and feature importance 136
Figure 4.9. Predictor variables for the February 13, 2025 storm that generated a post-fire debris flow in the Eaton Fire burn area, San Gabriel Mountains. 140
Figure 4.10. Predictive modeling in the Eaton fire and comparison with existing approaches. 142
Figure 5.1. Schematic overview of the analytical framework used to evaluate sequential extreme fire weather–rainfall events across California 164
Figure 5.2. Spatial distribution of mean annual counts of extreme fire-weather events (top row) and rainfall exceedances of the historical 1-year recurrence threshold (bottom row) across California.....167
Figure 5.3. Seasonal cycle of extreme fire-weather events (orange) and rainfall exceedances (blue) across California.....169
Figure 5.4. Mean annual frequency of temporally compound events across California, defined as an extreme fire-weather event followed by at least one rainfall exceedance 171
Figure 5.5. Conditional probability that an extreme fire-weather event is followed by at least one rainfall exceedance across California 173
Figure 5.6. Monthly distribution of compound events across California 176
Figure A1. Harmonic seasonal cycle of extreme fire-weather events and rainfall exceedance events 198

Chapter 1

1. Introduction

Post-fire debris flows (PFDFs) are among the most dangerous hazards affecting recently burned mountainous terrain (Gartner et al., 2024). They pose severe risks to communities, infrastructure, and transportation corridors located within and downstream of burn areas and are distinguished from other sediment-laden flows by their rapid onset, destructive power, and ability to occur with little warning. Even relatively small debris flows can strip vegetation, block drainage networks, erode roads, damage structures through impact and scour, and endanger human life (Cannon & Gartner, 2005). In addition, PFDFs can be particularly dangerous since they can be triggered by rainfall conditions that would not normally produce debris flows in unburned terrain, increasing susceptibility in the months following wildfire, including places where debris flows have not been observed in the past (Cannon et al., 2008; Kean et al., 2011).

Wildfire can fundamentally alter landscape response to rainfall and increase susceptibility of steep slopes to debris flow (Kean & Staley, 2021). The combustion of vegetation and litter reduces interception, while fire-induced changes in soil properties can reduce infiltration and promote rapid runoff generation. As a result, rainfall that might otherwise be stored or delayed by vegetation and soils can be converted quickly into overland flow and channel discharge. Burned hillslopes also often contain abundant loose sediment, ash, rock, and organic debris that can be readily mobilized and incorporated into flows (Santi et al., 2013).

In California, where steep terrain, frequent wildfire, and dense development often coexist, PFDFs represent a recurrent and highly consequential natural hazard. Past events have caused repeated damage to homes and infrastructure and, in some cases, major loss of life. For

example, the Christmas Day 2003 debris flows in the San Bernardino area caused 16 fatalities (Chong et al., 2004), and the January 2018 Montecito disaster, which occurred only weeks after the Thomas Fire, damaged hundreds of structures and claimed 23 lives (Keller et al., 2020).

1.1. Controls on post-fire debris flow occurrence

Post-fire debris flow occurrence reflects a combination of meteorological forcing, hydrologic response, sediment availability, and underlying watershed susceptibility. In recently burned terrain, rainfall can amplify or moderate infiltration, runoff generation, sediment supply, and slope stability. As a result, the conditions that lead to debris flow initiation depend not only on how much rain falls, but also on when it falls after fire, how intensely it is delivered, and the physical characteristics of the burned locations.

Two primary initiation mechanisms have been identified in the literature (McGuire et al., 2024). The first, and most documented in recently burned terrain is runoff-generated debris flow initiation. In this process, intense rainfall produces rapid overland flow that erodes and entrains sediment, ash, and rock from hillslopes and channels, progressively bulking into a debris flow. This mechanism is especially important in the period immediately following fire, when infiltration is reduced, bare soil is exposed, and sediment is readily available for mobilization. The second mechanism involves the failure of shallow landslides that mobilize into debris flows. Although less common in post-fire settings, this process can occur when rainfall and subsurface hydrologic changes increase pore-water pressures and reduce slope stability. Shallow landslides are characterized by high total rainfall accumulations and their susceptibility may emerge later, around 2–10 years after the fire or more, after root strength

declines and hydrologic conditions begin to recover in ways that favor infiltration and subsurface destabilization.

The effect of rainfall is therefore filtered through surface and landscape controls. Burn severity is one of the most consistent predictors of post-fire response, particularly where moderate to high severity burn occupies a substantial and spatially connected portion of a basin (Gartner et al., 2014; Staley et al., 2018). Topographic characteristics also strongly influence susceptibility. Post-fire debris flow probability and magnitude have been associated with watershed relief, watershed ruggedness, and the proportion of burned slopes steeper than 23°, while documented debris flow-producing basins commonly occur in steep, lower-order catchments with average gradients ranging from 14° to 42° (Cannon & Gartner, 2005; Staley et al., 2017). Soil properties such as clay content, organic matter, and erodibility have likewise been linked to post-fire debris flow likelihood in empirical modeling studies (Cannon et al., 2010; Staley et al., 2017). These factors collectively shape how burned watersheds respond to rainfall, influencing whether a storm produces limited runoff, sediment-laden flows, or a debris flow.

Across California, these controls interact with contrasting rainfall regimes and storm environments. In southern California, post-fire rainfall is commonly associated with cool-season frontal systems, including atmospheric rivers, which can deliver widespread moisture and periods of intense rainfall to steep coastal mountain ranges (Oakley et al., 2017a). These events may also contain mesoscale rainbands or embedded convection that locally enhance short-duration rainfall rates over burned terrain (Oakley et al., 2018). In the Sierra Nevada, by contrast, many documented post-fire events have been linked to warm-season convective storms, which tend to produce more localized but intense rainfall pulses (De Graff et al.,

2022). This diversity in storm type suggests that post-fire hazard in California cannot be understood through rainfall totals alone; it also requires attention to the broader meteorological setting, storm structure, and spatial distribution of rainfall over burned areas.

1.2. Rainfall conditions associated with post-fire debris flows in California

The variability in climatic, topographic, and fire-regime conditions in California complicates the transfer of knowledge regarding post-fire debris flow hazard from one part of the state to another. Differences in storm type and seasonal rainfall patterns suggest that the rainfall environments associated with PFDF occurrence are unlikely to be uniform. As large wildfires have become more widespread and post-fire impacts have been documented over a broader portion of the state, there is increasing need for a more comprehensive understanding of the rainfall conditions associated with these events.

Much of the foundational understanding of PFDFs has come from Southern California and from detailed analyses of the rainfall affecting events using rain gauges in monitored watersheds. This work has been critical for identifying short-duration, high-intensity rainfall as a common trigger for runoff-generated PFDFs (Kean et al., 2011; Staley et al., 2013) and for supporting the development of rainfall thresholds and post-fire early warning approaches (Cannon et al., 2008; Staley et al., 2017). Historical observations show that debris flows can occur under a wide range of storm durations and rainfall intensities, from storms lasting only minutes to prolonged multiday events, although most storms producing debris flows are between about 30 min and 24 hr in duration, with rainfall intensities greater than about 4 mm hr^{-1} (Cannon & Gartner, 2005).

Recent PFDF documentation from Central California and the Sierra Nevada has begun to expand the geographic basis for understanding this hazard (Kostelnik et al., 2021; Neptune et

al., 2021; Thomas et al., 2023a). These emerging datasets create an opportunity to move beyond descriptions of specific events and examine rainfall conditions across a larger and more regionally diverse sample of PFDF events. Such an approach is useful for identifying whether PFDF-triggering rainfall differs spatially and temporally, supporting the interpretation and refining of early warning methods.

Chapter 2 of this dissertation addresses that need by pairing a compiled inventory of post-fire debris flow events in California with rain-gauge observations characterizing rainfall conditions associated with PFDF occurrence across California, using metrics such as storm duration, rainfall accumulation, short-duration peak intensity, and antecedent rainfall. By examining these characteristics, the study provides insights on the range of rainfall environments under which PFDFs occur in California and establishes a foundation for informing subsequent work on storm characterization and potential efforts on hazard assessments.

1.3. Radar-based characterization of precipitation systems associated with post-fire debris flows

Rain gauges have been central to identifying rainfall conditions associated with PFDF occurrence, as they can capture local rainfall timing and intensity, yet they do not indicate whether intense rainfall affected only a small portion of a burn scar or a broader area, nor do they describe the organization, movement, or morphology of the precipitation systems producing those conditions. These limitations constrain a more complete understanding of the rainfall environments affecting burned areas and associated with PFDF occurrence.

Recent studies have increasingly used radar reflectivity to characterize rainfall in post-fire settings, particularly where in situ observations are sparse, unevenly distributed, or absent

altogether (Oakley et al., 2017b, 2018; Sukup et al., 2016). The high temporal resolution of radar data is especially valuable for examining the short-duration, high-intensity rainfall commonly associated with PFDF triggering, while its spatial coverage makes it possible to verify when and where hazardous rainfall overlapped previously burned areas (De Graff et al., 2022; Liu et al., 2022; McGuire et al., 2021; Schwartz et al., 2021).

Beyond improving rainfall characterization at short time scales, the gridded structure of radar data also makes it possible to examine broader properties of the precipitation systems affecting burned landscapes. Characteristics such as storm speed, direction of propagation, areal extent, shape, and reflectivity distribution over burn scars can be computed, providing insights into how hazardous rainfall is organized and delivered over burned terrain.

Area and speed of precipitation systems help describe the spatial extent of burned-area exposure and the residence time of precipitation over susceptible landscapes, while propagation direction provides context for storm movement relative to burn scar geometry, regional flow patterns, and terrain influences that may enhance orographic precipitation. The shape also offers information about precipitation system organization, with more elongated systems often reflecting linearly organized features such as rain bands or squall lines, and more circular systems suggesting clustered or cellular convection (Markowski & Richardson, 2010). Despite this potential, the structural and spatial characteristics of precipitation systems associated with PFDFs remain relatively understudied.

Chapter 3 describes the use of a radar-based tracking approach to characterize such characteristics as well as reflectivity patterns. Through its application to documented cases, we link storm evolution and burned area exposure to intense rainfall, providing a more spatially explicit view of the rainfall environments associated with PFDF occurrence while

illustrating the potential of radar-based tracking to support situational awareness and hazard monitoring in recently burned terrain.

1.4. Atmospheric drivers of post-fire debris-flow occurrence and prediction

While previous studies have shown that post-fire debris flow likelihood is influenced by rainfall, burn severity, slope, and soil properties (Cannon et al., 2008; Staley et al., 2017; Thomas et al., 2023b), these controls are often evaluated with greater emphasis on short-term rainfall metrics and watershed characteristics than on the broader meteorological environment in which triggering storms develop. While this focus has supported important advances in hazard assessment, it leaves open the question of whether broader atmospheric and storm-structure variables can further explain why some storms generate debris flows whereas others do not.

This gap is especially relevant because existing case studies suggest that PFDF-triggering rainfall is often embedded within distinct synoptic and mesoscale environments. In southern California, several documented events have occurred during atmospheric rivers or frontal systems characterized by strong moisture transport, favorable jet dynamics, and narrow rainbands capable of producing intense short-duration rainfall, even under weak to modest instability (Oakley et al., 2017b, 2018; Schwartz et al., 2021; Sukup et al., 2016). Other events, particularly outside the cool season, point to the importance of convective storm environments in generating localized but intense rainfall over burned terrain (Oakley et al., 2025). These studies indicate that variables describing moisture transport, atmospheric water vapor, instability, and storm structure may provide information not captured by rainfall intensity and surface metrics alone, yet they remain limitedly incorporated into post-fire debris flow predictive models.

In Chapter 4, a random forest model is developed to integrate atmospheric variables, rainfall metrics, radar-derived structural properties of precipitation systems, and commonly used surface susceptibility predictors. Applied to a dataset of storms known to have triggered PFDFs as well as non-triggering storms, this framework makes it possible to evaluate which variables emerge as the most important drivers of occurrence and whether the inclusion of meteorological factors improves PFDF predictability beyond traditional approaches. The results provide a more integrated perspective on how atmospheric processes and fire-altered landscapes interact to produce post-fire debris flow hazard in California, with implications for improving hazard assessment and refining the interpretation of predictive tools.

1.5. Post-fire debris flow hazard under future climate conditions

Future changes in fire weather and extreme precipitation have each been examined extensively, however they are often assessed independently, limiting understanding of how climate change may alter the seasonal timing, spatial distribution, and cascading nature of PFDF hazard. An exclusive focus on post-fire hydrologic responses is important because increases in extreme fire weather may expand the extent of recently burned and susceptible terrain, while changes in rainfall may alter how often those landscapes are exposed to triggering conditions (Cannon & DeGraff, 2009). In California, where fire season and the onset of the rainy season can occur in close succession, even modest shifts in timing may shorten the period available for landscape recovery and extend the window of post-fire susceptibility (Oakley, 2021).

Recent studies of compound climate extremes in the western United States have begun to highlight the increasing successive occurrence of fire-prone conditions and extreme precipitation (Moftakhari & AghaKouchak, 2019; Touma et al., 2022). These studies provide

important evidence that wildfire and rainfall should be viewed as linked hazards, but their use of daily precipitation and relatively coarse spatial resolution limits their application to PFDFs, which are commonly triggered by short-duration rainfall bursts at much finer scales. More recently, Thomas et al., (2024) examined future exceedance of rainfall intensity-duration thresholds relevant to debris flow initiation using convection-permitting simulations with sub-hourly output. However, these exceedances were evaluated independently of whether they occurred over landscapes recently affected by wildfire. As a result, the sequential relationship between fire and rainfall that makes PFDFs a cascading hazard remains poorly examined at the temporal and spatial scales most relevant to their occurrence.

To study how post-fire debris flow hazard may shift under climate change, a temporally compound event framework is defined in Chapter 5, in which PFDF hazard is evaluated as the successive occurrence of extreme fire weather and rainfall exceedances relevant to debris flow-triggering. This analysis allows to estimate changes in seasonal occurrence, annual frequency, and the conditional probability that extreme fire weather events are followed by rainfall capable of triggering debris flows, thereby capturing shifts in the temporal and spatial distribution of post-fire hazard. It also allows assessment of whether recovery windows may narrow under future climate scenarios. Such findings are important for anticipating future post-fire debris flow hazard and supporting long-term adaptation and resilience planning.

1.6. Research questions

Although substantial progress has been made in understanding post-fire debris flows, important knowledge gaps remain in the characterization of rainfall associated with PFDF occurrence in California. Addressing these limitations requires an approach that considers PFDFs not merely as a problem of rainfall metrics, but as a hazard shaped by interacting

meteorological and landscape controls across multiple spatial and temporal scales. Accordingly, this dissertation examines the rainfall dimension of post-fire debris flow hazard in California using multiple datasets and observational as well as predictive perspectives, guided around the following research questions:

- What rainfall characteristics are associated with documented post-fire debris flows in California, and how do these vary by season, region, and time since fire?
- What structural and radar reflectivity characteristics define precipitation systems associated with PFDFs in California, and do they capture hazardous conditions at the time of peak short-duration rainfall?
- Among rainfall, atmospheric, and surface variables, which factors are most important for predicting PFDF occurrence, and does the inclusion of atmospheric drivers improve event predictability?
- How might future climate change alter the spatial distribution and seasonal timing of PFDF hazard in California?

The remainder of this dissertation is organized into four research chapters followed by a concluding synthesis chapter.

1.7. References

Cannon, S. H., & DeGraff, J. (2009). The Increasing Wildfire and Post-Fire Debris-Flow Threat in Western USA, and Implications for Consequences of Climate Change. In K. Sassa & P. Canuti (Eds.), *Landslides – Disaster Risk Reduction* (pp. 177–190). Springer. https://doi.org/10.1007/978-3-540-69970-5_9

Cannon, S. H., & Gartner, J. E. (2005). Wildfire-related debris flow from a hazards perspective. In M. Jakob & O. Hungr (Eds.), *Debris-flow Hazards and Related Phenomena* (pp. 363–385). Springer. https://doi.org/10.1007/3-540-27129-5_15

Cannon, S. H., Gartner, J. E., Rupert, M. G., Michael, J. A., Rea, A. H., & Parrett, C. (2010). Predicting the probability and volume of postwildfire debris flows in the intermountain

western United States. *GSA Bulletin*, *122*(1–2), 127–144. https://doi.org/10.1130/B26459.1

Cannon, S. H., Gartner, J. E., Wilson, R. C., Bowers, J. C., & Laber, J. L. (2008). Storm rainfall conditions for floods and debris flows from recently burned areas in southwestern Colorado and southern California. *Geomorphology, Debris Flows Initiated by Runoff, Erosion, and Sediment Entrainment in Western North America*, *96*(3), 250–269. https://doi.org/10.1016/j.geomorph.2007.03.019

Chong, J.-R., Renaud, J.-P., & Ailsworth, E. (2004, January 3). *Flash Floods Washed Away Lives, Dreams*. Los Angeles Times. https://www.latimes.com/archives/la-xpm-2004-jan-03-me-floods3-story.html

De Graff, J. V., Staley, D. M., Stock, G. M., Takenaka, K., Gallegos, A. L., & Neptune, C. K. (2022). Rainfall Triggering of Post-Fire Debris Flows over a 28-Year Period near El Portal, California, USA. *Environmental & Engineering Geoscience*, *28*(1), 133–145. https://doi.org/10.2113/EEG-D-21-00031

Duan, S., Ullrich, P., & Boos, W. R. (2024). Meteorological Drivers of North American Monsoon Extreme Precipitation Events. *Journal of Geophysical Research: Atmospheres*, *129*(13), e2023JD040535. https://doi.org/10.1029/2023JD040535

Gartner, J. E., Cannon, S. H., & Santi, P. M. (2014). Empirical models for predicting volumes of sediment deposited by debris flows and sediment-laden floods in the transverse ranges of southern California. *Engineering Geology*, *176*, 45–56. https://doi.org/10.1016/j.enggeo.2014.04.008

Gartner, J. E., Kean, J. W., Rengers, F. K., McCoy, S. W., Oakley, N., & Sheridan, G. (2024). Post-Wildfire Debris Flows. In M. Jakob, S. McDougall, & P. Santi (Eds.), *Advances in Debris-flow Science and Practice* (pp. 309–345). Springer International Publishing. https://doi.org/10.1007/978-3-031-48691-3_11

Johnson, B. O., & Delworth, T. L. (2023). The Role of the Gulf of California in the North American Monsoon. *Journal of Climate*, *36*(6), 1541-1559.https://doi.org/10.1175/JCLI-D-22-0365.1

Kean, J. W., & Staley, D. M. (2021). Forecasting the Frequency and Magnitude of Postfire Debris Flows Across Southern California. *Earth's Future*, *9*(3), e2020EF001735. https://doi.org/10.1029/2020EF001735

Kean, J. W., Staley, D. M., & Cannon, S. H. (2011). In situ measurements of post-fire debris flows in southern California: Comparisons of the timing and magnitude of 24 debris-flow events with rainfall and soil moisture conditions. *Journal of Geophysical Research: Earth Surface*, *116*(F4). https://doi.org/10.1029/2011JF002005

Keller, E., Adamaitis, C., Alessio, P., Goto, E., & Gray, S. (2020). Montecito debris flows of 9 January 2018: Physical processes and social implications. In R. V. Heermance & J. J. Schwartz (Eds.), *From the Islands to the Mountains: A 2020 View of Geologic Excursions*

in Southern California (Vol. 59, p. 0). Geological Society of America. https://doi.org/10.1130/2020.0059(03)

Kostelnik, J., Rengers, F. K., Wald, L., & Schmitt, R. (2021, December 17). *Northern and Central California Debris Flows Overview*. ArcGIS StoryMaps. https://storymaps.arcgis.com/stories/d6c9dc95f0f84fb1994a164f18115fa5

Liu, T., McGuire, L. A., Oakley, N., & Cannon, F. (2022). Temporal changes in rainfall intensity–duration thresholds for post-wildfire flash floods in southern California. *Natural Hazards and Earth System Sciences*, *22*(2), 361–376. https://doi.org/10.5194/nhess-22-361-2022

Markowski, P., & Richardson, Y. (2010). *Mesoscale Meteorology in Midlatitudes*. John Wiley and Sons. https://doi.org/10.1002/9780470682104

McGuire, L. A., Ebel, B. A., Rengers, F. K., Vieira, D. C. S., & Nyman, P. (2024). Fire effects on geomorphic processes. *Nature Reviews Earth & Environment*, *5*(7), 486–503. https://doi.org/10.1038/s43017-024-00557-7

McGuire, L. A., Rengers, F. K., Oakley, N., Kean, J. W., Staley, D. M., Tang, H., de Orla-Barile, M., & Youberg, A. M. (2021). Time Since Burning and Rainfall Characteristics Impact Post-Fire Debris-Flow Initiation and Magnitude. *Environmental & Engineering Geoscience*, *27*(1), 43–56. https://doi.org/10.2113/EEG-D-20-00029

Moftakhari, H., & AghaKouchak, A. (2019). Increasing exposure of energy infrastructure to compound hazards: Cascading wildfires and extreme rainfall. *Environmental Research Letters*, *14*(10), 104018. https://doi.org/10.1088/1748-9326/ab41a6

Neptune, C. K., Degraff, J. V., Pluhar, C. J., Lancaster, J. T., & Staley, D. M. (2021). Rainfall Thresholds for Post-Fire Debris-Flow Generation, Western Sierra Nevada, CA. *Environmental & Engineering Geoscience*, *27*(4), 439–453. https://doi.org/10.2113/EEG-D-21-00039

Oakley, N. S. (2021). A Warming Climate Adds Complexity to Post-Fire Hydrologic Hazard Planning. *Earth's Future*, *9*(7), e2021EF002149. https://doi.org/10.1029/2021EF002149

Oakley, N. S., Cannon, F., Munroe, R., Lancaster, J. T., Gomberg, D., & Ralph, F. M. (2018). Brief communication: Meteorological and climatological conditions associated with the 9 January 2018 post-fire debris flows in Montecito and Carpinteria, California, USA. *Natural Hazards and Earth System Sciences*, *18*(11), 3037–3043. https://doi.org/10.5194/nhess-18-3037-2018

Oakley, N. S., Cheung, D. J., Lindsay, D. N., & Nash, D. (2025). Insights from a 25-year database of post-fire debris flows in California. *International Journal of Wildland Fire*, *34*(12), WF25136. https://doi.org/10.1071/WF25136

Oakley, N. S., Lancaster, J. T., Kaplan, M. L., & Ralph, F. M. (2017a). Synoptic conditions associated with cool season post-fire debris flows in the Transverse Ranges of southern California. *Natural Hazards*, *88*(1), 327–354. https://doi.org/10.1007/s11069-017-2867-6

Oakley, N. S., Lancaster, J. T., Kaplan, M. L., & Ralph, F. M. (2017b). Synoptic conditions associated with cool season post-fire debris flows in the Transverse Ranges of southern California. *Natural Hazards*, *88*(1), 327–354. https://doi.org/10.1007/s11069-017-2867-6

Santi, P., Cannon, S., & DeGraff, J. (2013). 13.16 Wildfire and Landscape Change. In J. F. Shroder (Ed.), *Treatise on Geomorphology* (pp. 262–287). Academic Press. https://doi.org/10.1016/B978-0-12-374739-6.00365-1

Schwartz, J. Y., Oakley, N. S., & Alessio, P. (2021). Assessment of a Post-Fire Debris Flow Impacting El Capitan Watershed, Santa Barbara County, California, U.S.A. *Environmental & Engineering Geoscience*, *27*(4), 423–437. https://doi.org/10.2113/EEG-D-21-00008

Staley, D. M., Kean, J. W., Cannon, S. H., Schmidt, K. M., & Laber, J. L. (2013). Objective definition of rainfall intensity–duration thresholds for the initiation of post-fire debris flows in southern California. *Landslides*, *10*(5), 547–562. https://doi.org/10.1007/s10346-012-0341-9

Staley, D. M., Negri, J. A., Kean, J. W., Laber, J. L., Tillery, A. C., & Youberg, A. M. (2017). Prediction of spatially explicit rainfall intensity–duration thresholds for post-fire debris-flow generation in the western United States. *Geomorphology*, *278*, 149–162. https://doi.org/10.1016/j.geomorph.2016.10.019

Staley, D. M., Tillery, A. C., Kean, J. W., McGuire, L. A., Pauling, H. E., Rengers, F. K., & Smith, J. B. (2018). Estimating post-fire debris-flow hazards prior to wildfire using a statistical analysis of historical distributions of fire severity from remote sensing data. *International Journal of Wildland Fire*, *27*(9), 595–608. https://doi.org/10.1071/WF17122

Sukup, S., Laber, J., Sweet, D., & Thompson, R. (2016). *Analysis of an Intense Narrow Cold Frontal Rainband and the Springs Fire Burn Area Debris Flows of 12 December 2014*. https://www.weather.gov/media/wrh/online_publications/TAs/TA1601.pdf

Thomas, M. A., Kean, J. W., McCoy, S. W., Lindsay, D. N., Kostelnik, J., Cavagnaro, D. B., Rengers, F. K., East, A. E., Schwartz, J. Y., Smith, D. P., & Collins, B. D. (2023a). Postfire hydrologic response along the Central California (USA) coast: Insights for the emergency assessment of postfire debris-flow hazards. *Landslides*, *20*(11), 2421–2436. https://doi.org/10.1007/s10346-023-02106-7

Thomas, M. A., Kean, J. W., McCoy, S. W., Lindsay, D. N., Kostelnik, J., Cavagnaro, D. B., Rengers, F. K., East, A. E., Schwartz, J. Y., Smith, D. P., & Collins, B. D. (2023b). Postfire hydrologic response along the Central California (USA) coast: Insights for the emergency assessment of postfire debris-flow hazards. *Landslides*. https://doi.org/10.1007/s10346-023-02106-7

Thomas, M. A., Michaelis, A. C., Oakley, N. S., Kean, J. W., Gensini, V. A., & Ashley, W. S. (2024). Rainfall intensification amplifies exposure of American Southwest to conditions that trigger postfire debris flows. *Npj Natural Hazards*, *1*(1), 14. https://doi.org/10.1038/s44304-024-00017-8

Touma, D., Stevenson, S., Swain, D. L., Singh, D., Kalashnikov, D. A., & Huang, X. (2022). Climate change increases risk of extreme rainfall following wildfire in the western United States. *Science Advances*, *8*(13), eabm0320. https://doi.org/10.1126/sciadv.abm0320

Chapter 2

2. Rainfall conditions of post-fire debris flows between 2014 – 2022 across regions in California

Abstract

Post-fire debris flows in California are commonly associated with Southern California, where the hazard has been studied most extensively. Yet PFDFs also occur in other regions of the state, where climate, storm type, and topography differ sharply. These regional differences suggest that rainfall conditions associated with PFDF occurrence may vary across California, but such environments remain less well understood. This study characterizes rainfall conditions using a compiled inventory of PFDF events paired with rain-gauge observations. Storm duration, cumulative rainfall, average intensity, and peak 15-, 30-, and 60-min intensity were examined through descriptive comparisons across regions, along with statistical testing by season and time since fire. In addition, a precipitation-cluster analysis was used to describe the broader antecedent rainfall context of PFDF occurrence. The strongest contrasts in the inventory were seasonal: Fall/Winter events were linked to longer and wetter storms, whereas Spring/Summer events were generally shorter and more intense on average. Events within the first year after fire were likewise associated with longer and more variable storms than those occurring later. By contrast, peak short-duration intensities showed substantial overlap across seasonal and post-fire timing groups, suggesting that similar high-intensity rainfall bursts can develop within markedly different storm environments. Regional contrasts were also apparent, particularly in Central California and Coastal Mountains, where PFDF events were associated with longer storm durations, higher

accumulations, and more persistent antecedent precipitation clustering. Overall, the results show that storms associated with PFDF occurrence in California range from short, relatively isolated events to prolonged wet-season storms embedded within broader storm sequences, highlighting the contrast of rainfall settings under which this hazard occurs.

2.1. Introduction

Post-fire debris flows are hazardous events generated by the interaction between wildfire and subsequent rainfall, often producing severe impacts on both landscapes and communities. Wildfire removes vegetation and alters soil properties, reducing soil strength, increasing water repellency, and enhancing runoff potential (Shakesby & Doerr, 2006). As a result, when rainfall occurs over recently burned terrain, the likelihood of triggering landslides, including debris flows, increases. A notable example occurred in the Thomas Fire burn area near Montecito, California, where a storm on 9 January 2018 triggered multiple debris flows that caused 23 fatalities and damaged more than 130 homes (Lukashov et al., 2019).

Research on PFDFs has focused primarily on Southern California, where important advances have been made in understanding the rainfall conditions associated with debris flow initiation (Cannon & Gartner, 2005; Gartner et al., 2008, 2014; Kean et al., 2013; Staley et al., 2018, 2020). These studies have contributed to the development of rainfall thresholds used to assess the potential for post-fire flooding and debris flows in recently burned areas. For example, (Cannon et al., 2008) proposed intensity-duration thresholds for Ventura County and for Southern California, where rainfall intensity is expressed as a function of storm duration. Likewise, after approximately one year of vegetative recovery and sediment removal, the threshold in Southern California mountains increases substantially relative to the first year after fire.

Using precise timing of debris flow initiation in instrumented watersheds, (Staley et al., 2013) further demonstrated that rainfall intensity over short intervals (≤ 60 min) is a better predictor of post-fire debris flow initiation than longer-duration rainfall measurements. Building on this work, (Staley et al., 2017) developed models to predict spatially explicit rainfall intensity-duration thresholds for post-fire debris flow generation in the western United States using Southern California events as training data. The results showed that the most accurate model incorporated variables such as, the normalized burn ratio, soil erodibility index in the fine fraction and the proportion of upslope area burned at high or moderate severity with gradients greater than 23°. When tested in locations outside California but within the southwestern United States, the model performed comparably or slightly better than other developed models, closely aligning with existing regional thresholds.

Despite these advances, comparatively less attention has been given to PFDFs in other parts of California, where hydroclimatic and landscape conditions differ markedly from those of Southern California. This limits the broader application of existing knowledge and complicates efforts to expand mitigation strategies across the state. California exhibits strong spatial contrasts in precipitation, with 1991–2020 annual totals ranging from about 100 mm in the southeastern desert regions to nearly 4000 mm in the northwestern part of the state (PRISM Climate Group, 2022). Wildfire occurrence and density also vary substantially across California because of differences in vegetation, terrain, and climate. For example Li & Banerjee (2021) showed that areas of very high wildfire density, once concentrated mainly in Los Angeles County, have expanded in recent decades into Ventura, Riverside, San Diego, and San Bernardino Counties. These variations suggest that the rainfall conditions associated

with PFDF occurrence may also vary across regions and should not be assumed to be uniform statewide.

This study addresses that gap by pairing a compiled inventory of post-fire debris flow events in California with rain-gauge observations to characterize the triggering storms. It examines storm duration, rainfall accumulation, short-duration peak intensity, and antecedent rainfall to describe how the rainfall environments associated with PFDF occurrence vary across regions, seasons, and time since fire. In doing so, this investigation provides a descriptive framework for understanding the diversity of rainfall settings under which PFDFs occur in California and for guiding future regional analyses of this hazard. The structure of the paper is as follows: Section 2.2 describes the methods used to compile the inventory and analyze the associated rainfall conditions, including the exploratory statistical comparisons and antecedent precipitation-cluster analysis. Section 2.3 presents the results, focusing on how rainfall variables vary across seasons, time since fire, and regions. Section 2.4 discusses the findings in the context of previous work on post-fire debris flows, outlines the main limitations of the study, and points to directions for future research.

2.2. Data and methods

2.2.1. Post-fire debris-flow inventory and spatial grouping

To analyze post-fire debris flow hazards, a catalog of events documented across California between 2014 and 2022 was compiled. Sources included existing landslide inventories, such as the Reported California Landslides Database (California Geological Survey, 2023) and the NASA Global Landslide Catalog (Kirschbaum et al., 2010), as well as events reported in newspapers, technical reports, and scientific studies (De Graff et al., 2022; Felling et al., 2019;

Graber, 2023; Guilinger et al., 2020; Kostelnik et al., 2021; McGuire et al., 2018; Neptune et al., 2021; Oakley et al., 2017; Schwartz et al., 2021; Staley et al., 2018; Thomas, Kean, et al., 2023; Thomas, Lindsay, et al., 2023). Because the inventory was assembled from multiple source types, only events described as post-fire debris flows or with evidence to be field verified were retained. Where initiation mechanisms were discussed in the original sources, events were described as runoff-dominated post-fire debris flows and no reclassification of initiation mechanisms was performed beyond the descriptions provided in the source material. The 2014–2022 period was selected based on the availability of high-temporal-resolution rainfall observations from publicly accessible rain gauges, which were used to characterize the storm conditions associated with each event.

To associate each debris flow event with a wildfire, events described in inventories as "debris flow" or "mudslide" were intersected with fire polygons, and only those occurring within three years after the fire were retained. Because rainfall–response relationships evolve following wildfire due to vegetation recovery and changes in sediment availability, analyses were conducted for two post-fire temporal windows; post-fire year 1, defined as events occurring within 365 days of wildfire ignition, and post-fire years > 1, defined as events occurring more than one year and up to two years following ignition. Comparing these subsets allows assessment of how inclusion of later post-fire events influences the distribution of rainfall characteristics.

To capture broad geographic differences in rainfall and landscape conditions across California, each event was initially assigned to one of the 13 ecoregions defined by Griffith et al., (2016). In the compiled inventory, however, events were represented in only six of these ecoregions: Southern California Mountains, Southern California/Northern Baja Coast, Sierra

Nevada, Central California Foothills and Coastal Mountains, Coast Range, and Central Basin and Range. Because sample sizes varied substantially among individual ecoregions, events were aggregated into three broader regional groups for analysis. Southern California Mountains and Southern California/Northern Baja Coast were combined into a Southern California group, Central California Foothills and Coastal Mountains and Coast Range, were grouped as Central California and Coastal Mountains, while Central Basin Range was integrated into Sierra Nevada as one category (Table 2.1). This aggregation reduced the influence of sparsely represented categories and allowed for more meaningful comparisons among regions.

2.2.2. Rain gauge selection and rainfall metrics

Rainfall conditions were characterized using sub-hourly observations from the nearest rain gauge located within 8 km of the event coordinates. This distance threshold is consistent with prior studies that balance spatial representativeness with sample-size limitations when using rain gauge observations to characterize rainfall conditions (Thomas, Kean, et al., 2023). Because the precise timing of debris flow initiation was not always available, the documented event date was used as a temporal reference for identifying the triggering storm.

Storm duration and peak-intensity intervals were defined following Staley et al. (2013). Specifically, storm duration was defined as a continuous rainfall period with no interruption longer than 8 h, a criterion used to distinguish short-duration, high-intensity convective storms from longer-duration, lower-intensity frontal storms in California. Peak intensities were calculated over intervals of 60 min or less because these short-duration intensities have been shown to be particularly relevant for post-fire debris flow initiation. For each PFDF event, rainfall metrics were computed to describe storm timing, magnitude, and intensity:

- Storm duration (h): elapsed time from storm start to storm end.
- Storm cumulative rainfall (mm): total rainfall accumulated over the storm.
- Peak rainfall intensities (mm h^{-1}): maximum intensities over 15-min, 30-min, and 60-min intervals (I_{15}, I_{30}, I_{60}).

2.2.3. Statistical analysis and antecedent precipitation clustering

Regional, seasonal, and fire-timing differences in rainfall variables were evaluated using nonparametric tests because the rainfall metrics did not meet assumptions of normality. For comparisons involving two independent groups, including season and time since fire, the Mann–Whitney U test was used. This test ranks all observations from both groups together and evaluates whether one group tends to have systematically higher or lower values than the other. Regional comparisons involved more than two groups and were therefore first evaluated using the Kruskal–Wallis test, which provides an overall test of whether at least one regional group differs from the others. When the Kruskal–Wallis test was significant, pairwise Mann–Whitney U tests were then used as comparisons to identify which specific regional pairs differed. In this context, "pairwise" means that the Mann–Whitney U test was applied separately to each pair of regions.

In addition, clusters of moderate-to-extreme antecedent rainfall were identified to characterize the broader hydroclimatic context in which triggering storms occurred. This analysis is not used to infer the direct trigger of post-fire debris flow initiation, which is more commonly associated with short-duration, high-intensity rainfall. Rather, it is used to examine whether PFDF events were accompanied by unusually frequent rainfall in the days preceding the event and how this context differed across regions and seasons.

Daily precipitation data were obtained from the Daymet dataset, a gridded surface weather product with 1 km spatial resolution and daily temporal resolution (Thornton et al., 2014). Daymet provides spatially continuous estimates of daily meteorological variables across North America, including precipitation, allowing antecedent precipitation conditions to be characterized at each PFDF location. Following the approach of Bevacqua et al. (2021), days with precipitation exceeding the 85th percentile of the local daily precipitation distribution during the year preceding each PFDF storm were classified as moderate-to-extreme precipitation events. For each PFDF event, antecedent precipitation was evaluated within a moving temporal window of up to 90 days preceding storm onset. A precipitation cluster was defined when the number of moderate-to-extreme precipitation days within a given window exceeded the 95th percentile of a binomial distribution, assuming a constant daily probability of precipitation exceedance. In this framework, each day in the antecedent window was treated as a binary outcome: either precipitation exceeded the local 85th percentile threshold, or it did not. For example, if a 30-day antecedent window contained more exceedance days than would be expected based on the local daily exceedance probability, that window was classified as a precipitation cluster. This approach identifies periods when moderate-to-extreme precipitation days were unusually concentrated before a PFDF event.

2.3.Results

The catalog includes 69 post-fire debris flow events between 2014 to 2022, associated with 21 wildfires that occurred between 2013 and 2021 (Figure 2.1), with burned areas ranging from 747 acres in the Silverado Fire to 963,406 acres in the Dixie Fire. Events were most frequent in Southern California (37 events; 54%), followed by Central California and Coastal Mountains (16 events; 23%) and the Sierra Nevada (16 events; 23%, Table 2.1). Most events

occurred during fall and winter (50 events, 72%), whereas the remainder were recorded in spring and summer, with no occurrences documented in April or May. All events in Central California and Coastal Mountains in this inventory occurred during fall and winter, while Southern California and Sierra Nevada events were distributed across both seasonal groupings.

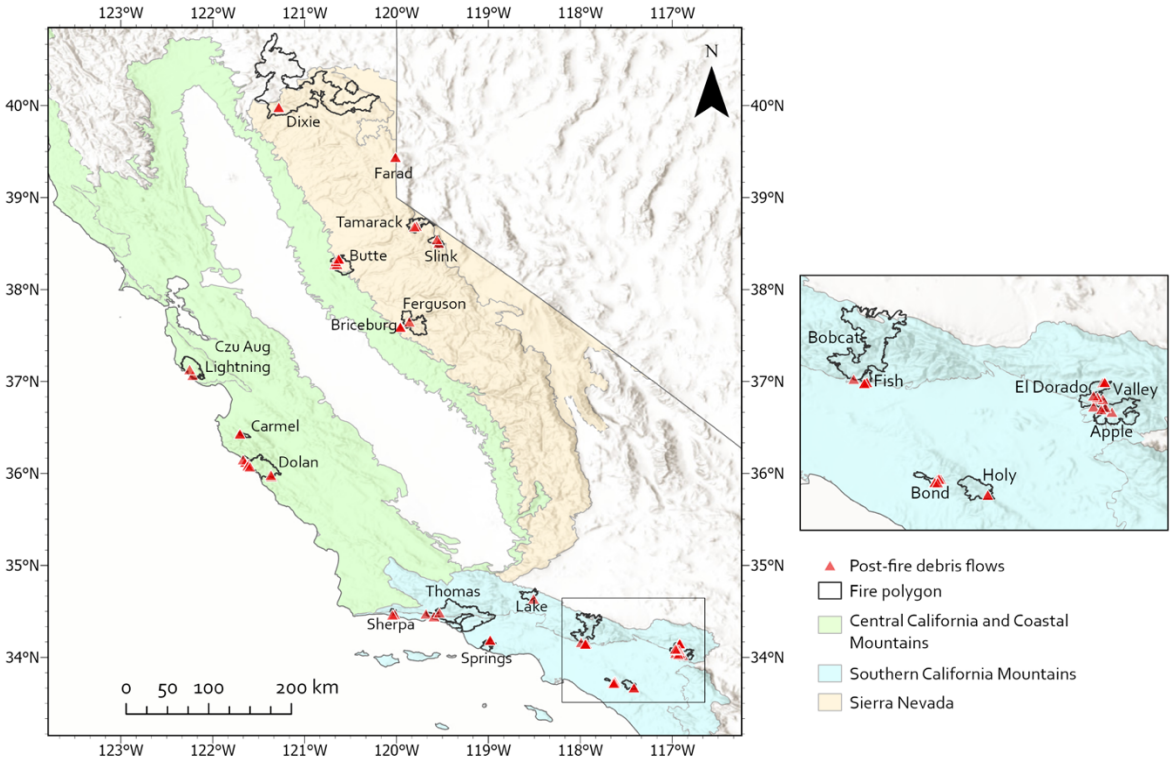


Figure 2.1. Post-fire debris flow events and associated fire perimeters across California. Red triangles indicate documented post-fire debris flow locations, and black outlined polygons show the corresponding fire perimeters. Colored polygons represent the broader regional groups used in the analysis, aggregated from California ecoregions defined by Griffith et al., (2016). The inset highlights Southern California, where events are more densely clustered.

Table 2.1. Distribution of post-fire debris flow events in California by broader regional group and original region classification (Griffith et al., 2016), with event counts for post-fire year 1 and post-fire years > 1.

Broader region	Ecoregion (Griffith et al., 2016)	Number of events ≤ 1 year	Number of events > 1 year

		after fire	after fire
Southern California	Southern California Mountains	9	10
	Southern California/Northern Baja Coast	14	4
	Total	**37**	
Sierra Nevada	Sierra Nevada	10	5
	Central Basin and Range	1	0
	Total	**16**	
Central California and Coastal Mountains	Central California Foothills and Coastal Mountains	12	2
	Coast Range	2	0
	Total	**16**	

Regarding the timing after the wildfire, debris flows in burned areas were triggered by 29 unique rainstorms, with the earliest occurring just 35 days after the ignition date, as seen in the Thomas fire. Additionally, 70% of the debris flows occurred within the first year following ignition, while 22% occurred in the second year. These temporal and spatial patterns are also reflected in the triggering rainfall, with fall and winter events showing a broader range of storm durations and spring and summer events tending to exhibit higher average rainfall intensities (Figure 2.2). More detailed comparisons of rainfall characteristics across region, season, and post-fire timing further highlight this variability. Regional differences first evaluated using the Kruskal–Wallis test, indicated significant differences in storm duration, cumulative rainfall, and peak 15-, 30-, and 60-minute rainfall intensity, but not in average storm intensity.

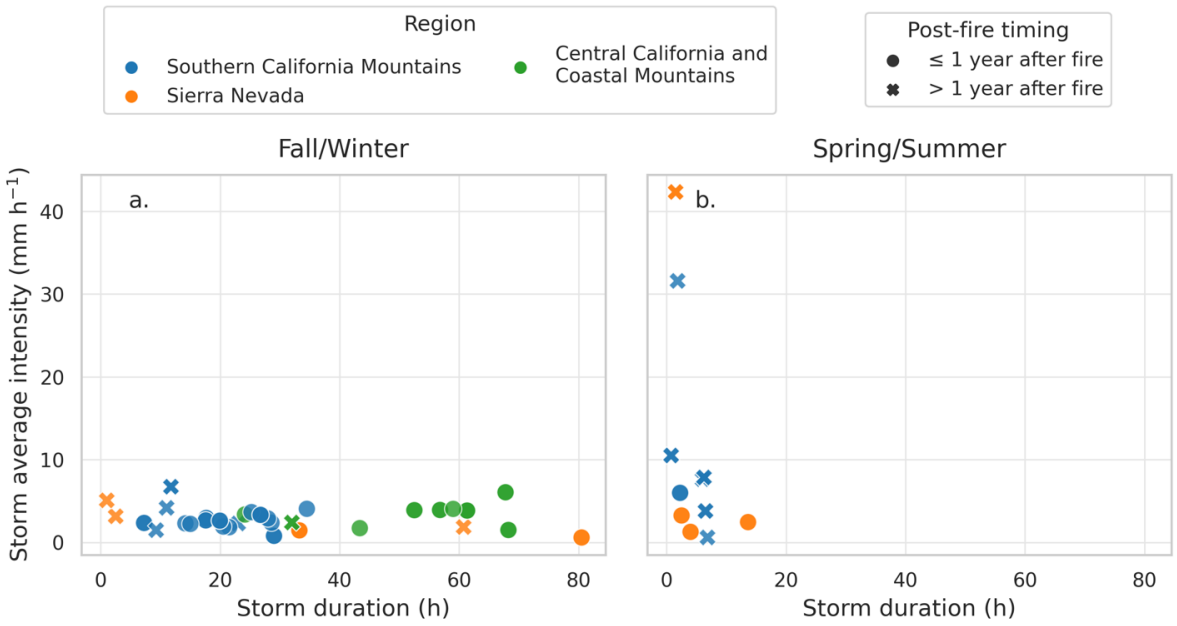


Figure 2.2. Relationship between storm duration and average storm intensity for post-fire debris flow events in California. Panels show events occurring during **a.** Fall/Winter and **b.** Spring/Summer. Point colors indicate the broader regional grouping used in the analysis, and marker type distinguishes events occurring within the first year after fire from those occurring later.

2.3.1. Storm duration

Storm durations associated with post-fire debris flow initiation ranged from 45 min to 80.5 h, indicating that these events were triggered by both short-duration storms and prolonged rainfall episodes, as described in the literature (Cannon & Gartner, 2005). The shortest duration was observed during a summer storm on September 12, 2022 associated with the El Dorado Fire, whereas the longest duration occurred during a winter storm in March 2016 associated with the Butte Fire. Differences are observed among regions (Figure 2.3a). Overall, storm duration in post-fire debris flow producing storms has a median of 19 h and a mean of 26 h, with an interquartile range between 6.5 and 33 h. Southern California is characterized by generally shorter storm durations, with approximately 75% of events occurring below 23 h and a median near 15 h. The Sierra Nevada shows a broader spread, including many short-

duration storms but also 37% of events extending beyond 30 h, including the longest duration event in the inventory. In contrast, Central California and Coastal Mountains is distinguished by consistently long-duration storms, with a median near 58 h and all values exceeding 24 h. This regional contrast was supported by pairwise Mann–Whitney U tests, which indicated that Central California and Coastal Mountains differed significantly from both Southern California Mountains and the Sierra Nevada, whereas no significant differences were identified between the latter two regions.

Seasonal differences are also pronounced (Figure 2.3b). Storms occurring in spring and summer are generally short-lived, with a median duration of 4 h, 90% of events lasting less than 10 h, and only two events reaching about 13 h. By comparison, fall and winter events span a much wider range, with a median and mean duration of 28 h and 34 h, respectively, from short storms to multiday rainfall episodes.

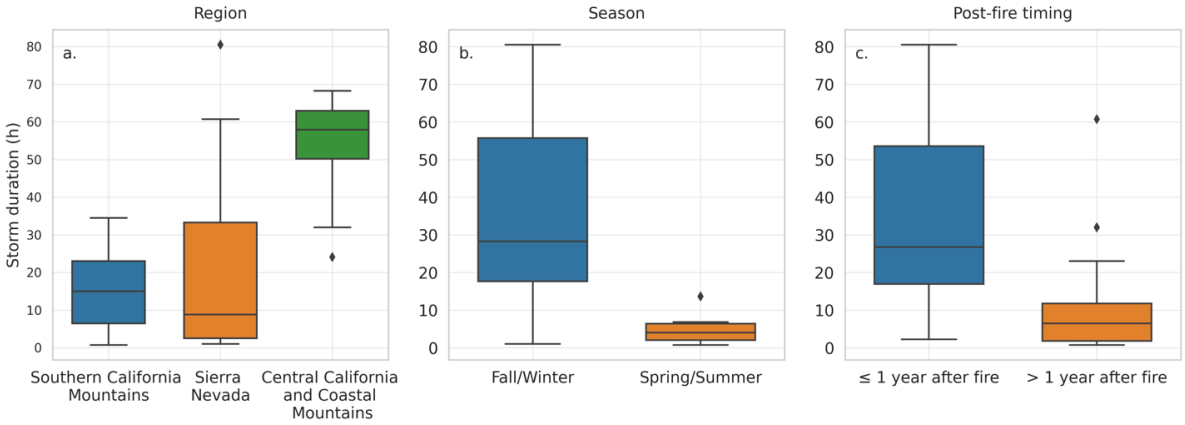


Figure 2.3. Distribution of storm duration for post-fire debris flow events across California by **a.** region, **b.** season, and **c.** post-fire timing. Boxes show the interquartile range, center lines indicate the median, whiskers extend to 1.5 times the interquartile range, and diamonds represent outliers.

A similar pattern is evident when durations are grouped by time since fire (Figure 2.3c). Events occurring within the first year after wildfire show substantially greater variability and include the longest-duration storms with a mean of 32 h and a median of 27 h, whereas events

occurring more than one year after fire are more concentrated at shorter durations, with 75% lasting less than about 12 h. Mann–Whitney U tests indicated that storm duration differed significantly both between seasonal groupings and between fire-timing classes ($p < 0.05$). These results indicate that long-duration storms are primarily associated with fall/winter conditions and with events occurring during the first year after fire, while shorter storm durations are more common in spring/summer and in later post-fire years.

2.3.2. Cumulative rainfall and average intensity

Storm cumulative rainfall associated with post-fire debris flow initiation showed clear differences across regions, seasons, and fire-timing classes (Figure 2.4). By region, Central California and Coastal Mountains exhibited the highest cumulative rainfall values, with a median near 213 mm, all events exceeding approximately 75 mm and the maximum reaching more than 400 mm in the Dolan fire. In contrast, although Southern California and the Sierra Nevada showed broadly comparable cumulative rainfall distributions, median values were below 50 mm, with Southern California showing a higher mean, 47 mm, compared to 36 mm in Sierra Nevada. Similar to storm duration, pairwise Mann–Whitney U tests indicated that Central California and Coastal Mountains differed significantly from both Southern California Mountains and the Sierra Nevada, while the latter two regions remained statistically similar.

Fall/Winter events were associated with greater cumulative rainfall, with a median of 71.2 mm, a wider spread with an interquartile range between 47 and 102 mm, and all of the largest totals in the inventory (Figure 2.4b). Spring/Summer events were generally characterized by lower rainfall totals, with a median and a mean of 24.64 and 27.2 mm, respectively, and most values below 65 mm. A similar but weaker contrast is observed by post-fire timing (Figure 2.4c). Events occurring within the first year after wildfire span a broader range of cumulative

rainfall values, including the highest totals, with a median of 52 mm and a higher mean of 94 mm. In contrast, events occurring more than one year after fire are concentrated at lower accumulations, with a median of 49.02 mm and a similar value for mean, 45 mm. Mann–Whitney U tests indicated that cumulative rainfall differed significantly between seasonal groupings, but not between post-fire timing classes.

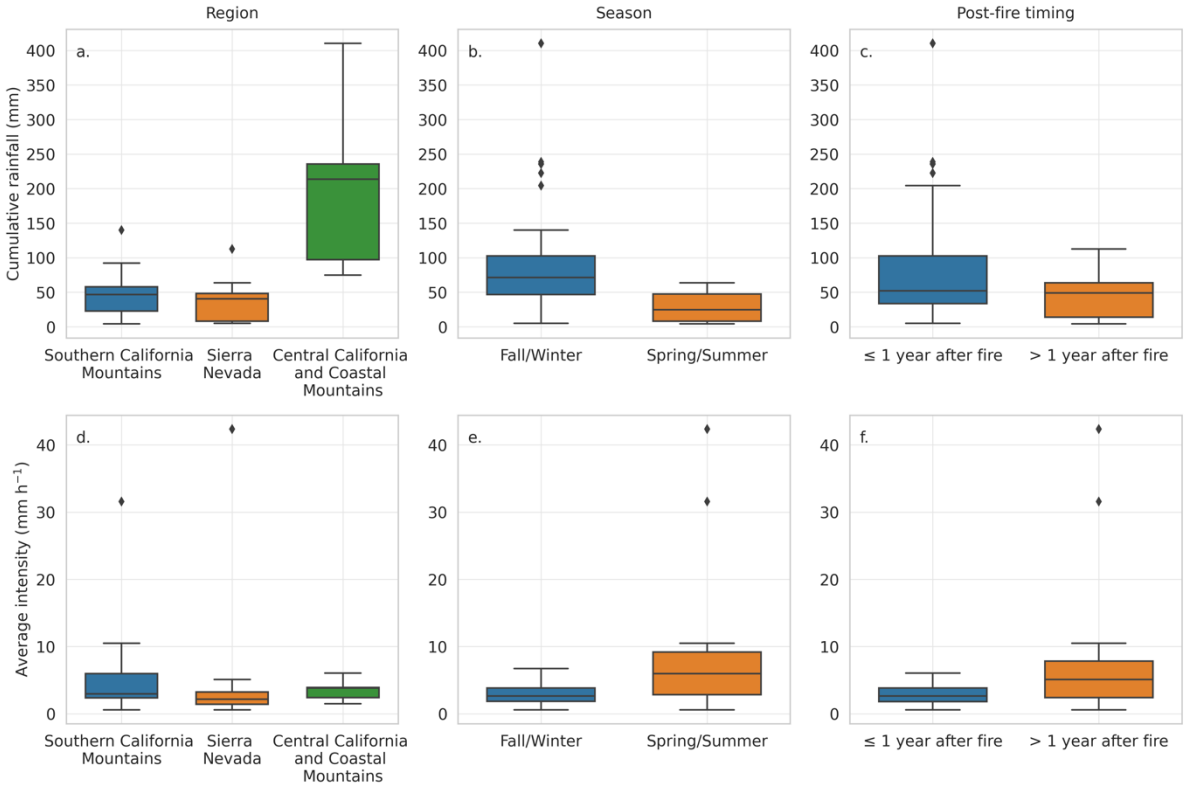


Figure 2.4. Distribution of storm cumulative rainfall **(a–c)** and average storm intensity **(d–f)** for post-fire debris flow events across California by region, season, and time since fire. Boxes show the interquartile range, center lines indicate the median, whiskers extend to 1.5 times the interquartile range, and diamonds represent outliers.

Average storm intensity varied less by region than cumulative rainfall, suggesting that regional contrasts are expressed more strongly in storm duration and total accumulation than in storm rate alone (Figure 2.4d). Values ranged from 0.42 to 42.33 mm h^{-1}, with Sierra Nevada exhibiting the lowest median intensity (2.15 mm h^{-1}). Southern California displayed the greatest spread, including an outlier of 31.6 mm h^{-1}, a summer storm in the Apple fire,

with a regional median and mean of 2.94 and 4.63 mm h^{-1}, respectively. Central California and Coastal Mountains was characterized by more moderate intensities overall (median = 3.84 mm h^{-1}, mean = 3.5 mm h^{-1}). Average storm intensity did not differ significantly across regions based on the Kruskal–Wallis test, consistent with the substantial overlap in regional distributions.

Differences emerged by season and fire timing. Spring/Summer events were associated with a higher median for average intensities than Fall/Winter events (5.98 versus 2.66 mm h^{-1}), and events occurring more than one year after fire also had higher median average intensities than those within the first year after fire (5.08 versus 2.66 mm h^{-1}). Mann–Whitney U tests indicated that average storm intensity differed significantly both between seasonal groupings and between post-fire timing classes.

2.3.3. Peak 15-min intensity

Peak 15-min rainfall intensities ranged from approximately 4 to 103 mm h^{-1}, capturing both relatively modest short-duration rainfall rates and highly intense bursts of rainfall associated with PFDF events. By region, Southern California and the Sierra Nevada showed similar median values, both near 23 mm h^{-1}, although Southern California Mountains displayed a broader spread and included the highest values in the inventory including the debris flows associated with the winter storm over the Thomas Fire burn area on 9 January 2018 (Figure 2.5a). In contrast, the Central California and Coastal Mountains region was characterized by generally higher peak 15-min intensities, with a median near 45 mm h^{-1} and the lower quartile of events in this group was above the median values observed in the other two regions. Pairwise comparisons indicated that the higher peak 15-min intensities in Central California and Coastal Mountains were statistically distinct from those in the other two

regions, while Southern California Mountains and the Sierra Nevada continued to show substantial overlap.

Seasonal and post-fire timing differences were less pronounced (Figure 2.5b,c). Spring/Summer events had a slightly higher median peak 15-min intensity than Fall/Winter events (28.45 versus 26.42 mm h^{-1}), but the interquartile ranges overlapped substantially. A similar pattern is observed in events occurring more than one year after fire, which showed similar values to those within the first year (28.45 versus 24.38 mm h^{-1}). Mann–Whitney U tests indicated that peak 15-min intensity did not differ significantly between seasonal groupings or between fire-timing classes.

Peak rainfall intensities calculated over 30-min and 60-min intervals showed patterns broadly consistent with those observed for peak 15-min intensity (Figure 2.5d–i). Central California and Coastal Mountains continued to exhibit generally higher values, particularly for peak 60-min intensity (median = 26.1 mm h^{-1}), whereas Southern California and the Sierra Nevada showed lower medians and greater overlap. This same regional contrast remained statistically supported in pairwise comparisons. Seasonal and fire-timing differences remained modest for both intervals. Despite Spring/Summer events and events occurring more than one year after fire tended to show slightly higher median values, the distributions overlapped substantially in all comparisons. Mann–Whitney U tests likewise indicated no significant differences in peak 30-min or peak 60-min intensity between seasonal groupings or fire-timing classes.

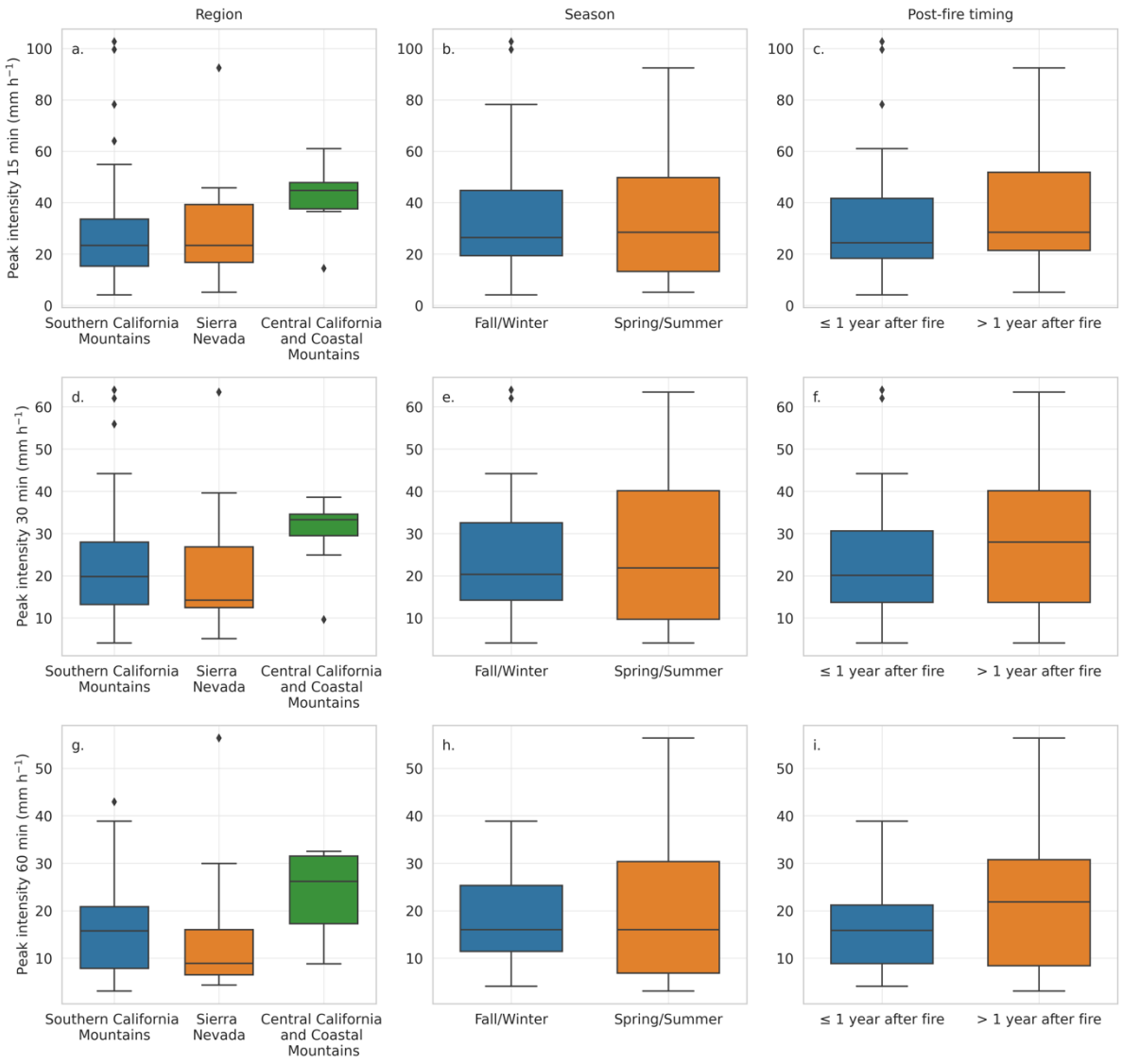


Figure 2.5. Distribution of peak rainfall intensity measured over 15-min (a–c), 30-min (d–f), and 60-min (g–i) intervals for post-fire debris flow events across California by region, season, and time since fire. Boxes show the interquartile range, center lines indicate the median, whiskers extend to 1.5 times the interquartile range, and diamonds represent outliers.

High values of 15-min intensities can occur under contrasting storm conditions. Figure 2.6 illustrates two representative examples. The highest peak 15-min intensity in the catalog, reaching 102.6 mm h^{-1}, was associated with the Montecito post-fire debris flows in the Thomas Fire burn area on 9 January 2018. This storm delivered 90.67 mm of rain over 26.6 h, beginning on 8 January at 00:08 PST, with peak intensity reached on 9 January at 04:02

PST. This event exemplifies how very high short-duration intensities can occur within prolonged winter storms, likely influenced by mesoscale features such as Narrow Cold Frontal Rainbands (NCFR; Oakley et al., 2018). In contrast, elevated peak 15-min intensities can also occur during short-duration summer storms (Figure 2.6b), as illustrated by the event within the Tamarack Fire perimeter in the Sierra Nevada. That storm delivered 63.5 mm of rain in just 1.5 h and reached a peak 15-min intensity of 92.45 mm h^{-1} at 15:50 PST on 3 August 2022, only 50 min after the beginning of the storm. No antecedent rainfall was recorded in the days preceding this event.

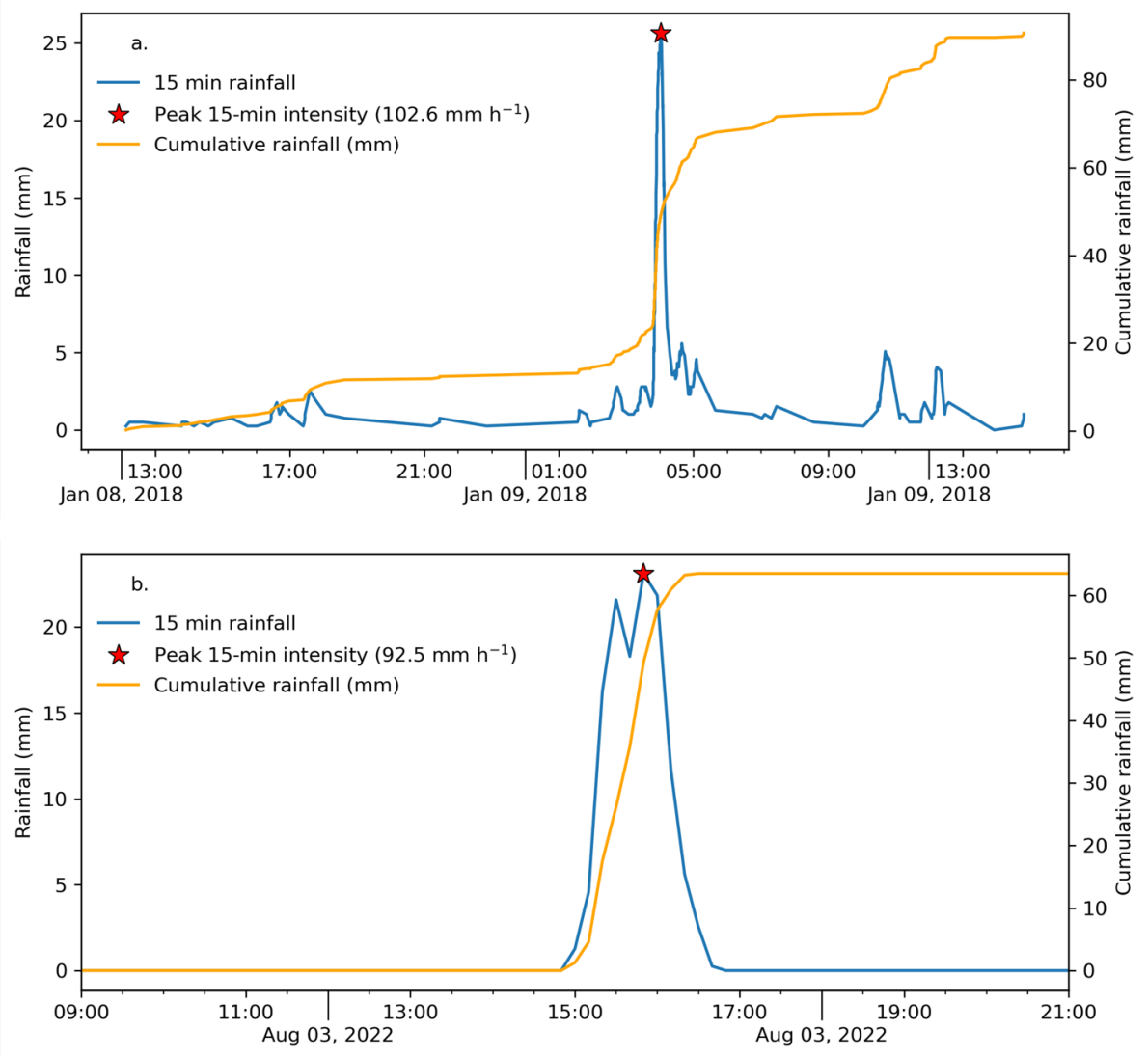


Figure 2.6. Rainfall time series depicting high peak-15 min intensity events **a.** during a winter storm in Southern California Mountains, **b.** during a short duration summer storm in Sierra Nevada.

2.3.4. Antecedent precipitation clustering

As described in Section 2.2.3, antecedent precipitation clusters were defined as periods within the 90 days before storm onset when the number of moderate-to-extreme precipitation days exceeded the 95th percentile expected from a binomial distribution. Antecedent precipitation clustering is interpreted here as describing the broader hydroclimatic preceding storms associated with PFDFs, rather than a necessary or direct trigger of initiation. Moderate-

to-extreme antecedent precipitation clusters were identified for 42 of the 69 post-fire debris flow events (62%), all during the wet season between October and March (Figure 2.7). Of these 42 clustered events, 48% occurred in Southern California Mountains, 38% in Central California and Coastal Mountains, and 14% in the Sierra Nevada. Central California and Coastal Mountains stands out for having the most persistent clustering, with events associated with 4 to 19 cluster days and a median of 10 days, especially during January and February. This pattern includes the longest clustering observed in the inventory, which comprised 19 consecutive days and was associated with debris flows triggered by storms on 27 January 2021 in the Dolan Fire and CZU Lightning Complex burn areas. Sierra Nevada showed a similar but slightly narrower range, with 4 to 10 cluster days and a median of 9 days. In contrast, Southern California Mountains displayed a more heterogeneous pattern, ranging from 1 to 16 cluster days but with a substantially lower median of 3.5 days, indicating that many events were associated with fewer clustered antecedent rainfall days.

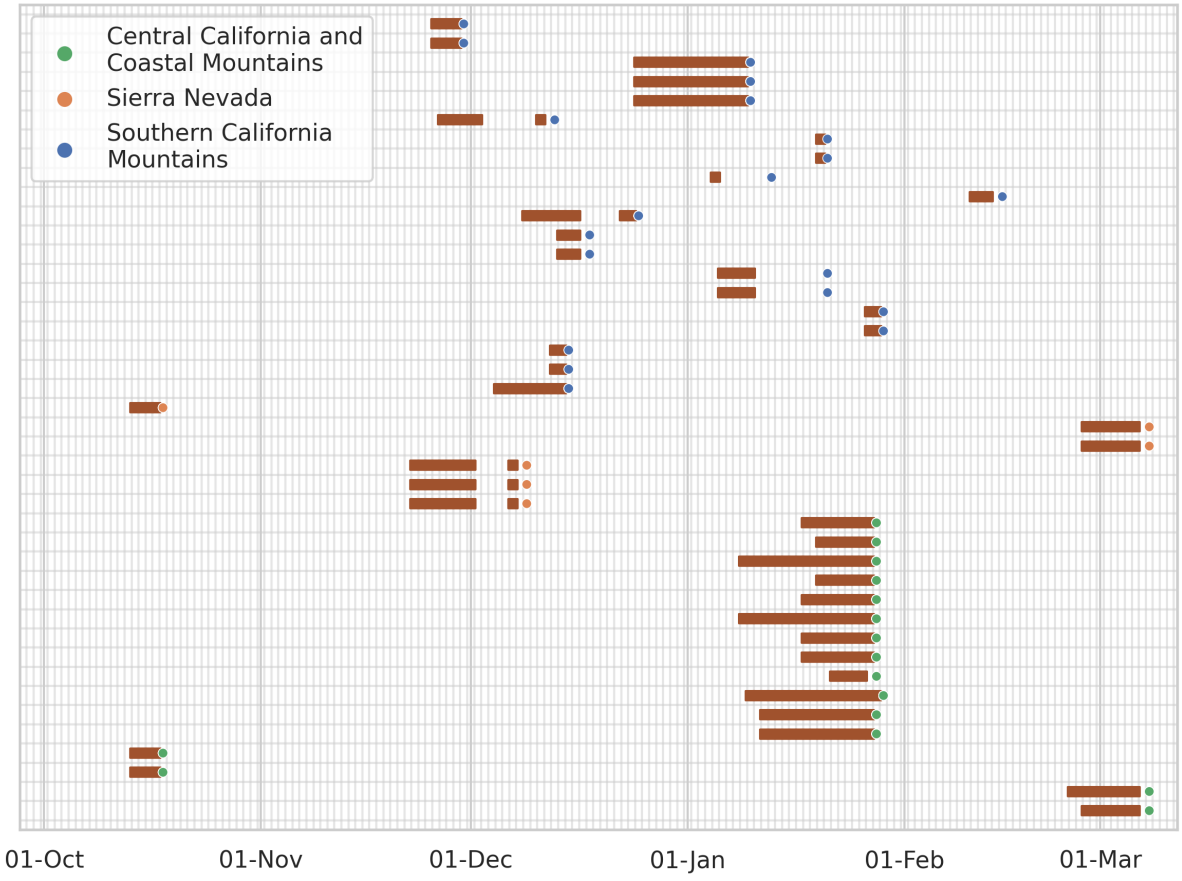


Figure 2.7. Precipitation clusters preceding post-fire debris flow events in the cool-season months in California. Dots indicate the date of occurrence of the debris flows and colors the regions where they happened. Brown bars represent the dates where precipitation clusters were identified. For instance, the first event in the Southern California Mountains region (i.e., blue dot) has four brown bars indicating that there was moderate-to-extreme precipitation between one to four days before the day the debris flow was documented, that was November 29 2018, in the Valley Fire.

The remaining events were not preceded by any antecedent precipitation cluster, showing that PFDFs can also be triggered by storms occurring outside broader wet-period conditions, particularly during spring and summer. The strong seasonal concentration of clustered events likely reflects the prevalence of multi-storm winter sequences and is consistent with the storm-duration results, which showed longer-duration storms in Central California and Coastal Mountains and greater variability in the other regions.

2.4. Discussion and conclusions

This study examined rainfall conditions associated with post-fire debris flow events across California, utilizing an inventory of occurrences from 2014 to 2022. Broadly, the results indicate that storm duration, cumulative rainfall, and average intensity show the clearest contrasts among events, whereas peak 15-min intensity displays substantial overlap across seasonal and time after fire groupings. This does not diminish the importance of short-duration rainfall intensity for PFDF initiation; instead, it suggests that rainfall bursts of similar magnitude may occur within markedly different broader storm environments.

Moreover, the seasonal contrasts identified here are consistent with the hydroclimatic setting of California's Mediterranean climate, in which most annual precipitation is delivered during the cool season by a relatively limited number of storms, while summers are generally dry but may still produce localized high-intensity rainfall (Dettinger et al., 2011; Gershunov et al., 2019). In the present inventory, Fall/Winter PFDF-producing storms were characterized by longer durations and greater cumulative rainfall, whereas Spring/Summer events were generally shorter and exhibited higher average storm intensities. These cool-season storms are commonly associated with large-scale synoptic and mesoscale systems such as atmospheric rivers, upper-level cutoff lows, and narrow cold-frontal rainbands, all of which can produce prolonged rainfall and, in some cases, embedded periods of high short-duration intensity through frontal forcing, orographic enhancement, and mesoscale organization (de Orla-Barile et al., 2022; DeFlorio et al., 2024; Ralph & Dettinger, 2011). Narrow cold-frontal rainbands are especially relevant in this context because they can generate short-duration, high-intensity rainfall capable of producing flooding and debris flows in California, including in post-fire

settings such as the Thomas and Spring fires (Oakley et al., 2018; Sukup et al., 2016; Zou et al., 2023).

By contrast, shorter durations and higher average intensities associated with Spring/Summer PFDF-producing storms are consistent with more localized convective systems. These storms may reflect intense thunderstorms, moisture intrusions associated with the North American Monsoon, or remnants of tropical systems transporting moisture northward from the eastern Pacific (Cannon et al., 2008; Duan et al., 2024; Johnson & Delworth, 2023). Although such storms can produce very high short-duration rainfall intensities, their shorter lifetimes and more limited spatial extent reduce the likelihood of sustaining elevated rainfall over longer periods. This interpretation is reflected in the narrower warm-season distributions of peak 30- and 60-min intensities, suggesting that intense summer storms are typically shorter-lived and less likely to maintain high rainfall rates over extended intervals.

Field observations from the northern Sierra Nevada illustrate the importance of short-duration peak intensities for post-fire debris flow initiation (Thomas, Lindsay, et al., 2023). In this region, a Category 5 atmospheric river in October 2021 deposited high storm totals but generated only minor streamflow responses in a recently burned area, whereas a brief summer thunderstorm with low cumulative rainfall but peak 15-min intensities approximately twice as high triggered debris flows that were volumetrically five times larger. This contrast reinforces the interpretation that short-duration rainfall intensity may be more relevant to post-fire debris flow initiation than storm duration or cumulative rainfall alone, even though the broader storm environment still shapes the conditions under which those intense bursts occur.

A similar contrast appears when the events are grouped by time since fire. Events occurring within the first year after wildfire were associated with longer and more variable storms, likely reflecting the dominance of the first rainy season after burning, whereas events occurring later were generally shorter and had higher average intensities. However, peak short-duration intensities again did not differ significantly by post-fire timing.

Regional differences were also apparent, but they should be interpreted cautiously. Central California and Coastal Mountains differed significantly from both Southern California Mountains and the Sierra Nevada in storm duration, cumulative rainfall, and peak short-duration rainfall intensity. This region was associated with the longest storm durations, greatest cumulative rainfall totals, and most persistent antecedent rainfall clustering in the inventory. However, all events from this group occurred during winter, which limits the extent to which regional effects can be separated from seasonal concentration. Consequently, the rainfall characteristics observed in Central California and Coastal Mountains likely reflect winter storm dominance over that regional hydroclimatic setting. Southern California Mountains and the Sierra Nevada, by contrast, include events across a broader range of seasonal conditions and therefore provide a wider representation of PFDF-producing storm types in the inventory.

The antecedent precipitation-cluster analysis adds a complementary perspective to these findings. In this study, anteceded rainfall describes whether PFDF-producing storms occurred within broader wet-period settings without implying causation for initiation. Under this interpretation, the results are informative: clustered antecedent rainfall was identified for 62% of the events, restricted to the wet season, and most persistent in Central California and Coastal Mountains. This pattern reflects the longer-duration storms observed in that region and

suggests that some PFDFs occur within sustained wet-season sequences, whereas others, particularly in Southern California Mountains and during Spring/Summer, occur in more isolated storm environments.

Several limitations should be considered when interpreting these findings. First, although the compiled inventory represents progress toward broader statewide coverage of PFDF occurrence in California, it remains dominated by events from Southern California. This spatial imbalance could reflect differences in post-fire debris flow documentation, monitoring density, or reporting practices across the state. Similarly, events from Central California and Coastal Mountains in this inventory are represented only by winter events, preventing fair comparison of rainfall conditions from the same region across seasons.

Second, storms triggering post-fire debris flows occurring more than one year after wildfire ignition are relatively few in number and are disproportionately associated with spring and summer seasons. This imbalance limits the ability to fully assess how rainfall characteristics evolve with time since fire and underscores the need for additional observations of later post-fire responses. Third, the analysis focuses exclusively on rainfall characteristics and does not explicitly account for other factors known to influence PFDF occurrence, including burn severity, sediment availability, slope, and channel morphology. These landscape controls likely modulate susceptibility to PFDF initiation under similar rainfall environments and may contribute to variability that cannot be explained by rainfall metrics alone.

Finally, the lack of consistent information on debris flow initiation timing means that the rainfall metrics described here represent storm environments associated with PFDF occurrence rather than the precise rainfall bursts responsible for initiation. Continued

documentation of PFDF events, especially outside Southern California, and improved rainfall observations in areas with limited gauge coverage will be important for advancing hazard assessment and supporting effective risk-mitigation efforts. Recent applications of debris flow prediction models to Central California have highlighted the need for additional inventories to support regional model calibration and to better distinguish between hydrologic responses (Thomas, Kean, et al., 2023). Despite limitations, the descriptive framework in this study characterizes the range of storm environments associated with PFDF occurrence across California's varied hydroclimatic settings, contributing to PFDF documentation efforts and complementing future regional hazard assessments.

2.5. References

Bevacqua, E., De Michele, C., Manning, C., Couasnon, A., Ribeiro, A. F. S., Ramos, A. M., Vignotto, E., Bastos, A., Blesić, S., Durante, F., Hillier, J., Oliveira, S. C., Pinto, J. G., Ragno, E., Rivoire, P., Saunders, K., van der Wiel, K., Wu, W., Zhang, T., & Zscheischler, J. (2021). Guidelines for Studying Diverse Types of Compound Weather and Climate Events. *Earth's Future*, *9*(11), e2021EF002340. https://doi.org/10.1029/2021EF002340

California Geological Survey. (2023). Reported California Landslides [Dataset]. Retrieved from https://cadoc.maps.arcgis.com/apps/webappviewer/index.html?id=bc48ad40e3504134a1fc8f3909659041&_gl=1*1kr33eo*_ga*MjE0MDgyODE2NS4xNzQ1NjA2MTg0*_ga_N4MB98DBXY*MTc0NTYwNjE4NC4xLjAuMTc0NTYwNjE4NC4wLjAuMA

Cannon, S. H., & Gartner, J. E. (2005). Wildfire-related debris flow from a hazards perspective. In M. Jakob & O. Hungr (Eds.), *Debris-flow Hazards and Related Phenomena* (pp. 363–385). Springer. https://doi.org/10.1007/3-540-27129-5_15

Cannon, S. H., Gartner, J. E., Wilson, R. C., Bowers, J. C., & Laber, J. L. (2008). Storm rainfall conditions for floods and debris flows from recently burned areas in southwestern Colorado and southern California. *Geomorphology, Debris Flows Initiated by Runoff, Erosion, and Sediment Entrainment in Western North America*, *96*(3), 250–269. https://doi.org/10.1016/j.geomorph.2007.03.019

De Graff, J. V., Staley, D. M., Stock, G. M., Takenaka, K., Gallegos, A. L., & Neptune, C. K. (2022). Rainfall Triggering of Post-Fire Debris Flows over a 28-Year Period near El Portal, California, USA. *Environmental & Engineering Geoscience*, *28*(1), 133–145. https://doi.org/10.2113/EEG-D-21-00031

de Orla-Barile, M., Cannon, F., Oakley, N. S., & Ralph, F. M. (2022). A Climatology of Narrow Cold-Frontal Rainbands in Southern California. *Geophysical Research Letters*, *49*(2), e2021GL095362. https://doi.org/10.1029/2021GL095362

DeFlorio, M. J., Sengupta, A., Castellano, C. M., Wang, J., Zhang, Z., Gershunov, A., Guirguis, K., Niño, R. L., Clemesha, R. E. S., Pan, M., Xiao, M., Kawzenuk, B., Gibson, P. B., Scheftic, W., Broxton, P. D., Switanek, M. B., Yuan, J., Dettinger, M. D., Hecht, C. W., … Anderson, M. L. (2024). *From California's Extreme Drought to Major Flooding: Evaluating and Synthesizing Experimental Seasonal and Subseasonal Forecasts of Landfalling Atmospheric Rivers and Extreme Precipitation during Winter 2022/23*. https://doi.org/10.1175/BAMS-D-22-0208.1

Dettinger, M. D., Ralph, F. M., Das, T., Neiman, P. J., & Cayan, D. R. (2011). Atmospheric Rivers, Floods and the Water Resources of California. *Water*, *3*(2), Article 2. https://doi.org/10.3390/w3020445

Duan, S., Ullrich, P., & Boos, W. R. (2024). Meteorological Drivers of North American Monsoon Extreme Precipitation Events. *Journal of Geophysical Research: Atmospheres*, *129*(13), e2023JD040535. https://doi.org/10.1029/2023JD040535

Felling, G., Myers, A., & McCoy, S. W. (2019). *Post-fire debris-flow hazard analysis for Interstate 80, Truckee River Canyon, near the California-Nevada state line, USA.* https://repository.mines.edu/server/api/core/bitstreams/9d5f5165-27bf-44c3-9593-7d1a6a322797/content

Gartner, J. E., Cannon, S. H., & Santi, P. M. (2014). Empirical models for predicting volumes of sediment deposited by debris flows and sediment-laden floods in the transverse ranges of southern California. *Engineering Geology*, *176*, 45–56. https://doi.org/10.1016/j.enggeo.2014.04.008

Gartner, J. E., Cannon, S. H., Santi, P. M., & Dewolfe, V. G. (2008). Empirical models to predict the volumes of debris flows generated by recently burned basins in the western U.S. *Geomorphology, Debris Flows Initiated by Runoff, Erosion, and Sediment Entrainment in Western North America*, *96*(3), 339–354. https://doi.org/10.1016/j.geomorph.2007.02.033

Gershunov, A., Shulgina, T., Clemesha, R. E. S., Guirguis, K., Pierce, D. W., Dettinger, M. D., Lavers, D. A., Cayan, D. R., Polade, S. D., Kalansky, J., & Ralph, F. M. (2019). Precipitation regime change in Western North America: The role of Atmospheric Rivers. *Scientific Reports*, *9*(1), 9944. https://doi.org/10.1038/s41598-019-46169-w

Graber, A. P. (2023). *Compilation of runoff-generated debris-flow inventories for 17 fires across Arizona, California, Colorado, New Mexico, and Washington, USA* [Dataset]. U.S. Geological Survey. https://doi.org/10.5066/P98Q4CDH

Griffith, G. E., Omernik, J. M., Smith, D. W., Cook, T. D., Tallyn, E., Moseley, K., & Johnson, C. B. (2016). Ecoregions of California. In *Open-File Report* (2016–1021). U.S. Geological Survey. https://doi.org/10.3133/ofr20161021

Guilinger, J. J., Gray, A. B., Barth, N. C., & Fong, B. T. (2020). The Evolution of Sediment Sources Over a Sequence of Postfire Sediment-Laden Flows Revealed Through Repeat High-Resolution Change Detection. *Journal of Geophysical Research: Earth Surface*, *125*(10), e2020JF005527. https://doi.org/10.1029/2020JF005527

Johnson, B. O., & Delworth, T. L. (2023). The Role of the Gulf of California in the North American Monsoon. *Journal of Climate*, *36*(6), 1541-1559. https://doi.org/10.1175/JCLI-D-22-0365.1

Kean, J. W., McCoy, S. W., Tucker, G. E., Staley, D. M., & Coe, J. A. (2013). Runoff-generated debris flows: Observations and modeling of surge initiation, magnitude, and frequency. *Journal of Geophysical Research: Earth Surface*, *118*(4), 2190–2207. https://doi.org/10.1002/jgrf.20148

Kirschbaum, D. B., Adler, R., Hong, Y., Hill, S., & Lerner-Lam, A. (2010). A global landslide catalog for hazard applications: Method, results, and limitations. *Natural Hazards*, *52*(3), 561–575. https://doi.org/10.1007/s11069-009-9401-4

Kostelnik, J., Rengers, F. K., Wald, L., & Schmitt, R. (2021, December 17). *Northern and Central California Debris Flows Overview*. ArcGIS StoryMaps. https://storymaps.arcgis.com/stories/d6c9dc95f0f84fb1994a164f18115fa5

Li, S., & Banerjee, T. (2021). Spatial and temporal pattern of wildfires in California from 2000 to 2019. *Scientific Reports*, *11*(1), Article 1. https://doi.org/10.1038/s41598-021-88131-9

Lukashov, S. G., Lancaster, J. T., Oakley, N. S., & Swanson, B. J. (2019). Post-fire debris flows of 9 January 2018, Thomas Fire, southern California: Initiation areas, precipitation and impacts. *Seventh International Conference on Debris-Flow Hazards Mitigation – Proceedings.* http://dx.doi.org/10.25676/11124/173144

McGuire, L. A., Rengers, F. K., Kean, J. W., Staley, D. M., & Mirus, B. B. (2018). Incorporating spatially heterogeneous infiltration capacity into hydrologic models with applications for simulating post-wildfire debris flow initiation. *Hydrological Processes*, *32*(9), 1173–1187. https://doi.org/10.1002/hyp.11458

Neptune, C. K., Degraff, J. V., Pluhar, C. J., Lancaster, J. T., & Staley, D. M. (2021). Rainfall Thresholds for Post-Fire Debris-Flow Generation, Western Sierra Nevada, CA. *Environmental & Engineering Geoscience*, *27*(4), 439–453. https://doi.org/10.2113/EEG-D-21-00039

Oakley, N. S., Cannon, F., Munroe, R., Lancaster, J. T., Gomberg, D., & Ralph, F. M. (2018). Brief communication: Meteorological and climatological conditions associated with the 9 January 2018 post-fire debris flows in Montecito and Carpinteria, California, USA. *Natural Hazards and Earth System Sciences*, *18*(11), 3037–3043. https://doi.org/10.5194/nhess-18-3037-2018

Oakley, N. S., Lancaster, J. T., Kaplan, M. L., & Ralph, F. M. (2017). Synoptic conditions associated with cool season post-fire debris flows in the Transverse Ranges of southern California. *Natural Hazards*, *88*(1), 327–354. https://doi.org/10.1007/s11069-017-2867-6

PRISM Climate Group (2022) Oregon State University. 30-year normals. Available at https://prism.oregonstate.edu/. [Accessed 05 Jun 2023].

Ralph, F. M., & Dettinger, M. D. (2011). Storms, floods, and the science of atmospheric rivers. *Eos, Transactions American Geophysical Union*, *92*(32), 265–266. https://doi.org/10.1029/2011EO320001

Schwartz, J. Y., Oakley, N. S., & Alessio, P. (2021). Assessment of a Post-Fire Debris Flow Impacting El Capitan Watershed, Santa Barbara County, California, U.S.A. *Environmental & Engineering Geoscience*, *27*(4), 423–437. https://doi.org/10.2113/EEG-D-21-00008

Shakesby, R. A., & Doerr, S. H. (2006). Wildfire as a hydrological and geomorphological agent. *Earth-Science Reviews*, *74*(3), 269–307. https://doi.org/10.1016/j.earscirev.2005.10.006

Staley, D. M., Kean, J. W., Cannon, S. H., Schmidt, K. M., & Laber, J. L. (2013). Objective definition of rainfall intensity–duration thresholds for the initiation of post-fire debris flows in southern California. *Landslides*, *10*(5), 547–562. https://doi.org/10.1007/s10346-012-0341-9

Staley, D. M., Kean, J. W., & Rengers, F. K. (2020). The recurrence interval of post-fire debris-flow generating rainfall in the southwestern United States. *Geomorphology*, *370*, 107392. https://doi.org/10.1016/j.geomorph.2020.107392

Staley, D. M., Negri, J. A., Kean, J. W., Laber, J. L., Tillery, A. C., & Youberg, A. M. (2017). Prediction of spatially explicit rainfall intensity–duration thresholds for post-fire debris-flow generation in the western United States. *Geomorphology*, *278*, 149–162. https://doi.org/10.1016/j.geomorph.2016.10.019

Staley, D. M., Tillery, A. C., Kean, J. W., McGuire, L. A., Pauling, H. E., Rengers, F. K., & Smith, J. B. (2018). Estimating post-fire debris-flow hazards prior to wildfire using a statistical analysis of historical distributions of fire severity from remote sensing data. *International Journal of Wildland Fire*, *27*(9), 595–608. https://doi.org/10.1071/WF17122

Sukup, S., Laber, J., Sweet, D., & Thompson, R. (2016). *Analysis of an Intense Narrow Cold Frontal Rainband and the Springs Fire Burn Area Debris Flows of 12 December 2014*. https://www.weather.gov/media/wrh/online_publications/TAs/TA1601.pdf

Thomas, M. A., Kean, J. W., McCoy, S. W., Lindsay, D. N., Kostelnik, J., Cavagnaro, D. B., Rengers, F. K., East, A. E., Schwartz, J. Y., Smith, D. P., & Collins, B. D. (2023). Postfire hydrologic response along the Central California (USA) coast: Insights for the emergency assessment of postfire debris-flow hazards. *Landslides*. https://doi.org/10.1007/s10346-023-02106-7

Thomas, M. A., Lindsay, D. N., Cavagnaro, D. B., Kean, J. W., McCoy, S. W., & Graber, A. P. (2023). The Rainfall Intensity-Duration Control of Debris Flows After Wildfire. *Geophysical Research Letters*, *50*(10), e2023GL103645. https://doi.org/10.1029/2023GL103645

Thornton, P. E., Thornton, M. M., Mayer, B. W., Wilhelmi, N., Wei, Y., Devarakonda, R., & Cook, R. B. (2014). Daymet: Daily Surface Weather Data on a 1-km Grid for North America, Version 2. *ORNL DAAC*. https://doi.org/10.3334/ORNLDAAC/1219

Zou, X., Cordeira, J. M., Bartlett, S. M., Kawzenuk, B., Roj, S., Castellano, C., Hecht, C., & Ralph, F. M. (2023). Mesoscale and Synoptic Scale Analysis of Narrow Cold Frontal Rainband During a Landfalling Atmospheric River in California During January 2021. *Journal of Geophysical Research: Atmospheres*, *128*(20), e2023JD039426. https://doi.org/10.1029/2023JD039426

Chapter 3

3. Structural properties and reflectivity patterns of precipitation systems linked to post-fire debris flows in California

Abstract

Post-fire debris flows are triggered by short-duration, high-intensity rainfall that mobilizes sediment on recently burned slopes. These events present a serious hazard in California, where intense rainfall often follows wildfire activity. This study uses radar reflectivity data to introduce a modified tracking algorithm that identifies and tracks coherent precipitation systems intersecting burned areas. The algorithm is applied to an inventory of post-fire debris flow events to characterize storm-scale structural properties, including area, propagation speed, direction, and eccentricity, as well as reflectivity patterns occurring within fire perimeters. The algorithm was applied successfully across long- and short-duration storms and revealed significant seasonal differences. Fall and winter storms generally featured larger, more elongated, and faster-moving reflectivity precipitation systems, while spring and summer storms were typically smaller, more circular, and slower. Within fire perimeters, warmer-month precipitation systems more frequently produced localized bursts of high reflectivity (>45 dBZ), whereas colder-month events showed broader zones of moderate reflectivity (25–45 dBZ). Temporal comparisons show that the timing of maximum radar reflectivity over burned areas and at reported debris flow locations has stronger alignment with peak 15-minute rainfall intensities from nearby rain gauges than reflectivity-threshold–based metrics. Together, these findings demonstrate that reflectivity tracking provides meaningful spatial and temporal context for identifying near-peak rainfall conditions over

burned landscapes and offers a practical outline for characterizing precipitation system structure in support of fire-wide situational awareness of post-fire debris flow hazards.

3.1. Introduction

Wildfires occurring on steep terrain can significantly elevate the risk of debris flows by enhancing the transport of sediment from hillslopes into nearby channels, floodplains, and alluvial fans (McGuire et al., 2024). This increased susceptibility results from post-fire changes in hydrologic and soil conditions, including elevated runoff, reduced infiltration, and greater sediment availability, which together create favorable conditions for debris flow initiation (Shakesby & Doerr, 2006). These events are often triggered when intense rainfall rapidly mobilizes loose material on burned slopes. However, extreme rainfall is not a prerequisite for them to occur. Instead, post-fire debris flows are more commonly initiated by short bursts of sub-hourly, high-intensity rainfall (Staley et al., 2013) often associated with recurrence intervals of less than two years (Staley et al., 2020).

California has a Mediterranean climate, with wet winters and long, dry summers (Dettinger et al., 2011). However, precipitation patterns vary regionally. Most of Northern California's precipitation comes from winter storms, often fueled by atmospheric rivers. The jet stream tends to steer storms into this region, especially from the Bay Area northward. Conversely, the transverse mountain ranges of Southern California block moisture, contributing to arid conditions. The persistent subtropical high-pressure system often suppresses storm activity in winter, leading to long dry spells. This often results in a see-saw pattern in precipitation between Northern and Southern California. Moreover, Southern California exhibits significant interannual variability, with more precipitation often observed during strong El Niño events (Abatzoglou et al., 2009). Across much of the state, the

hydrologic cycle is shaped by a few extreme rainfall events, most of which occur during the fall and winter months (November–April) and account for over 90% of the state's annual precipitation (Gershunov et al., 2019; Mo & Higgins, 1998; Swain et al., 2016). Narrow cold-frontal rain bands, upper-level cutoff lows, and atmospheric rivers are frequent drivers of extreme rainfall across California (e.g., de Orla-Barile et al., 2022; DeFlorio et al., 2024; Dettinger et al., 2011; Dong et al., 2018; Harris & Carvalho, 2018; Nash & Carvalho, 2020; Ralph & Dettinger, 2012). These systems interact with California's rugged terrain and extensive mountain ranges, producing intense orographic precipitation and pronounced rainfall gradients.

Although they contribute less than 10% to the annual hydrologic cycle, spring and summer thunderstorms, often triggered by moisture plumes associated with the northward progression of the North American Monsoon, can interact with topography to produce extreme rainfall and flash floods (Duan et al., 2024). Tropical systems that form over the warm waters off the coast of Baja California during summer may also track northeastward, advecting substantial moisture into California and enhancing the potential for thunderstorm activity (B. O. Johnson & Delworth, 2023). Recent trends demonstrated a delayed onset of the rainy season (Luković et al., 2021) extending dry conditions into the autumn/winter offshore wind season and amplifying wildfire risk (Abatzoglou et al., 2021; Goss et al., 2020; Oakley, 2021; Swain, 2021). This shift shortens the gap between large wildfires and the arrival of winter storms, increasing the likelihood of post-fire hydrologic hazards.

Short-duration, high-intensity rainfall bursts, particularly in regions like Southern California where narrow cold-frontal rain bands can produce rapid spikes in rainfall intensity over burned terrain, create ideal conditions for post-fire debris flow initiation (de Orla-Barile

et al., 2022; Kean et al., 2011; McGuire et al., 2021). To better understand meteorological conditions and corroborate the presence of high-intensity rainfall in storms associated with post-fire debris flows, studies have increasingly relied on radar reflectivity data, particularly composite reflectivity mosaics from the National Weather Service Next-Generation Weather Radar system (NWS NEXRAD; NOAA National Weather Service, 1991). Radar data provide a valuable alternative to rain gauges in many post-fire landscapes, where in situ observations are often sparse, poorly distributed, or entirely absent. In addition, the sub-hourly temporal resolution of radar data makes it well-suited for studying short-duration, high-intensity rainfall events, which are commonly associated with post-fire debris flows. In these cases, radar data have been used to analyze meteorological conditions (Oakley et al., 2017, 2018; Sukup et al., 2016), evaluate rainfall intensity as well as to confirm the timing and spatial extent of rainfall over previously burned areas (De Graff et al., 2022; Liu et al., 2022; McGuire et al., 2021; Schwartz et al., 2021).

While these efforts underscore the importance of short-duration rainfall intensity in post-fire debris flow events, far less attention has been given to the structure and evolution of the storms that produce these conditions over burned landscapes. Rainfall associated with post-fire debris flows often occurs within organized precipitation systems at the meso-γ to meso-β scales, sub-categories of the mesoscale spatial and temporal classification of atmospheric phenomena (Orlanski, 1975; Fujita, 1981). At the meso-γ scale (2–20 km), phenomena include thunderstorms, convective cells, and narrow rainbands, with short life spans of 30 minutes to half a day. At the meso-β scale (20–200 km), processes typically encompass larger regional or topographically driven dynamics such as mesoscale convective systems and frontal rainfall bands, lasting from hours to more than a day. At these scales, storm organization governs

where intense rainfall is concentrated, how long it persists over a given area, and the occurrence of repeated high-intensity rainfall pulses over vulnerable landscapes. Individual convective elements may be short-lived and difficult to track consistently at fine spatial resolution, but their organization into coherent precipitation systems enables characterization using radar-based tracking algorithms.

Tracking algorithms based on radar reflectivity and brightness temperature have long been developed to identify and monitor mesoscale atmospheric features, such as Mesoscale Convective Systems (MCSs) and isolated convective cells. These methods help bridge the gap in observing transient, high-impact weather phenomena using remotely sensed data (Carvalho & Jones, 2001; Dixon & Wiener, 1993; Haberlie & Ashley, 2018; J. T. Johnson et al., 1998; Machado et al., 1998; Prein et al., 2024). As summarized by Raut et al., (2021), common approaches for tracking include overlap methods (Carvalho & Jones, 2001; Machado et al., 1998; Moseley et al., 2013), clustering (Lakshmanan et al., 2015), and centroid-based techniques (Goswami & Bhandari, 2013), along with more advanced techniques such as adaptive Kalman filtering (Rossi et al., 2015), fuzzy logic algorithms (Jung & Lee, 2015), and machine learning (Haberlie & Ashley, 2018). More recently, similar tracking approaches have been adapted for applications beyond precipitation, including monitoring fire progression in wildfire events (Lareau et al., 2022).

The primary goal of this study is to evaluate the structural properties and reflectivity patterns of precipitation systems associated with post-fire debris flows in California based on NEXRAD reflectivity. To achieve this, we adapted the Maximum Spatial Correlation Tracking Technique (MASCOTTE; Carvalho & Jones, 2001) to identify and track precipitation systems intersecting burned areas with a specific focus on storm-scale evolution

and fire-wide reflectivity conditions. The algorithm quantifies structural properties, such as area, speed and direction of propagation, and eccentricity of precipitation systems, while also capturing reflectivity-based metrics within fire perimeters and near documented debris flow locations.

By integrating storm-scale structure with reflectivity information over burned landscapes, this approach offers a framework for understanding when and where burned terrain is exposed to organized, intense rainfall relevant to post-fire debris flow hazards. Because rain gauges provide point-based measurements and can be distant from debris flow sites, radar-based tracking serves as a complementary tool by capturing the spatial extent and evolution of rainfall conditions across entire burn scars. When applied to an inventory of post-fire debris-flow events, the algorithm enabled the relationship between storm evolution, fire-wide exposure to intense rainfall and the timing of short-duration rainfall peaks recorded by nearby gauges, thereby illustrating the potential of this tool to support situational awareness and hazard monitoring efforts.

3.2. Data and methods

3.2.1. Radar reflectivity data and post-fire debris flow inventory

Our study uses mosaics of NEXRAD base reflectivity data, obtained from the Iowa State Environmental Mesonet Archive (https://mesonet.agron.iastate.edu). These mosaics combine observations from more than 130 individual radars in the NEXRAD network and provide reflectivity field at 5-minute temporal resolution and 0.5 km horizontal grid spacing, making them suitable for examining the evolution of high-intensity, short-duration rainfall commonly associated with post-fire debris flows. As described on the archive's website, to systematically reduce false echoes and mitigate radar beam blockage, the mosaics are initially quality

controlled before product generation. Despite these procedures, radar-derived reflectivity remains subject to sampling limitations, including increasing beam height with range, partial beam blockage in complex terrain, and uncertainty in relating reflectivity to surface rainfall intensity, particularly in mountainous regions.

The sample analyzed in this chapter differs slightly from the broader inventory used in Chapters 2 and 4 because it reflects the event subset available when this analysis was developed. Specifically, summer events from the Dixie and Farad fires were not included, whereas events from the Silverado Fire not used in Chapter 2 were incorporated here. As a result, an inventory of 67 post-fire debris flow events between 2014–2022 from 20 fires across California (Figure 3.1) was used to implement and evaluate the tracking tool. Of these, 50 events were associated with storms in the fall and winter months, while the remaining 17 occurred during spring and summer storms. The 2014–2022 period was selected based on the availability of high-temporal resolution rainfall station data, as the study relied on publicly available rain gauges rather than monitored or instrumented watershed data to characterize rainfall conditions.

Debris flow event locations were compiled from previously published inventories and reports, including peer-reviewed studies and agency datasets. Sources include the Reported California Landslides Database (California Geological Survey, 2023), NASA Global Landslide Catalog (Kirschbaum et al., 2010), and events documented in scientific literature (De Graff et al., 2022; Graber, 2023; Guilinger et al., 2020; Kostelnik et al., 2021; McGuire et al., 2018; Neptune et al., 2021; Oakley et al., 2017; Schwartz et al., 2021; Staley et al., 2018; Thomas et al., 2023b). Coordinate definitions follow the original sources and were not reinterpreted in this study. In many cases, these sources do not specify whether the reported

coordinates correspond to debris flow initiation points, channel heads, outlets, or downstream impact locations. Accordingly, reported locations are treated here as representative reference points associated with documented debris flow occurrences, rather than as precise initiation locations. This treatment is consistent with previous studies that use existing landslide inventories as conservative, location-based records to contextualize hydrometeorological conditions relevant to the hazard (Culler et al., 2023; Li et al., 2025).

Each debris flow event was paired with the nearest rain gauge within an 8 km radius. This distance was chosen to account for the lower density of rain gauges in parts in California and to maintain consistency with prior studies that used similar spatial thresholds to characterize storm conditions associated with debris flows (Thomas et al., 2023a). Across the inventory, the median distance between debris flow reference locations and the nearest rain gauge was 2.7 km, with a mean of 3.1 km, indicating that most events were paired with gauges substantially closer than the maximum search radius. Sub-hourly rainfall data from the nearest gauge were used to describe event-specific rainfall conditions as short-duration rainfall intensities (≤60 min) are considered effective predictors of post-fire debris flow initiation (Staley et al., 2013).

Although the existing data in the inventories includes the event date, the precise timing of when debris flows occurred is not always available, which limits the ability to directly identify triggering rainfall intensities. Therefore, the peak 15-minute rainfall intensity (i.e. the maximum 15-min rainfall intensity registered during a storm) recorded by the associated rain gauge was used as a proxy for debris flow triggering (Selander et al., 2025; Thomas et al., 2023a). Moreover, storm duration and peak 15-, 30- and 60-min intensities were calculated

(Supplementary Material, S1). Storm duration was determined using the criteria from (Staley et al., 2013), which defines a storm as a period of rainfall with no breaks longer than 8 hours.

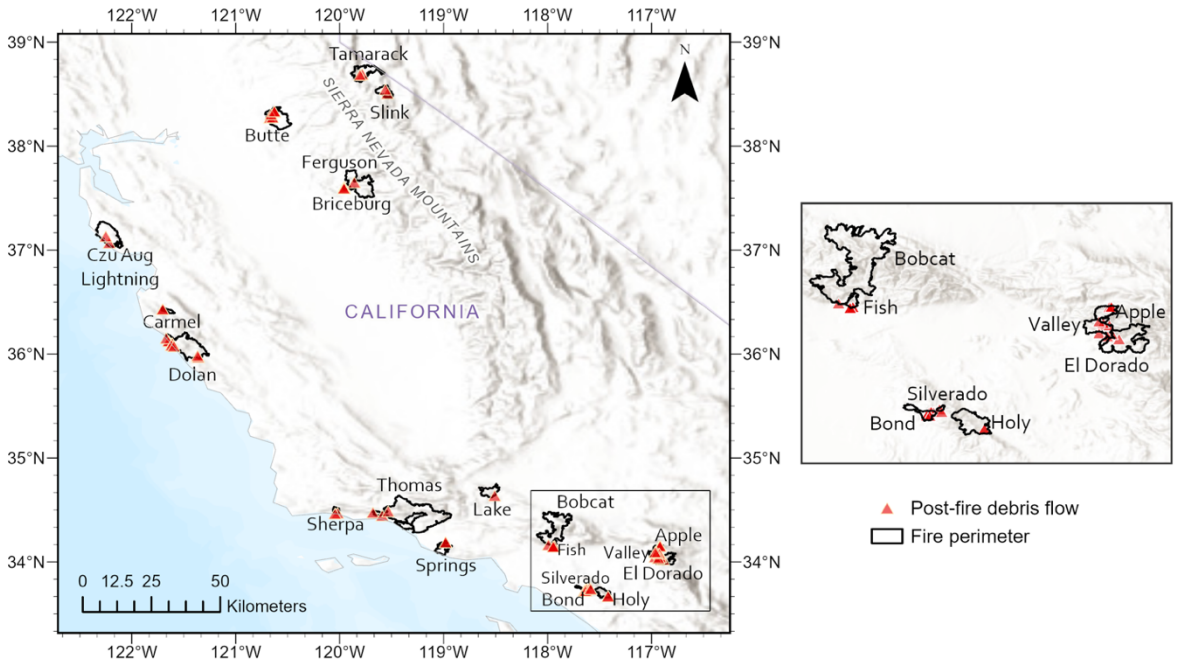


Figure 3.1. Locations of documented post-fire debris flows (2014–2022; red triangles) and associated wildfire perimeters (2013–2021; black outlines) across California. Fire names are labeled adjacent to each perimeter, and the inset highlights events in Southern California.

3.2.2. Modified tracking algorithm

The modified tracking algorithm builds on the Maximum Spatial Correlation Tracking Technique (MASCOTTE; Carvalho & Jones, 2001) to identify and follow the evolution of radar reflectivity regions associated with storms that produced post-fire debris flows. The method preserves the original spatial-correlation framework used to tracking coherent features through time and adapts it for application to radar reflectivity fields and precipitation systems intersecting recently burned areas. Figure 3.2 summarizes the main steps of the algorithm. Each storm event consists of N radar reflectivity mosaics (dependent on storm duration), available at a time interval Δt of 5 minutes. To optimize algorithm performance and reduce the computational load of tracking long-duration storms, several threshold parameters were

selected based on repeated test runs designed to ensure consistent detection of storm regions across all debris flow events in the inventory. These parameters include:

(1) Reflectivity threshold: A minimum reflectivity of 20 dBZ was applied to identify regions contributing meaningful precipitation. While previous studies have used higher reflectivity thresholds to isolate reflectivity elements (e.g., 35 dBZ in Jung & Lee, 2015; >30 dBZ in (J. T. Johnson et al., 1998), a lower threshold was used in this study, as higher cutoffs failed to consistently capture storms known to have produced post-fire debris flows. An exception was made for the November 15, 2016 storm over the Butte Fire burn area, where predominantly low reflectivity required reducing the threshold to 10 dBZ to adequately track the precipitating region and capture the timing of peak 15-minute rainfall intensity.

(2) Area threshold: A minimum contiguous area of 45 km^2 was required for a reflectivity region to be tracked. This threshold ensures spatial coherence and continuity of identified features across consecutive time steps and supports consistent tracking of organized precipitation systems at meso-γ to meso-β scales. Smaller precipitation features may still be capable of triggering post-fire debris flows at watershed scales (e.g., ~1 km^2), but such features often lack the spatial extent needed for robust storm-scale tracking within this framework. Contiguous regions satisfying these reflectivity and area criteria are hereafter referred to as precipitating systems (PS).

(3) Tracking domain: Tracking was restricted to a spatial bounding box extending 5 degrees in latitude and longitude, centered on the centroid of each fire polygon. This domain limits computational cost and reduces interference from unrelated PS.

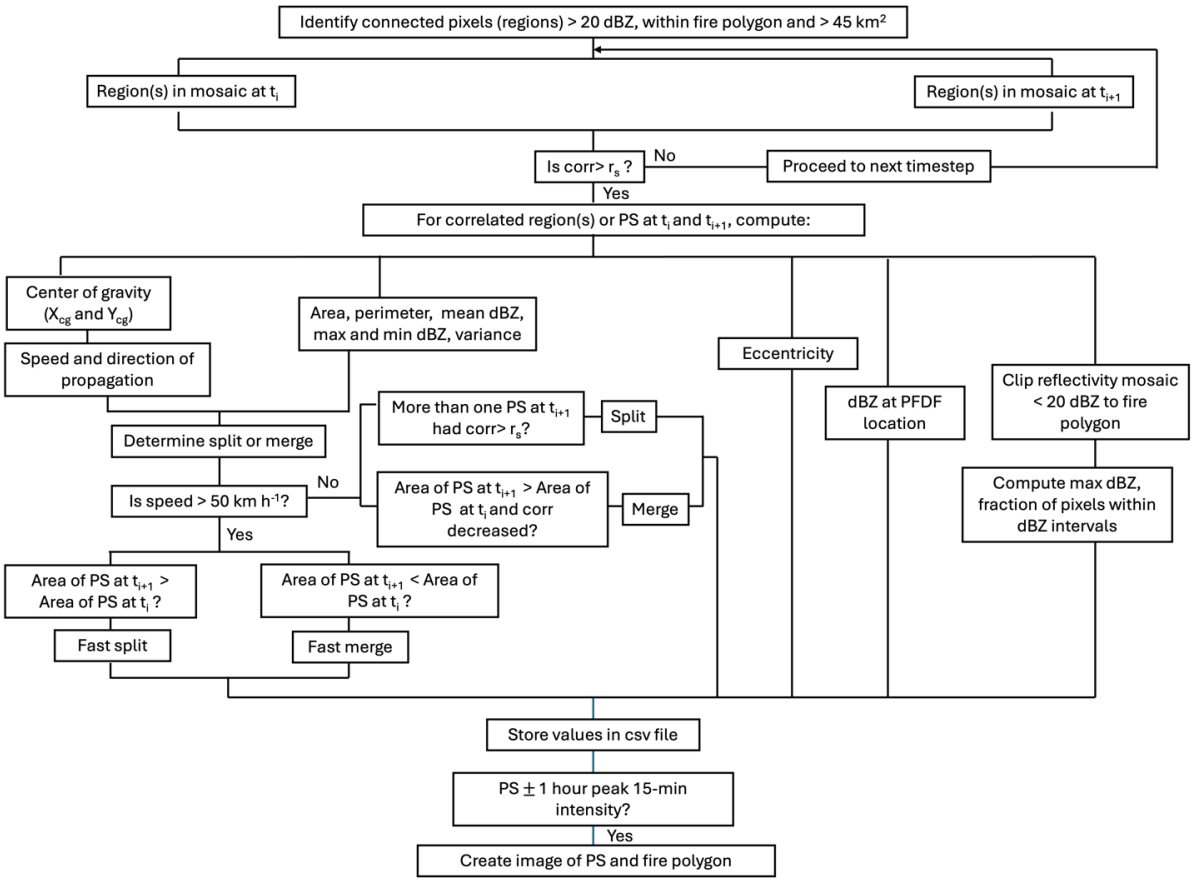


Figure 3.2. Flowchart of the modified tracking algorithm executed once inputs such as reflectivity mosaic, debris flow data, and fire polygons are provided.

At each timestep t_i, n PS of radar reflectivity are identified based on the previously defined reflectivity threshold and minimum area. Once the PS at t_i are determined, the algorithm proceeds to the next mosaic at t_{i+1} to identify corresponding PS at the new timestamp. A region at t_{i+1} is considered a continuation of a PS from t_i if the spatial correlation coefficient (r_s) between them is equal or greater than 0.30. This spatial correlation threshold successfully captured the timing of peak 15-min rainfall intensity from rain gauges in 95% of the events in the inventory (88% using a threshold of 0.5), while a reduced threshold of 0.20 was sufficient for the remaining cases. This process is applied to all PS at each time step and repeated iteratively across the duration of the storm.

For each spatially correlated PS, structural properties are calculated, including eccentricity, speed of displacement, direction of propagation, area, perimeter, and the minimum, maximum, mean, and variance of reflectivity values. Area and speed describe fire-wide exposure and rainfall residence time, eccentricity reflects storm morphology and organization, and propagation direction characterizes storm movement relative to burned areas, regional flow patterns, and topographic influences that can modulate orographic precipitation. In this study, these variables are used to characterize the broader storm environments associated with debris flow–producing events and are not intended to resolve initiation mechanisms of the hazard. The calculation of speed and direction of propagation is enabled by defining a Center of Gravity (CG) for each PS, which is a reflectivity-weighted average represented by spatial coordinates X_{CG} , Y_{CG} (Equation 3.1).

$$\boldsymbol{X_{CG}} = \frac{\sum_{i=1}^{Np} \boldsymbol{X_i\, dBZ_i}}{\sum_{i=1}^{Np} \boldsymbol{dBZ_i}},\ \boldsymbol{Y_{CG}} = \frac{\sum_{i=1}^{Np} \boldsymbol{Y_i\, dBZ_i}}{\sum_{i=1}^{Np} \boldsymbol{dBZ_i}} \qquad 3.1$$

Where X_i and Y_i are the region pixel coordinates in the east–west and north–south directions, respectively, dBZ_i represents the reflectivity values, and the summation is executed over all N_p pixels within the given PS. The direction of propagation is expressed as an angle in degrees ranging from 0 to 360 and follows a mathematical convention based on the x- and y-axis orientation: 0° indicates eastward, 90° northward, 180° westward, and 270° southward motion. Because direction of propagation is a circular variable, where values are distributed across the 0°/360° boundary, summary statistics and seasonal comparisons for this metric were computed using circular methods. The circular median was identified as the angle minimizing the sum of arc distances to all observations, and the Kuiper two-sample test, a

non-parametric test designed for circular data, was used in place of the Mann-Whitney U test to assess seasonal differences.

Eccentricity is computed exclusively using the Empirical Orthogonal Functions (EOF) method following Carvalho & Jones, (2001). Specifically, eccentricity is defined as the ratio of the norms of the second to the first eigenvectors (|EOF2|/|EOF1|), where EOF1 and EOF2 represent the dominant and secondary modes of spatial variability in the PS reflectivity. Lower values indicate more elongated structures whereas values closer to one indicate more circular or isotropic shapes. These patterns provide insight into precipitation system organization, with elongated systems often associated with narrow cold-frontal rain bands or squall lines and more circular PS associated with convective clusters or isolated cells (Markowski & Richardson, 2010).

As in the original algorithm, splits and merges of PS were identified across timestamps, which may indicate the intensification or weakening of precipitation. A split was flagged when more than one PS at t_{i+1} showed spatial correlation with a single PS at t_i. Conversely, a merge was identified when the PS at t_{i+1} had a larger area than the corresponding PS at t_i, and the correlation decreased by more than 5% from the previous value. To improve detection during rapid storm evolution, an additional criterion based on propagation speed and area change was implemented following Carvalho & Jones (2001). Specifically, a fast split was identified when PS propagation speeds exceeded 50 km h^{-1} and its area decreased from t_i to t_{i+1} while, a fast merge was flagged when propagation speeds exceeded 50 km h^{-1} and PS area increased between successive time steps.

For analysis and visualization, the algorithm generates three outputs: a CSV file containing structural properties at each timestamp for correlated PS, and two sets of images,

one showing the identified PS and center of gravity within the 5-degree latitude, longitude bounding box, and another displaying reflectivity values within the fire polygon. Images are only generated when at least one PS is detected within one hour before or after the peak 15-minute rainfall intensity. In such cases, frames are produced at 10-minute intervals across that two-hour window. To provide context for the algorithm modifications, Table 3.1 summarizes the structural parameters and metrics computed in this study, along with their correspondence to the original MASCOTTE framework (Carvalho & Jones, 2001).

Table 3.1. Structural parameters and metrics computed by Carvalho & Jones (2001) and this study. T_B corresponds to brightness temperature fields.

	Carvalho & Jones (2001)	This study
Center of gravity	Yes	Yes
Average T_B / radar reflectivity in tracked PS	Yes	Yes
Minimum T_B / radar reflectivity in tracked PS	Yes	Yes
Maximum T_B / radar reflectivity in tracked PS	Yes	Yes
Variance T_B / radar reflectivity in tracked PS	Yes	Yes
Eccentricity of tracked PS	Yes	Yes
Speed of propagation	Yes	Yes
Direction of propagation	Yes	Yes
Perimeter	Yes	Yes
Identification of splits and merges	Yes	Yes
Area of tracked PS	Yes	Yes
Reflectivity at debris flow location	Not applicable	Yes
Maximum reflectivity within fire polygon	Not applicable	Yes
Proportion of fire pixels > 30 dBZ	Not applicable	Yes

Fraction of pixels within 5 dBZ intervals	Not applicable	Yes

3.2.3. Reflectivity metrics

Within fire perimeters, reflectivity-based metrics were designed to characterize spatial and temporal patterns of rainfall intersecting burned landscapes, capturing how organized precipitation systems evolve in susceptible terrain. Metrics include maximum reflectivity within the fire perimeter, reflectivity sampled at debris flow reference coordinates and the fraction of burned area pixels exceeding specified reflectivity thresholds. Reflectivity sampled at debris flow reference locations is interpreted as indicative of rainfall conditions in the broader vicinity of reported debris flow occurrences, not as precise estimates of rainfall at initiation points.

The fraction of burned area within reflectivity intervals was computed by counting pixels within each fire polygon that fell into 5 dBZ bins, ranging from 10 to 70 dBZ and above, and then normalizing by the total number of pixels in the polygon. This metric is intended to describe the spatial extent of elevated rainfall over the burn scar at a given time, providing situational awareness of fire-wide exposure to intense rainfall rather than localized values.

Radar reflectivity values are commonly related to rainfall intensity; however, this relationship is not unique and depends on the dynamical and microphysical processes governing precipitation formation and drop size distributions, which can vary across storm types and regions (Fabry, 2015; Marshall & Palmer, 1948). Because reflectivity–rainfall relationships are highly variable, reflectivity values in this study are interpreted qualitatively as indicators of relative rainfall intensity rather than converted to rainfall rates using a single Z–R relationship.

As a general reference, reflectivity values of approximately 10–35 dBZ are often associated with drizzle to light rainfall, 35–45 dBZ with moderate and more widespread rainfall, and values exceeding ~45–55 dBZ with heavy rainfall or convective precipitation, though these ranges may vary by precipitation regime (e.g., Houze Jr., 2014). Higher reflectivity values (>55 dBZ) are commonly linked to very heavy rainfall or hail associated with the cores of intense convective storms (Fabry, 2015).

To assess how radar reflectivity varies across spatial scales during storms, two comparisons were performed. First, reflectivity at debris flow reference locations was compared with the maximum reflectivity within the corresponding fire perimeter to evaluate whether the reference locations experienced near-maximum reflectivity within the burned area or occurred under lower reflectivity conditions. Second, maximum reflectivity within the fire perimeter was compared with the maximum reflectivity across the entire precipitation system, serving as a reference indicating whether reflectivity values experienced in the burned area are comparable to the most intense portions of the system.

Temporal relationships between radar-derived metrics and rainfall observations were evaluated to determine whether periods identified by the tracking algorithm correspond to near-peak storm conditions as recorded by nearby rain gauges. This comparison recognizes that point-based gauges, often located several kilometers from debris flow sites, may not capture localized variability within burned areas and is therefore used as an indicator of periods when hazardous rainfall conditions relevant to post-fire debris flows were present over the burn scar. Timing offsets were assessed using ±15-, ±30-, and ±60-minute windows to account for uncertainty in debris flow timing and rainfall measurement resolution. In addition, two representative storm events were selected as case studies to illustrate algorithm

performance under contrasting precipitation regimes, including a long-duration, winter-season storm and a short-duration, convective warm-season storm.

The tracking algorithm implemented in this study operates at the meso-γ to meso-β storm scales resolved by NEXRAD composite reflectivity mosaics and is designed to characterize storm-scale precipitation structure and fire-wide reflectivity patterns over burned landscapes. Because post-fire debris flows are initiated by highly localized rainfall occurring over very small watersheds, typically orders of magnitude smaller than the spatial scale of the tracked meso-scale precipitation systems, the algorithm and radar-derived metrics are interpreted as providing contextual information on storm evolution and fire-wide exposure to intense rainfall, rather than as predictors of localized debrismflow initiation within individual watersheds.

3.3. Results

3.3.1. Structural properties and reflectivity patterns of precipitation systems

To explore the structural characteristics of storms linked to post-fire debris flows, we analyzed properties such as area, speed and direction of propagation, and eccentricity of precipitation systems (PS) at or near the time of peak 15-minute rainfall intensity. These properties were then separated by season to highlight potential seasonal influences. Figure 3.3 provides an example of precipitation system features extracted by the tracking algorithm for an event associated with the Springs Fire on December 12, 2014. This event exhibited the largest contiguous radar reflectivity area in the inventory and illustrates how PS area, propagation, and shape metrics are derived (Figure 3.3). In addition, reflectivity metrics within fire perimeters and at debris flow reference locations were examined to characterize the spatial distribution and temporal context of rainfall over burned areas.

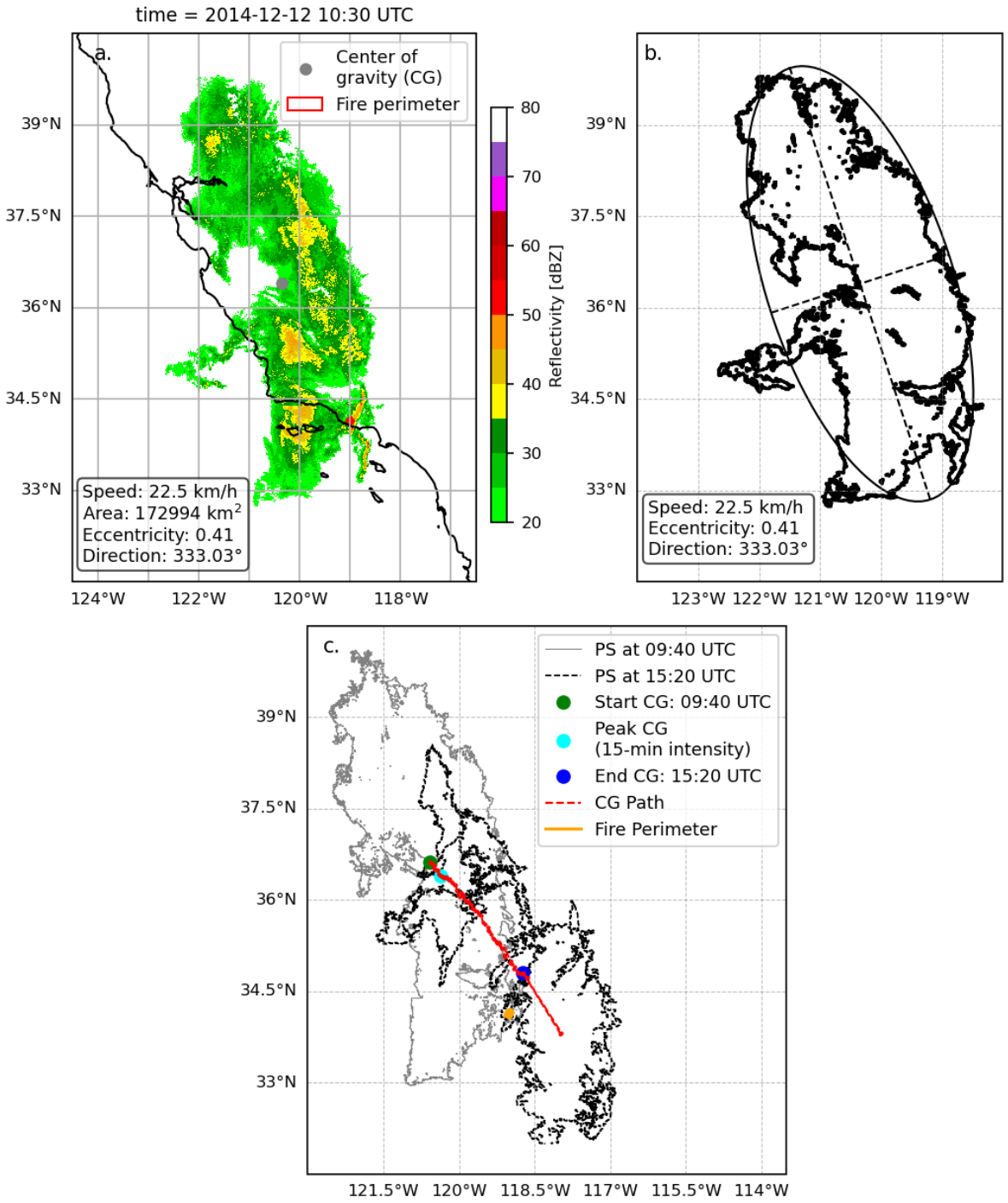


Figure 3.3. Structural properties and radar reflectivity of a precipitation system over the Springs Fire. **a.** Radar reflectivity area of PS identified at peak 15-minute intensity during the storm on December 12, 2014; **b.** Ellipse adjusted to the PS with major and minor axes used to compute eccentricity. The PS contour outlines the perimeter at the time of peak 15-minute rainfall intensity**; c.** Propagation path of the PS's center of gravity from 09:40 to 15:20 UTC.

3.3.1.1. Area, eccentricity, speed and direction of propagation of precipitation systems

The seasonal variability of PS structural properties at the approximate time of debris flow is summarized in Figure 3.4. PS reflectivity area across all events ranged from 698 km^2 in the Apple Fire burn area in the San Bernardino Mountains to approximately 173,000 km^2 in the Springs Fire burn area in Ventura County, both located in Southern California. Notably, 94% of the events occurring in spring and summer were associated with relatively small PS (less than 15,000 km^2), consistent with the development of isolated thunderstorms (Figure 3.4a). In contrast, fall and winter PS were characterized by significantly larger and more widespread reflectivity areas, in some cases exceeding 100,000 km^2. These reflectivity patterns are likely associated with organized frontal systems, narrow cold bands, and atmospheric rivers typical of the region during cold seasons (de Orla-Barile et al., 2022; Oakley et al., 2017; Young et al., 2017).

PS in spring and summer were typically slow-moving systems, with approximately 71% of cases concentrated in the lowest speed bins, whereas fall and winter systems exhibited a broader range of propagation speeds and a more pronounced tail toward higher values. (Figure 3.4c). Slow-moving systems are associated with longer residence times of precipitation over burned areas, whereas fast-moving storms, often driven by strong synoptic forcing such as intensified upper-level jets, typically generate high precipitation rates, hail, and damaging winds (Houze Jr., 2014), all of which describe storm environments capable of producing hazardous rainfall over burned landscapes.

The extreme speeds (e.g., >200 km h^{-1}) observed were likely artifacts of rapid system fragmentation, evidenced by significant area loss and abrupt shifts in the center of gravity

coordinates. Elongated frontal systems and narrow cold fronts, common in California during fall and winter, interact with complex orography, leading to apparent fragmentation with enhanced precipitation on windward slopes and drier conditions on the lee side of mountains. Differences in area and speed between seasons were found statistically significant, according to the Mann–Whitney test with p-values < 0.05.

PS predominantly moved northeastward. About 41% of PS propagated in this direction during spring/summer debris flow events, compared to 36% in fall/winter (Figure 3.4d). However, these seasonal differences are not statistically significant, according to the Kuiper two-sample test. The predominant direction is consistent with the typical orientation of atmospheric rivers (Harris & Carvalho, 2018) and narrow cold fronts (de Orla-Barile et al., 2022) that typically develop along the warm sector of the extratropical cyclones during winter. During summer and spring, a possible mechanism influencing PS propagation is the northward transport of moisture driven by the North American Monsoon (Duan et al., 2024). Rather than as predictor of post-fire debris flow susceptibility, propagation direction helps characterize the rainfall environments triggering this hazard, by providing context on storm movement relative to burned terrain, prevailing flow regimes, dominant storm tracks and intersection with topographic features that can modulate orographic precipitation, information relevant for monitoring how organized precipitation intersects vulnerable landscapes.

Clear seasonal differences are also evident in PS eccentricity. Approximately 60% of cases occurring in fall/winter have eccentricities less than 0.5, consistent with the elongated shapes of narrow cold frontal bands and atmospheric rivers (Figure 3.4b). In contrast, the majority of the summer/spring events (76%) have eccentricity greater than 0.5, reflecting more circular

structures, characteristic of orographic thunderstorms and less organized convection. This seasonal difference in eccentricity is found statistically significant ($p < 0.05$).

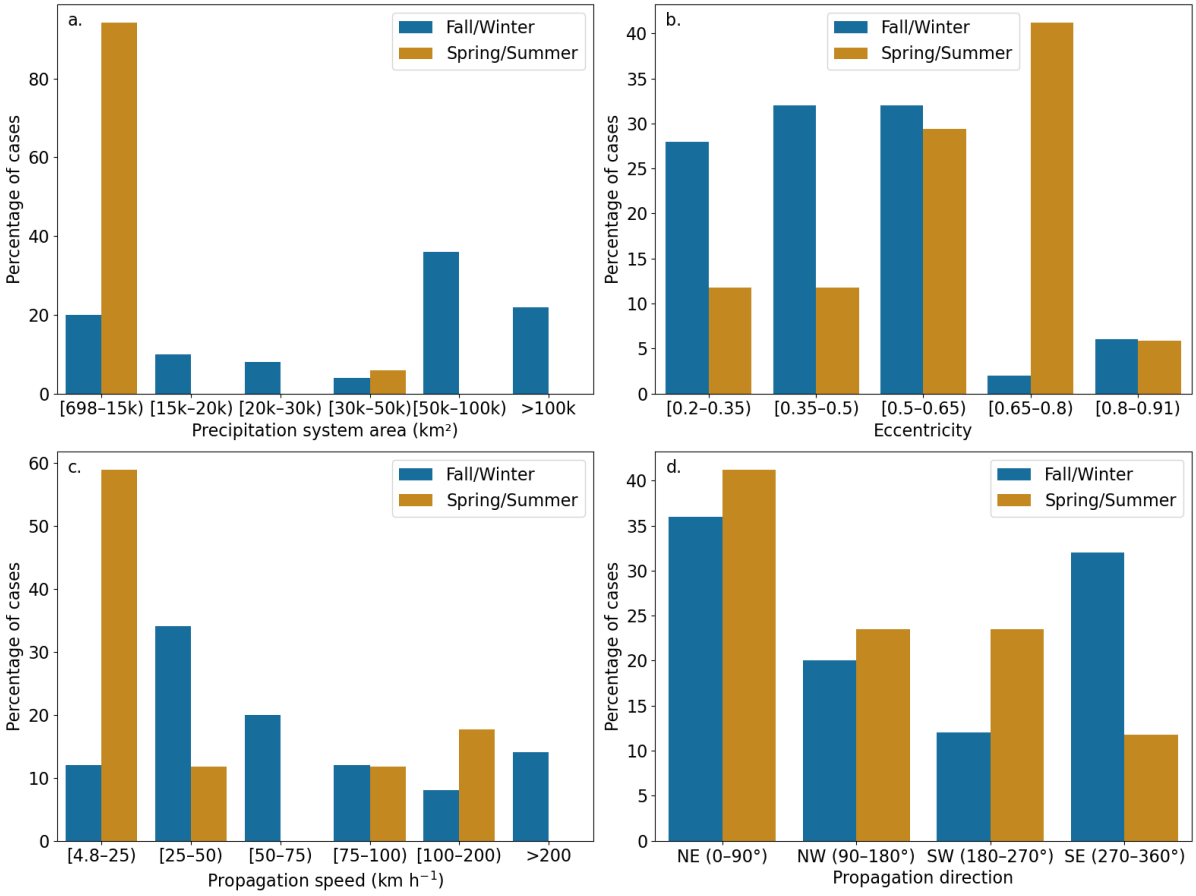


Figure 3.4. Distribution of values by seasonal groups for precipitation systems at the time of peak 15-minute rainfall intensity: **a.** Area, **b.** Eccentricity, **c.** Speed of propagation, and **d.** Direction of propagation.

3.3.1.2.Radar reflectivity in burned areas

Radar reflectivity metrics extracted within burned areas, including reflectivity at debris flow reference locations, the fraction of pixels exceeding specified reflectivity thresholds, and the maximum reflectivity within fire perimeters, provide information on the spatial and temporal distribution of rainfall intensity intersecting burned landscapes. Since radar reflectivity values can be associated with rainfall intensity, they are useful for characterizing

storm conditions during debris flow–producing events. Post-fire debris flow events analyzed in this study occurred under radar reflectivity values ranging from 10.5 to 54 dBZ (drizzle to heavy rain), with distinct seasonal distributions (Figure 3.5a). During spring and summer, the median reflectivity was higher at 42 dBZ (moderate rain), with the upper quartile around 49.5 dBZ (heavy rain). In contrast, fall and winter events showed lower reflectivity percentiles, with a median of 34.5 dBZ (light rain) and an upper quartile of 40 dBZ (moderate rain), and a maximum value of 48 dBZ. These seasonal differences in reflectivity at debris flow locations were statistically significant.

Multiple factors may contribute to the occurrence of debris flows during storms with lower reflectivity in fall and winter. Debris flows can occur after a short interval between wildfire occurrence and the onset of the rainy season (Oakley, 2021), when vegetation has not recovered, soils remain water-repellent, and loose debris is abundant, conditions that maximize susceptibility. Additionally, mesoscale features such as narrow cold frontal rainbands can further concentrate rainfall over portions of burned terrain. Even if radar reflectivity at debris flow reference locations may not fully capture these features, their upstream rainfall can still trigger downstream responses, leading to debris flow occurrence.

Maximum reflectivity within the fire polygon at assumed debris flow timing was generally higher than reflectivity sampled at debris flow reference locations, but remained lower than the peak reflectivity within the PS. Within fire polygons, maximum reflectivity values ranged from 28 dBZ to 60.5 dBZ (light to very heavy rain). Reflectivity values between 50-60 dBZ (heavy rain) has been described in the literature at peak 15-minute intensity for post-fire debris flows occurring in the Springs and Thomas Fire in Southern California (Oakley et al., 2018; Sukup et al., 2016). In spring and summer events, values as low as 39 dBZ (moderate rain)

were recorded, and the median and upper quartiles were equal to 51 and 55.5 dBZ (heavy rain), respectively. In colder months, these percentiles were lower: 43.5 and 49.5 dBZ (moderate-heavy rain), respectively.

To examine reflectivity variability across spatial scales, differences were calculated between (1) the maximum reflectivity within fire perimeters and reflectivity at debris flow reference locations, indicating whether debris flows occurred under near-peak rainfall conditions within the burned area or under comparatively lower values and (2) the fire-perimeter maximum and the overall maximum reflectivity within the PS, serving as a storm-scale reference indicating whether reflectivity values experienced in the burned area are comparable to the most intense portions of the storm system (Figure 3.5b). Excluding outliers, the maximum difference was 21 dBZ for the fire-versus-PS and 23 dBZ for the fire-versus-debris flow location, with a median difference of 8 dBZ in both cases. In 75% of events, differences remained below 14.5 dBZ, indicating that debris flows occurred under broadly intense rainfall rather than at absolute reflectivity maxima. Strong reflectivity features in a system, such as convective cores or narrow rainbands commonly intersect fire perimeters and may contribute to spatial variability in rainfall intensity across burned areas.

Despite these spatial differences, the timing of peak 15-minute rainfall generally coincided with elevated reflectivity within the storm lifecycle. At this time, over half of cases exhibited maximum reflectivity within fire perimeters above the 90th percentile of all values observed during the tracked PS, with similar patterns at debris flow reference locations. Considering the 75th percentile threshold, the majority of events, 78% for fire-perimeter maxima and 72% at debris flow sites, met or exceeded this level. These findings show that the assumed debris

flow timing generally coincides with near-peak phases of storm evolution, regardless of absolute reflectivity magnitudes varying substantially between seasons and storm types.

Analysis of the fraction of burned area pixels exceeding specific reflectivity thresholds also revealed clear seasonal contrasts at the estimated timing of debris flows. For fall and winter events, over 50% of burned-area pixels fell within the 25–35 dBZ range (light to moderate intensities), with higher median fractions in the 25–30, 30–35, and 35–40 dBZ bins compared to spring and summer months. In some cases, more than 60% of the burned area was concentrated within a single bin (30–35 dBZ), indicating widespread, moderate-intensity rainfall during storms linked to debris flows (Figure 3.5c).

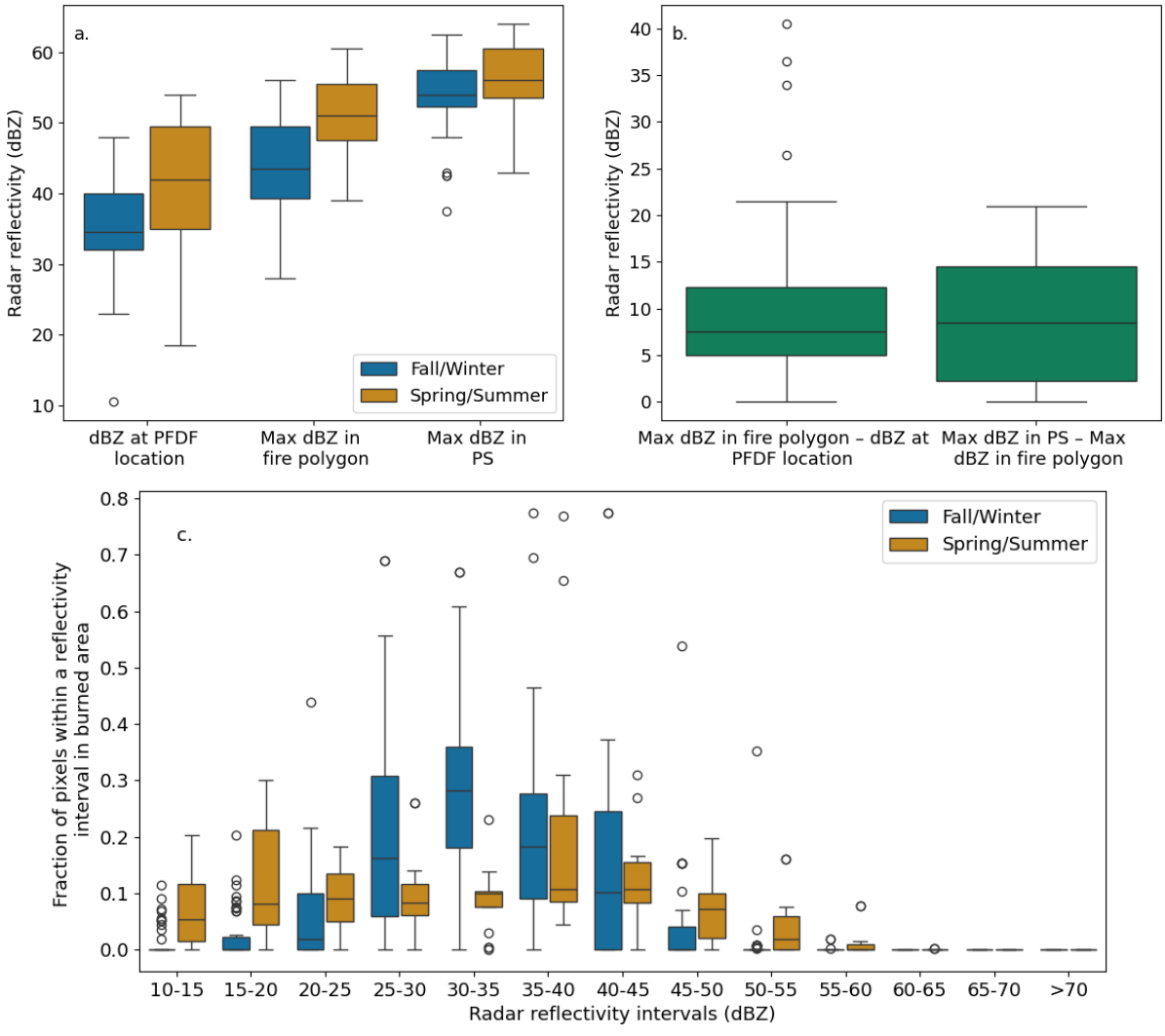


Figure 3.5. Radar reflectivity (dBZ) statistics at the time of peak 15-min rainfall intensity, as measured by the nearest rain gauge to post-fire debris flow location. **a.** Boxplots showing reflectivity at debris flow location, the maximum value within the fire perimeter, and the maximum within the tracked PS, **b.** Boxplots of differences in reflectivity: (left) maximum in fire perimeter minus debris flow location; (right) PS maximum minus fire perimeter maximum, **c.** Boxplots of the fraction of burned area experiencing reflectivity within 5 dBZ intervals. In all panels, boxplots show the median (center line), interquartile range (box edges: 25th–75th percentiles), whiskers extending to 1.5x the interquartile range, and individual points representing outliers beyond this range.

In contrast, spring and summer events displayed a broader reflectivity distribution. Light to moderate rainfall (15–20 dBZ and 35–40 dBZ) affected up to 30% of the burned area, while higher reflectivity above 45 dBZ (heavy precipitation) occurred more frequently than in fall and winter, particularly in the 45–50 and 50–55 dBZ intervals. These high values, however, typically affected less than 15% of the burned area, excluding outliers. Overall, these seasonal differences suggest that fall and winter storms tend to deliver more uniform moderate-intensity rainfall, while spring and summer storms are characterized by a mix of light and moderate rainfall, with more frequent, but spatially limited, bursts of high reflectivity (heavy precipitation), likely reflecting the convective nature of these storms. PS structural properties and reflectivity metrics at estimated debris flow timing are summarized in Table 3.2, allowing comparison between fall/winter and spring/summer storms.

Although previous studies have not quantified the fraction of burned area affected by specific reflectivity thresholds, radar analyses of individual events provide useful context. For instance, the January 9, 2018 Montecito debris flow (Oakley et al., 2018) showed elevated reflectivity in a narrow cold frontal rainband over the western portion of the burned area, while the eastern portion remained moderate to low. Similarly, during the December 12, 2014 Springs Fire, roughly 63% of the burned area experienced reflectivity of 40–55 dBZ (moderate-to-heavy rain) about 30 minutes before the assumed debris flow timing (Sukup et al., 2016).

At a broader scale, Liu et al., (2022) identified four spatial precipitation patterns linked to post-fire debris flows: broad contiguous rainfall, scattered cells, isolated cells, and narrow cold frontal rainbands. Our results show clear seasonal correspondence to these patterns. Fall and winter storms typically resemble broad or narrow rainband patterns, producing widespread moderate-to-high reflectivity across burned areas, as observed in the January 9, 2018 Montecito debris flow and the December 12, 2014 Springs Fire. In contrast, spring and summer storms are more fragmented, with cells of moderate-to-high reflectivity interspersed with low reflectivity, consistent with the isolated pattern described by Liu et al., (2022) and reflected in events such as the Valley Fire on November 29, 2018.

Table 3.2. Summary statistics of structural properties and reflectivity values at peak 15-minute rainfall intensity for post-fire debris flow events. Values are shown as the median (50th percentile) and 75th percentile for each season. If seasonal differences were not statistically significant, the median and 75th percentile represent all cases combined, without seasonal classification.

Metric	Median		75^{th} Percentile	
	Fall/Winter	Spring/Summer	Fall/Winter	Spring/Summer
PS Area (km^2)	67,764	2,112	97,530	3,366
PS Eccentricity	0.43	0.64	0.55	0.69
Speed of propagation (km h^{-1})	53.64	23.51	81.36	79.66
Direction of propagation (degrees)	60 (NE)		93 (N)	
dBZ at post-fire debris flow location	34.5	42	40	49.5
Max dBZ in fire polygon	43.5	51	49.5	55.5

3.3.1.3.Timing relationships among reflectivity-based indicators

To evaluate the temporal correspondence between radar-based indicators and rainfall observations, we compared the timing of fire-wide reflectivity metrics with peak 15-minute rainfall intensities recorded by the nearest rain gauges. Our analysis showed that maximum reflectivity within fire perimeters exhibited the closest temporal alignment with nearest gauge's peak 15-minute intensity, with 34% of events occurring within ±15 minutes, increasing to 53% within ±30 minutes and 65% within ±1 hour (Figure 3.6a). In contrast, the threshold-based metric (>30 dBZ across most of the burned area) showed weaker alignment, with 28%, 41%, and 62% of events falling within the same respective time windows (Figure 3.6b).

We also examined the temporal relationship between fire-wide maximum reflectivity and the timing of maximum reflectivity at debris flow reference locations. Maximum reflectivity at debris flow reference locations corresponds to the highest reflectivity value recorded at each reference location across the full storm duration. Under this comparison, alignment improved: 45% of events fell within ±15 minutes of the fire-wide maximum reflectivity, increasing to 52% within ±30 minutes and 63% within ±1 hour (Figure 3.6c). When maximum reflectivity at debris flow reference locations was compared against the threshold-based metric, the latter showed weaker alignment, capturing only 28%, 46%, and 55% of events within the same respective time windows (Figure 3.6d).

Overall, both rain gauge peak 15-min intensities and maximum reflectivity at debris-flow reference locations exhibited reasonable temporal alignment with fire-wide maximum reflectivity, but the maxima at debris-flow reference locations produced shorter lag times. This indicates that fire-wide maximum reflectivity more consistently coincides with near-peak

storm conditions than fixed reflectivity-threshold metrics and provides stronger temporal context for characterizing rainfall environments associated with post-fire debris-flow events.

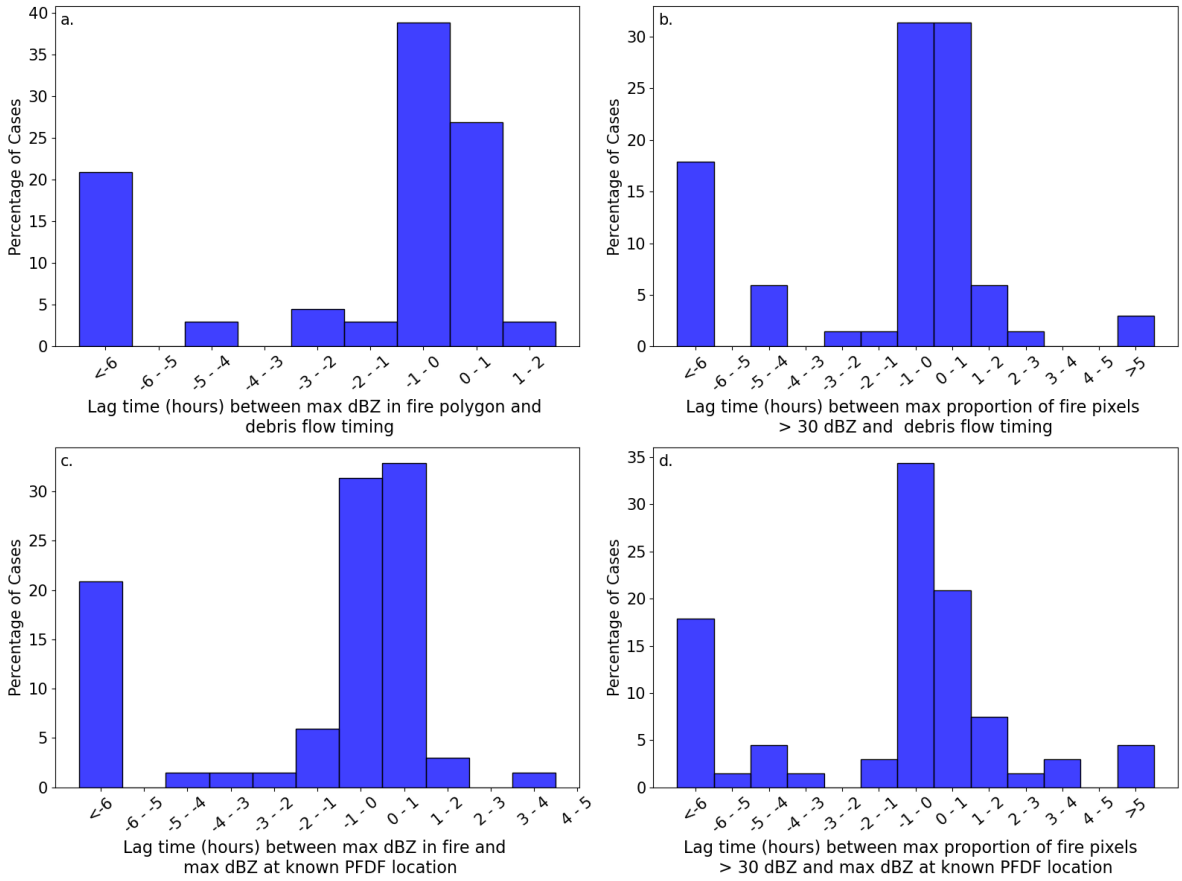


Figure 3.6. Lag times between reflectivity metrics. Time alignment between **a.** maximum reflectivity within the fire polygon vs. peak 15-min rainfall intensity from the nearest rain gauge; **b.** time when most of the burned area exceeded 30 dBZ vs. peak 15-min rainfall intensity from the nearest rain gauge; **c.** maximum reflectivity within the fire polygon vs. maximum reflectivity at post-fire debris flow location; **d.** time when most of the burned area exceeded 30 dBZ vs. maximum reflectivity at post-fire debris flow location.

3.3.2. Application to short- and long-duration storms

3.3.2.1. Long-Duration Storm – Butte Fire (March 4, 2016)

The tracking algorithm was applied to the longest storm in the inventory to demonstrate the tool's applicability to long-duration storms. This instance is associated with post-fire debris flows in the Butte Fire, which burned 287 km^2 and was active for 36 days,

from September 9 to October 15, 2015. The fire began in the Sierra Nevada foothills when a tree branch encountered a power line. Extremely dry vegetation, following four years of drought and a rainless summer, fueled its rapid spread and the fire quickly expanded southward across the region (Schmidt, 2020).

The storm system that affected the burned area began on March 4, 2016, at 22:45 UTC as recorded by a nearby rain gauge located 0.8 to 1.4 km from the documented debris flow sites in Graber (2023). Post-fire debris flows were reported at several road locations, all of which had previously been identified in hazard assessments as susceptible sites for debris flow and flooding at culverts, bridges, and roadside ditches (Post Fire Watershed Emergency Response Team, 2015). Beyond their identification in the post-fire debris flow inventory (Graber, 2023), published documentation of these events remains limited.

To better capture the storm's initial conditions, the PS tracking was initiated 10 minutes earlier, on March 4, 22:35 UTC. The final timestamp in the tracking file is March 7, 2016, at 22:40 UTC, covering approximately 72 out of the 80.5 total storm hours estimated from rain gauge observations. Across the tracking period, 35.4 hours of storm conditions were successfully captured, including the time of peak 15-minute rainfall intensity (23.36 mm h^{-1} on March 6 08:15 UTC), which is used here as a proxy for debris flow timing. The remaining hours could not be detected by the algorithm, likely due to minimal or no rainfall activity as indicated by rain gauge data (Figure 3.7). These low-intensity periods result in weak or absent radar reflectivity, limiting PS identification. Four distinct periods of PS tracking were analyzed, each characterized by unique spatial and geometric properties.

- Period 1 (March 4, 22:35 – March 5, 05:35 UTC): This block exhibited a median PS area of roughly 45,300 km^2. The system was relatively linear, with 75% of

eccentricity values below 0.4, indicating elongated rather than circular shapes. More circular geometries appeared briefly around 01:00 UTC and again near the end of the block. Although 75% of timestamps show the PS moving generally in the north direction, propagation angles varied widely, with a circular median direction of 57° (NE) and a median speed of 46 km h^{-1}. Extreme propagation speeds (~1000 km h^{-1}) occurred near the end of the block, consistent with rapid splitting and loss of spatial coherence in the tracked precipitation system. Average reflectivity at the post-fire debris flow location was 24.5 dBZ, peaking at 38.0 dBZ at 01:50 UTC, coinciding with peak 15-minute rainfall intensity from rain gauge data for this period (3 mm, 12.19 mm h^{-1}). Within the fire polygon, the maximum reflectivity (52.0 dBZ – heavy rain) was recorded 35 minutes later at 02:25 UTC, a magnitude only matched in this and the third analyzed period. The highest reflectivity values were observed in the tracked precipitation system, with peaks of 61 dBZ (very heavy rain) at both 01:20 and 02:35 UTC, that is 30 minutes before peak reflectivity at the debris flow reference location and 10 minutes after the maxima within the fire polygon (Figure 3.7).

- Period 2 (March 5, 11:05 – 14:35 UTC): The PS in the shortest tracked period exhibited more variability in shape, with eccentricity values between 0.27 and 0.96 (median: 0.61), and median area of 28,800 km^2. Directional displacement remained close to period 1 in the north direction, while speed was more variable due to frequent splits and merges, with a median of 78 km h^{-1}. Reflectivity was generally lower in this period, consistent with lower rainfall recorded by the rain gauge. Reflectivity at the post-fire debris flow reference location peaked at 34.0

dBZ at 12:15 UTC, with an average of 23.2 dBZ (light rain). In the fire polygon, reflectivity peaked 25 minutes later at 12:40 UTC with 39.0 dBZ (moderate rain), while the PS reached its maximum of 59.0 dBZ (very heavy rain) earlier, at 11:35 UTC.

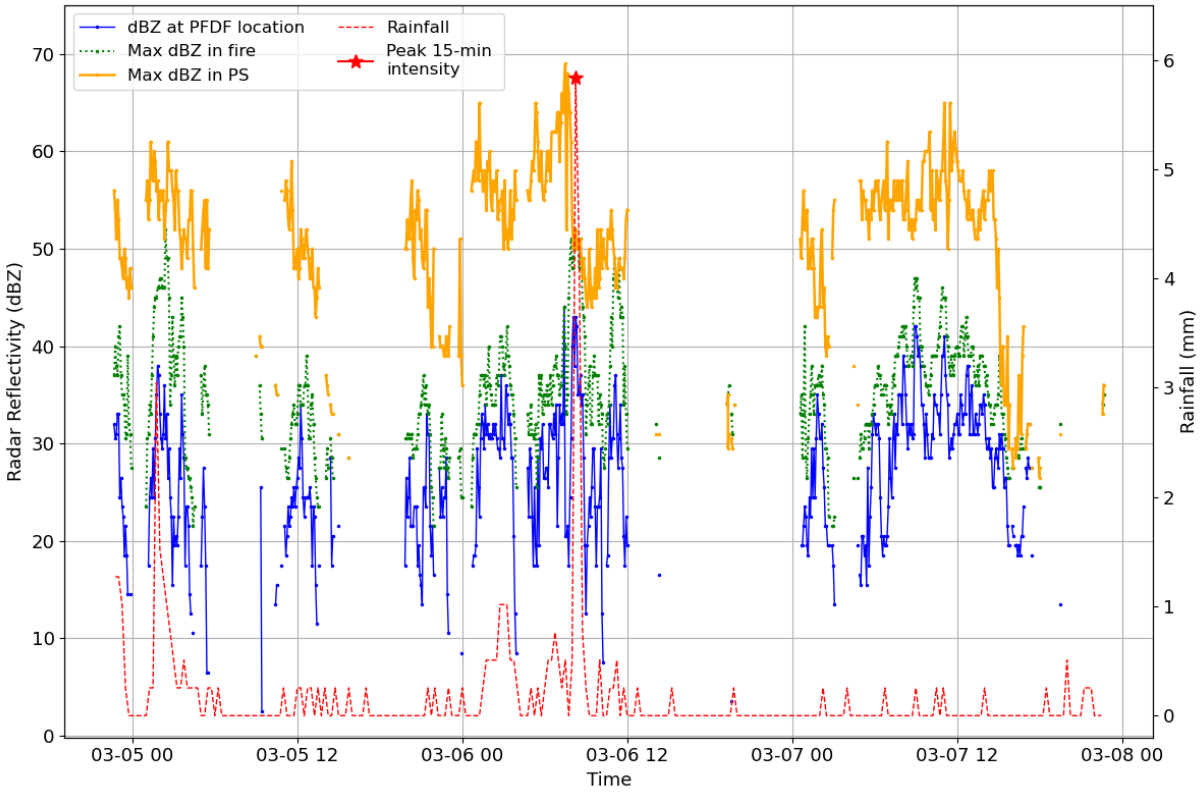


Figure 3.7. Reflectivity metrics tracked and rainfall recorded by nearest rain gauge during storm in Butte Fire in March 2016.

- Period 3 (March 5, 19:50 – March 6, 12:00 UTC): The PS in the longest continuous tracking period featuring debris flow timing had the largest areas, with a median of 89,400 km^2. While eccentricity ranged from 0.18 to 0.71, 75% of values were below 0.48. At the assumed debris flow timing (08:15 UTC), area and eccentricity were ~75,650 km^2 and 0.34, respectively. More circular shapes appeared between 09:10 and 10:20 UTC, shifting to more linear geometries toward the end of the period. Direction

of propagation varied widely but circular median and mean show angles in the eastward direction, with a median speed of 72 km h^{-1}, slower than Period 2. At debris flow timing, speed was 46.4 km h^{-1} and direction was 85° (N). Synchronously, reflectivity peaked in the fire polygon at 52.0 dBZ (heavy rain). The post-fire debris flow reference location had a slightly earlier peak of 44.0 dBZ (moderate-to-heavy rain) at 07:25 UTC, just above the 43.0 dBZ recorded during the peak 15-minute rainfall intensity recorded by rain gauge. The tracked PS experienced its maximum reflectivity of 69.0 dBZ (very heavy rain) shortly after, at 07:30 UTC. Average reflectivity values for this block period were 26 dBZ (light rain) at the post-fire debris flow location, 35 dBZ within the fire perimeter, and 53 dBZ across the tracked PS. The reflectivity values in this period were predominantly low (<30 dBZ – light rain) until 1:10 UTC, after which they gradually increased to around 45 dBZ until 03:20 UTC. During this period, up to 97% of the burned area fell within the 30-40 dBZ range. Higher reflectivity values indicating enhanced precipitation, reaching up to 55 dBZ, were observed briefly between 7:55 and 8:35 UTC, coinciding with the peak 15-minute intensity. At this peak, the portion of the burned area exhibiting 50–55 dBZ (heavy rain) reflectivity reached its maximum, covering 0.7% of the fire polygon, while 91% of the burned area fell within the 25–50 dBZ range (Figure 3.8). Another increase in reflectivity, up to 50 dBZ, occurred between 11:00 and 11:25 UTC, although up to 81% of the burned area remained within the 30-40 dBZ range (moderate rain).

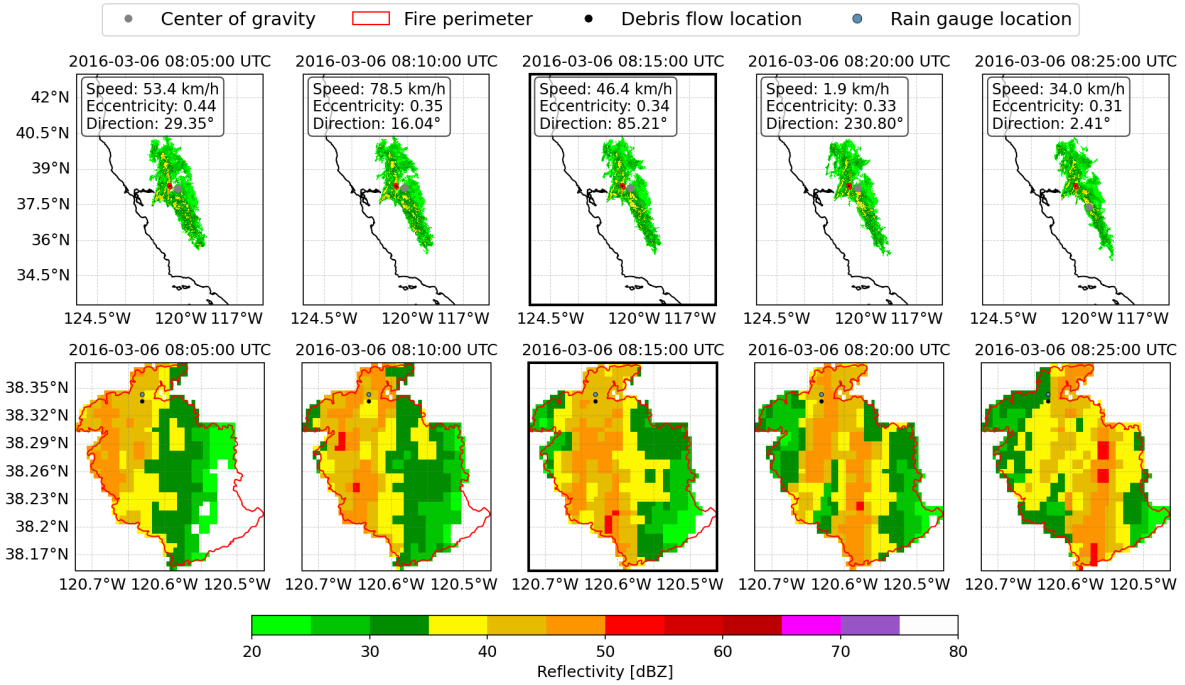


Figure 3.8. Precipitation system and reflectivity within the Butte fire perimeter during a storm in March 2016. Top row: PS tracked 10 minutes before and after recorded peak 15 min intensity by the nearest rain gauge, Bottom row: Reflectivity conditions within fire polygon 10 minutes before and after recorded peak 15 min intensity (thicker frame).

- Period 4 (March 7, 00:35 – 17:15 UTC): Compared to period 3, this time interval featured smaller areas, with half of the values around 73,600 km^2. Eccentricity values were predominantly (75%) less than 0.5 and more circular geometries were found near tracking gaps. Propagation remained variable, though the system exhibited its strongest southeast orientation during this period, with a circular median direction of 327° and median speed of 41 km h^{-1}. This tracked period showed slightly elevated reflectivity, with the post-fire debris flow location averaging 28.5 dBZ and peaking at 42.0 dBZ at 08:55 UTC. Fire perimeter reflectivity peaked simultaneously at 47.0 dBZ (moderate-to-heavy rain), consistent with enhanced precipitation over the burn scar. As in Period 3, the tracked PS peaked later at 11:05 UTC, reaching 65.0 dBZ, with an

average of 51 dBZ, which indicates continued storm intensification within the evolving mesoscale system and very heavy rainfall at some locations.

3.3.2.2. Short-Duration Storm: Tamarack Fire (August 3, 2022)

The Tamarack Fire ignited on July 4, 2021, and burned for 113 days, affecting approximately 278 km² in Alpine County, California. High winds, dry fuels, and extreme conditions allowed the fire to spread rapidly, threatening communities and nearby highways. Roughly 13 months after ignition, a short convective storm passed over the burn area on August 3, 2022. The storm lasted 1.5 hours, from 22:00 to 23:30 UTC (Figure 3.9), producing intense rainfall with a peak 15-minute intensity of 92.45 mm h^{-1} recorded at 22:50 UTC by a rain gauge located 0.65 km from the debris flow site. The rainfall event was associated with reported post-fire debris flows at two locations, causing long-term road closures. Like the winter case, tracking started 10 minutes earlier, capturing the duration of the storm without temporal gaps.

Throughout the tracking period, the PS remained relatively small and consistent, increasing from 686 to 2,695 km^2, with a mean of 1,561 km^2 and a median of 1,465 km^2. PS shape, described by eccentricity, ranged from 0.40 to 0.82. Eccentricity increased steadily until 22:30 UTC before declining to 0.65 toward the end of the storm, with a median value of 0.74 suggesting a predominance of near-circular storm cells. Direction of propagation spanned a wide range (6.3° to 310°), though both circular mean and median directions, 62.2° and 66.5°, respectively indicate a general northeastward movement. Speed of propagation ranged from 3.9 to 42.1 km h^{-1}, with an average and a median of 17 km h^{-1}, indicative of slow, steady progression and minimal displacement of center of gravity, consistent with a localized system.

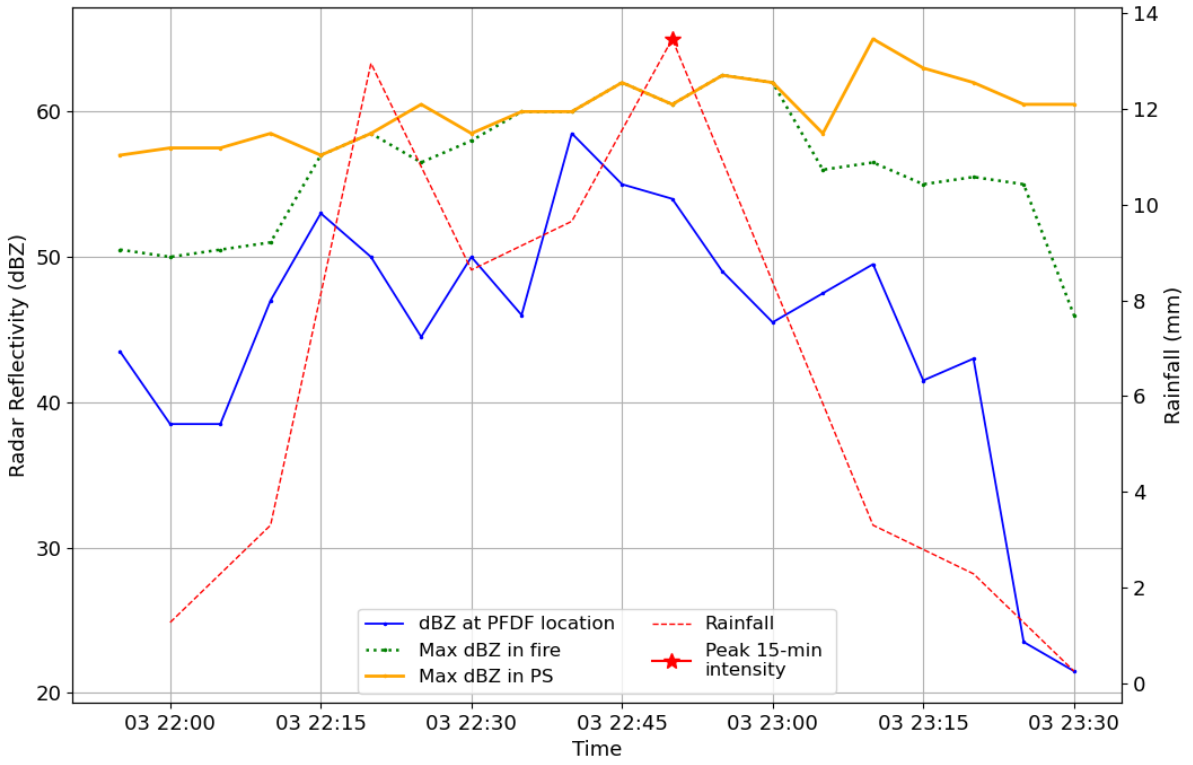


Figure 3.9. Reflectivity metrics tracked and rainfall recorded by nearest rain gauge during storm in Tamarack Fire on August 3, 2022.

Reflectivity values at the post-fire debris flow reference location indicated moderate-to-heavy rain, with initially 43.5 dBZ at 21:55 UTC, peaking at 58.5 dBZ at 22:40 UTC, ten minutes before the estimated timing of debris flow occurrence, when reflectivity measured 54 dBZ. Afterward, reflectivity declined to 21.5 dBZ (light rain) by the end of the storm. The average and median reflectivity at debris flow reference coordinates were 44.98 dBZ and 46.5 dBZ (moderate-to-heavy rain), respectively. Similar to the event location, maximum reflectivity within the fire perimeter ranged from 50.5 dBZ at the onset of the storm to a peak of 62.5 dBZ, occurring five minutes after the peak 15-minute rainfall intensity recorded by the nearby rain gauge. These values then decreased to 46 dBZ by the end of the storm, with an average of 56.15 dBZ.

Across the PS, reflectivity peaked at 65.0 dBZ at 23:10 UTC and averaged 60 dBZ, highlighting intense convective activity that persisted even after within fire polygon peaks. Notably, from 22:35 to 23:00 UTC, reflectivity in the PS matched the maximum values within the fire perimeter and peak rainfall intensity, emphasizing spatial and temporal alignment of the storm with the burned area. The distribution of reflectivity values within the burned area varied across the duration of the storm. Until 22:10 UTC, up to 77% of the fire perimeter was characterized by moderate reflectivity values between 25–45 dBZ (light-to-moderate rain). After this point, higher intensity values between 45–65 dBZ (heavy-to-very heavy rain) began to expand, covering as much as 35% of the perimeter by 23:00 UTC, before declining again toward the end of the storm. At the time of peak 15-minute rainfall intensity given by a nearby rain gauge, most of the burned area remained within the 25–45 dBZ range, with the largest proportions in the 35–40 dBZ and 40–45 dBZ intervals (each 15.4%). Reflectivity values in the 50–55 dBZ range reached 16.1%, the highest observed across all timesteps, indicating the presence of intense convective activity (Figure 3.10). In contrast, areas with reflectivity below 25 dBZ (light rain) were minimal.

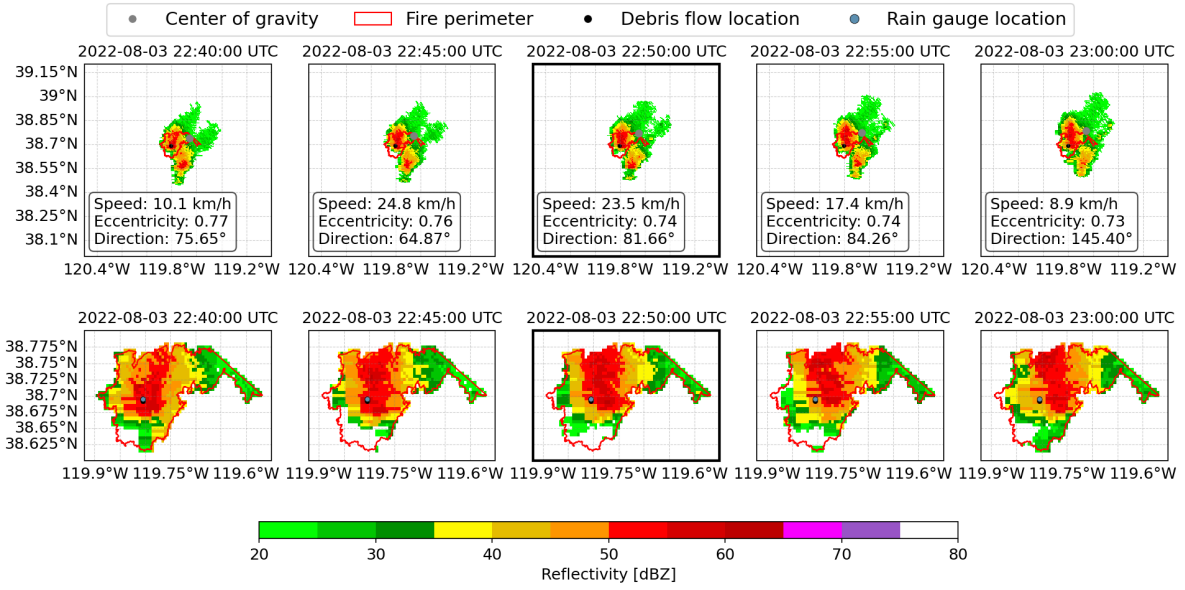


Figure 3.10. Precipitation system and reflectivity within the Tamarack fire perimeter during a storm on August 3, 2022. Top row: PS tracked 10 minutes before and after recorded peak 15-min intensity by the nearest rain gauge, Bottom row: Reflectivity conditions within fire polygon 10 minutes before and after recorded peak 15-min intensity (thicker frame).

These case studies demonstrate the versatility of the PS tracking algorithm in capturing storm evolution across both long- and short-duration rainfall events associated with post-fire debris flow. In the long-duration Butte Fire storm, the algorithm captured multiple phases of storm development, propagation, and fragmentation, while resolving the timing of elevated reflectivity within the burned perimeter relative to peak 15-min intensities from nearby rain gauges. During low-intensity periods, tracked reflectivity patterns were consistent with minimal or absent rainfall observed by nearby gauges. In the short-duration Tamarack Fire storm, the algorithm tracked the full PS lifecycle with minimal temporal gaps, including rapid intensification, localized propagation, and alignment of high-reflectivity cores with documented debris flow reference locations. Across both cases, the tool consistently identified periods and regions within burned areas experiencing elevated rainfall intensity, highlighting its utility for characterizing storm environments relevant to post-fire debris flow hazards.

3.4. Discussion and conclusions

This study demonstrates the applicability of a spatial correlation-based tracking algorithm for supporting the monitoring of rainfall conditions relevant to post-fire debris flow hazards. By tracking coherent precipitation systems and their evolution across entire burn scars, the modified MASCOTTE algorithm captures the organization and evolution of precipitation at meso-β to meso-γ scales, offering insight into when and where burned landscapes are exposed to organized, high-intensity rainfall environments often linked to debris flow–producing storms. This information supports situational awareness and contextual assessment of hazardous storm conditions over vulnerable terrain.

Application across multiple post-fire debris flow events revealed clear seasonal contrasts in precipitation-system structure, reflecting differences in dominant storm regimes and their influence on rainfall exposure over burned areas. At assumed debris flow timing, spring and summer PS were found to have smaller spatial extents (typically under 10,000 km^2) and slower propagation speeds, consistent with short-lived, highly localized, slow-moving systems. In contrast, fall and winter PS exhibited a broader range of sizes and speeds, with events exceeding 100,000 km^2 in area and propagating at speeds greater than 200 km h^{-1}. Eccentricity, which characterizes the shape of PS and is relevant for identifying mesoscale features like squall lines, tends to be higher in spring and summer cases, indicating more circular geometries, whereas fall and winter events generally exhibit more elongated shapes. Conversely, the direction of propagation did not exhibit significant seasonal differences, suggesting it may be less influenced by seasonal variations in storm regimes.

The propagation speeds observed in this study are broadly consistent with previously reported values for winter convective features in California. For example, de Orla-Barile et al., (2022) reported that a subsample of 10 narrow cold frontal rainband cores in Southern California during the winter season propagated with an average speed of 14.2 m s^{-1} (approximately 51 km h^{-1}), ranging from 10 to 18.5 m s^{-1} (36–67 km h^{-1}), based on 1-hour tracking periods using 5-minute radar reflectivity imagery. It is worth mentioning that high propagation speed values using the modified algorithm may result from the method's reliance on changes in the center of gravity coordinates between time steps. Sudden shifts in this center, often caused by merging or splitting of the system, can result in elevated speed estimates. While such transitions can still be captured during peak 15-minute intensity timestamps, they

are more frequently observed during periods of lower rainfall rates, often coinciding with the end of the storm or following the dissipation of one of its rainfall "pulses".

The difference in area size between seasonal groups may be related to the type of hydrometeorological events that tend to occur during specific months. In California, larger-scale meteorological phenomena such as Atmospheric Rivers (ARs) are more frequent in the fall and winter months. These events are long, narrow corridors of enhanced integrated water vapor transport, typically over 2,000 km in length and less than 1,000 km in width (Zhu & Newell, 1998). They occur predominantly during the cold season (Neiman et al., 2008; Ralph & Dettinger, 2012) and impact both Northern and Southern California, with a larger proportion of landfalling atmospheric rivers affecting Northern California compared to Southern California (Young et al., 2017). These widespread rainfall events have also been linked to debris flow occurrences, including those affecting recently burned landscapes (Oakley et al., 2017; Young et al., 2017). Consequently, the larger PS areas and faster propagation speeds observed in fall/winter events likely reflect the influence of these broader-scale systems, in contrast to the smaller, more localized convective thunderstorms typical of spring and summer (Cannon et al., 2008).

We also analyzed reflectivity values at post-fire debris flow reference location and maximum reflectivity within the burned area as well as the proportion of burned area within specific reflectivity intervals for each identified PS. Reflectivity at post-fire debris flow reference location was consistently lower than maxima in fire polygons and large tracked PS, with median differences of <8.5 dBZ. In addition, at estimated debris flow timing in fall and winter months, most burned areas were characterized by spatially widespread moderate rainfall, with values between 25-40 dBZ, including events with approximately 60% of the

perimeter experiencing reflectivity between 30-35 dBZ. In contrast, spring and summer events showed a larger portion of the burned area (up to 30% in some cases) exposed to lower reflectivity values (<25 dBZ, light rain) but with more frequent localized bursts of intense reflectivity (>45 dBZ, heavy rain), and in several cases surpassing 50 dBZ, more frequently than in the cooler months.

Timing comparisons showed that maximum reflectivity within fire perimeters provided the strongest correspondence with peak 15-min rainfall intensities from nearby rain gauges, with 34% of events within ±15 minutes and 65% within ±1 hour, compared to weaker alignment for the >30 dBZ proportion metric (28% and 62%, respectively). Assuming debris flows occurred at the time of maximum radar reflectivity at the debris flow reference location further improved alignment with fire-perimeter maximum reflectivity (+11% within ±15 min), whereas the >30 dBZ threshold metric showed little change. Timing differences appeared to depend strongly on storm duration: short-duration storms generally showed closer alignment between peak rainfall intensity and burned-area reflectivity, whereas long-duration storms with multiple rainfall pulses often produced lag times exceeding one hour. Nearly all events with differences greater than one hour (33% of cases) occurred during storms longer than 15 hours.

Overall, radar-based maxima, both at reference locations and within fire perimeters, demonstrated closer temporal correspondence with elevated rainfall intensity periods than fixed reflectivity thresholds. Although the location of maximum reflectivity within a burn perimeter may not coincide spatially with debris-flow reference locations, its timing reflects near-peak storm evolution over burned terrain. This period corresponds to phases when organized precipitation systems are most dynamically active and when short-duration, high-

intensity rainfall is likely to occur somewhere within the fire area. Accordingly, fire-wide maximum reflectivity is interpreted as providing useful temporal context for hazardous rainfall conditions associated with post-fire debris-flow events.

It is worth mentioning that radar sampling limitations may influence the performance of reflectivity-based metrics, particularly in mountainous terrain common to many burned areas in California. Beam blockage is more pronounced in complex terrain and urban environments, where mountains and built structures can partially or fully obstruct the radar beam, leading to underestimation of reflectivity values downstream of the blockage (Gou & Chen, 2020). In addition, increasing radar beam height with range, compounded by Earth curvature, limits the ability of weather radar to sample the low-level processes, where many hazardous precipitation processes occur (National Research Council, 2005; Wang et al., 2023), including narrow cold-frontal rainbands (Thompson, R. A., 2001). As a result, reflectivity-based threshold metrics that rely on areal coverage may be more susceptible to underestimation in regions affected by beam blockage or reduced low-level sampling, which could contribute to weaker temporal correspondence with debris-flow timing in some events.

The application of the algorithm to two case studies further highlights the algorithm's versatility to track precipitation systems under contrasting storm regimes associated with debris flows in the inventory. The long-duration Butte Fire storm reflects multi-pulse winter systems that subject burned areas to repeated rainfall, whereas the short-duration Tamarack Fire storm demonstrates the role of brief but intense convective bursts in summer. In long-duration storms, particularly during the early and late stages of individual rainfall pulses, reflectivity over burned areas may be weak or spatially fragmented. Under such low-precipitation conditions, the tracking algorithm may not identify coherent reflectivity regions

due to insufficient pixel connectivity, resulting in brief gaps in tracking. Nevertheless, the algorithm consistently captured in both storm types, structural properties and reflectivity patterns at periods of organized, elevated reflectivity relevant to post-fire debris flow hazards.

This analysis focuses solely on peak rainfall intensities as potential triggers of post-fire debris flows. Yet susceptibility is also shaped by other factors such as burn severity, soil erodibility, and terrain steepness, which are central to existing hazard assessment frameworks (Staley et al., 2017), but beyond the scope of this study. Radar-based rainfall metrics instead provide critical temporal and spatial context for when burned landscapes are exposed to rainfall conditions conducive to debris-flow initiation. Furthermore, while this study uses radar reflectivity mosaics, the algorithm could be extended to other remotely sensed or gridded datasets that exhibit rainfall characteristics relevant to this hazard, provided the data comprises spatial connectivity and are available at comparable temporal resolution. Moreover, because radar mosaics data employed in this study provide conterminous United States (CONUS) coverage, the approach could also be used to investigate reflectivity conditions associated with post-fire debris flows in other regions of the southwestern United States.

These results support the modified MASCOTTE tracking algorithm as a practical framework for identifying periods when burned landscapes are exposed to organized precipitation environments capable of producing short-duration intense rainfall, providing complementary information to rain-gauge networks. In its current form, the framework is best suited for real-time operational monitoring by tracking how precipitation systems evolve and intersect burned areas as storms unfold. Three aspects of the tracking output were particularly informative in this regard:

- Storm evolution and organization: Transitions from weakly organized precipitation to coherent convective or frontal structures signal shifts toward more efficient rainfall production. Clear seasonal contrasts emerge, with winter systems generally larger, faster, and more linear with widespread moderate-to-heavy rain, and summer systems smaller, slower, more circular, and more heterogeneous with localized high-reflectivity cores.
- Maximum reflectivity within the fire perimeter: This metric provided the most consistent temporal marker of enhanced precipitation and near-peak storm intensity over burned terrain, indicating periods when rainfall conditions relevant to debris-flow hazards are most likely present.
- Spatial growth of moderate reflectivity across the burn scar: Expansion of moderate reflectivity over substantial portions of a burn scar reflects increasing exposure of vulnerable landscapes to organized rainfall.

These elements provide actionable context on storm motion, persistence, and exposure that can support real-time situational awareness during storms affecting burned terrain. The framework could be extended toward a nowcasting capacity by applying the tracking algorithm to gridded quantitative precipitation forecasts or model-derived reflectivity fields, for example, from numerical weather prediction outputs, allowing structural properties and rainfall intensity over burn scars to be anticipated ahead of arrival of the system. Advancing from monitoring toward predictive debris flow assessment would require linking the structural properties and reflectivity metrics described here with landscape susceptibility factors, including burn severity, slope and sediment availability. The tracking method described here could then serve as the meteorological component of a coupled hazard monitoring system,

where storm evolution and rainfall intensity over burned terrain inform alert levels when paired with known susceptibility conditions in targeted locations. The integration of storm-scale rainfall information with terrain and soil-based susceptibility factors, therefore, remains an important direction for future research that could further clarify how meteorological forcing interacts with landscape conditions in post-fire settings, strengthening hazard assessments and operational decision support.

3.5. References

Abatzoglou, J. T., Hatchett, B. J., Fox-Hughes, P., Gershunov, A., & Nauslar, N. J. (2021). Global climatology of synoptically-forced downslope winds. *International Journal of Climatology*, *41*(1), 31–50. https://doi.org/10.1002/joc.6607

Abatzoglou, J. T., Redmond, K. T., & Edwards, L. M. (2009). Classification of Regional Climate Variability in the State of California. *Journal of Applied Meteorology and Climatology*, *48*(8), 1527-1541. https://doi.org/10.1175/2009JAMC2062.1

California Geological Survey. (2023). Reported California Landslides [Dataset]. Retrieved from https://cadoc.maps.arcgis.com/apps/webappviewer/index.html?id=bc48ad40e3504134a1fc8f3909659041&_gl=1*1kr33eo*_ga*MjE0MDgyODE2NS4xNzQ1NjA2MTg0*_ga_N4MB98DBXY*MTc0NTYwNjE4NC4xLjAuMTc0NTYwNjE4NC4wLjAuMA.

Cannon, S. H., Gartner, J. E., Wilson, R. C., Bowers, J. C., & Laber, J. L. (2008). Storm rainfall conditions for floods and debris flows from recently burned areas in southwestern Colorado and southern California. *Geomorphology, Debris Flows Initiated by Runoff, Erosion, and Sediment Entrainment in Western North America*, *96*(3), 250–269. https://doi.org/10.1016/j.geomorph.2007.03.019

Carvalho, L. M. V., & Jones, C. (2001). A Satellite Method to Identify Structural Properties of Mesoscale Convective Systems Based on the Maximum Spatial Correlation Tracking Technique (MASCOTTE). *Journal of Applied Meteorology*, *40*(10), 1683-1701. https://journals.ametsoc.org/view/journals/apme/40/10/1520-0450_2001_040_1683_asmtis_2.0.co_2.xml

Culler, E. S., Livneh, B., Rajagopalan, B., & Tiampo, K. F. (2023). A data-driven evaluation of post-fire landslide susceptibility. *Natural Hazards and Earth System Sciences*, *23*(4), 1631–1652. https://doi.org/10.5194/nhess-23-1631-2023

De Graff, J. V., Staley, D. M., Stock, G. M., Takenaka, K., Gallegos, A. L., & Neptune, C. K. (2022). Rainfall Triggering of Post-Fire Debris Flows over a 28-Year Period near El Portal,

California, USA. *Environmental & Engineering Geoscience*, *28*(1), 133–145. https://doi.org/10.2113/EEG-D-21-00031

de Orla-Barile, M., Cannon, F., Oakley, N. S., & Ralph, F. M. (2022). A Climatology of Narrow Cold-Frontal Rainbands in Southern California. *Geophysical Research Letters*, *49*(2), e2021GL095362. https://doi.org/10.1029/2021GL095362

DeFlorio, M. J., Sengupta, A., Castellano, C. M., Wang, J., Zhang, Z., Gershunov, A., Guirguis, K., Niño, R. L., Clemesha, R. E. S., Pan, M., Xiao, M., Kawzenuk, B., Gibson, P. B., Scheftic, W., Broxton, P. D., Switanek, M. B., Yuan, J., Dettinger, M. D., Hecht, C. W., … Anderson, M. L. (2024). *From California's Extreme Drought to Major Flooding: Evaluating and Synthesizing Experimental Seasonal and Subseasonal Forecasts of Landfalling Atmospheric Rivers and Extreme Precipitation during Winter 2022/23*. https://doi.org/10.1175/BAMS-D-22-0208.1

Dettinger, M. D., Ralph, F. M., Das, T., Neiman, P. J., & Cayan, D. R. (2011). Atmospheric Rivers, Floods and the Water Resources of California. *Water*, *3*(2), Article 2. https://doi.org/10.3390/w3020445

Dixon, M., & Wiener, G. (1993). TITAN: Thunderstorm Identification, Tracking, Analysis, and Nowcasting—A Radar-based Methodology. *Journal of Atmospheric and Oceanic Technology*, *10*(6), 785-797 https://journals.ametsoc.org/view/journals/atot/10/6/1520-0426_1993_010_0785_ttitaa_2_0_co_2.xml

Dong, L., Leung, L. R., Song, F., & Lu, J. (2018). Roles of SST versus Internal Atmospheric Variability in Winter Extreme Precipitation Variability along the U.S. West Coast. *Journal of Climate*, *31*(19), 8039-8058. https://doi.org/10.1175/JCLI-D-18-0062.1

Duan, S., Ullrich, P., & Boos, W. R. (2024). Meteorological Drivers of North American Monsoon Extreme Precipitation Events. *Journal of Geophysical Research: Atmospheres*, *129*(13), e2023JD040535. https://doi.org/10.1029/2023JD040535

Fabry, F. (2015). *Radar Meteorology: Principles and Practice*. Cambridge University Press. https://doi.org/10.1017/CBO9781107707405

Fujita, T. T. (1981). Tornadoes and Downbursts in the Context of Generalized Planetary Scales. *Journal of Atmospheric Sciences*, *38*(8), 1511-1534. https://journals.ametsoc.org/view/journals/atsc/38/8/1520-0469_1981_038_1511_taditc_2_0_co_2.xml

Gershunov, A., Shulgina, T., Clemesha, R. E. S., Guirguis, K., Pierce, D. W., Dettinger, M. D., Lavers, D. A., Cayan, D. R., Polade, S. D., Kalansky, J., & Ralph, F. M. (2019). Precipitation regime change in Western North America: The role of Atmospheric Rivers. *Scientific Reports*, *9*(1), 9944. https://doi.org/10.1038/s41598-019-46169-w

Goss, M., Swain, D. L., Abatzoglou, J. T., Sarhadi, A., Kolden, C. A., Williams, A. P., & Diffenbaugh, N. S. (2020). Climate change is increasing the likelihood of extreme autumn

wildfire conditions across California. *Environmental Research Letters*, *15*(9), 094016. https://doi.org/10.1088/1748-9326/ab83a7

Goswami, B., & Bhandari, G. (2013). Convective Cloud Detection and Tracking from Series of Infrared Images. *Journal of the Indian Society of Remote Sensing*, *41*(2), 291–299. https://doi.org/10.1007/s12524-012-0234-3

Gou, Y., & Chen, H. (2020). Combining Radar Attenuation and Partial Beam Blockage Corrections for Improved Quantitative Application. *Journal of Hydrometeorology*, *22*(1), 139-153. https://doi.org/10.1175/JHM-D-20-0121.1

Graber, A. P. (2023). *Compilation of runoff-generated debris-flow inventories for 17 fires across Arizona, California, Colorado, New Mexico, and Washington, USA* [Dataset]. U.S. Geological Survey. https://doi.org/10.5066/P98Q4CDH

Guilinger, J. J., Gray, A. B., Barth, N. C., & Fong, B. T. (2020). The Evolution of Sediment Sources Over a Sequence of Postfire Sediment-Laden Flows Revealed Through Repeat High-Resolution Change Detection. *Journal of Geophysical Research: Earth Surface*, *125*(10), e2020JF005527. https://doi.org/10.1029/2020JF005527

Haberlie, A. M., & Ashley, W. S. (2018). A Method for Identifying Midlatitude Mesoscale Convective Systems in Radar Mosaics. Part II: Tracking. *Journal of Applied Meteorology and Climatology*, *57*(7), 1599-1621. https://doi.org/10.1175/JAMC-D-17-0294.1

Harris, S. M., & Carvalho, L. M. V. (2018). Characteristics of southern California atmospheric rivers. *Theoretical and Applied Climatology*, *132*(3), 965–981. https://doi.org/10.1007/s00704-017-2138-1

Houze R.A., Jr. (2014). *Cloud Dynamics* (2nd ed., Vol. 104). Academic Press.

Johnson, B. O., & Delworth, T. L. (2023). The Role of the Gulf of California in the North American Monsoon. *Journal of Climate*, *36*(6), 1541-1559. https://doi.org/10.1175/JCLI-D-22-0365.1

Johnson, J. T., MacKeen, P. L., Witt, A., Mitchell, E. D. W., Stumpf, G. J., Eilts, M. D., & Thomas, K. W. (1998). The Storm Cell Identification and Tracking Algorithm: An Enhanced WSR-88D Algorithm. *Weather and Forecasting*, *13*(2), 263-276. https://journals.ametsoc.org/view/journals/wefo/13/2/1520-0434_1998_013_0263_tsciat_2_0_co_2.xml

Jung, S.-H., & Lee, G. (2015). Radar-based cell tracking with fuzzy logic approach. *Meteorological Applications*, *22*(4), 716–730. https://doi.org/10.1002/met.1509

Kean, J. W., Staley, D. M., & Cannon, S. H. (2011). In situ measurements of post-fire debris flows in southern California: Comparisons of the timing and magnitude of 24 debris-flow events with rainfall and soil moisture conditions. *Journal of Geophysical Research: Earth Surface*, *116*(F4). https://doi.org/10.1029/2011JF002005

Kirschbaum, D. B., Adler, R., Hong, Y., Hill, S., & Lerner-Lam, A. (2010). A global landslide catalog for hazard applications: Method, results, and limitations. *Natural Hazards*, *52*(3), 561–575. https://doi.org/10.1007/s11069-009-9401-4

Kostelnik, J., Rengers, F. K., Wald, L., & Schmitt, R. (2021, December 17). *Northern and Central California Debris Flows Overview*. ArcGIS StoryMaps. https://storymaps.arcgis.com/stories/d6c9dc95f0f84fb1994a164f18115fa5

Lakshmanan, V., Herzog, B., & Kingfield, D. (2015). A Method for Extracting Postevent Storm Tracks. *Journal of Applied Meteorology and Climatology*, *54*(2), 451-462. https://doi.org/10.1175/JAMC-D-14-0132.1

Lareau, N. P., Donohoe, A., Roberts, M., & Ebrahimian, H. (2022). Tracking Wildfires With Weather Radars. *Journal of Geophysical Research: Atmospheres*, *127*(11), e2021JD036158. https://doi.org/10.1029/2021JD036158

Li, C., Handwerger, A. L., & Horton, D. E. (2025). Mixed Hydrometeorological Processes Explain Regional Landslide Potential. *Geophysical Research Letters*, *52*(14), e2025GL115912. https://doi.org/10.1029/2025GL115912

Liu, T., McGuire, L. A., Oakley, N., & Cannon, F. (2022). Temporal changes in rainfall intensity–duration thresholds for post-wildfire flash floods in southern California. *Natural Hazards and Earth System Sciences*, *22*(2), 361–376. https://doi.org/10.5194/nhess-22-361-2022

Luković, J., Chiang, J. C. H., Blagojević, D., & Sekulić, A. (2021). A Later Onset of the Rainy Season in California. *Geophysical Research Letters*, *48*(4), e2020GL090350. https://doi.org/10.1029/2020GL090350

Machado, L. a. T., Rossow, W. B., Guedes, R. L., & Walker, A. W. (1998). Life Cycle Variations of Mesoscale Convective Systems over the Americas. *Monthly Weather Review*, *126*(6), 1630-1654. https://journals.ametsoc.org/view/journals/mwre/126/6/1520-0493_1998_126_1630_lcvomc_2.0.co_2.xml

Markowski, P., & Richardson, Y. (2010). *Mesoscale Meteorology in Midlatitudes*. John Wiley and Sons. https://doi.org/10.1002/9780470682104

Marshall, J. S., & Palmer, W. M. K. (1948). THE DISTRIBUTION OF RAINDROPS WITH SIZE. *Journal of Atmospheric Sciences*, *5*(4), 165-166. https://journals.ametsoc.org/view/journals/atsc/5/4/1520-0469_1948_005_0165_tdorws_2_0_co_2.xml

McGuire, L. A., Ebel, B. A., Rengers, F. K., Vieira, D. C. S., & Nyman, P. (2024). Fire effects on geomorphic processes. *Nature Reviews Earth & Environment*, *5*(7), 486–503. https://doi.org/10.1038/s43017-024-00557-7

McGuire, L. A., Rengers, F. K., Kean, J. W., Staley, D. M., & Mirus, B. B. (2018). Incorporating spatially heterogeneous infiltration capacity into hydrologic models with applications for simulating post-wildfire debris flow initiation. *Hydrological Processes*, *32*(9), 1173–1187. https://doi.org/10.1002/hyp.11458

McGuire, L. A., Rengers, F. K., Oakley, N., Kean, J. W., Staley, D. M., Tang, H., de Orla-Barile, M., & Youberg, A. M. (2021). Time Since Burning and Rainfall Characteristics Impact Post-Fire Debris-Flow Initiation and Magnitude. *Environmental & Engineering Geoscience*, *27*(1), 43–56. https://doi.org/10.2113/EEG-D-20-00029

Mo, K. C., & Higgins, R. W. (1998). Tropical Influences on California Precipitation. *Journal of Climate*, *11*(3), 412-430. https://journals.ametsoc.org/view/journals/clim/11/3/1520-0442_1998_011_0412_tiocp_2.0.co_2.xml

Moseley, C., Berg, P., & Haerter, J. O. (2013). Probing the precipitation life cycle by iterative rain cell tracking. *Journal of Geophysical Research: Atmospheres*, *118*(24), 13,361-13,370. https://doi.org/10.1002/2013JD020868

Nash, D., & Carvalho, L. M. V. (2020). Brief Communication: An electrifying atmospheric river – understanding the thunderstorm event in Santa Barbara County during March 2019. *Natural Hazards and Earth System Sciences*, *20*(7), 1931–1940. https://doi.org/10.5194/nhess-20-1931-2020

National Research Council. (2005). *Flash flood forecasting over complex terrain: With an assessment of the Sulphur Mountain NEXRAD in Southern California*. The National Academies Press. https://doi.org/10.17226/11727

Neiman, P. J., Ralph, F. M., Wick, G. A., Lundquist, J. D., & Dettinger, M. D. (2008). Meteorological Characteristics and Overland Precipitation Impacts of Atmospheric Rivers Affecting the West Coast of North America Based on Eight Years of SSM/I Satellite Observations. *Journal of Hydrometeorology*, *9*(1), 22-47. https://doi.org/10.1175/2007JHM855.1

Neptune, C. K., Degraff, J. V., Pluhar, C. J., Lancaster, J. T., & Staley, D. M. (2021). Rainfall Thresholds for Post-Fire Debris-Flow Generation, Western Sierra Nevada, CA. *Environmental & Engineering Geoscience*, *27*(4), 439–453. https://doi.org/10.2113/EEG-D-21-00039

NOAA National Weather Service, R. O. C. (1991). *NOAA Next Generation Radar (NEXRAD) Level II Base Data* [Dataset]. NOAA National Centers for Environmental Information. https://doi.org/10.7289/V5W9574V

Oakley, N. S. (2021). A Warming Climate Adds Complexity to Post-Fire Hydrologic Hazard Planning. *Earth's Future*, *9*(7), e2021EF002149. https://doi.org/10.1029/2021EF002149

Oakley, N. S., Cannon, F., Munroe, R., Lancaster, J. T., Gomberg, D., & Ralph, F. M. (2018). Brief communication: Meteorological and climatological conditions associated with the 9 January 2018 post-fire debris flows in Montecito and Carpinteria, California, USA. *Natural*

Hazards and Earth System Sciences, *18*(11), 3037–3043. https://doi.org/10.5194/nhess-18-3037-2018

Oakley, N. S., Lancaster, J. T., Kaplan, M. L., & Ralph, F. M. (2017). Synoptic conditions associated with cool season post-fire debris flows in the Transverse Ranges of southern California. *Natural Hazards*, *88*(1), 327–354. https://doi.org/10.1007/s11069-017-2867-6

Orlanski, I. (1975). A Rational Subdivision of Scales for Atmospheric Processes. *Bulletin of the American Meteorological Society*, *56*(5), 527–530.

Post Fire Emergency Watershed Response Team. (2015). Assessment of Post fire Debris-Flow Hazards for the 2015 Butte Fire CA AEU-024918. https://ucanr.edu/sites/default/files/2020-06/327652.pdf

Prein, A. F., Feng, Z., Fiolleau, T., Moon, Z. L., Núñez Ocasio, K. M., Kukulies, J., Roca, R., Varble, A. C., Rehbein, A., Liu, C., Ikeda, K., Mu, Y., & Rasmussen, R. M. (2024). Km-Scale Simulations of Mesoscale Convective Systems Over South America—A Feature Tracker Intercomparison. *Journal of Geophysical Research: Atmospheres*, *129*(8), e2023JD040254. https://doi.org/10.1029/2023JD040254

Ralph, F. M., & Dettinger, M. D. (2012). Historical and National Perspectives on Extreme West Coast Precipitation Associated with Atmospheric Rivers during December 2010. *Bulletin of the American Meteorological Society,* 93*(6), 783-790.* https://doi.org/10.1175/BAMS-D-11-00188.1

Raut, B. A., Jackson, R., Picel, M., Collis, S. M., Bergemann, M., & Jakob, C. (2021). An Adaptive Tracking Algorithm for Convection in Simulated and Remote Sensing Data. *Journal of Applied Meteorology and Climatology*, *60*(4), 513-526. https://doi.org/10.1175/JAMC-D-20-0119.1

Rossi, P. J., Chandrasekar, V., Hasu, V., & Moisseev, D. (2015). Kalman Filtering–Based Probabilistic Nowcasting of Object-Oriented Tracked Convective Storms. *Journal of Atmospheric and Oceanic Technology*, *32*(3), 461-477. https://doi.org/10.1175/JTECH-D-14-00184.1

Schmidt, J. (2020, April 10). *The Butte Fire: A Case Study in Using LIDAR Measures of Pre-Fire Vegetation to Estimate Structure Loss Rates* [MPRA Paper]. https://mpra.ub.uni-muenchen.de/99699/

Schwartz, J. Y., Oakley, N. S., & Alessio, P. (2021). Assessment of a Post-Fire Debris Flow Impacting El Capitan Watershed, Santa Barbara County, California, U.S.A. *Environmental & Engineering Geoscience*, *27*(4), 423–437. https://doi.org/10.2113/EEG-D-21-00008

Selander, B. D., Calhoun, N., Burns, W. J., Kean, J. W., & Rengers, F. K. (2025). Assessment of western Oregon debris-flow hazards in burned and unburned environments. *Earth Surface Processes and Landforms*, *50*(4), e70045. https://doi.org/10.1002/esp.70045

Shakesby, R. A., & Doerr, S. H. (2006). Wildfire as a hydrological and geomorphological agent. *Earth-Science Reviews*, *74*(3), 269–307. https://doi.org/10.1016/j.earscirev.2005.10.006

Staley, D. M., Kean, J. W., Cannon, S. H., Schmidt, K. M., & Laber, J. L. (2013). Objective definition of rainfall intensity–duration thresholds for the initiation of post-fire debris flows in southern California. *Landslides*, *10*(5), 547–562. https://doi.org/10.1007/s10346-012-0341-9

Staley, D. M., Kean, J. W., & Rengers, F. K. (2020). The recurrence interval of post-fire debris-flow generating rainfall in the southwestern United States. *Geomorphology*, *370*, 107392. https://doi.org/10.1016/j.geomorph.2020.107392

Staley, D. M., Negri, J. A., Kean, J. W., Laber, J. L., Tillery, A. C., & Youberg, A. M. (2017). Prediction of spatially explicit rainfall intensity–duration thresholds for post-fire debris-flow generation in the western United States. *Geomorphology*, *278*, 149–162. https://doi.org/10.1016/j.geomorph.2016.10.019

Staley, D. M., Tillery, A. C., Kean, J. W., McGuire, L. A., Pauling, H. E., Rengers, F. K., & Smith, J. B. (2018). Estimating post-fire debris-flow hazards prior to wildfire using a statistical analysis of historical distributions of fire severity from remote sensing data. *International Journal of Wildland Fire*, *27*(9), 595. https://doi.org/10.1071/WF17122

Sukup, S., Laber, J., Sweet, D., & Thompson, R. (2016). *Analysis of an Intense Narrow Cold Frontal Rainband and the Springs Fire Burn Area Debris Flows of 12 December 2014*. https://www.weather.gov/media/wrh/online_publications/TAs/TA1601.pdf

Swain, D. L. (2021). A Shorter, Sharper Rainy Season Amplifies California Wildfire Risk. *Geophysical Research Letters*, *48*(5), e2021GL092843. https://doi.org/10.1029/2021GL092843

Swain, D. L., Horton, D. E., Singh, D., & Diffenbaugh, N. S. (2016). Trends in atmospheric patterns conducive to seasonal precipitation and temperature extremes in California. *Science Advances*, *2*(4), e1501344. https://doi.org/10.1126/sciadv.1501344

Thomas, M. A., Kean, J. W., McCoy, S. W., Lindsay, D. N., Kostelnik, J., Cavagnaro, D. B., Rengers, F. K., East, A. E., Schwartz, J. Y., Smith, D. P., & Collins, B. D. (2023a). Postfire hydrologic response along the Central California (USA) coast: Insights for the emergency assessment of postfire debris-flow hazards. *Landslides*. https://doi.org/10.1007/s10346-023-02106-7

Thomas, M. A., Kean, J. W., McCoy, S. W., Lindsay, D. N., Kostelnik, J., Cavagnaro, D. B., Rengers, F. K., East, A., Schwartz, J. Y., Smith, D., & Collins, B. (2023b). *Field-verified inventory of postfire hydrologic response for the 2020 CZU Lightning Complex, River, Camel, and Dolan Fires following a 26-29 January 2021 atmospheric river storm sequence* [Dataset]. U.S. Geological Survey. https://doi.org/10.5066/P91O03Y7

Thompson, R. A. (2001). *Flash flood event of 6 February 1998: A case study (NWS Western Region Technical Attachment 01-08)*. National Weather Forecast Office. https://www.weather.gov/media/wrh/online_publications/TAs/ta0108.pdf

Wang, L., Chen, H., Cifelli, R., & Li, Z. (2023). Improving Surface Rainfall Mapping in Complex Terrain Regions Through Lowering the Minimum Scan Elevation Angle of Operational Weather Radar. *IEEE Geoscience and Remote Sensing Letters*, *20*, 1–5. https://doi.org/10.1109/LGRS.2023.3270912

Young, A. M., Skelly, K. T., & Cordeira, J. M. (2017). High-impact hydrologic events and atmospheric rivers in California: An investigation using the NCEI Storm Events Database. *Geophysical Research Letters*, *44*(7), 3393–3401. https://doi.org/10.1002/2017GL073077

Zhu, Y., & Newell, R. E. (1998). A Proposed Algorithm for Moisture Fluxes from Atmospheric Rivers. *Monthly Weather Review*, *126*(3), 725-735. https://journals.ametsoc.org/view/journals/mwre/126/3/1520-0493_1998_126_0725_apafmf_2.0.co_2.xml

Chapter 4

4. Integrating atmospheric and surficial controls to predict post-fire debris flows in California

Abstract

Although short-duration, high-intensity rainfall is a well-known trigger of post-fire debris flows, the synoptic and mesoscale atmospheric processes that generate these conditions remain less well understood and are rarely incorporated into predictive models. This study addresses that gap by developing a Random Forest (RF) model that combines surface predictors used in hazard assessments with structural and atmospheric variables that describe processes producing intense rainfall. These include peak rainfall intensity, slope, burn severity, atmospheric river strength, convective instability, low-level wind speed, terrain–wind interaction, precipitation-system structure and radar reflectivity. Results show that atmospheric variables provide stronger predictive skill than terrain variables alone, with radar reflectivity, moisture transport, and low-level wind speed emerging as the most influential predictors. Seasonal contrasts were also evident: PFDFs in the cool season were linked to large, moisture-rich systems associated with atmospheric rivers, whereas those in the warm season were linked to smaller, slower-moving convective storms with higher reflectivity and moderate instability. The model achieved high accuracy (0.91) and precision (1.00), although recall (0.64) and F1-score (0.78) remained moderate, reflecting challenges likely associated with class imbalance. Validation using a case study showed that the model resolved contrasts in susceptibility across the burn perimeter, distinguishing drainages with lower predicted probabilities from areas of elevated hazard rather than assigning uniformly high likelihood

across the landscape. These results suggest that incorporating atmospheric conditions can complement existing approaches by providing additional context for PFDF hazard, although further refinement is needed before such methods can be applied reliably in operational settings.

4.1. Introduction

Post-fire debris flows are frequently triggered by intense rainfall, including short-duration thunderstorms and long-duration frontal storms, particularly in the southwestern United States (Cannon et al., 2008; Ralph et al., 2006). California has a Mediterranean climate, with wet winters and long, dry summers (Dettinger et al., 2011). Most of the state's annual precipitation is delivered by a small number of extreme storms in fall and winter seasons (November–April), which account for over 90% of total rainfall (Gershunov et al., 2019; Mo & Higgins, 1998; Swain et al., 2016). A common feature of these long-duration storms is the presence of atmospheric rivers in the winter season, which are narrow corridors of concentrated water vapor transport in the lower atmosphere that can extend over 2,000 km and typically contain more than 20 mm of water vapor (Neiman et al., 2008; Ralph et al., 2004).

Spring and summer storms contribute a smaller fraction to California's annual rainfall but can deliver intense, short-duration downpours capable of triggering flash floods and debris flows. Many of these events are associated with the northward progression of the North American Monsoon, when surges of moisture interact with California's complex topography to fuel strong thunderstorms (Adams & Comrie, 1997; Duan et al., 2024). Tropical systems forming off the coast of Baja California can also track inland, delivering additional moisture that enhances rainfall potential (Johnson & Delworth, 2023). Across the broader monsoon region, tropical cyclones, mesoscale convective systems, and Gulf of California moisture

surges have been shown to increase humidity, destabilize the atmosphere, and create favorable conditions for convection (Bordoni & Stevens, 2006; Englehart & Douglas, 2001; Mejia et al., 2016).

Rainfall characteristics such as intensity, duration, and antecedent rainfall are commonly used to describe post-fire debris flow events (Alessio et al., 2021; Cannon et al., 2008; De Graff et al., 2022; Nikolopoulos et al., 2018; Thomas, Lindsay, et al., 2023). Many of these studies have focused on short-term rainfall intensity, particularly the peak 15-minute rate, as measurements over intervals of ≤ 60 minutes provide the most reliable predictor of debris flow initiation (Staley et al., 2013). While this emphasis has improved operational thresholds used to monitor conditions favorable for postfire debris flows, the large-scale atmospheric environment of storms leading to postfire debris flow remains insufficiently studied. Synoptic and mesoscale drivers such as storm structure, instability, and atmospheric river characteristics, remain comparatively underexplored and are not yet incorporated comprehensively into predictive post-fire debris flow models.

Case studies demonstrate that broader atmospheric conditions often play a critical role in generating debris flow–triggering rainfall. Sukup et al., (2016) analyzed the December 12, 2014, storm that produced multiple debris flows in the Springs Fire burn area. The event featured a negatively tilted 500 mb trough over the eastern Pacific, a jet streak on the trough's eastern flank, a synoptic configuration typical of a "Pineapple Express" atmospheric river. Radar imagery revealed a strong convective line with Narrow Cold Frontal Rainbands (NCFRs) reaching 50–60 dBZ, while instability remained weak (Convective Available Potential Energy, CAPE 200–300 J kg^{-1}; Lift Index 0 to –1). The nearest gauge recorded 15.24 mm in 10 minutes, equivalent to a 500-year return period rainfall rate for Camarillo,

demonstrating how intense, short bursts of rainfall embedded within larger storm systems can trigger debris flows.

Expanding beyond individual events, Oakley et al., (2017) examined 19 cool-season (November–March) debris flow–triggering storms in Southern California's Transverse Ranges. Atmospheric rivers were present in 68% of events, while 26% were associated with closed lows - mid-latitude cyclones with cyclonic circulation aloft (Oakley & Redmond, 2014). All atmospheric river events had Integrated Vapor Transport (IVT) values at or above the 90th percentile ($\geq$ 277 kg m^{-1} s^{-1}), and 75% also exceeded 20 mm of Integrated Water Vapor (IWV). In most cases, an upper-level jet south of the Transverse Ranges placed the region in a divergent jet exit zone favorable for upward motion. Additional features included moderate southerly low-level winds (5–10 m s^{-1}), predominantly moist-neutral stability in the 1–2 km layer, and modest median CAPE values (20–40 J kg^{-1}, ranging 0–1300 J kg^{-1} across events). Radar also revealed high reflectivity (>50 dBZ) and, in several storms, NCFRs. Collectively, these patterns demonstrate that strong moisture transport and favorable jet dynamics can produce high-intensity rainfall even in weakly unstable environments.

Other case studies further emphasize the role of intense, short-duration rainfall embedded within large storm systems. Schwartz et al., (2021) and Oakley et al., (2018) documented post-fire debris flows linked to weak-to-moderate atmospheric rivers containing high-intensity narrow rainbands, delivering 19 mm in 15 minutes (Sherpa Fire) and 13.72 mm in 5 minutes (Thomas Fire). Oakley et al., (2018) also identified a cyclonically curved upper-level jet at 250 hPa and a low-level jet aligned with a cold front, favoring NCFR development and rapid rainfall intensification.

Statistical methods have been widely applied to predict post-fire debris flows, particularly in basins with limited empirical data. Logistic regression is commonly used to estimate the probability of debris flow occurrence based on basin characteristics and rainfall (Rupert et al., 2008), with extensions enabling rainfall Intensity–Duration (ID) thresholds (Staley et al., 2017). These models underpin operational tools such as the US Geological Survey (USGS) M1 model, which combines burn severity, slope, soil erodibility, and short-term rainfall to estimate debris-flow likelihood (Staley et al., 2016). More recently, tree-based approaches, including gradient-boosted decision trees, have assessed variable importance across scales, showing that M1 metrics perform well for basin-level hazard but their predictive power relative to rainfall climatology at larger scales remains uncertain (Cavagnaro et al., 2025).

These studies highlight that post-fire debris flows are influenced not only by rainfall intensity but also by mesoscale and synoptic atmospheric features. Yet despite their recurring presence in case studies, these drivers remain underrepresented in predictive modeling, presenting an opportunity to refine our understanding and improve hazard assessment.

The objective of this study is to advance the understanding of the conditions that trigger post-fire debris flows in California by quantifying the relative influence of atmospheric and environmental factors. Building on previous case studies, we develop a statistical model integrating s atmospheric drivers including atmospheric river strength (IVT, Integrated Water Vapor; IWV), convective instability indexes (CAPE, Showalter Index and K-Index), and storm structural characteristics (area, speed, and eccentricity), with surface susceptibility factors such as peak rainfall intensity, slope, burn severity, vegetation cover, and an erosion index (Staley et al., 2017). This method is designed to capture both seasonal and contrasts in atmospheric processes, with winter PFDF events expected to be more strongly associated with

moisture transport characteristic of atmospheric rivers, and summer events more closely tied to convective systems with higher reflectivity and instability. By quantifying these relationships, this study offers a more comprehensive understanding of how specific weather processes interact with fire-altered landscapes to generate debris flows and offers insight that can strengthen hazard assessment and inform interpretation of existing predictive tools.

4.2. Data and methods

This study develops a statistical classification model to estimate the probability of post-fire debris flow occurrence during storm events in California. Figure 4.1 summarizes the workflow for data collection, predictor extraction, model development, and evaluation. The model is based on a database of PFDF and non-PFDF storm instances and uses predictors describing precipitation-system structure, atmospheric, rainfall and surface conditions. Storm events were compiled and characterized using explanatory variables derived from several data sources: surficial datasets and rain gauges, ERA5 reanalysis, and NEXRAD radar mosaics. These predictors were then used to train and test a random forest model to predict post-fire debris flow occurrence. Model performance was evaluated using standard classification metrics (precision, recall, accuracy, F1-score, AUC) and stratified K-fold cross-validation to assess robustness. The final model was then applied to a case study to generate spatially probability maps, which were compared with existing operational tools to illustrate the model's predictive behavior. We next explain in detail each data source used in the model development.

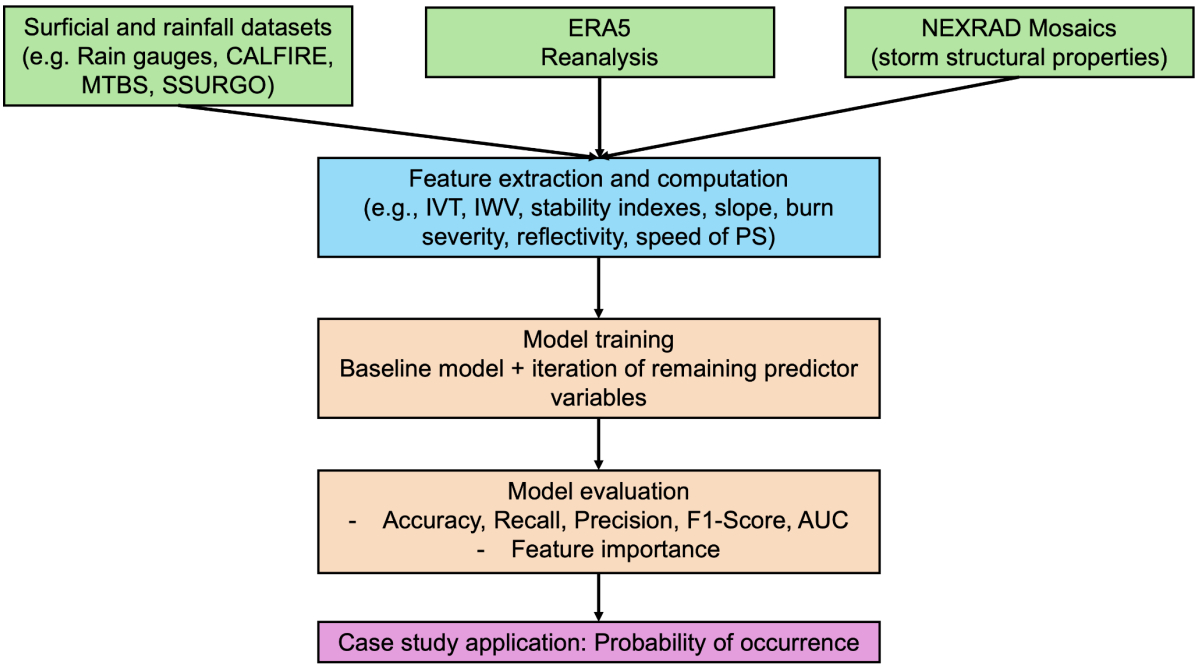


Figure 4.1. Workflow schematic showing the data pipeline from input datasets (surficial and rainfall, ERA5, and NEXRAD mosaics) through feature extraction, model training, and model evaluation. Predictors include meteorological, structural properties of precipitation systems, topographic and environmental variables. A case study is used to validate the model and demonstrate its ability to predict the probability of post-fire debris flow occurrence.

4.2.1. Event database

A database of 268 storm instances in California was assembled, including 69 PFDF events from 21 wildfires documented between 2014 and 2022 (Figure 4.2). Events were compiled from published inventories and existing literature (California Geological Survey, 2023; De Graff et al., 2022; Felling et al., 2019; Graber, 2023; Guilinger et al., 2020; Kirschbaum et al., 2010; Kostelnik et al., 2021; McGuire et al., 2018; Neptune et al., 2021; Oakley et al., 2017; Schwartz et al., 2021; Staley et al., 2018; Thomas, Kean, et al., 2023b; Thomas, Lindsay, et al., 2023). Only events explicitly noted by the source as field-verified were included. Of these, 50 PFDF events occurred during fall and winter storms, while 19 were linked to spring and summer storms.

The study period was chosen to align with the availability of high-temporal resolution rainfall data from publicly operated gauges as we relied on publicly available rain gauges rather than monitored or instrumented watershed data to characterize rainfall conditions. To provide comparison cases, 199 non-PFDF storm instances (150 in fall/winter and 49 in spring/summer) were extracted from the same rain gauges and fire perimeters associated with a subset of PFDF events. These storms were identified from the rainfall time series recorded during the first two years after fire ignition, when recently burned watersheds are most susceptible to debris-flow occurrence (De Graff, 2018; Graber et al., 2023). Storms were selected from the 75th percentile of each gauge's post-fire rainfall distribution to focus on relatively high-magnitude rainfall events. Selected storm datetimes were then cross-checked against existing debris flow inventories, to confirm their classification as non-PFDF cases.

Each debris flow event was paired with the nearest rain gauge within an 8 km radius. This threshold was selected to account for the lower density of rain gauges in central California and to align with previous studies using similar spatial criteria to characterize storm conditions associated with debris flows (Thomas, Kean, et al., 2023a). Sub-hourly rainfall data from the nearest gauge were used to describe rainfall conditions as rainfall intensity within ≤ 60 min has been shown to be an effective predictor of post-fire debris-flow initiation (Staley et al., 2013). Although the existing data in the inventories includes the event date, the precise timing of when debris flows occurred is not always available, which limits the ability to directly identify triggering rainfall intensities. Because of this, the peak 15-minute rainfall intensity recorded during each storm was used as a proxy for triggering intensity (Selander et al., 2025; Thomas, Kean, et al., 2023a) and included as a predictor in the model to capture short-

duration, high-intensity rainfall. Storm duration was defined following Staley et al., (2013) as a period of rainfall with no breaks longer than 8 hours.

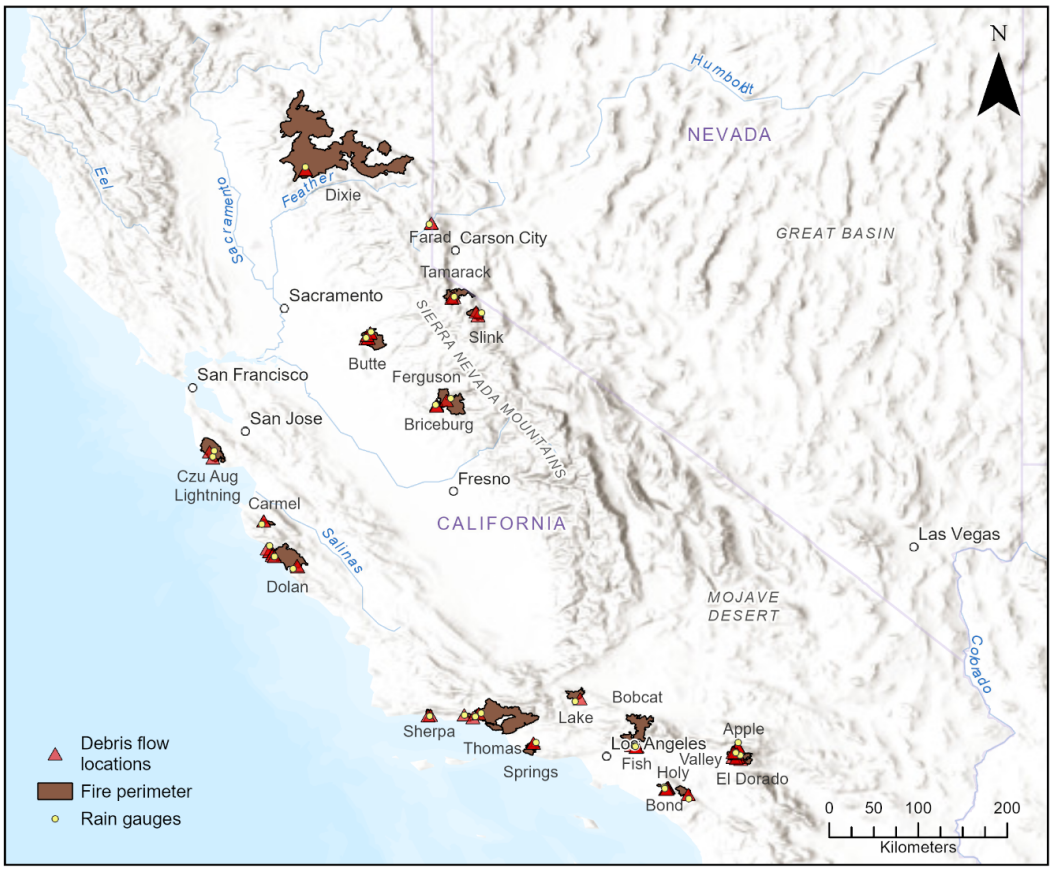


Figure 4.2. Map of post-fire debris flow locations (2014–2022) and associated wildfire perimeters (2013–2021) across California. These locations were also used to extract conditions from non-debris flow storms for model development. Fire names are labeled adjacent to their perimeters. Major cities, terrain, and rain gauges are shown for spatial context.

4.2.2. Predictor variables

Predictor variables were derived from publicly available geospatial datasets describing surface and morphological conditions, ERA5 atmospheric reanalysis, and NEXRAD radar mosaics. These datasets were used to characterize the rainfall, atmospheric environment, precipitation-system structure, and landscape properties associated with each storm instance.

Table 4.1 summarizes the predictor variables used in the model, including their source datasets and spatial and temporal resolution.

4.2.2.1.Surface variables

This category includes slope and vegetation type from LANDFIRE (2023), soil erodibility (K-factor) from the USA-SSURGO Erodibility Factor geospatial layer (USDA NRCS, 2024), and burn severity from Monitoring Trends in Burn Severity (MTBS Project, 2017). The geospatial datasets were used at 30 m spatial resolution.

Slope influences the gravitational movement of sediment on hillslopes and within channels, directly affecting erosion, sediment availability, and runoff processes that contribute to post-fire debris flows (Cannon, 2001; Lamb et al., 2013). Burn severity represents changes induced by wildfires in terms of vegetation and soil that can reduce soil cohesion, increase water repellency, and enhance surface runoff. These changes, including the loss or alteration of vegetation cover, also affect hillslope stability by weakening root strength, reducing infiltration capacity, and lowering resistance to surface erosion, factors that collectively increase the occurrence of post-fire debris flows (Shakesby & Doerr, 2006). Vegetation type was included as a descriptor of land cover because vegetation types may influence fire effects, stabilization provided by root systems, and post-fire hydrologic response and recovery (Santi et al., 2013; Thomas et al., 2021). Moreover, post-wildfire hazard has been shown to vary across vegetation types and fire regimes, indicating that land cover characteristics may provide useful context for explaining variation in post-fire debris flow susceptibility (Graber et al., 2023).

The susceptibility of soils to erosion is represented by the K-factor, or soil erodibility index, which reflects the average long-term response of soils to the erosive power of rainfall. It characterizes processes such as detachment, transport by raindrop impact and surface flow, as well as infiltration capacity (Römkens et al., 1997). K-factor values vary by soil texture: fine-textured soils rich in clay typically have low values (0.05–0.15) due to their resistance to detachment, while coarse-textured sandy soils also exhibit relatively low values (0.05–0.20) because they generate limited runoff despite being more easily detached. Medium-textured soils, such as silt loams, have moderate values (0.25–0.45), reflecting moderate susceptibility to detachment and runoff. Soils with high silt content are the most erodible, often exceeding 0.45 and reaching up to 0.65, as they detach easily, crust readily, and produce large amounts of runoff (USDA, 2001).

Surface and morphological predictors were extracted at geographic coordinates corresponding to documented post-fire debris flow reference locations. For non-debris flow storms, the same points were used, enabling a comparison of storm outcomes (i.e., PFDF vs. non-PFDF) while holding surface conditions constant. Differences in predictor distributions may arise because some burned areas contributed more non-PFDF storms than others.

4.2.2.2.Atmospheric and storm rainfall variables

Atmospheric variables were included to represent large-scale moisture transport, atmospheric instability, orographic forcing, and synoptic conditions associated with intense precipitation. This category includes IVT, IWV, 925-hPa wind speed, 925-hPa wind orientation relative to terrain aspect, CAPE, the Showalter Stability Index, the K-Index, warm cloud layer depth, and vorticity advection. These predictors were derived from ERA5 hourly reanalysis (0.25° × 0.25°; ~31 km resolution; Hersbach et al., 2023) using both single-level

and pressure-level fields. ERA5 was selected because it provides complete temporal coverage for all events in the inventory and includes precomputed variables such as vertical integrals and the K-Index. In addition, rainfall is represented by peak 15-minute rainfall intensity derived from nearby rain gauges.

Integrated Vapor Transport (IVT) and Integrated Water Vapor (IWV) account for the occurrence of atmospheric rivers. IVT, the vertically integrated product of specific humidity and wind speed, represents the strength and direction of moisture transport in the atmosphere. In ERA5, IVT was derived from the vertical integrals of eastward and northward water-vapor flux (Equation 4.1), which were combined to calculate IVT magnitude as:

$$IVT = \sqrt{{IVT_u}^2 + {IVT_v}^2} \qquad 4.1$$

where IVT_u is the vertical integral of eastward water-vapor flux and IVT_v is the vertical integral of northward water-vapor flux. IWV, on the other hand, measures the total amount of water vapor in a vertical atmospheric column and was represented using the total column water vapor variable from ERA5. Typical thresholds used to identify atmospheric river conditions include IVT values exceeding 250 kg m^{-1} s^{-1} and IWV values greater than 20 mm (Neiman et al., 2008; Ralph et al., 2004; Rutz et al., 2014), which together capture both the moisture content and the transport dynamics associated with these precipitation events.

The orientation of the 925 hPa wind flow with respect to local terrain aspect was computed to represent orographic precipitation. This phenomenon tends to occur when moist air masses are forced to ascend over topographic barriers, particularly when a low-level wind speed maximum containing moisture is oriented orthogonally to the terrain (Lin et al., 2001). The 925 hPa wind speed was also considered alongside orthogonality to capture low-level

atmospheric dynamics that influence moisture transport, storm organization, and potential for localized convective enhancement.

Several atmospheric instability indices assess the potential for convective storm development. Convective Available Potential Energy (CAPE) quantifies buoyancy and represents the energy available to support convective updrafts. Conceptually, CAPE is defined as the vertical integral of parcel buoyancy between the level of free convection and the equilibrium level:

$$CAPE = g \int_{Z_{LFC}}^{Z_{EL}} \frac{T_{vp} - T_{ve}}{T_{ve}} dz \qquad 4.2$$

where g is gravitational acceleration, T_{vp} is the virtual temperature of the lifted air parcel, T_{ve} is the virtual temperature of the environment, *LFC* is the level of free convection, and *EL* is the equilibrium level. CAPE is a key indicator of convective storm intensity, with higher values reflecting a greater likelihood of strong vertical motions and deep convection (Doswell, 2001).

The Showalter Stability Index provides a complementary measure of instability, calculated by lifting a parcel upward until it cools to saturation, then carried to 500 hPa along a moist adiabat, and the difference between its temperature and the observed 500-hPa temperature gives the index value as in Equation 4.3.

$$SI = T_{500} - T_{p\,500} \qquad 4.3$$

where *SI* is the Showalter Index, T_{500} is the environmental temperature at 500 hPa, and $T_{p\,500}$ is the temperature of an air parcel lifted from 850 hPa to 500 hPa. Positive values indicate stability, while negative values indicate instability, with more negative values linked to stronger convective potential. Empirical thresholds suggest that values near +3 or lower are

often associated with showers, values between +1 and –2 correspond to a higher probability of thunderstorms, and values below –3 can signal severe thunderstorms, with –6 or lower occasionally linked to tornado conditions (Showalter, 1953).

Similarly, the K-Index is a parameter used for assessing thunderstorm potential, especially those capable of producing heavy rainfall and flash flooding (DeRubertis, 2006). It is calculated using temperature at 850, 700, and 500 hPa, along with dew point temperature at 850 and 700 hPa, thereby incorporating both thermal and moisture conditions in the lower troposphere (George, 1960).

$$K = (T_{850} - T_{500}) + T_{d,850} - \left(T_{700} - T_{d,700}\right) \quad 4.4$$

where $T_{850}, T_{700}, T_{500}$ are air temperatures at 850, 700, and 500 hPa, respectively, and $T_{d,850}$ and $T_{d,700}$ are dew point temperatures at 850 and 700 hPa. Higher K-Index values generally correspond to a greater likelihood of thunderstorm development: values below 20 typically indicate no thunderstorms, 20–25 isolated storms, 26–30 widely scattered storms, 31–35 scattered storms, and values above 35 are associated with numerous thunderstorms in moist, unstable environments.

In addition, the depth of the warm cloud layer was considered, since deeper layers (exceeding 3–4 km, or about 10,000 feet) promote greater atmospheric moisture content and enhance the collision–coalescence process. This “warm rain” mechanism facilitates the growth of larger raindrops that fall more rapidly and efficiently reach the surface, thereby increasing rainfall rates (Prein et al., 2017). Furthermore, advection of vorticity was computed to capture synoptic-scale dynamics that can influence storm development as in Equation 4.5.

$$VA = -\left(u\frac{\partial}{\partial x} + v\frac{\partial}{\partial y}\right) \quad 4.5$$

where VA is horizontal vorticity advection, u and v are the zonal and meridional wind components. Cyclonic vorticity advection promotes upward motion, low-level convergence, and enhanced lifting of air. Strong cyclonic vorticity advection, often found upstream of mid-tropospheric troughs or near frontal boundaries (Konrad, 1997; Maddox & Doswell, 1982), has been linked to severe-weather outbreaks (Miller, 1972) and may favor intense rainfall over burned areas, thereby increasing the likelihood of post-fire debris flow occurrence.

Atmospheric variables were evaluated up to six hours prior to both the storm starting time and the hour closest to the peak 15-minute rainfall intensity. Values were extracted at the debris flow reference locations and across all ERA5 grid cells within fire perimeters; the latter were aggregated using the median to capture broader fire-scale atmospheric conditions. This approach enabled the characterization of the temporal and spatial patterns associated with most post-fire debris flow–producing storms. Vorticity advection was treated differently due to its synoptic-scale relevance: values were computed relative to the storm start time over a 12-hour window and evaluated on a 0.5° × 0.5° grid centered on the fire perimeter centroid, based on multiple tests that balanced spatial resolution and synoptic-scale pattern detection.

4.2.2.3. Structural properties of precipitation systems

Structural properties of precipitation systems including area, propagation speed, and eccentricity, along with radar reflectivity values were also included as explanatory variables in the model. High reflectivity values indicate intense rainfall, while structural characteristics help distinguish between storm types and mesoscale features. For instance, slow-moving systems often correspond to localized convective events typical of California summers, whereas larger, elongated systems can represent features such as atmospheric rivers or

NCFRs, which are closely linked to post-fire debris flow occurrence. For each event, area, speed, eccentricity of precipitation systems, and reflectivity at the debris flow location as well maximum reflectivity within the burned area (at the time of peak 15-minute rainfall intensity) were computed using a tracking algorithm based on spatial correlation, as explained in Chapter 3. These variables were derived from NEXRAD base reflectivity mosaics from the Iowa State Environmental Mesonet Archive (https://mesonet.agron.iastate.edu), with 5-minute temporal and 0.5 km spatial resolution. Together, these radar-derived metrics complement rainfall intensity measurements and capture structural properties of precipitation systems, which, when combined with the broader-scale atmospheric variables from ERA5, provide a more complete characterization of conditions conducive to post-fire debris flows.

Table 4.1. Predictor variables used in the statistical model. Variables marked with an asterisk (*) were included in the baseline model.

Category	Variable	Dataset	Dataset resolution
Atmospheric and storm rainfall	Peak 15-min intensity *	Publicly operated rain gauges	Sub-hourly
Atmospheric and storm rainfall	Integrated Vapor Transport (IVT)	ERA5 Single-level variables (Hersbach et al., 2023)	0.25° × 0.25° (31 km), hourly
Atmospheric and storm rainfall	Integrated Water Vapor (IWV)	ERA5 Single-level variables (Hersbach et al., 2023)	0.25° × 0.25° (31 km), hourly
Atmospheric and storm rainfall	925 hPa wind speed	ERA5 Pressure-level variables (Hersbach et al., 2023)	0.25° × 0.25° (31 km), hourly
Atmospheric and storm rainfall	925 hPa wind orthogonality	ERA5 Pressure-level variables (Hersbach et al., 2023)	0.25° × 0.25° (31 km), hourly

Atmospheric and storm rainfall	CAPE	ERA5 Single-level variables (Hersbach et al., 2023)	0.25° × 0.25° (31 km), hourly
Atmospheric and storm rainfall	Showalter Stability Index	Computed from ERA5 pressure-level variables	0.25° × 0.25° (31 km), hourly
Atmospheric and storm rainfall	K-Index	ERA5 Single-level variables (Hersbach et al., 2023)	0.25° × 0.25° (31 km), hourly
Atmospheric and storm rainfall	Warm cloud layer depth	Computed from ERA5 pressure-level variables	0.25° × 0.25° (31 km), hourly
Atmospheric and storm rainfall	Vorticity advection	Computed from ERA5 pressure-level variables	0.5° × 0.5°, hourly
Storm Structure	Storm area	Iowa State Environmental Mesonet Archive	0.5 km, 5-min
Storm Structure	Storm propagation speed	Iowa State Environmental Mesonet Archive	0.5 km, 5-min
Storm Structure	Storm eccentricity	Iowa State Environmental Mesonet Archive	0.5 km, 5-min
Storm Structure	Reflectivity at debris flow location	Iowa State Environmental Mesonet Archive	0.5 km, 5-min
Storm Structure	Maximum reflectivity within burn area	Iowa State Environmental Mesonet Archive	0.5 km, 5-min
Surface	Slope *	LANDFIRE (LANDFIRE, 2023)	30 m
Surface	Burn severity *	Monitoring Trends in Burn Severity (MTBS Project, 2017)	30 m
Surface	Soil erodibility (K-factor) *	USA-SSURGO Erodibility Factor (USDA NRCS, 2024)	30 m
Surface	Vegetation type *	LANDFIRE (LANDFIRE, 2023)	30 m

4.3. Model development

Random forests are an ensemble learning method that combines predictions from many decision trees rather than relying on a single tree. Each tree is grown from a bootstrap sample of the training data, and at each split only a random subset of predictors is considered. The final prediction or classification is obtained by aggregating the votes (or averages) across all trees. This additional randomness de-correlates the trees, and the aggregation step reduces the variance associated with individual tree models, often improving predictive performance and generalization relative to a single decision tree (Breiman, 2001).

Random forests are particularly appropriate for the present application because they are nonparametric and do not require distributional assumptions about either the predictor or response variables (Strobl et al., 2007). This flexibility is advantageous for a predictor set that integrates heterogeneous atmospheric, rainfall, storm-structure, and surface variables. It is also important because methods such as logistic regression classify observations using linear combinations of predictor variables (Cutler et al., 2007), which may be less suitable for representing the interactions and nonlinear responses expected in post fire debris flow hazard. The random forest framework can also incorporate both continuous and categorical predictors within the same framework and typically performs well with relatively modest tuning requirements (Hastie et al., 2009). In addition, random forests provide measures of variable importance that help identify the predictors most strongly associated with post-fire debris flow occurrence (Catani et al., 2013).

4.3.1. Model training

To predict post-fire debris flow occurrence, an 80/20 train-test split was applied, and a random forest model was trained. Prior to modeling, variables were screened for

multicollinearity using a correlation matrix with the aim to identify highly correlated predictors that could affect model robustness and interpretability.

A baseline model was first constructed using only surficial and morphological variables, including peak 15-minute rainfall intensity, slope, burn severity, soil erodibility (K-factor), and vegetation type. Vegetation categories from LANDFIRE were encoded as separate binary variables representing sparse tree canopy, open tree canopy, shrubland, herbaceous–grassland, and areas with no dominant lifeform. This baseline model captured predictors commonly used in operational tools and previous studies, providing a foundation for assessing additional features. We then tested different combinations of the baseline model along with atmospheric and storm-scale variables to determine which predictors improved skill versus those that could be omitted without reducing model performance.

4.3.2. Model evaluation

4.3.2.1. Performance metrics

Model performance was assessed using standard classification metrics: precision, recall, accuracy, F1-score and the area under the receiver operating characteristic curve (AUC). These metrics are derived from a confusion matrix comprising four key components: true positives (TP), which represent events correctly predicted as post-fire debris flows; true negatives (TN), which are non-debris flow events correctly identified as such; false positives (FP), where non-debris flow events are incorrectly classified as debris flows; and false negatives (FN), where debris flows are incorrectly predicted as non-events.

Precision, by comparing false positives to true positives rather than true negatives, captures the effect of the large number of negative examples and measures that fraction of examples classified as positive that are truly positive. Recall, also known as sensitivity, measures the proportion of actual debris flow events that were correctly identified; high recall indicates few false negatives (Davis & Goadrich, 2006). Accuracy is defined as the fraction or count of correct predictions, corresponding to the sum of true positives and true negatives divided by the total number of samples. However, when classes are imbalanced, accuracy can be misleading because correct classification of the majority class can dominate the metric, even if the model performs poorly on the minority class. For this reason, F1-score was also used to evaluate model performance. F1-score is the harmonic mean of precision and recall and provides a more balanced measure of classification performance when both false positives and false negatives are important to consider, especially in imbalanced datasets such as ours (Forman & Scholz, 2010). In addition, the AUC provides a single scalar measure of model performance that summarizes the tradeoff between true positive rate and false positive rate across all possible classification thresholds. The AUC can be interpreted as the probability that the classifier will rank a randomly chosen debris flow event higher than a randomly chosen non-event, making it a widely used and threshold-independent measure of predictive skill (Fawcett, 2006).

4.3.2.2.Cross-validation

To assess model stability, Stratified K-Fold cross-validation with 10 folds was implemented. In this resampling approach, the dataset is divided into 10 approximately equal-sized subsets, or folds, while preserving the original class distribution (debris flow vs. non-debris flow) within each fold. During each iteration, one-fold is used as the validation set and

the remaining nine folds are used for training. This process cycles through all folds until every instance has served once as validation data, while ensuring balanced representation of both classes across training and validation sets (Refaeilzadeh et al., 2009). For each fold, we computed precision, recall, F1-score, and AUC, and then calculated the mean and standard deviation across folds. This process enabled a robust evaluation of applicability and quantified variability in model performance across different data subsets.

4.3.2.3. Case study application

After developing the final model and selecting predictors that optimized performance and robustness, we applied it to a case study of a storm that triggered a debris flow and was not used in model training or testing, in order to explore the model's predictive behavior in a real-world context. The model generated spatially explicit probabilities of occurrence, which were compared with outputs from the USGS M1 model to highlight areas of agreement and discrepancy. This analysis provided insight into how including atmospheric and storm-scale variables influences hazard estimates relative to traditional surficial and rainfall-based approaches, illustrated the model's behavior under real-world conditions, and identified patterns in predicted probabilities that could guide future refinements or interpretation for operational tools.

4.4. Results

4.4.1. Atmospheric and storm rainfall variables

We begin this section by discussing the statistical distributions of the data used to model PFDF. Predictor variables were assessed at both debris flow locations and across burned area pixels multiple lead times before storm onset or peak 15-minute rainfall intensity. Across all

cases, values of atmospheric variables nearest the peak 15-minute rainfall most clearly captured the conditions associated with post-fire debris flow occurrence. These representative conditions are emphasized in the results.

Integrated Vapor Transport ≥ 250 kg m^{-1} s^{-1} and Integrated Water Vapor ≥ 20 mm are commonly used thresholds to identify atmospheric river (AR) conditions, which have been linked to landslides and post-fire debris flows in California (Young et al., 2017). Although both variables describe atmospheric moisture, they represent different aspects of the storm environment: IWV measures the total amount of water vapor contained in a vertical atmospheric column, whereas IVT measures the horizontal transport of that moisture by the wind. In other words, IWV describes how much moisture is available, while IVT describes how strongly that moisture is being transported into a region. Across all documented PFDF events during winter, 54% met both AR classification thresholds (30% in non-PFDF storms). IVT values during PFDF storms ranged from 0 to 910 kg m^{-1} s^{-1} (Figure 4.3a), with the maximum observed within the hour of debris flow occurrence during a winter storm on January 12, 2019, in the Holy Fire area, Orange County, Southern California. High IVT values have also been documented in historical PFDF-producing storms, such as 750 kg m^{-1} s^{-1} during the Springs Fire in December 2014 (Sukup et al., 2016). Mean and median at the nearest hour were 307 and 350 kg m^{-1} s^{-1}, respectively, while non-PFDF storms showed slightly lower values (mean 285; median 264 kg m^{-1} s^{-1}). In both groups, more than half of the cases exceeded the 250 kg m^{-1} s^{-1} threshold at the nearest and three-hour time steps. At six hours prior, IVT medians diverged slightly, with 221 kg m^{-1} s^{-1} in PFDF storms versus 243 kg m^{-1} s^{-1} in non-PFDF storms. Trends are consistent with Oakley et al., (2017) that reported median IVT slightly above 300 kg m^{-1} s^{-1} nearest to event time and three hours prior,

falling below this value at six hours. Seasonality seems to play an important role: most high-IVT cases occurred in fall and winter, while spring/summer storms rarely exceeded the AR threshold (9% of non-PFDF vs. 3% of PFDF storms), underscoring that strong IVT is predominantly a cool-season characteristic.

IWV ≥ 20 mm did not exhibit strong seasonality. In PFDF storms, over 60% of events in each season exceeded this threshold, reaching 79% in spring/summer, compared to 67% in non-PFDF storms (Figure 4.3b). In fact, the highest IWV linked to a debris flow was 38 mm during the July 31, 2022 storm in the El Dorado Fire area, when remnants of Tropical Storm Kay triggered multiple debris flows that damaged or destroyed at least 16 homes and caused one fatality. At debris flow reference locations, median IWV was 22 mm (vs. 20 mm when averaged across burned areas), with a maximum of 66% of cases exceeding 20 mm at the nearest hour. These results are similar to those found in Oakley et al. (2017), who found ~75% of burned area grid points exceeded 20 mm, with higher medians (~26 mm) from the nearest hour through 6 h prior. Non-PFDF storms remained near the threshold (median = 19 mm), approaching 19.8 mm at the nearest hour, with exceedance rates falling from 48% at the nearest hour to 40% at 6 h prior.

Nearest-hour IWV (66%) and IVT (62%) at debris flow locations captured the highest proportion of PFDF events exceeding atmospheric river thresholds and were therefore selected as model predictors. IWV provided stronger separation between PFDF and non-PFDF storms: medians were consistently above the 20 mm threshold in PFDF cases but remained below it in non-PFDF storms. IVT, by contrast, exceeded the AR threshold in the median for both storm types, limiting its discriminatory value. However, its seasonality was informative,

as strong IVT occurred almost exclusively in the cool season, coinciding with the majority of PFDF events.

Positive values of advection vorticity indicate enhanced upward motion, promoting conditions that favor intense rainfall. For each storm, median vorticity values were calculated at 12 h, 6 h, 3 h, and the hour nearest to storm onset to capture the evolving synoptic environment leading up to rainfall events. Positive advection vorticity occurred in about half of all PFDF cases, with the highest median (1.62 s^{-2}, vs. 0.31 s^{-2} in non-PFDF storms) and largest proportion of positive cases (64%) observed three hours prior to onset (Figure 4.3c). Positive values were slightly less frequent at 6 h (56%), the nearest hour (55%), and 12 h (43%). Non-PFDF storms showed 50–52% positive values across all times. The maximum value across the dataset (38.66 s^{-2}) occurred at the nearest hour during a winter storm on February 13, 2019, in the Holy Fire burn scar near Lake Elsinore, CA. Positive vorticity was more common in fall/winter PFDF events than in spring/summer (68% vs. 53% at 3 h prior), while non-PFDF storms showed an even larger seasonal contrast (57% vs. 35%). Based on these patterns, median advection vorticity three hours prior to storm onset was selected as a predictor variable for PFDF modeling. Overall, PFDF storms were more often linked to positive advection vorticity, peaking three hours before storm onset, with fall/winter cases showing the strongest signal.

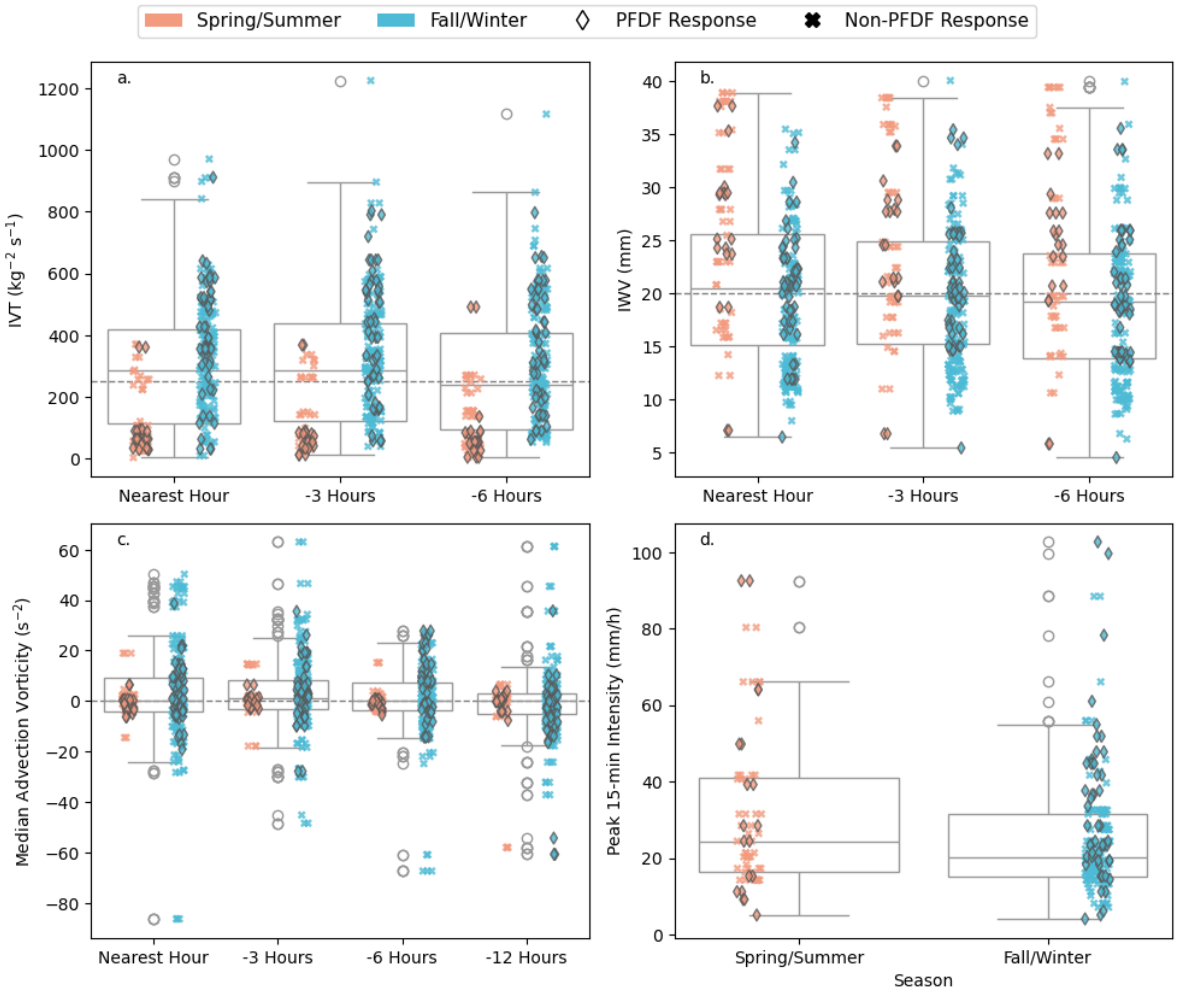


Figure 4.3. Atmospheric and rainfall predictors considered for modeling post-fire debris flow occurrence in California. **a.** Integrated Vapor Transport (IVT) and **b.** Integrated Water Vapor (IWV) are shown at the nearest hour, and 3 and 6 hours prior to the peak 15-minute rainfall intensity. **c.** Median advection vorticity values are calculated over pixels surrounding the burned area at the nearest, 3, 6, and 12 hours prior to storm onset. **d.** Peak 15-minute rainfall intensity, grouped by season. Box plots show distributions for all events (PFDF and non-PFDF), including the median (center line), interquartile range (box edges: 25th–75th percentiles), whiskers extending to 1.5x the interquartile range, and individual points representing outliers beyond this range. Dashed lines in a. and b. denote atmospheric river thresholds from Ralph et al., (2004) and Rutz et al., (2014); in c., positive advection vorticity values indicate favorable conditions for heavy rainfall.

The peak 15-minute rainfall intensity of storms resulting in post-fire debris flows, measured by rain gauges near event locations, ranged from 4.06 to 102.62 mm h^{-1}, with a median of 28.45 mm h^{-1} and a mean of 33.62 mm h^{-1}. In contrast, non-PFDF storms ranged

between 7.11 and 88.39 mm h^{-1}, with a median of 19.3 mm $h^{-1}$and a mean of 24.5 mm h^{-1} (Figure 4.3d). The most intense rainfall associated with a debris flow occurred during a winter storm over the Thomas Fire burn area on December 9, 2018, which triggered debris flows in Montecito and Carpinteria, resulting in 23 fatalities and extensive property losses (Lukashov et al., 2019). 70% of PFDF cases occurred at 15-min intensities >20 mm h^{-1} (vs. 50% of non-PFDF storms), and 43% exceeded 30 mm h^{-1} (vs. 24% of non-PFDF storms). When stratified by season, median intensities were slightly lower in fall/winter (26.42 mm h^{-1}) compared to spring/summer (28.45 mm h^{-1}), with means of 35.41 and 32.94 mm h^{-1}, respectively. A similar seasonal pattern appeared in non-PFDF storms with lower values, where fall/winter medians and means were 19.3 and 22.6 mm h^{-1}, respectively, and warmer-season values corresponded to 21.3 and 30.5 mm h^{-1}.

Interquartile range also differed by season: PFDF storms showed a greater spread in spring/summer (13.21– 49.78 mm h^{-1}) than in fall/winter (19.30 – 44.70 mm h^{-1}). Non-PFDF storms exhibited a narrower range in fall/winter cases (14.22–27.43 mm h^{-1}), with many clustering at lower intensities. These results suggest that storms associated with post-fire debris flows tend to produce more intense short-duration rainfall than non-PFDF storms, with more frequent exceedance of values > 30 mm h^{-1}. Also, PFDF storms show greater spread in peak 15-minute intensity rainfall, especially during the warm season.

Orthogonality between low-level winds and terrain aspect in PFDF areas was generally higher several hours before peak rainfall intensity and decreased as the event approached. Six hours prior, 22% of PFDF events (vs. 12% of non-PFDF events) had near-perpendicular winds (orthogonality 0–0.25), but this dropped to 4% at 3 hours and 7% at the nearest hour. Using a broader threshold (0–0.5), 41% of PFDF events (36% of non-PFDF) met this criterion six

hours prior, compared to 25% at 3 hours and 13% at the nearest hour. Many cases reflected southeast winds approaching southwest-facing slopes, consistent with the dominant terrain orientation of PFDF sites (86% between 180–270°). Seasonally, near-perpendicular alignment (0–0.25) occurred in 24% of PFDFs during fall/winter (42% at 0–0.5) and 21% in spring/summer (36% at 0–0.5).

In PFDF cases, 925 hPa wind speeds were generally stronger near the peak 15-min rainfall hour. At this time, speeds ranged from 1–23 m s^{-1} (median 6.3 m s^{-1}), compared to 0.7–22 m s^{-1} (median 4.3 m s^{-1}) in non-PFDF storms, with 25% of PFDF events exceeding 14 m s^{-1} (vs. 11% in non-PFDF). Seasonal differences were pronounced (Figure 4.4): spring/summer PFDFs occurred under weak winds (means and medians ~2–3 m s^{-1}), while fall/winter PFDFs were associated with much stronger flow (mean and median ~11 m s^{-1}, vs. ~7 m s^{-1} in non-PFDF), with only 25% of cases below 5 m s^{-1}. Overall, PFDFs were most likely on south–southwest-facing slopes under moderately strong southerly low-level winds. While PFDF orthogonality values overlap with those in non-PFDF storms, more debris flows often occur under stronger winds, particularly in fall/winter, underscoring the role of wind–terrain interactions (e.g., orographic precipitation) in enhancing seasonal susceptibility. Because orthogonality peaking about six hours before the event and wind speeds at the nearest hour to peak rainfall were most discriminative of PFDF response, we selected those times as predictors in the statistical model.

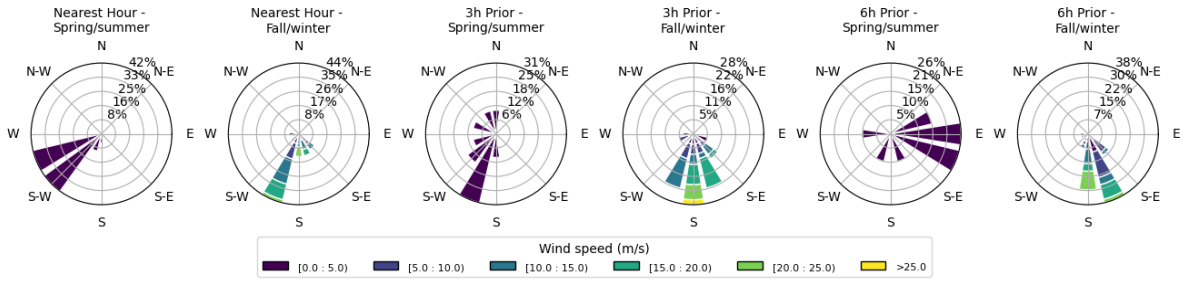


Figure 4.4. Wind rose diagrams of 925-hPa wind direction and speed for post-fire debris flow events, shown separately for spring/summer and fall/winter seasons at the nearest hour, 3 hours prior, and 6 hours prior to event initiation. Radial axes indicate the frequency of wind directions (percent), and colors indicate wind speed bins (m s^{-1}).

Regarding the statistical distributions of stability indices (Figure 4.5), higher CAPE values reflect greater atmospheric instability and the potential for severe weather. In PFDF storms, CAPE values were generally low, ranging from 0 to 985 J kg^{-1}, with the highest recorded during a summer storm over the Slink Fire in July 2021 at the nearest hour before peak 15-minute rainfall intensity. Values above 400 J kg^{-1} were uncommon but occurred more often in PFDF cases (10%) than in non-PFDF cases (5%) (Figure 4.5a). Very high CAPE (> 600 J kg^{-1}) was rare and limited to spring/summer storms, observed in 38% of cases at the nearest hour and 16% three hours prior. CAPE also showed a consistent rising trend from six hours before the peak rainfall intensity, indicating that instability often built in the hours leading up to debris-flow triggering rainfall. For modeling, we selected CAPE at the nearest hour at the event location, where PFDF storms had a mean of 134 J kg^{-1} (median of 48 J kg^{-1}) compared to 100 J kg^{-1} in non-PFDF storms (median of 47 J kg^{-1}). These values are broadly consistent with Oakley et al. (2017), who reported median CAPE of 20–40 J kg^{-1} (ranges up to ~1300 J kg^{-1}) for winter PFDFs in the Transverse Ranges. In general, although CAPE values were modest across events, PFDF storms more frequently exhibited elevated instability compared to non-PFDF storms, particularly in spring and summer months.

The K-Index is a measure of lower- to mid-tropospheric moisture and instability, commonly used to assess thunderstorm potential. Higher values indicate more favorable conditions for convective development. In PFDF events, the highest K-Index was 32.97, recorded three hours before peak 15-minute rainfall intensity during the January 9, 2018 storm over the Thomas Fire. This value falls within the range associated with scattered

thunderstorms and coincided with the event that produced the highest observed peak 15-minute rainfall intensity (102 mm h^{-1} at a nearby gauge). Median K-Index values were generally highest at the nearest event hour (whether measure relative to storm onset or peak 15-minute rainfall intensity) and declined thereafter. For modeling, we used median values within fire perimeters at the nearest hour, where 93% of PFDF cases exceeded the convective threshold (>20). These values ranged from 13.95 to 31.98, with a mean and median of 24.4 (Figure 4.5b), closely comparable to non-PFDF storms (23–24). Based on standard classification, 45% of PFDF cases fell in the isolated thunderstorm category (vs. 27% for non-PFDF), 34% in widely scattered (32% non-PFDF), and 13% in scattered (14% non-PFDF). No PFDF events reached the "numerous" thunderstorm category.

At the nearest hour to peak 15-minute rainfall intensity, exceedance rates were high in both seasons (~90% in spring/summer and 86–90% in fall/winter), while at earlier lead times warm-season storms maintained higher exceedance rates (79–84%) than fall/winter storms (48–78%). Overall, PFDF events generally occur under moderate atmospheric instability, with K-Index values exceeding convective thresholds near peak rainfall intensity. Exceedances are especially common in spring and summer, indicating that even modest convective potential can trigger intense rainfall capable of initiating debris flows.

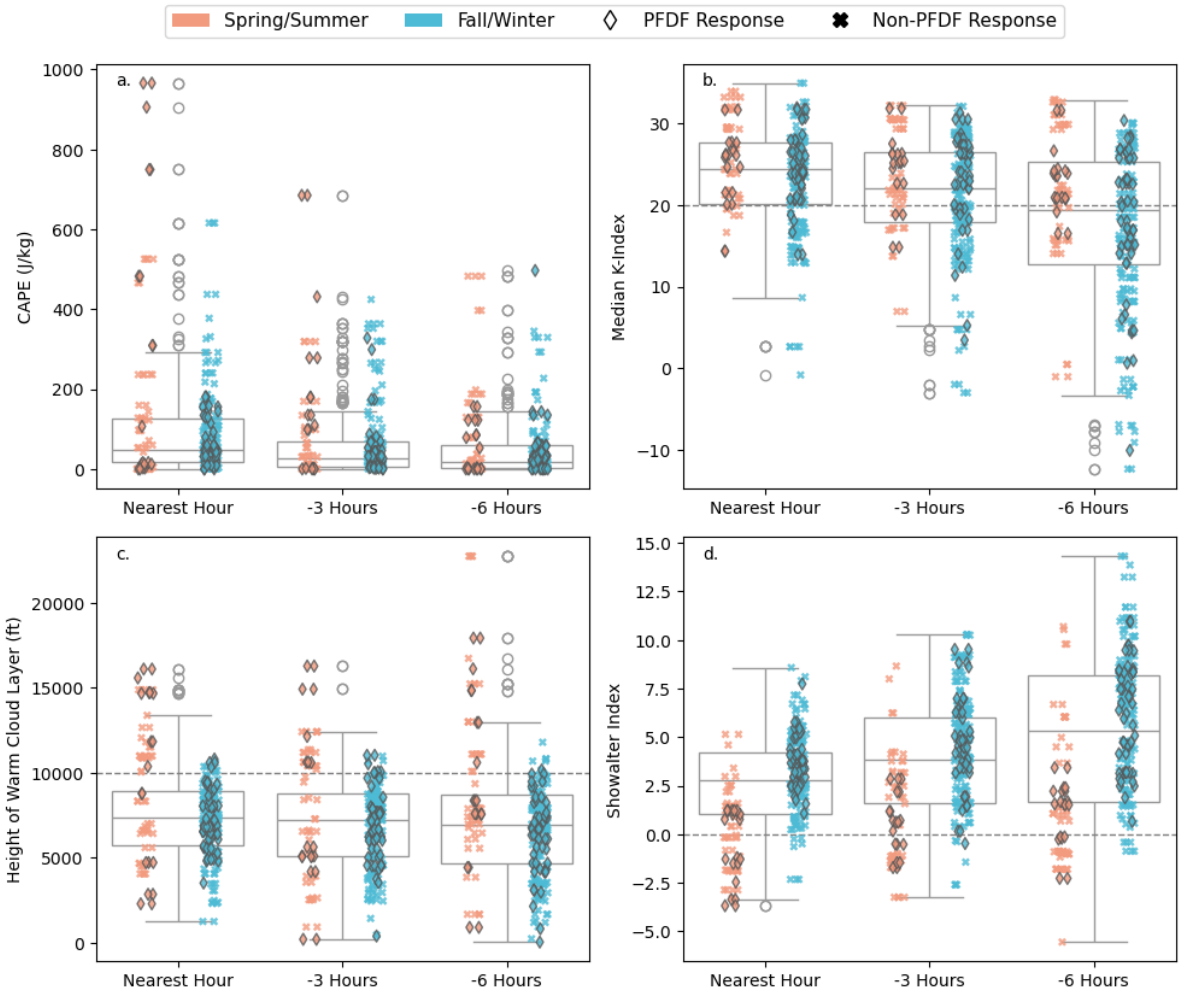


Figure 4.5. Stability index predictors considered for modeling post-fire debris flow (PFDF) occurrence in California, shown by season and lead time (nearest, 3, and 6 hours prior to peak 15-minute rainfall intensity). **a.** Convective Available Potential Energy (CAPE), **b.** median K-index within the burned area, **c.** height of the warm cloud layer, and **d.** Showalter Index. Panels a., c., and d. reflect values at specific point coordinates; panel b. shows median value across the burned area. Box plots show distributions for all events (PFDF and non-PFDF), including the median (center line), interquartile range (box edges: 25th–75th percentiles), whiskers extending to 1.5x the interquartile range, and individual points representing outliers beyond this range. Dashed lines in b. indicate K-index values >20 suggestive of thunderstorm potential; in c., warm cloud heights >10,000 ft (~3–4 km) enhance rainfall efficiency; in d., Showalter Index negative values indicate increased instability.

Warm cloud layer depth is an important parameter for convective precipitation, as greater depths enhance the potential for warm-rain processes and efficient precipitation production. In PFDF events, however, warm cloud depths exceeding 10,000 ft (~3 km) were relatively

uncommon (Figure 4.5c). Six warm-season storms produced the highest values, while only two winter events approached the threshold: one during the Butte Fire (October 15, 2016) and another during the Thomas Fire (January 8, 2018). The highest median depth was 7,212 ft (2.2 km) at the nearest hour to peak 15-minute rainfall intensity, well below the 10,000 ft threshold. The maximum observed value, 17,938 ft (5.5 km), occurred six hours prior to peak rainfall in the El Dorado Fire scar during a summer storm (July 31, 2022), which also recorded the highest IWV (38 mm). At specific debris flow reference locations, exceedance rates were slightly higher than when computing the median of all pixels in burned area: 20% of PFDF events exceeded 10,000 ft at the nearest hour (vs. 15% in non-PFDF storms), rising to 22% three hours prior (12% in non-PFDF). For this reason, warm cloud depth three hours prior to peak 15-minute intensity at the debris-flow location was selected as the representative model variable.

Seasonally, exceedances above 10,000 ft were dominated by spring and summer storms across all lead times. In the selected predictor (3 hours prior to peak 15-min rainfall intensity), 42% of PFDF events were warm-season, nearly identical to non-PFDF storms (43%), compared to just 14% of PFDF and 2% of non-PFDF fall/winter cases. In general, PFDF-producing storms were not characterized by unusually deep warm cloud layers, indicating that deep warm-rain processes are not necessarily a requirement for debris flow initiation. Although both PFDF and non-PFDF storms exhibited higher warm cloud depths in spring and summer, a small subset of PFDF events consistently occurred under slightly deeper clouds than non-PFDF storms at debris flow reference locations.

In our study, Showalter Index (SI) with stable conditions values (>0) dominated post-fire debris flow events, occurring in up to 85% of cases. Very unstable and extremely unstable

conditions were essentially absent, as median and 75th-percentile values were positive (Figure 4.5d). For modeling, we selected the SI at the hour nearest to peak 15-minute rainfall intensity, when 14% of events exhibited moderately unstable conditions (15% in non-PFDF storms), that is values between 0 and -3. This condition also occurred in 11% of events three hours before peak 15-min rainfall intensity, and 8% six hours prior (14% in non-PFDF storms for both datetimes). In non-PFDF storms, spring and summer events showed more unstable conditions, accounting for 46% of cases compared to only 4% in fall/winter. For PFDF storms, the same seasonal dominance was observed: all events at the nearest hour and six hours prior to peak 15-minute rainfall occurred in warmer months, with only a single fall/winter case observed three hours before the peak 15-min rainfall. Overall, these results indicate that storms producing post-fire debris flows in the study region generally occurred under stable atmospheric conditions, with only occasional moderate instability mostly in spring/summer months.

In summary, storms producing post-fire debris flows in California consistently featured higher peak 15-minute rainfall intensities (often exceeding 20–30 mm) than non-PFDF storms. These events were associated with 1) positive advection vorticity peaking three hours before the storm, 2) elevated IVT and IWV frequently surpassing atmospheric river thresholds, and 3) pronounced low-level wind speeds and orthogonality with terrain near the peak rainfall. Moderate convective instability, reflected in CAPE, K-Index, and Showalter Index values, was generally sufficient to support intense rainfall, while warm cloud depths rarely exceeded thresholds for deep warm-rain processes. Seasonal differences were notable: spring and summer PFDFs were linked to more convective activity, slower winds, and slightly

deeper warm clouds, whereas fall and winter events corresponded with stronger synoptic forcing, more moisture transport, and faster low-level winds.

4.4.2. Structural properties of precipitation systems

Structural characteristics of precipitation systems and their reflectivity were analyzed at the time of peak 15-minute rainfall, used as a proxy for peak debris-flow occurrence. System area, eccentricity, and propagation speed exhibited strong seasonal differences. PFDF-associated systems ranged from 300 to 170,000 km², with half exceeding 36,000 km², compared to a median of 20,200 km² for non-PFDF storms. The largest PFDF systems occurred exclusively in fall and winter, with 16% exceeding 100,000 km² versus 10% of non-PFDF storms (Figure 4.6b). Non-PFDF storms above the median area were also concentrated in cooler months, with only 10% in spring/summer. In contrast, spring/summer PFDF events were all linked to smaller systems (<10,000 km²), whereas non-PFDF storms in this season were more variable, with 24% exceeding 10,000 km². This seasonal pattern highlights a key distinction: isolated thunderstorms dominate warm-season PFDF events, while larger reflectivity areas in cooler months reflect the influence of frontal systems, narrow cold-frontal rain bands, and atmospheric rivers (de Orla-Barile et al., 2022; Harris & Carvalho, 2018; Oakley et al., 2017).

Eccentricity, which describes precipitation system shape from elongated (near 0) to circular (near 1), varied across PFDF events. Systems linked to debris flows had eccentricities from 0.19 to 0.91 (median 0.49; 0.47 in non-PFDF storms). Seasonal differences were clear: fall/winter PFDF systems were generally elongated (Figure 4.6a), with 60% below 0.5 (55% in non-PFDF) and 92% below 0.65 (78% in non-PFDF), reflecting narrow cold-frontal rain bands and atmospheric rivers. In contrast, spring/summer PFDF systems were more circular,

with 68% exceeding 0.5 (40% in non-PFDF), consistent with orographic thunderstorms and less organized convection. Non-PFDF storms in the warm season displayed a broader shape distribution, with 55% between 0.35–0.5 and 28% above 0.75, indicating that non-debris-flow storms are not uniformly circular and span a wider range of geometries.

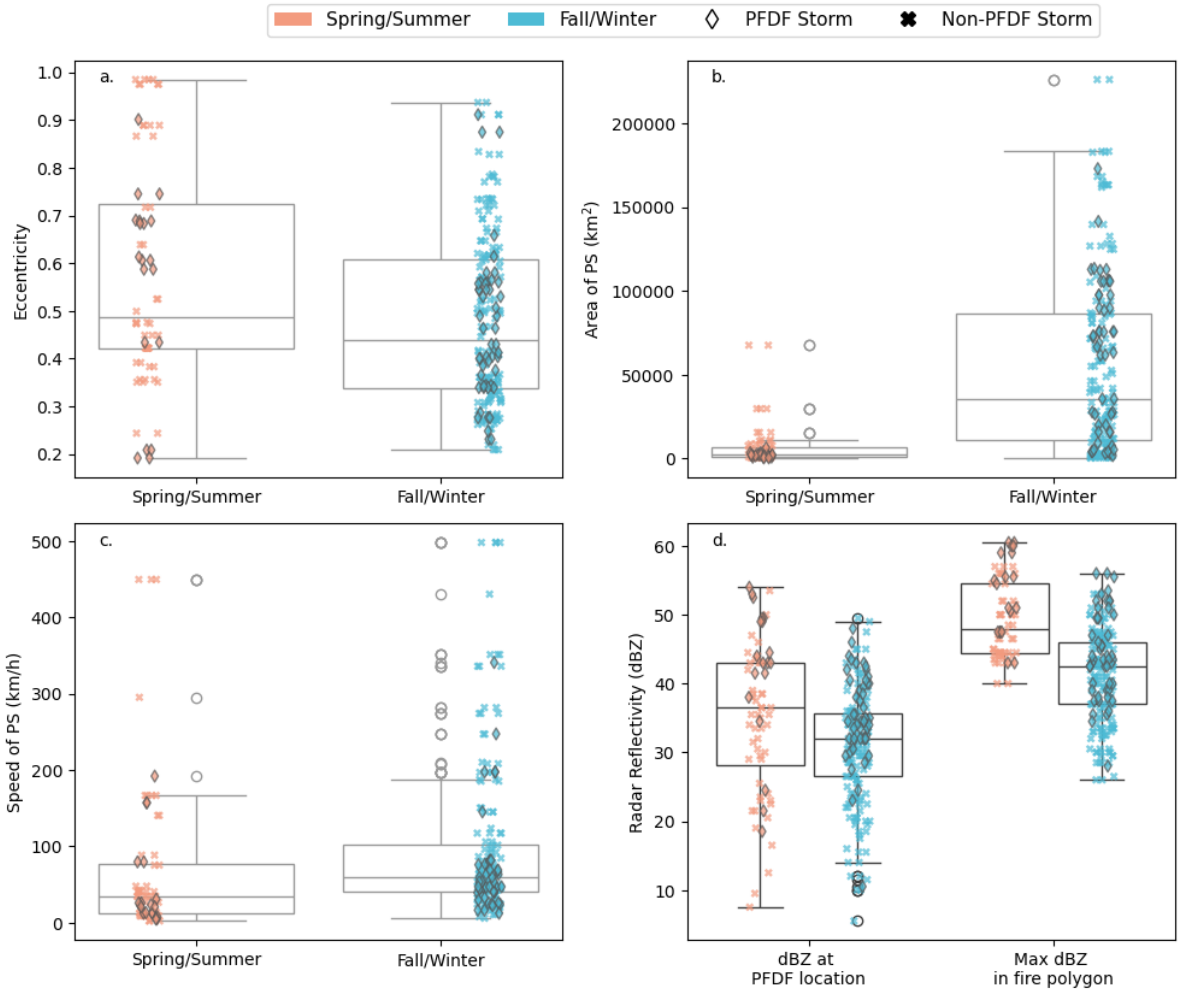


Figure 4.6. Precipitation system characteristics at the time of peak 15-minute rainfall intensity associated with post-fire debris flow (PFDF) and non-PFDF storms in California, separated by season. **a.** Eccentricity, **b.** area of the precipitation system (PS), **c.** PS speed, and **d.** radar reflectivity at the PFDF location and maximum within the burned area. Box plots show distributions for all events (PFDF and non-PFDF), including the median (center line), interquartile range (box edges: 25th–75th percentiles), whiskers extending to 1.5x the interquartile range, and individual points representing outliers beyond this range.

This seasonal contrast was also evident in system propagation speed. Across PFDF storms, median speed was 47 km h^{-1} (59 km h^{-1} in non-PFDF storms), with 68% moving slower than 75 km h^{-1} (60% in non-PFDF). Warm-season PFDF storms were generally slow: 58% moved below 25 km h^{-1} and 72% below 50 km h^{-1}, similar to non-PFDF events (Figure 4.6c). Fall and winter storms, however, were more variable, with 54% between 25–75 km h^{-1} (43% in non-PFDF) and 14% exceeding 200 km h^{-1} (21% in non-PFDF). Slow-moving systems can sustain high rainfall over burn scars, while very fast systems, often driven by strong synoptic forcing such as upper-level jets, may trigger flows through intense precipitation, hail, or damaging winds (Houze, Jr., 2014). Overall, warm-season PFDF storms do not differ markedly in speed from non-PFDF storms, but cold-season events show greater contrasts, with both unusually slow and exceptionally fast systems associated with debris flows.

Reflectivity patterns were evaluated both at debris flow reference locations and as maximum reflectivity within the burned area. At reference locations, reflectivity resulting in debris flows ranged from 10.5 to 54 dBZ, with mean and median values of 37 and 36.5 dBZ, compared to 30.4 and 31.5 dBZ, respectively, in non-PFDF storms. Most PFDF cases (81%) occurred between 30 and 50 dBZ, consistent with moderate to high reflectivity, whereas 76% of non-PFDF cases were confined to the lower 20–40 dBZ range (Figure 4.6d). A seasonal contrast was also evident: spring and summer PFDF events exhibited higher reflectivity, with a median of 43 dBZ (34 dBZ in non-PFDF storms) and an upper quartile of 49.25 dBZ (38.5 dBZ in non-PFDF cases). Values higher than 50 dBZ are only observed in this season, corresponding to 15% in PFDF storms and 4% in non-PFDF storms. In contrast, fall and winter PFDF events were weaker, with a median of 34.5 dBZ (30.5 dBZ in non-PFDF), an upper quartile of 40 dBZ (34.5 dBZ), and a maximum of 48 dBZ. Overall, spring and summer

storms exhibited higher reflectivity than fall and winter storms, but regardless of season, PFDF events were associated with higher reflectivity than non-PFDF storms.

Within fire perimeters, maximum reflectivity was generally higher than at individual debris flow reference locations. Across all PFDF events, values ranged from 28 to 60.5 dBZ, with a median of 46 dBZ (43 dBZ in non-PFDF storms), and 62% of cases fell between 40–60 dBZ (68% in non-PFDF storms). Spring and summer PFDFs had no values below 40 dBZ, with median and upper quartiles of 54.5 and 59 dBZ (46.5 and 51.5 dBZ in non-PFDF storms), while fall and winter events were lower, with medians and upper quartiles of 43.5 and 49.5 dBZ (30.5–34.5 dBZ in non-PFDF storms). These seasonal patterns align with prior observations, where peak 15-minute reflectivity for PFDFs in the Springs and Thomas Fires reached 50–60 dBZ (Oakley et al., 2018; Sukup et al., 2016). Overall, PFDF-producing storms consistently exhibit higher maximum reflectivity within burned areas compared to non-PFDF storms, emphasizing reflectivity as a potential distinguishing feature of debris flow-triggering precipitation systems.

To summarize, post-fire debris flow storms in California are structurally distinct from non-PFDF storms, with pronounced seasonal differences. Fall and winter events are generally large, elongated, and highly variable in speed, reflecting frontal systems, narrow cold-frontal rain bands, and atmospheric rivers, whereas spring and summer events are smaller, more circular, and slower, consistent with isolated thunderstorms. Across all seasons, PFDF storms exhibit higher reflectivity both at debris flow reference locations and within burned areas, highlighting reflectivity as a potential indicator of debris flow occurrence.

4.4.3. Surface variables

Surficial conditions (slope, burn severity, vegetation, and soil erodibility) play a role in post-fire susceptibility. Slopes in PFDF cases ranged from 5° to 37° (Figure 4.7a), with half of the events occurring on slopes steeper than 15° (compared to 13° in non-PFDF storms), and 20% exceeding 25° (21% in non-PFDF cases), reflecting conditions that favor rapid runoff and sediment mobilization. Burn severity at these locations was predominantly low (36% PFDF vs. 41% non-PFDF) or moderate (39% PFDF vs. 36% non-PFDF), while only 9% occurred in high burn severity locations (5% non-PFDF, Figure 4.7b). These few high burn severity PFDF cases were observed in the Dolan, CZU Lightning Complex, Farad, and Dixie fires.

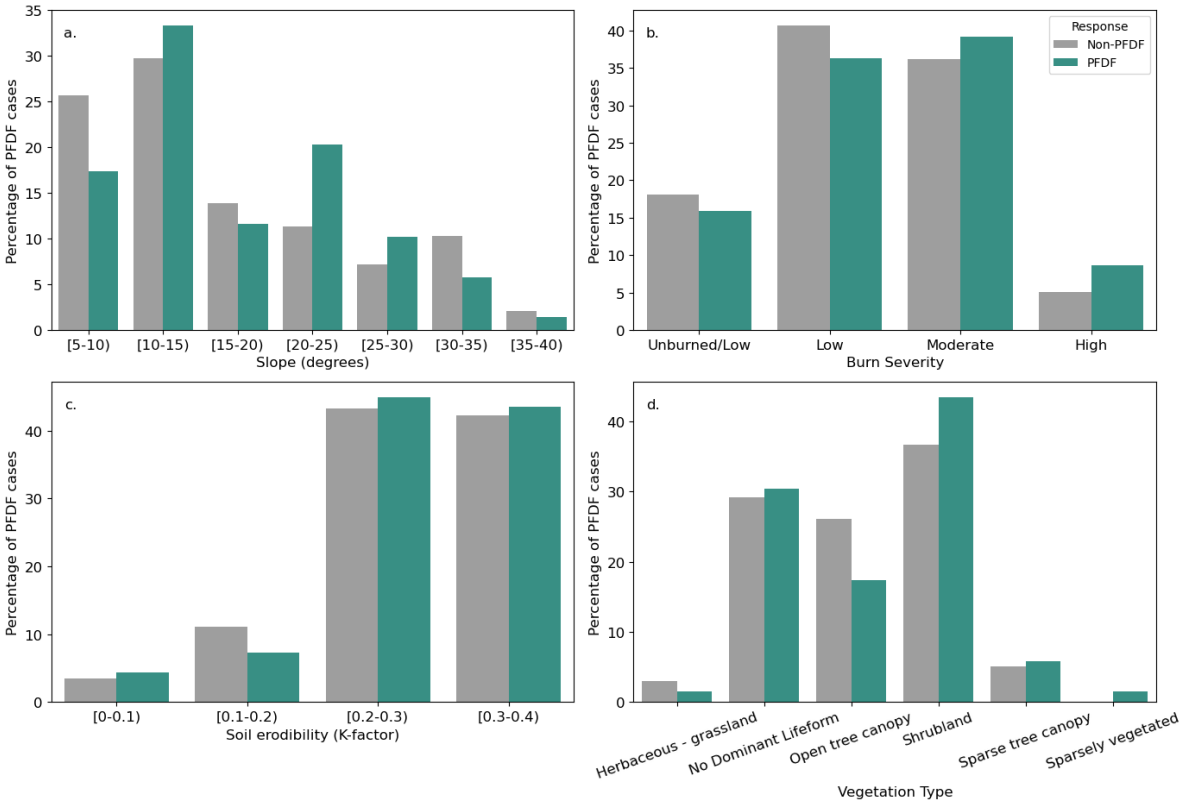


Figure 4.7. Distribution by PFDF response of **a.** Slope, **b.** Burn severity, **c.** Soil erodibility, and **d.** Vegetation type.

Higher soil erodibility further enhances sediment detachment and transport potential. PFDF cases, represented by the K-factor, ranged from 0.04 to 0.38 with a median of 0.28. Figure 4.7c shows that most events (88%) were associated with values between 0.2 and 0.4 (85% in non-PFDF cases), indicative of moderately erodible soils such as silt loams which are more susceptible than clay-rich or sandy soils (0.05–0.2) but less extreme than highly silty soils (K > 0.45). Regarding vegetation, nearly half of the PFDF events (43% vs. 37% in non-PFDF storms) occurred in shrublands (Figure 4.7d), 30% in areas lacking a dominant lifeform (29% non-PFDF), and 17% in open tree canopies (26% non-PFDF). Debris flows in shrub-dominated landscapes likely reflect the combined influence of steep slopes and limited canopy interception, whereas flows in forested areas may highlight the role of canopy loss following moderate to high burn severities.

4.4.4. Model performance

The correlation analysis showed that pairwise correlations among predictors were below |0.8|, indicating no strong correlation between predictor pairs, although several moderate relationships were observed. This threshold was used as a conservative screening criterion, given that problematic multicollinearity is typically associated with substantially higher correlations (e.g., around 0.9 or above; Tabachnick & Fidell, 2013). Median K-index and IWV at the nearest hour showed the highest correlation (77%), followed by IVT with 925-hPa wind speed (70%) and IVT with area of precipitation systems (65%). The strong link between IWV and the K-Index likely reflects their shared sensitivity to atmospheric moisture: IWV quantifies the total column water vapor, while the K-Index incorporates dew point depression at 850 and 700 hPa as part of its calculation (i.e., low-level moisture content). As a result, both metrics tend to increase during moist and unstable conditions conducive to convective rainfall,

and in our dataset often peaked during the same storms across burned areas and captured conditions in both winter/fall and spring/summer events. Maximum reflectivity within burned area and reflectivity at the PFDF location were moderately correlated (52%), likely reflecting that when the burned area experienced maximum reflectivity, it coincided with high reflectivity at PFDF reference locations. A notable negative correlation (−58%) was observed between the Showalter Index and CAPE, which is physically consistent since both measure instability but in opposite directions: CAPE increases as instability strengthens, while the Showalter Index decreases. When analyzing the correlation between post-fire debris flow response (i.e., occurrence, non-occurrence) and individual predictors, it was found they were generally low to moderate, with no single variable strongly explaining debris flow occurrence. Reflectivity at the post-fire debris flow location (r = 0.31), maximum reflectivity (r = 0.27), and peak 15-minute rainfall intensity (r = 0.23) showed the strongest associations.

We began with a baseline random forest model trained and tested using only surficial and morphological variables, that is, 15-minute peak rainfall intensity, slope, burn severity, soil erodibility, and vegetation type. On the test set, the model achieved an accuracy of 0.72, meaning that 72% of predictions were correct overall, but a recall of only 0.29, indicating limited ability to identify post-fire debris flow occurrences. To improve performance, we tested multiple combinations of additional atmospheric and storm-scale predictors. Incorporating radar reflectivity at debris flow locations did not improve performance. However, adding Integrated Water Vapor (IWV) enhanced overall discrimination, raising accuracy to 0.81 and the F1 score to 0.50, alongside higher precision (0.83). Including orthogonality, 925-hPa wind speed, and Integrated Vapor Transport (IVT) further increased

recall to 0.64 while maintaining perfect precision (1.0). Finally, the addition of CAPE and precipitation system area consolidated these improvements, boosting AUC to 0.93.

Several predictors, including median advection vorticity and warm cloud layer depth, offered minimal or inconsistent contributions and were excluded, as their effects appear captured by broader indicators of convective instability and moisture transport (IWV, IVT). We also tested the removal of system speed and eccentricity, finding that performance remained unchanged as long as maximum reflectivity in the burn area, the Showalter Index, and CAPE were retained. Reflectivity at debris flow points was also kept. While it did not substantially improve metrics over the baseline model, it encodes event-specific location information that complements maximum reflectivity in the burn area, which represents broader storm-scale structure.

The final Random Forest model achieved an overall accuracy of 0.91, perfect precision (1.00), moderate recall (0.64), an F1 score of 0.78 and an AUC score of 0.93 (Figure 4.8a). This indicates a moderate ability to identify most events while minimizing false positives, though some debris flows were missed. Feature importance analysis revealed a clear hierarchy: reflectivity, rainfall intensity and atmospheric variables dominated the model. Reflectivity within burned areas (11.7%) and maximum reflectivity within burned area (9.4%) were the strongest contributors (Figure 4.8b), followed closely by peak 15-minute rainfall intensity (8.6%), IWV (8.5%), wind speed at 925 hPa (8.2%) and K-index (7.8%). Instability indices such as the Showalter index (7.3%) and CAPE (6.9%) continued to provide additional signal along with area of precipitation system (6.7%), IVT (6.2%) and terrain–storm interaction variables such as orthogonality (6%). Variables representing local terrain and surficial conditions (slope, burn severity, soil erodibility, and vegetation categories) ranked

lower, with individual contributions below 5%. This pattern highlights that localized rainfall intensity and atmospheric structure provide the strongest predictive signal, while surficial features complement these features by setting the baseline susceptibility across the landscape.

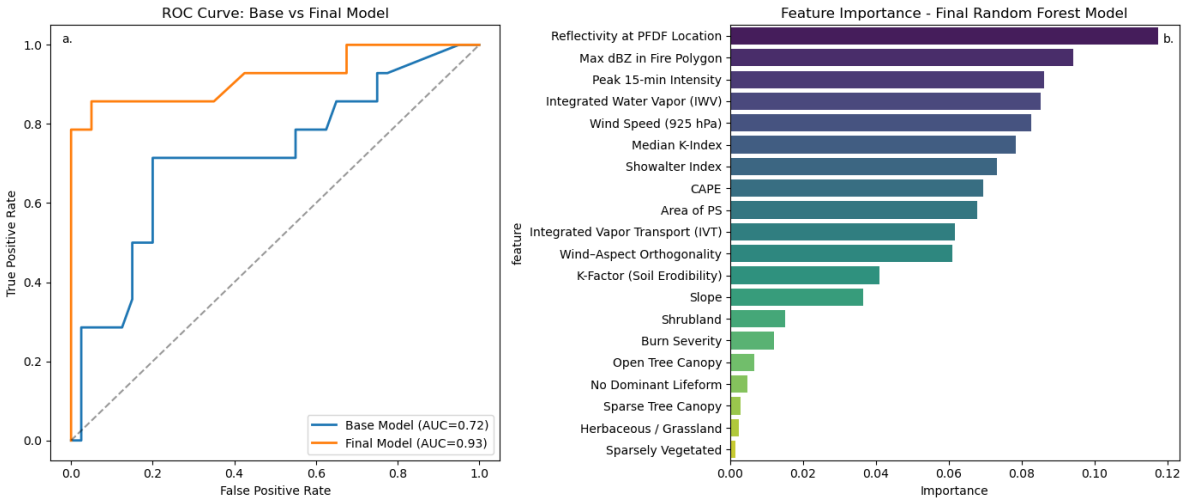


Figure 4.8. Model performance and feature importance **a.** Receiver Operating Characteristic (ROC) curves for Random Forest (RF) models predicting post-fire debris flow (PFDF) occurrence. The blue curve represents the baseline model using only surface and fire-related predictors: peak 15-minute rainfall intensity, slope, burn severity, soil erodibility, and vegetation type. The orange curve represents the final model incorporating both base and atmospheric predictors. **b.** Feature importance rankings for all predictors used in the final RF model, including radar reflectivity at the debris flow location, integrated water vapor (IWV), integrated vapor transport (IVT), wind speed at 925 hPa, orthogonality, K-index, maximum radar reflectivity within the burned area, precipitation system area, CAPE and Showalter index.

To evaluate the robustness and applicability of the final model, we implemented 10-fold stratified cross-validation. Across all folds, the model achieved a mean accuracy of 0.91 (±0.04), with consistently strong performance for the negative class (precision = 0.89 ± 0.04, recall = 1.00 ± 0.02, F1-score = 0.94 ± 0.03), reflecting its ability to reliably identify non-debris flow events. For the positive class, precision remained high (0.98 ± 0.08), but recall was more variable (0.66 ± 0.14), resulting in an average F1-score of 0.79 (±0.12), which highlights the challenge likely posed by the limited number of positive cases and inherent

class imbalance. Most folds (e.g., 1,3,4,6,7,8,9) achieved both high recall and overall accuracy (up to 0.96), showing that the model can capture positive events under favorable training partitions. These findings highlight both the strengths and limitations of the model: while it generalizes well for non-events, reliably identifying debris flows remains difficult. This underscores the importance of careful interpretation for operational hazard applications and the need to consider class imbalance when interpreting model performance and reliability for event prediction.

Table 4.2. Summary of Random Forest model performance for PFDF classification. Cross-validation fields report mean ± standard deviation across 10 stratified folds for the positive PFDF class and negative non-PFDF class.

	Final model	**10-fold cross-validation Positive class**	**10-fold cross-validation Negative class**
Accuracy	0.91	0.91 ± 0.04	0.91 ± 0.04
Precision	1.00	0.98 ± 0.08	0.89 ± 0.04
Recall	0.64	0.66 ± 0.14	1.00 ± 0.02
F1-score	0.78	0.79 ± 0.12	0.94 ± 0.03

4.4.5. Model validation

To evaluate the performance of the final model in a real-world context, we applied it to a debris flow event in the Eaton Fire, Southern California. The fire started on January 7, 2025, and remained active for 24 days, resulting in 19 fatalities and the destruction of more than 9,000 structures. Driven by strong Santa Ana winds and following eight months without rainfall, the fire ignited in the foothills of the San Gabriel Mountains about 56 km east of the Palisades Fire and nearly devastated the historic community of Altadena in Los Angeles County (Woolcott, 2025).

On February 13, 2025, intense rainfall triggered a debris flow within the Eaton Fire burn area. Officially reported by the U.S. Geological Survey (2025) in Rubio Canyon, this flow was described as a deposit of mud- to boulder-sized sediment that damaged trees along the channel. While the precise initiation point of the debris flow was not available, for this analysis we assigned the event to the representative drainage at coordinates 34.205°N, −118.12°W. Rainfall conditions were characterized using data from the Eaton Dam gauge, located approximately 4 km downstream from Rubio Canyon. According to the gauge record, the storm began at 00:15 PST (08:15 UTC) on February 13 and persisted for ~28 hours, producing 85 mm of total rainfall. Peak 15-minute intensity reached 31.5 mm h^{-1} at 17:05 PST (01:05 UTC on February 14).

For model evaluation, the final predictor set (reflectivity at the debris flow location, IWV, IVT, wind speed at 925 hPa, orthogonality, K-index, maximum reflectivity within burned area, precipitation system area, CAPE, Showalter index, slope, peak 15 min rainfall intensity, burn severity, soil erodibility and vegetation type) was extracted for the Eaton event. Predictor values were derived for 215 coordinates distributed across the burn perimeter, using a 500 m grid consistent with the radar reflectivity dataset. Large-scale atmospheric variables were taken from ERA5 reanalysis, providing coverage for two longitude and one latitude grid cells over the fire area, which was insufficient to fully resolve the event's variability. To address this, inverse distance weighting (IDW) interpolation was applied across the burn perimeter for water vapor (IWV), integrated vapor transport (IVT), wind speed at 925 hPa, CAPE and orthogonality.

Some predictors were represented by single values. For example, both median K-index and maximum reflectivity summarize conditions across the burned area rather than at

individual points. Similarly, the precipitation system area was defined as a single value to reflect the overall storm structure. In contrast, radar reflectivity at the debris flow reference location and surficial variables (e.g., slope, burn severity, soil erodibility, vegetation) were extracted at each coordinate to preserve local-scale variability.

ERA5 reanalysis variables, interpolated across the burn perimeter, indicated IVT ranging from 418.3 to 431.8 kg m^{-1} s^{-1} (original: 445.4, 410.3), and IWV between 20.6 and 21.5 mm (original: 22.3, 20.2), consistent with conditions favorable for an atmospheric river. Wind speeds at 925 hPa interpolated between 6.53 and 7.65 m s-1 (original: 8.77, 5.86, Figure 4.9f), and orthogonality ranged from 0.943 to 0.95 (original: 0.936, 0.953), capturing local terrain-storm interactions. Showalter index was constant at 3.48 (corresponding to stable conditions), and median K-index, summarizing convective instability across the perimeter, was 24.95 (equivalent to isolated thunderstorms). The precipitation system covered an area of 56,631 km^2, while maximum radar reflectivity within the burned area reached 58.5 dBZ at the 15-minute peak intensity. At the same time, reflectivity across all coordinates in the burned area had a mean of 46.6, median of 46.5, 75th percentile of 50, and a value of 51 dBZ at the assigned debris flow reference location (Figure 4.9c).

Surficial variables highlighted local topography and burn severity: slope across the burned area ranged from 2° to 51° (mean 26°, median 30°) with 35° at the debris flow location (Figure 4.9a). Burn severity was moderate over 75% of the perimeter, while the debris flow site itself had low severity; only 4% of the burned area, mainly in the northeast, exhibited high burn severity (Figure 4.9b). Soil erodibility (K-factor) spanned 0.02 - 0.46, with the maximum also corresponding to the debris flow site and a median of 0.34, indicating moderately erosive

soils. Vegetation cover consisted of 45% shrubland, 18% open tree canopy, and 18% areas with no dominant lifeform, with the debris flow location situated in shrubland.

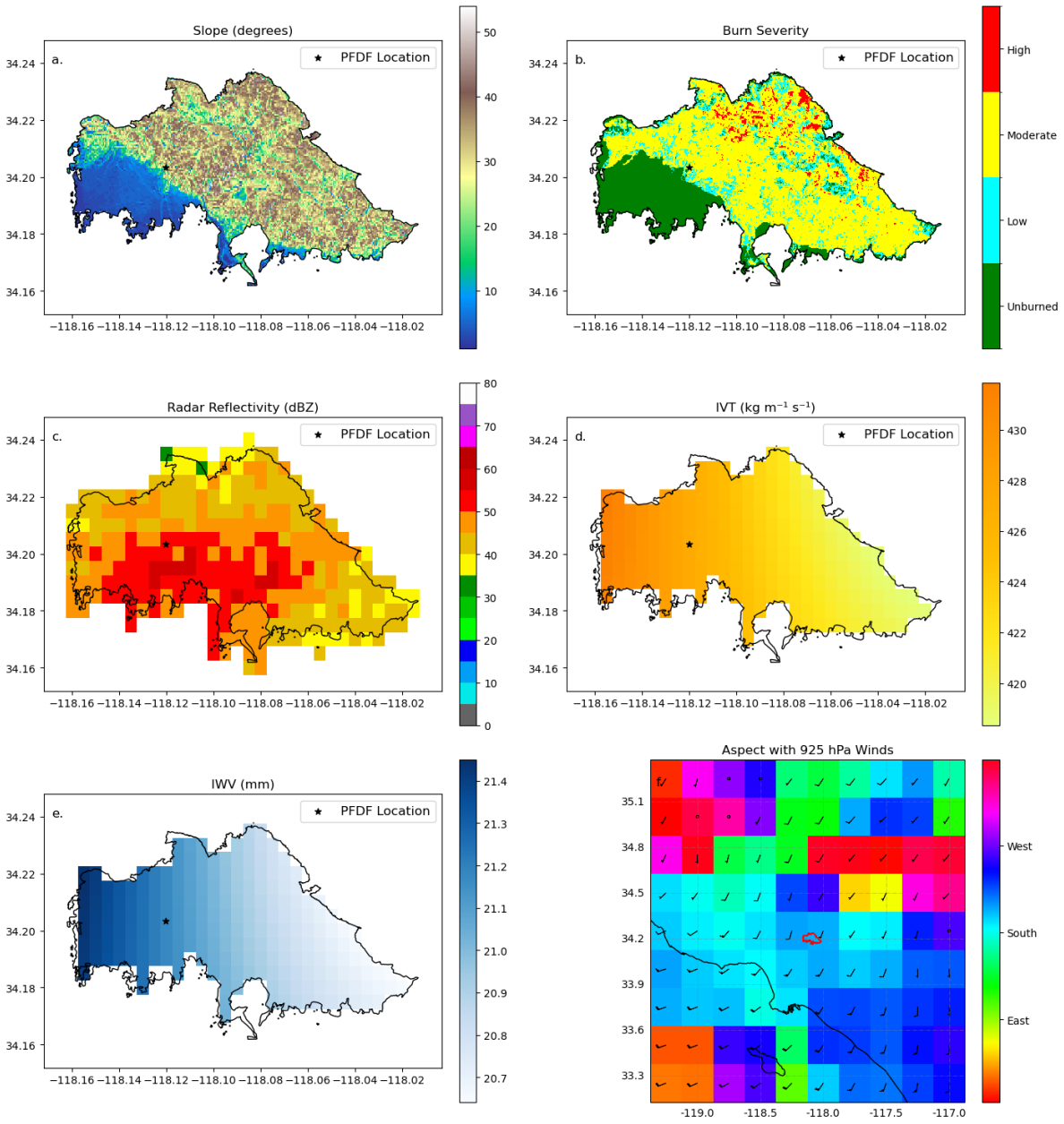


Figure 4.9. Predictor variables for the February 13, 2025 storm that generated a post-fire debris flow in the Eaton Fire burn area, San Gabriel Mountains. **a.** Slope, **b.** burn severity, **c.** radar reflectivity, **d**. interpolated integrated vapor transport (IVT), **e.** interpolated integrated water vapor (IWV), and **f.** aspect overlaid with 925 hPa wind vectors (red contour corresponds to

Eaton fire perimeter). Panels c–f represent conditions at the nearest hour to the peak 15-minute rainfall intensity.

Predictor values were input to the Random Forest model to estimate the probability of post-fire debris flow occurrence across the burned area. Predicted probabilities ranged from 0.42 to 0.68, with a mean of 0.58 (SD = 0.05) and 25th, 50th, and 75th percentiles of 0.54, 0.58, and 0.62, respectively, indicating that the majority of the area had probabilities close to the median value. At the assigned debris flow reference location, the model predicted a probability of 0.53 (Figure 4.10a), closely aligning with the overall distribution.

The spatial pattern of predicted probabilities reflects an interplay between atmospheric and surficial controls. In the western portion of the fire perimeter, several streams exhibited lower predicted probabilities, coinciding with gentler slopes, lower burn severity, and areas classified as having “no dominant lifeform” vegetation. This occurred despite the presence of strong atmospheric indicators such as elevated moisture transport and wind speed, that may have contributed to higher predicted probabilities in other western drainages. Notably, radar reflectivity peaked in the central-southern portion of the perimeter (Figure 4.9c), near the documented debris flow reference location, aligning with the moderate probability assigned to that segment.

Consistently high probabilities were observed along streams in the central-northern and southeastern regions. While surficial variables were ranked lower in global feature importance, they may have played a more influential role in the Eaton Canyon event, where local variations in terrain and vegetation appear to have modulated susceptibility. This highlights a key distinction: global importance scores capture the average predictive contribution across all events, whereas local assessments can reveal context-specific

interactions, with surficial factors shaping spatial variability when atmospheric and storm-scale conditions are relatively uniform.

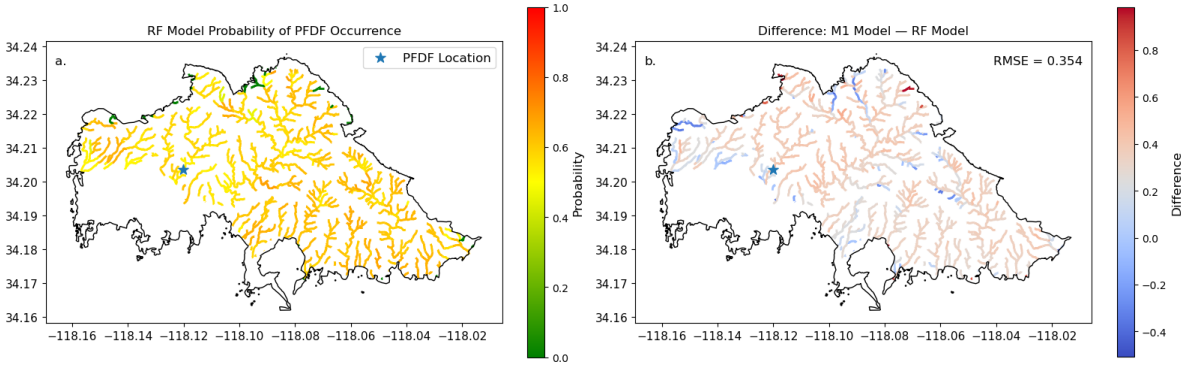


Figure 4.10. Predictive modeling in the Eaton fire and comparison with existing approaches. **a.** Predicted probabilities of post-fire debris-flow occurrence from the Random Forest (RF) model developed in this study for the Eaton Fire burn area. **b.** Differences in predicted likelihood between the USGS M1 model and the RF model (M1 – RF). Positive values (red) indicate higher probabilities from the M1 model, while negative values (blue) indicate higher probabilities from the RF model.

To contextualize our Random Forest model predictions, we compared them with the USGS M1 model (Staley et al., 2017), a widely used logistic regression tool that estimates post-fire debris flow likelihood and provides hazard assessments to emergency managers. For the Eaton Fire case, we used the same stream segments defined by the USGS and extracted debris flow likelihoods from the M1 model for a 15-minute rainfall intensity of 32 mm h^{-1}, closely matching the peak intensity observed during the storm on February 13. This allows a direct comparison between our RF model, which incorporates atmospheric and storm-structural variables in addition to surficial predictors, and the M1 model, which emphasizes terrain and rainfall drivers.

The M1 model predicted consistently high probabilities across the Eaton Fire burn area, with values at the segment level ranging from 0.11 to 0.99 (mean 0.87, median 0.95). Most of the perimeter (81%) fell in the 0.8–1 probability range, with lower probabilities confined to

small areas in the steep northern drainages. In contrast, the RF model produced probabilities ranging from 0.36 to 0.70 (mean 0.56, median 0.57), reflecting a broader spatial variability influenced by local storm intensity, atmospheric transport, and surficial features.

Comparing the two models directly (M1 – RF) highlights areas where the M1 model predicts higher likelihood (positive values, red) versus areas where the RF model predicts higher probability (negative values, blue). Differences are moderately dispersed, with a root mean square error (RMSE) of 0.354 (Figure 4.10b), suggesting general agreement between the models. However, localized deviations are notable, particularly in the northern and northwestern portions of the burned area, where the M1 model frequently predicts higher probabilities than our RF model. In contrast, some central and western stream segments show areas where RF predicts higher probabilities. At the segment corresponding to the documented debris flow, the M1 model predicted a very high probability (>90%), while the RF model assigned a more moderate probability of 0.55.

Overall, this comparison illustrates that while traditional surficial and rainfall-based models like M1 produce consistently high hazard probabilities, integrating atmospheric and storm-scale predictors tend to modulate these estimates, revealing spatial variability that may be relevant for identifying localized areas of elevated or reduced risk. Although the RF model does not necessarily outperform M1 in this case, it provides complementary insight, emphasizing the value of including dynamic atmospheric conditions when interpreting post-fire debris flow hazard.

4.5. Discussion

To understand the drivers of post-fire debris flow initiation, we evaluated a broad set of predictors encompassing atmospheric, storm structural, reflectivity, and surficial factors.

These included metrics of moisture transport (e.g., integrated vapor transport, integrated water vapor), convective stability indices (CAPE, Showalter Index, K-Index), orographic precipitation proxies, radar reflectivity patterns and structural properties of precipitation systems such as area, eccentricity, and propagation speed. Many variables exhibited strong seasonal contrasts reflecting distinct storm regimes: winter storms were primarily associated with large-scale moisture transport via atmospheric rivers, while summer events were dominated by compact, slower-moving convective systems with higher reflectivity and instability. Other variables, including the K-Index and integrated water vapor, were influential across seasons, capturing baseline atmospheric instability and moisture availability. These seasonal patterns could have played a role in why certain predictors gained more importance in the Random Forest (RF) model, pointing to the potential value of incorporating temporally sensitive atmospheric metrics in debris flow modeling.

The Random Forest (RF) model was developed iteratively, testing different combinations of predictors to evaluate their incremental contributions to predictive skill. This process highlighted which predictors consistently strengthened the model and which offered limited additional value. Atmospheric and storm-scale variables (including IWV, low-level wind speed, and radar reflectivity) produced clear gains in accuracy, F1 score, and AUC, while other factors, such as advection vorticity and system eccentricity, contributed less consistently. Surficial variables, including slope, burn severity, soil erodibility, and vegetation type, provided the baseline context for susceptibility, ensuring that local terrain and surface conditions were represented alongside dynamic storm conditions.

The final model demonstrated strong overall predictive capability, with accuracy of 0.91, an F1 score of 0.78, and an AUC of 0.93. Feature importance rankings indicated that

reflectivity at debris flow reference location, maximum reflectivity within burned area, peak 15-min rainfall intensity, IWV, and low-level wind speed were among the most influential predictors, while surficial factors such as slope and burn severity ranked lower. Similar findings were reported by Cavagnaro et al., (2025), who showed that climate-related predictor variables in a decision tree model, such as rainfall climatology derived from gridded precipitation datasets, have higher predictive power compared to the USGS M1 topographic and fire-related variables, particularly when analyses are conducted at fire or regional scales rather than at the basin level. They hypothesize that these results arise from the fact that climate metrics vary over larger spatial scales than fire severity or topography.

To contextualize RF model predictions, we compared them with the USGS M1 model (Staley et al., 2017), a logistic regression framework that estimates post-fire debris flow likelihood and produces a conservative screening of high-risk areas, reflected in a tendency toward false positives (Thomas, Kean, et al., 2023a). For the Eaton Fire case study, M1 probabilities were extracted for the same stream segments using a 15-minute rainfall intensity matching the observed peak rainfall intensity. The M1 model predicted consistently high probabilities across the burned area (mean = 0.87), with 79% of stream segments classified in the "High" hazard class and over 95% of values exceeding 0.80. In contrast, our RF model produced a narrower probability range (0.42–0.68, mean = 0.58), assigning a moderate 0.53 probability at the observed debris flow reference location. The RF model differentiated susceptibility across the perimeter, with higher probabilities in the eastern portion, coinciding in some areas with steeper slopes and locally elevated burn severity, and lower probabilities toward the west, where slopes were gentler, and vegetation cover less flammable. This case illustrates an important nuance of machine learning models: global importance scores provide

an averaged perspective across all events, but local interactions between storm and surficial conditions can strongly influence hazard estimates at specific sites.

The comparison highlights complementary trade-offs between the models. M1's conservative design minimizes false negatives but can overpredict hazard in gentler terrain, generating more false positives. In contrast, the RF model integrates atmospheric predictors to capture relative spatial variability in susceptibility, potentially reducing false positives. However, it may underpredict extreme local hazard, as seen at the observed debris flow reference location (0.53 versus >0.90 in M1).

Uncertainty in RF predictions could arise from multiple factors. Atmospheric predictors dominate feature importance but are coarse-scale in spatial and temporal resolution, limiting resolution of short-duration convective bursts or localized moisture convergence. Fine-scale storm dynamics remain largely unknown, except for reflectivity at post-fire debris flow reference locations. The model's robustness is also constrained by the number and geographic distribution of post-fire debris flow events: while the RF model incorporates events from across California, regions with fewer observations are more prone to underprediction. Expanding the observational dataset would improve the ability to capture rare or extreme events and better resolve interactions between atmospheric dynamics and local terrain. Additionally, the imbalance between debris flow and non-debris flow cases biases predictions toward moderate probabilities. To address this, oversampling techniques such as SMOTE (Synthetic Minority Oversampling Technique) were tested, which increased recall to 0.71 when additional predictors were included; however, this approach carries the risk of introducing synthetic locations that may not correspond to physically realistic debris flow occurrences (Chawla, 2005; Gupta & Shukla, 2023).

Future work could evaluate additional atmospheric diagnostics that better capture instability in West Coast storm environments. Although CAPE provides a broad measure of convective potential, event-hour values may not fully describe conditional or elevated instability, particularly during atmospheric river or cool-season storms when CAPE is often modest. For instance, diagnostics based on vertical equivalent potential temperature profiles could help identify unstable layers that are not reflected by CAPE magnitude alone. Similarly, while warm cloud layer depth provides information about the depth of the above-freezing cloud layer, freezing-level height could be examined more directly to better understand how this factor influences triggering rainfall conditions associated with PFDFs.

This study provides an early step toward integrating storm dynamics, moisture transport, and seasonality into PFDF prediction. While the Random Forest framework demonstrates potential to refine susceptibility estimates, relatively low recall highlights the need for caution in hazard management. More broadly, the trade-off between global feature importance and local sensitivity remains critical. With further refinement and expanded datasets, the approach could move closer to operational application, complementing existing conservative tools and offering new perspectives on the atmospheric drivers of PFDFs.

4.6. Conclusions

This study advances understanding of post-fire debris flow hazards in California by quantifying how atmospheric drivers and precipitation system structure as well as reflectivity patterns contribute to debris flow occurrence. The Random Forest model integrated stability indices, moisture transport, synoptic conditions, radar reflectivity and storm structural properties along with surficial predictors, achieving high overall accuracy (0.91) and perfect precision, though recall and F1-score remained moderate, 0.64 and 0.78, respectively, limiting

its ability to capture all true events. Feature importance underscored the dominant role of dynamic meteorological conditions, particularly radar reflectivity and atmospheric moisture while terrain and burn characteristics provided secondary but necessary baseline susceptibility.

Application of the model to the Eaton Fire case highlighted both strengths and limitations. The RF model captured spatial variability in susceptibility across the burn perimeter and revealed contrasts with the USGS M1 model, which predicted uniformly high probabilities. However, predicted probabilities at the documented debris flow reference location were moderate rather than extreme, reflecting challenges potentially tied to coarse atmospheric reanalysis data, unresolved fine-scale storm dynamics, and the limited number of positive events in the dataset.

Overall, the results show that incorporating atmospheric and storm-scale predictors provides complementary insights to terrain and rainfall-based models, enabling improved spatial differentiation of PFDF hazard. At the same time, class imbalance, data resolution, and event rarity present ongoing challenges, emphasizing the need for cautious interpretation of model outputs in operational contexts. These findings highlight the promise of integrating dynamic atmospheric predictors into PFDF hazard assessment, while underscoring that further refinement and expansion of observational datasets are required to fully realize the model's operational potential.

4.7. References

Adams, D. K., & Comrie, A. C. (1997). The North American Monsoon. *Bulletin of the American Meteorological Society*, *78*(10), 2197–2214. https://doi.org/10.1175/1520-0477(1997)078<2197:TNAM>2.0.CO;2

Alessio, P., Dunne, T., & Morell, K. (2021). Post-Wildfire Generation of Debris-Flow Slurry by Rill Erosion on Colluvial Hillslopes. *Journal of Geophysical Research: Earth Surface*, *126*(11), e2021JF006108. https://doi.org/10.1029/2021JF006108

Bordoni, S., & Stevens, B. (2006). Principal Component Analysis of the Summertime Winds over the Gulf of California: A Gulf Surge Index. *Monthly Weather Review*, *134*(11), 3395-3414. https://doi.org/10.1175/MWR3253.1

Breiman, L. (2001). Random Forests. *Machine Learning*, *45*(1), 5–32. https://doi.org/10.1023/A:1010933404324

California Geological Survey. (2023). Reported California Landslides [Dataset]. Retrieved from https://cadoc.maps.arcgis.com/apps/webappviewer/index.html?id=bc48ad40e3504134a1fc8f3909659041&_gl=1*1kr33eo*_ga*MjE0MDgyODE2NS4xNzQ1NjA2MTg0*_ga_N4MB98DBXY*MTc0NTYwNjE4NC4xLjAuMTc0NTYwNjE4NC4wLjAuMA.

Cannon, S. H. (2001). Debris-flow generation from recently burned watersheds. *Environmental & Engineering Geoscience*, *7*(4), 321–341. https://doi.org/10.2113/gseegeosci.7.4.321

Cannon, S. H., Gartner, J. E., Wilson, R. C., Bowers, J. C., & Laber, J. L. (2008). Storm rainfall conditions for floods and debris flows from recently burned areas in southwestern Colorado and southern California. *Geomorphology, Debris Flows Initiated by Runoff, Erosion, and Sediment Entrainment in Western North America*, *96*(3), 250–269. https://doi.org/10.1016/j.geomorph.2007.03.019

Catani, F., Lagomarsino, D., Segoni, S., & Tofani, V. (2013). Landslide susceptibility estimation by random forests technique: Sensitivity and scaling issues. *Natural Hazards and Earth System Sciences*, *13*(11), 2815–2831. https://doi.org/10.5194/nhess-13-2815-2013

Cavagnaro, D. B., McCoy, S. W., Lindsay, D. N., McGuire, L. A., Kean, J. W., & Trugman, D. T. (2025). Rainfall Thresholds for Postfire Debris-Flow Initiation Vary With Short-Duration Rainfall Climatology. *Journal of Geophysical Research: Earth Surface*, *130*(6), e2024JF007781. https://doi.org/10.1029/2024JF007781

Chawla, N. V. (2005). Data Mining for Imbalanced Datasets: An Overview. In O. Maimon & L. Rokach (Eds.), *Data Mining and Knowledge Discovery Handbook* (pp. 853–867). Springer US. https://doi.org/10.1007/0-387-25465-X_40

Cutler, D. R., Edwards Jr., T. C., Beard, K. H., Cutler, A., Hess, K. T., Gibson, J., & Lawler, J. J. (2007). Random Forests for Classification in Ecology. *Ecology*, *88*(11), 2783–2792. https://doi.org/10.1890/07-0539.1

Davis, J., & Goadrich, M. (2006). The relationship between Precision-Recall and ROC curves. *Proceedings of the 23rd International Conference on Machine Learning - ICML '06*, 233–240. https://doi.org/10.1145/1143844.1143874

De Graff, J. V. (2018). A rationale for effective post-fire debris flow mitigation within forested terrain. *Geoenvironmental Disasters*, *5*(1), 7. https://doi.org/10.1186/s40677-018-0099-z

De Graff, J. V., Staley, D. M., Stock, G. M., Takenaka, K., Gallegos, A. L., & Neptune, C. K. (2022). Rainfall Triggering of Post-Fire Debris Flows over a 28-Year Period near El Portal, California, USA. *Environmental & Engineering Geoscience*, *28*(1), 133–145. https://doi.org/10.2113/EEG-D-21-00031

de Orla-Barile, M., Cannon, F., Oakley, N. S., & Ralph, F. M. (2022). A Climatology of Narrow Cold-Frontal Rainbands in Southern California. *Geophysical Research Letters*, *49*(2), e2021GL095362. https://doi.org/10.1029/2021GL095362

DeRubertis, D. (2006). Recent Trends in Four Common Stability Indices Derived from U.S. Radiosonde Observations. *Journal of Climate*, *19*(3), 309-323. https://doi.org/10.1175/JCLI3626.1

Dettinger, M. D., Ralph, F. M., Das, T., Neiman, P. J., & Cayan, D. R. (2011). Atmospheric Rivers, Floods and the Water Resources of California. *Water*, *3*(2), Article 2. https://doi.org/10.3390/w3020445

Doswell, C. A. (2001). Severe Convective Storms—An Overview. In C. A. Doswell (Ed.), *Severe Convective Storms* (pp. 1–26). American Meteorological Society. https://doi.org/10.1007/978-1-935704-06-5_1

Duan, S., Ullrich, P., & Boos, W. R. (2024). Meteorological Drivers of North American Monsoon Extreme Precipitation Events. *Journal of Geophysical Research: Atmospheres*, *129*(13), e2023JD040535. https://doi.org/10.1029/2023JD040535

Englehart, P. J., & Douglas, A. V. (2001). The role of eastern North Pacific tropical storms in the rainfall climatology of western Mexico. *International Journal of Climatology*, *21*(11), 1357–1370. https://doi.org/10.1002/joc.637

Fawcett, T. (2006). An introduction to ROC analysis. *Pattern Recognition Letters, ROC Analysis in Pattern Recognition*, *27*(8), 861–874. https://doi.org/10.1016/j.patrec.2005.10.010

Felling, G., Myers, A., & McCoy, S. W. (2019). *Post-fire debris-flow hazard analysis for Interstate 80, Truckee River Canyon, near the California-Nevada state line, USA.* https://repository.mines.edu/server/api/core/bitstreams/9d5f5165-27bf-44c3-9593-7d1a6a322797/content

Forman, G., & Scholz, M. (2010). Apples-to-apples in cross-validation studies: Pitfalls in classifier performance measurement. *SIGKDD Explor. Newsl.*, *12*(1), 49–57. https://doi.org/10.1145/1882471.1882479

George, J.J. (1960). *Weather Forecasting for Aeronautics*. Academic Press, Waltham, MA, 673 p.

Gershunov, A., Shulgina, T., Clemesha, R. E. S., Guirguis, K., Pierce, D. W., Dettinger, M. D., Lavers, D. A., Cayan, D. R., Polade, S. D., Kalansky, J., & Ralph, F. M. (2019). Precipitation regime change in Western North America: The role of Atmospheric Rivers. *Scientific Reports*, *9*(1), 9944. https://doi.org/10.1038/s41598-019-46169-w

Graber, A. P. (2023). *Compilation of runoff-generated debris-flow inventories for 17 fires across Arizona, California, Colorado, New Mexico, and Washington, USA* [Dataset]. U.S. Geological Survey. https://doi.org/10.5066/P98Q4CDH

Graber, A. P., Thomas, M. A., & Kean, J. W. (2023). How Long Do Runoff-Generated Debris-Flow Hazards Persist After Wildfire? *Geophysical Research Letters*, *50*(19), e2023GL105101. https://doi.org/10.1029/2023GL105101

Guilinger, J. J., Gray, A. B., Barth, N. C., & Fong, B. T. (2020). The Evolution of Sediment Sources Over a Sequence of Postfire Sediment-Laden Flows Revealed Through Repeat High-Resolution Change Detection. *Journal of Geophysical Research: Earth Surface*, *125*(10), e2020JF005527. https://doi.org/10.1029/2020JF005527

Gupta, S. K., & Shukla, D. P. (2023). Handling data imbalance in machine learning based landslide susceptibility mapping: A case study of Mandakini River Basin, North-Western Himalayas. *Landslides*, *20*(5), 933–949. https://doi.org/10.1007/s10346-022-01998-1

Harris, S. M., & Carvalho, L. M. V. (2018). Characteristics of southern California atmospheric rivers. *Theoretical and Applied Climatology*, *132*(3), 965–981. https://doi.org/10.1007/s00704-017-2138-1

Hastie, T., Tibshirani, R., & Friedman, J. (2009). *The Elements of Statistical Learning*. Springer. https://doi.org/10.1007/978-0-387-84858-7

Hersbach, H., Bell, B., Berrisford, P., Biavati, G., Horányi, A., Muñoz Sabater, J., Nicolas, J., Peubey, C., Radu, R., Rozum, I., Schepers, D., Simmons, A., Soci, C., Dee, D., & Thépaut, J.-N. (2023). ERA5 hourly data on single levels from 1940 to present. Copernicus Climate Change Service (C3S) Climate Data Store (CDS). https://doi.org/10.24381/cds.adbb2d47. Accessed February, 21 2024

Houze R.A., Jr. (2014). Cloud Dynamics (2nd ed., Vol. 104). Academic Press.

Johnson, B. O., & Delworth, T. L. (2023). The Role of the Gulf of California in the North American Monsoon. *Journal of Climate*, *36*(6), 1541-1559. https://doi.org/10.1175/JCLI-D-22-0365.1

Kirschbaum, D. B., Adler, R., Hong, Y., Hill, S., & Lerner-Lam, A. (2010). A global landslide catalog for hazard applications: Method, results, and limitations. *Natural Hazards*, *52*(3), 561–575. https://doi.org/10.1007/s11069-009-9401-4

Konrad, C. E. (1997). Synoptic-Scale Features Associated with Warm Season Heavy Rainfall over the Interior Southeastern United States. *Weather and Forecasting*, *12*(3), 557–571. https://doi.org/10.1175/1520-0434(1997)012<0557:SSFAWW>2.0.CO;2

Kostelnik, J., Rengers, F. K., Wald, L., & Schmitt, R. (2021, December 17). *Northern and Central California Debris Flows Overview*. ArcGIS StoryMaps. https://storymaps.arcgis.com/stories/d6c9dc95f0f84fb1994a164f18115fa5

LANDFIRE. (2023). Existing Vegetation Type Layer, LANDFIRE 2.0.0, U.S. Department of the Interior, Geological Survey, and U.S. Department of Agriculture. Accessed September 5 2024 at http://www.landfire/viewer

Lamb, M. P., Levina, M., DiBiase, R. A., & Fuller, B. M. (2013). Sediment storage by vegetation in steep bedrock landscapes: Theory, experiments, and implications for postfire sediment yield. *Journal of Geophysical Research: Earth Surface*, *118*(2), 1147–1160. https://doi.org/10.1002/jgrf.20058

Lin, Y.-L., Chiao, S., Wang, T.-A., Kaplan, M. L., & Weglarz, R. P. (2001). Some Common Ingredients for Heavy Orographic Rainfall. *Weather and Forecasting*, *16*(6), 633-660. https://journals.ametsoc.org/view/journals/wefo/16/6/1520-0434_2001_016_0633_scifho_2_0_co_2.xml

Lukashov, S. G., Lancaster, J. T., Oakley, N. S., & Swanson, B. J. (2019). Post-fire debris flows of 9 January 2018, Thomas Fire, southern California: Initiation areas, precipitation and impacts. *Seventh International Conference on Debris-Flow Hazards Mitigation – Proceedings.* http://dx.doi.org/10.25676/11124/173144

Maddox, R. A., & Doswell, C. A. (1982). An Examination of Jet Stream Configurations, 500 mb Vorticity Advection and Low-Level Thermal Advection Patterns During Extended Periods of Intense Convection. *Monthly Weather Review*, *110*(3), 184-197. https://journals.ametsoc.org/view/journals/mwre/110/3/1520-0493_1982_110_0184_aeojsc_2_0_co_2.xml

McGuire, L. A., Rengers, F. K., Kean, J. W., Staley, D. M., & Mirus, B. B. (2018). Incorporating spatially heterogeneous infiltration capacity into hydrologic models with applications for simulating post-wildfire debris flow initiation. *Hydrological Processes*, *32*(9), 1173–1187. https://doi.org/10.1002/hyp.11458

Mejia, J. F., Douglas, M. W., & Lamb, P. J. (2016). Observational investigation of relationships between moisture surges and mesoscale- to large-scale convection during the North American monsoon. *International Journal of Climatology*, *36*(6), 2555–2569. https://doi.org/10.1002/joc.4512

Miller, R. C. (1972). Notes on analysis and severe-storm forecasting procedures of the Military Weather Warning Center (Vol. 200, Air Weather Service Tech. Rept. 200, Rev.). Air Weather Service. https://apps.dtic.mil/sti/citations/AD0744042

Mo, K. C., & Higgins, R. W. (1998). Tropical Influences on California Precipitation. *Journal of Climate*, *11*(3), 412-430. https://journals.ametsoc.org/view/journals/clim/11/3/1520-0442_1998_011_0412_tiocp_2.0.co_2.xml

MTBS Data Access: Fire Level Geospatial Data. (2017, July – last revised). MTBS Project (USDA Forest Service/U.S. Geological Survey). Available online: http://mtbs.gov/direct-download. Accessed August 23, 2024

Neiman, P. J., Ralph, F. M., Wick, G. A., Lundquist, J. D., & Dettinger, M. D. (2008). Meteorological Characteristics and Overland Precipitation Impacts of Atmospheric Rivers Affecting the West Coast of North America Based on Eight Years of SSM/I Satellite Observations. *Journal of Hydrometeorology*, *9*(1), 22-47. https://doi.org/10.1175/2007JHM855.1

Neptune, C. K., Degraff, J. V., Pluhar, C. J., Lancaster, J. T., & Staley, D. M. (2021). Rainfall Thresholds for Post-Fire Debris-Flow Generation, Western Sierra Nevada, CA. *Environmental & Engineering Geoscience*, *27*(4), 439–453. https://doi.org/10.2113/EEG-D-21-00039

Nikolopoulos, E. I., Destro, E., Bhuiyan, M. A. E., Borga, M., & Anagnostou, E. N. (2018). Evaluation of predictive models for post-fire debris flow occurrence in the western United States. *Natural Hazards and Earth System Sciences*, *18*(9), 2331–2343. https://doi.org/10.5194/nhess-18-2331-2018

Oakley, N. S., Cannon, F., Munroe, R., Lancaster, J. T., Gomberg, D., & Ralph, F. M. (2018). Brief communication: Meteorological and climatological conditions associated with the 9 January 2018 post-fire debris flows in Montecito and Carpinteria, California, USA. *Natural Hazards and Earth System Sciences*, *18*(11), 3037–3043. https://doi.org/10.5194/nhess-18-3037-2018

Oakley, N. S., Lancaster, J. T., Kaplan, M. L., & Ralph, F. M. (2017). Synoptic conditions associated with cool season post-fire debris flows in the Transverse Ranges of southern California. *Natural Hazards*, *88*(1), 327–354. https://doi.org/10.1007/s11069-017-2867-6

Oakley, N. S., & Redmond, K. T. (2014). *A Climatology of 500-hPa Closed Lows in the Northeastern Pacific Ocean, 1948–2011*. *Journal of Applied Meteorology and Climatology, 53*(6), 1578-1592. https://doi.org/10.1175/JAMC-D-13-0223.1

Prein, A. F., Liu, C., Ikeda, K., Trier, S. B., Rasmussen, R. M., Holland, G. J., & Clark, M. P. (2017). Increased rainfall volume from future convective storms in the US. *Nature Climate Change*, *7*(12), 880–884. https://doi.org/10.1038/s41558-017-0007-7

Ralph, F. M., Neiman, P. J., & Wick, G. A. (2004). Satellite and CALJET Aircraft Observations of Atmospheric Rivers over the Eastern North Pacific Ocean during the Winter of 1997/98. *Monthly Weather Review*, *132*(7), 1721-1745. https://journals.ametsoc.org/view/journals/mwre/132/7/1520-0493_2004_132_1721_sacaoo_2.0.co_2.xml

Ralph, F. M., Neiman, P. J., Wick, G. A., Gutman, S. I., Dettinger, M. D., Cayan, D. R., & White, A. B. (2006). Flooding on California's Russian River: Role of atmospheric rivers. *Geophysical Research Letters*, *33*(13). https://doi.org/10.1029/2006GL026689

Refaeilzadeh, P., Tang, L., & Liu, H. (2009). Cross-Validation. In *Encyclopedia of Database Systems* (pp. 532–538). Springer, Boston, MA. https://doi.org/10.1007/978-0-387-39940-9_565

Römkens, M. J. M., Young, R. A., Poesen, J. W. A., McCool, D. K., El-Swaify, S. A., & Bradford, J. M. (1997). Soil erodibility factor (K). Compilers) In: Renard KG, Foster GR, Weesies GA, McCool DK, Yoder DC, editors. Predicting soil erosion by water: a guide to conservation planning with the Revised Universal Soil Loss Equation (RUSLE). Washington, DC, USA: Agric. HB, (703), 65-99. https://www.tucson.ars.ag.gov/unit/publications/PDFfiles/717.pdf. Accessed September, 14 2024

Rupert, M. G., Cannon, S. H., Gartner, J. E., Michael, J. A., & Helsel, D. R. (2008). Using logistic regression to predict a probability of debris flows in areas burned by wildfires, southern California, 2003-2006. In *Open-File Report* (2008–1370). U.S. Geological Survey. https://doi.org/10.3133/ofr20081370

Rutz, J. J., Steenburgh, W. J., & Ralph, F. M. (2014). Climatological Characteristics of Atmospheric Rivers and Their Inland Penetration over the Western United States. *Monthly Weather Review*, *142*(2), 905-921. https://doi.org/10.1175/MWR-D-13-00168.1

Santi, P., Cannon, S., & DeGraff, J. (2013). 13.16 Wildfire and Landscape Change. In J. F. Shroder (Ed.), *Treatise on Geomorphology* (pp. 262–287). Academic Press. https://doi.org/10.1016/B978-0-12-374739-6.00365-1

Schwartz, J. Y., Oakley, N. S., & Alessio, P. (2021). Assessment of a Post-Fire Debris Flow Impacting El Capitan Watershed, Santa Barbara County, California, U.S.A. *Environmental & Engineering Geoscience*, *27*(4), 423–437. https://doi.org/10.2113/EEG-D-21-00008

Selander, B. D., Calhoun, N., Burns, W. J., Kean, J. W., & Rengers, F. K. (2025). Assessment of western Oregon debris-flow hazards in burned and unburned environments. *Earth Surface Processes and Landforms*, *50*(4), e70045. https://doi.org/10.1002/esp.70045

Shakesby, R. A., & Doerr, S. H. (2006). Wildfire as a hydrological and geomorphological agent. *Earth-Science Reviews*, *74*(3), 269–307. https://doi.org/10.1016/j.earscirev.2005.10.006

Showalter, A. K. (1953). A Stability Index for Thunderstorm Forecasting. *Bulletin of the American Meteorological Society*, *34*(6), 250-252. https://doi.org/10.1175/1520-0477-34.6.250

Staley, D. M., Kean, J. W., Cannon, S. H., Schmidt, K. M., & Laber, J. L. (2013). Objective definition of rainfall intensity–duration thresholds for the initiation of post-fire debris flows in southern California. *Landslides*, *10*(5), 547–562. https://doi.org/10.1007/s10346-012-0341-9

Staley, D. M., Negri, J. A., Kean, J. W., Laber, J. L., Tillery, A. C., & Youberg, A. M. (2016). Updated logistic regression equations for the calculation of post-fire debris-flow likelihood in the western United States. In *Open-File Report* (2016–1106). U.S. Geological Survey. https://doi.org/10.3133/ofr20161106

Staley, D. M., Negri, J. A., Kean, J. W., Laber, J. L., Tillery, A. C., & Youberg, A. M. (2017). Prediction of spatially explicit rainfall intensity–duration thresholds for post-fire debris-flow generation in the western United States. *Geomorphology*, *278*, 149–162. https://doi.org/10.1016/j.geomorph.2016.10.019

Staley, D. M., Tillery, A. C., Kean, J. W., McGuire, L. A., Pauling, H. E., Rengers, F. K., & Smith, J. B. (2018). Estimating post-fire debris-flow hazards prior to wildfire using a statistical analysis of historical distributions of fire severity from remote sensing data. *International Journal of Wildland Fire*, *27*(9), 595. https://doi.org/10.1071/WF17122

Strobl, C., Boulesteix, A.-L., Zeileis, A., & Hothorn, T. (2007). Bias in random forest variable importance measures: Illustrations, sources and a solution. *BMC Bioinformatics*, *8*(1), 25. https://doi.org/10.1186/1471-2105-8-25

Sukup, S., Laber, J., Sweet, D., & Thompson, R. (2016). *Analysis of an Intense Narrow Cold Frontal Rainband and the Springs Fire Burn Area Debris Flows of 12 December 2014*. https://www.weather.gov/media/wrh/online_publications/Tas/TA1601.pdf

Swain, D. L., Horton, D. E., Singh, D., & Diffenbaugh, N. S. (2016). Trends in atmospheric patterns conducive to seasonal precipitation and temperature extremes in California. *Science Advances*, *2*(4), e1501344. https://doi.org/10.1126/sciadv.1501344

Tabachnick, B. G., & Fidell, L. S. (2013). *Using Multivariate Statistics*. Pearson Education.

Thomas, M. A., Kean, J. W., McCoy, S. W., Lindsay, D. N., Kostelnik, J., Cavagnaro, D. B., Rengers, F. K., East, A. E., Schwartz, J. Y., Smith, D. P., & Collins, B. D. (2023a). Postfire hydrologic response along the Central California (USA) coast: Insights for the emergency

assessment of postfire debris-flow hazards. *Landslides*. https://doi.org/10.1007/s10346-023-02106-7

Thomas, M. A., Kean, J. W., McCoy, S. W., Lindsay, D. N., Kostelnik, J., Cavagnaro, D. B., Rengers, F. K., East, A., Schwartz, J. Y., Smith, D., & Collins, B. (2023b). *Field-verified inventory of postfire hydrologic response for the 2020 CZU Lightning Complex, River, Camel, and Dolan Fires following a 26-29 January 2021 atmospheric river storm sequence* [Dataset]. U.S. Geological Survey. https://doi.org/10.5066/P91O03Y7

Thomas, M. A., Lindsay, D. N., Cavagnaro, D. B., Kean, J. W., McCoy, S. W., & Graber, A. P. (2023). The Rainfall Intensity-Duration Control of Debris Flows After Wildfire. *Geophysical Research Letters*, *50*(10), e2023GL103645. https://doi.org/10.1029/2023GL103645

Thomas, M. A., Rengers, F. K., Kean, J. W., McGuire, L. A., Staley, D. M., Barnhart, K. R., & Ebel, B. A. (2021). Postwildfire Soil-Hydraulic Recovery and the Persistence of Debris Flow Hazards. *Journal of Geophysical Research: Earth Surface*, *126*(6), e2021JF006091. https://doi.org/10.1029/2021JF006091

USDA Natural Resources Conservation Service. (2024). USA SSURGO – Erodibility Factor [Geospatial layer]. Esri Living Atlas of the World. Available online: https://www.arcgis.com/home/item.html?id=ac1bc7c30bd4455e85f01fc51055e586. Accessed August 11, 2024

USDA. (2001). Revised Universal Soil Loss Equation: RUSLE2 handbook. U.S. Department of Agriculture. https://www.nrcs.usda.gov/sites/default/files/2022-10/RUSLE2%20Handbook_0.pdf

U.S. Geological Survey. (2025). Debris flow in the 2025 Eaton Fire burn area, California. https://www.usgs.gov/media/images/debris-flow-2025-eaton-fire-burn-area-california

Woolcott, O. O. (2025). Los Angeles County in flames: Responsibilities on fire. *The Lancet Regional Health – Americas*, *42*. https://doi.org/10.1016/j.lana.2025.101005

Young, A. M., Skelly, K. T., & Cordeira, J. M. (2017). High-impact hydrologic events and atmospheric rivers in California: An investigation using the NCEI Storm Events Database. *Geophysical Research Letters*, *44*(7), 3393–3401. https://doi.org/10.1002/2017GL073077

Chapter 5

5. Sequential occurrence of fire weather and debris flow triggering rainfall in California: Implications for post-fire debris flow hazard under future climate.

Abstract

Post-fire debris flows are cascading hazards that can threaten communities, infrastructure, and ecosystems. Triggered by intense rainfall over recently burned landscapes, they depend on the temporal overlap of wildfire and precipitation, two hazards expected to shift under future climate conditions. However, little is known about how occurrence and overlap of these drivers may change, especially at spatial and temporal scales relevant to debris flow initiation. This study introduces a temporally compound event approach to evaluate the historical and projected occurrence of extreme fire-weather conditions and debris flow-triggering rainfall across California, combining fire-weather projections from 16 CMIP5 models with a convection-permitting rainfall simulation at sub-hourly resolution. Seasonal occurrence, annual event frequency and conditional probability are evaluated for historical (1990–2004) and end-of-century (2085–2099) conditions under RCP4.5 and RCP8.5. Under RCP4.5, projected changes are modest and largely uncertain, whereas under RCP8.5 both hazard components increase substantially. Post-fire debris flow frequencies exceed 1.5–2 events per year in parts of the Sierra Nevada foothills, Northern Coast Ranges, Cascades, and Klamath Mountains, where conditional probabilities indicate that nearly all extreme fire-weather events are followed by debris flow triggering rainfall within a year. Seasonal analysis further indicates a narrowing of the interval between fire-weather extremes and rainfall exceedance,

as rainfall in the cool season intensifies earlier while extreme fire-weather conditions persist into autumn, reducing the time available for post-fire recovery and emergency preparedness. These findings highlight increasing potential for sequential fire-weather and rainfall extremes across California and provide a method for assessing regional post-fire debris flow hazard under a changing climate.

5.1. Introduction

When a wildfire burns through a hillslope, it leaves behind a landscape fundamentally more susceptible to rainfall. Vegetation that once intercepted precipitation and stabilized soils is gone, infiltration capacity decreases, and overland flow accelerates. These conditions, when met with short-duration, intense rainfall, can mobilize water, sediment, and debris into fast-moving flows capable of traveling long distances downslope (Rengers & McGuire, 2021; Shakesby & Doerr, 2006). The interaction between two independent hazards, fire, which preconditions the landscape, and intense rainfall acting as trigger, defines post-fire debris flows as a cascading hazard (Kean & Staley, 2021; Tilloy et al., 2019; Yanites et al., 2025). As such, they can also be interpreted as temporally compound events because their occurrence depends on the successive interaction of two drivers (Zscheischler et al., 2020).

California's Mediterranean climate, characterized by wet winters and hot, dry summers, creates strong seasonal fuel drying that is inherently conducive to wildfire. Fire activity is shaped by climatic drivers, particularly drought and elevated Vapor Pressure Deficit (VPD), and non-climatic factors such as fire suppression history, fuel accumulation, and expanding development in fire-prone areas (Williams et al., 2015). Across the state, the importance of fire weather is expressed not only in summer fires driven by heat and drought that dry out fuels, but also in large and destructive autumn fires associated with Santa Ana winds and

delayed onset of the wet season (C. Dong et al., 2022; Goss et al., 2020; Guzman-Morales et al., 2016; Keeley et al., 2024). This seasonal range matters for post-fire hazards because it determines when burned landscapes are created relative to the first intense storms of the wet season.

Fire-prone conditions across California and the broader western United States are projected to intensify under a warmer climate. Anthropogenic increases in extreme Fire Weather Index (FWI) days have already emerged across global fire-prone regions, including Mediterranean climates, and are projected to expand as temperatures rise (Abatzoglou et al., 2018). In California specifically, projections show more days indicative of large fires, earlier seasonal onset, and fire-season extending later into the year, with Northern California facing increased potential for very large fires (Barbero et al., 2015; C. Dong et al., 2022). Behind these trends lies an increase in atmospheric aridity (Williams et al., 2019) that prolongs the window during which landscapes are vulnerable, and therefore the period during which intense rainfall events could trigger post-fire debris flows.

California's cool-season rainfall is largely delivered by landfalling atmospheric rivers (ARs), which transport large amounts of water vapor from the Pacific and produce intense precipitation when interacting with the Coastal Ranges and the Sierra Nevada (Gershunov et al., 2019). Under warming, both the intensity and character of these events are projected to change. As the atmosphere holds more moisture, precipitation rates are expected to increase, with simulations showing rises in hourly intensity that in some cases exceed Clausius–Clapeyron scaling (Huang et al., 2020; Prein et al., 2017). Future ARs are also projected to be longer, wider, and associated with stronger vapor transport, amplifying precipitation extremes even as the total number of AR events may decline slightly (Espinoza et al., 2018). Beyond

AR dynamics, climate projections suggest a sharpening of California's seasonal precipitation cycle, with a more concentrated wet season and declining precipitation during the shoulder seasons (Dong et al., 2019; Swain et al., 2018). This combination of fewer precipitation events but more intense storms implies increasing precipitation volatility across the region and a greater likelihood of high-intensity rainfall capable of triggering geomorphic hazards, particularly when storms occur over recently burned landscapes.

Recent studies have examined compound climate extremes involving wildfire and precipitation across the western United States, highlighting increasing successive occurrence of fire-prone conditions and extreme rainfall (Moftakhari & AghaKouchak, 2019; Touma et al., 2022). These contributions are valuable in establishing the compound nature of the hazard, but they rely on daily precipitation data and relatively coarse spatial resolution, limitations that are significant for debris flow science, where initiation is governed by sub-hourly rainfall intensity.

Thomas et al., (2024) addressed the rainfall side of this problem directly, employing convection-permitting simulations (~3.75 km, 15-minute output) to evaluate future exceedance of debris flow rainfall intensity–duration thresholds across the Southwest. Their results show a 2.3- to 6.5-fold increase in threshold exceedance for California under RCP 4.5 and RCP 8.5, with the Sierra Nevada, Northern Coast Ranges, and Klamath Mountains showing the strongest signal. Yet this analysis evaluates rainfall thresholds in isolation, without assessing whether exceedances could occur over landscapes recently affected by wildfire. The sequential relationship between fire and rainfall, which is what makes debris flows a cascading hazard, remains unexamined at the temporal and spatial scales governing these processes.

Here, we build on this foundation to evaluate the historical and projected sequential occurrence of fire-weather extremes and sub-hourly rainfall capable of triggering post-fire debris flows across California. Following Touma et al., (2022), we define compound events as the successive occurrence of extreme fire-weather conditions and exceedance of rainfall intensity thresholds relevant to debris flow initiation. By combining downscaled fire-weather projections from CMIP5 (Coupled Model Intercomparison Project Phase 5) models with a convection-permitting rainfall simulation at 4 km spatial and sub-hourly temporal resolution – scales rarely available in climate projections but critical for capturing the short-duration intensities that govern debris flow triggering– we assess post-fire debris flow frequency, conditional probability, and seasonal hazard occurrence for historical (1990–2004) and end-of-century (2085–2099) conditions under RCP 4.5 and RCP 8.5. These findings provide a regionally explicit picture of how the temporal relationship between these two hazards may shift under a changing climate, information directly relevant to post-fire emergency response and landscape recovery planning.

5.2. Data and methods

Fire weather conditions were characterized using the Canadian Forest Fire Weather Index (FWI; Wagner, 1987), a widely used dimensionless index representing the influence of meteorological conditions on vegetation flammability and fire risk (Jones et al., 2022). In this study, FWI was computed from daily maximum temperature, precipitation, minimum relative humidity, and surface wind speed, following previous studies (Abatzoglou et al., 2018; Bowman et al., 2017). The FWI is derived through a sequence of intermediate fuel-moisture and fire-behavior codes and can be conceptually expressed as:

$$FWI = f(ISI, BUI) \quad 5.1$$

where ISI, the Initial Spread Index, which uses the Fine Fuel Moisture Code (FFMC) and wind speed to estimate potential of fire spread, and BUI, the Buildup Index, derive from Duff Moisture Code (DMC) and Drought Code (DC) to indicate the amount of fuel available for combustion.

Meteorological inputs used to calculate daily FWI were obtained from 16 downscaled global climate models (Table A0.1) from the MACAv2-METDATA dataset (Abatzoglou & Brown, 2012), which provides statistically downscaled climate projections at 4 km spatial resolution across the conterminous United States, making it well suited for regional analyses of wildfire activity and associated hydrologic hazards. Extreme fire-weather days were identified as days on which daily FWI exceeded the grid-cell's historical 99.9^{th}-percentile FWI value, which was then applied to both future periods to identify projected extreme fire-weather events (Figure 5.1). This high percentile threshold was selected to focus on rare, extreme fire-weather conditions while maintaining consistency with previous studies that define extreme fire weather using the upper tail of the FWI distribution. Because this analysis uses fire weather as a proxy for fire-conducive conditions and does not explicitly model ignition, fuel continuity, or burned area, the 99.9th-percentile threshold helps avoid classifying broadly favorable but less extreme days as fire-weather events. Although this choice may exclude some moderately elevated fire-weather conditions, it is appropriate for isolating the most extreme atmospheric conditions relevant to consequential post-fire hazard. Consecutive exceedance days were grouped into a single fire-weather event, such that a new event began only after at least one non-exceedance day. Event timing was assigned to the first identified exceedance day. A sensitivity analysis using the 99th percentile threshold yielded similar

spatial patterns but smaller relative changes in event frequency. Therefore, the 99.9th percentile was retained as it better captured the magnitude of changes in extreme fire-weather conditions.

Rainfall exceedances relevant to post-fire debris flow initiation were characterized following the statewide approach in Thomas et al., (2024), using convection-permitting climate simulations dynamically downscaled with the Weather Research and Forecasting model (WRF), at 3.75 km horizontal grid spacing and 15-minute temporal resolution. Boundary conditions were obtained from the National Center for Atmospheric Research Community Earth System Model (CESM). These 15-minute WRF–BCC (Weather Research and Forecasting Model–Bias Corrected Community Earth System Model) rainfall simulations were available for historical, RCP4.5, and RCP8.5 conditions (Gensini et al., 2023). CCSM4, a predecessor of the CESM2 model used in the rainfall analysis, was not included in the fire-weather ensemble because MACAv2-METDATA does not provide minimum relative humidity for this model, a variable required to compute FWI.

The statewide method consisted of identifying rainfall exceedances at each grid cell by selecting all events exceeding the minimum value of the historical annual maximum series (Dunne & Leopold, 1978; Edwards et al., 2019). A power-law curve was fitted to these exceedances to derive 1-year recurrence-interval rainfall thresholds, an interval that closely corresponds to rainfall intensities associated with debris flow triggering storms in California (Staley et al., 2020). Historically derived thresholds were applied to both future periods, so changes in exceedance frequency reflect shifts in rainfall intensity rather than changes in the threshold itself. Thresholds were applied exclusively in mountainous terrain, identified using

Sayre (2022) topographic data, reflecting the terrain conditions under which post-fire debris flows predominantly initiate.

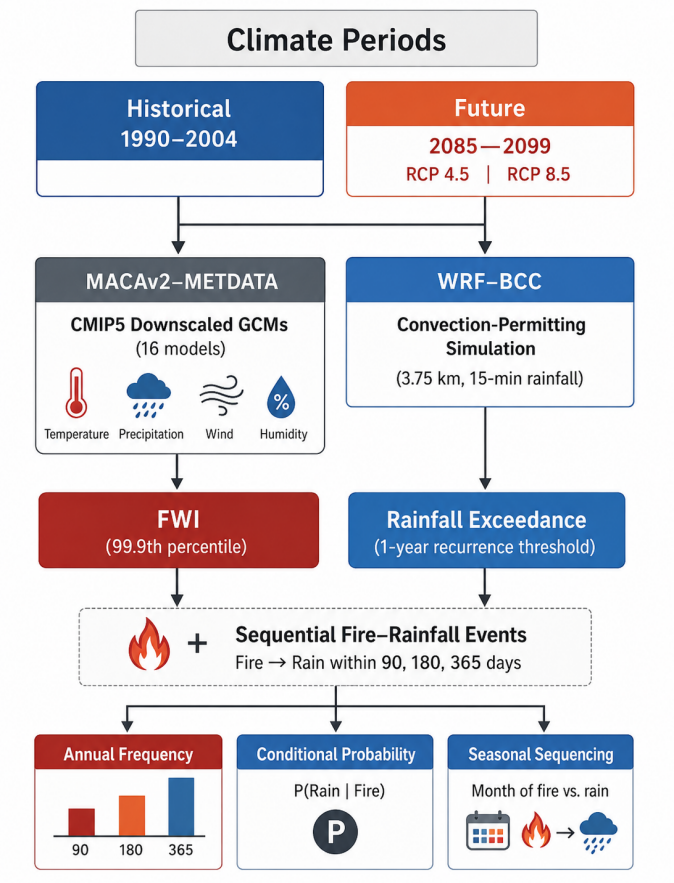


Figure 5.1. Schematic overview of the analytical framework used to evaluate sequential extreme fire weather–rainfall events across California for historical (1990–2004) and end-of-century (2085–2099) conditions under RCP 4.5 and RCP 8.5.

To evaluate the meteorological conditions relevant to post-fire debris flow hazard, we analyzed two hazard drivers, extreme fire weather and rainfall exceedances, both individually and in sequence. We quantified the annual frequency and seasonal distribution of each driver during the historical and future periods. For each grid cell, annual event counts were averaged over each analysis period to obtain mean annual frequency. For extreme fire weather, these values were then averaged across the 16 model realizations to calculate the multi-model mean. To characterize seasonality, event dates were converted to day-of-year and aggregated into

daily climatologies for each analysis period and scenario. A harmonic analysis was then applied using the first three harmonics of the annual cycle to smooth short-term variability while preserving the dominant seasonal cycle and secondary seasonal features. The reconstructed harmonic series was used to identify the approximate month or seasonal window when event occurrence was greatest and to assess whether events were concentrated within a narrow seasonal peak or distributed across a broader portion of the year.

The temporal sequencing of these hazards was then evaluated to represent potential post-fire debris flow conditions, defined as an extreme fire-weather event followed by a 15-minute rainfall exceedance capable of triggering debris flows. For each grid cell and model realization, a forward search was conducted from each extreme fire-weather event to identify whether at least one rainfall exceedance occurred within three time windows following Touma et al., (2022): 90 days, 180 days, and 365 days. These windows capture the period of elevated post-fire debris flow susceptibility, which typically persists for up to one year following wildfire (Kean & Staley, 2021). Rainfall exceedance was regridded from the native 3.75 km WRF grid to the 4 km MACAv2-METDATA grid using nearest-neighbor resampling for use in the forward search.

Using this framework, we quantified annual frequency and the conditional probability that extreme fire weather is followed by at least one rainfall exceedance, as well as the seasonal distribution of events based on the month of fire-weather occurrence and subsequent rainfall. Conditional probability is defined as (Equation 5.2):

$$P\ (R_w \mid F)_i = \frac{N_{F \to R,w}(i)}{N_F(i)} \qquad 5.2$$

Where $P\ (R_w \mid F)_i$ is the conditional probability that an extreme fire-weather event at grid cell i is followed by at least one rainfall exceedance within w days, $N_F(i)$ is the total number of extreme fire-weather events, and $N_{F \to R,w}(i)$ is the number of those events followed by at least one rainfall exceedance within the specified window.

Statistical significance was evaluated using nonparametric tests appropriate to the structure of each dataset. For rainfall exceedances, annual exceedance counts in the historical and future periods were compared at each grid cell using a Mann–Whitney U test. Because rainfall was derived from a single convection-permitting simulation, significance reflects differences between periods within that simulation rather than ensemble robustness. For extreme fire-weather frequency and compound metrics derived from the multi-model ensemble, paired historical and future values were compared at each grid cell using a Wilcoxon signed-rank test. Projected changes were considered robust where at least two-thirds of models agreed on the sign of change.

5.3. Results

Historically (1990–2004), extreme fire-weather events defined by the 99.9th percentile FWI threshold were rare across California, with a statewide mean of approximately 0.14 events per year and reaching up to 0.4 in localized mountainous regions (Figure 5.2a). By end of century (2085–2099), projected frequencies increase substantially across much of the state, especially under RCP8.5, with several areas reaching approximately 2–2.9 events per year, particularly in the Sierra Nevada foothills, southern Cascades and parts of the Northern Coast Ranges and Klamath Mountains (Figure 5.2c). Under RCP4.5, projected increases are more modest and spatially heterogeneous, with many regions reaching approximately 1–2 events per year, though model agreement is lower, and changes are less spatially consistent than

under RCP8.5 (Figure 5.2b). The largest increases occur in mountainous regions of northern and eastern California, where model agreement is generally strong and projected changes are significant across much of the domain. Smaller increases and lower model agreement are evident along parts of the coast and in southern California.

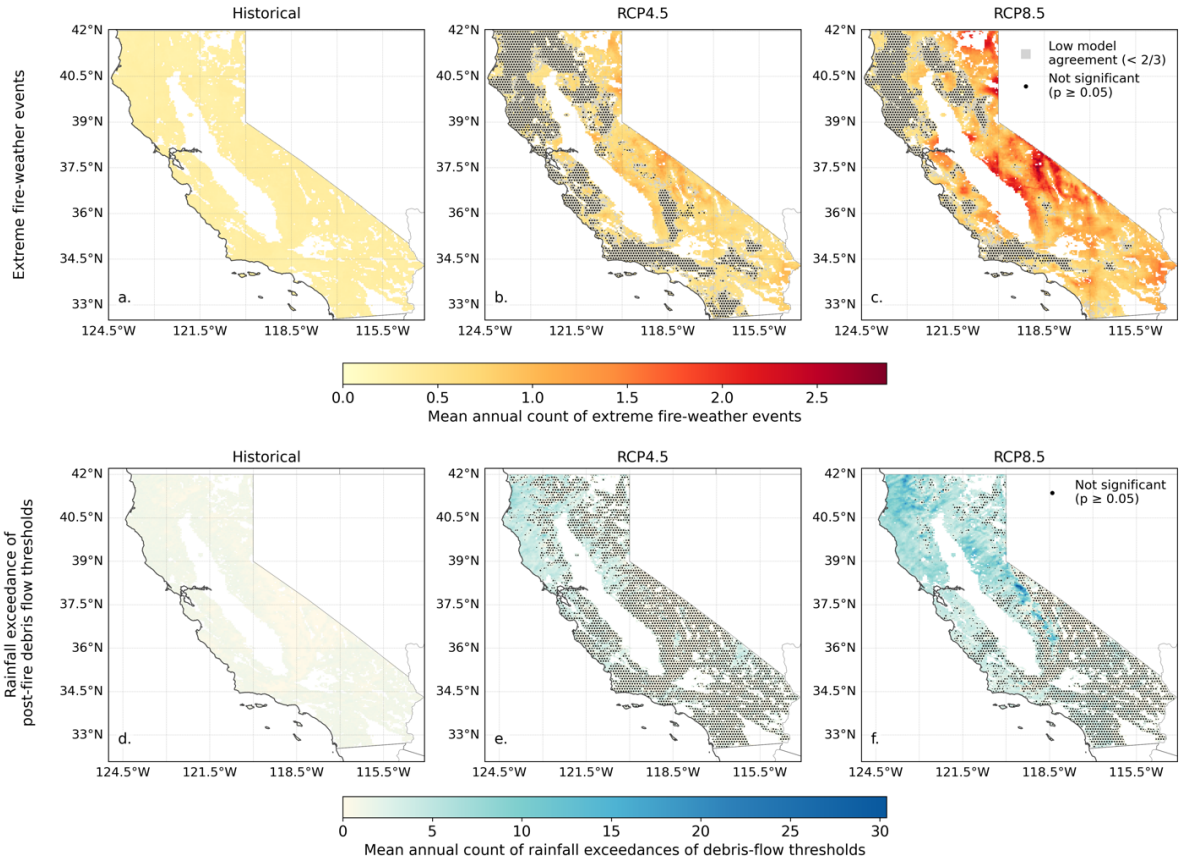


Figure 5.2. Spatial distribution of mean annual counts of extreme fire-weather events (top row) and rainfall exceedances of the historical 1-year recurrence threshold (bottom row) across California for the historical period (1990–2004) and end-of-century projections (2085–2099) under RCP4.5 and RCP8.5. Extreme fire-weather events are defined using the grid-cell-specific 99.9th-percentile FWI threshold. Rainfall exceedances are derived from 15-minute convection-permitting WRF simulations using thresholds based on the historical annual maximum series.

Rainfall exceedances of the historical 1-year recurrence-interval threshold were also relatively infrequent across California, with most of the state experiencing fewer than 1.9 exceedances per year (Figure 5.2d). By end of century, exceedance frequency increases across

much of the state under both scenarios, with the largest increases concentrated in the Klamath Mountains, Sierra Nevada, and Northern Coast Ranges. Under RCP8.5, exceedance frequencies reach up to 30 events per year in some mountainous areas, whereas under RCP4.5 increases are smaller and generally remain below about 11 exceedances per year across most of northern California (Figure 5.2e). In southern California, projected changes are comparatively limited and are non-significant across much of the region. These spatial patterns are consistent with Thomas et al., (2024), which identified the same mountainous regions as showing the strongest increases in rainfall capable of triggering post-fire debris flows. As these results are derived from a single convection-permitting simulation, they reflect one realization of possible future rainfall changes rather than a model-ensemble estimate.

To examine seasonal timing, we analyzed the harmonic reconstructions of extreme fire-weather events and rainfall exceedances based on day-of-year climatologies (Figure 5.3). extreme fire-weather events are concentrated from late spring through early autumn and exhibit a broad bimodal structure, with peaks in early summer and again in autumn, the latter consistent with autumn wind-driven fire activity in California. In contrast, rainfall exceedances are concentrated during the cool season, with highest occurrence rates from approximately November through February. The two hazards are therefore separated seasonally, with the transition from fire-weather-dominated to rainfall-dominated conditions occurring in early autumn.

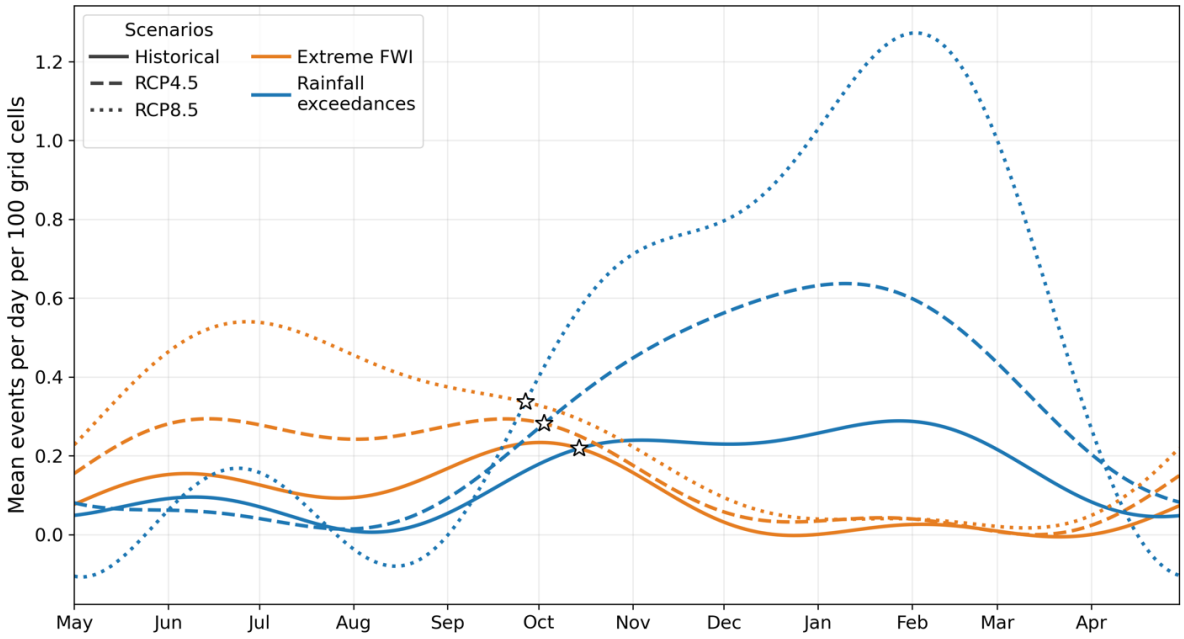


Figure 5.3. Seasonal cycle of extreme fire-weather events (orange) and rainfall exceedances (blue) across California for historical (1990–2004), RCP4.5, and RCP8.5 (2085–2099) conditions. Curves are based on day-of-year climatologies and were reconstructed using the first three harmonics of the annual cycle. Fire-weather curves represent the multi-model mean across the 16 MACA realizations, whereas rainfall exceedance curves reflect the single convection-permitting WRF simulation. Values are expressed as events per day per 100 grid cells (~16,000 km² at model resolution). Star symbols indicate the first overlap between the extreme fire-weather and rainfall exceedance curves, an approximate indicator of the transition from fire-weather to rainfall season.

Under both future scenarios, this seasonal structure is largely preserved but the magnitude of both hazards increases. Extreme fire-weather events intensify under both RCP4.5 and RCP8.5, with the largest increases occurring in early summer. At the seasonal peaks, RCP4.5 is approximately 1.3 times historical levels in autumn and nearly 2 times historical levels in early summer, whereas RCP8.5 reaches about 2.2 times historical levels in autumn and more than 3 times historical levels in early summer. Rainfall exceedances intensify even more strongly during the cool season, primarily between November and February, with peak winter occurrence approximately doubling under RCP4.5 and increasing by more than a factor of 4 under RCP8.5 relative to historical levels.

While most models agree on the sign and general timing of these changes, inter-model spread increases considerably under future scenarios, particularly under RCP8.5, as reflected in the wider ±1 standard deviation envelope (Figure A1). Under RCP4.5, most models retain the historical bimodal structure, though the autumn peak becomes less distinct in several instances. Under RCP8.5, inter-model differences become more pronounced, with some models showing a single dominant summer peak while others retain a weaker bimodal pattern closer to historical levels. This growing spread indicates increasing uncertainty not only in the magnitude of extreme fire-weather occurrence, but also in its seasonal distribution under higher emissions.

The seasonal transition between extreme fire weather and rainfall exceedances shifts earlier under future warming, from mid-October historically to early October under RCP4.5 and late September under RCP8.5. This shift reduces the time between late season fire weather extremes and the onset of intense rainfall capable of triggering post-fire debris flows, leaving less time for burned areas to recover before the early storms of the wet season.

The annual frequency of compound events was defined as the occurrence of an extreme fire-weather event followed by one rainfall exceedance within 90-, 180-, or 365-day windows. During the historical period, these events remained uncommon across California under all three windows (Figure 5.4), with the highest frequencies occurring for the longer 180- and 365-day windows (< 0.3 events per year) and the lowest frequencies for the 90-day window (< 0.2 events per year; Figure 5.4a).

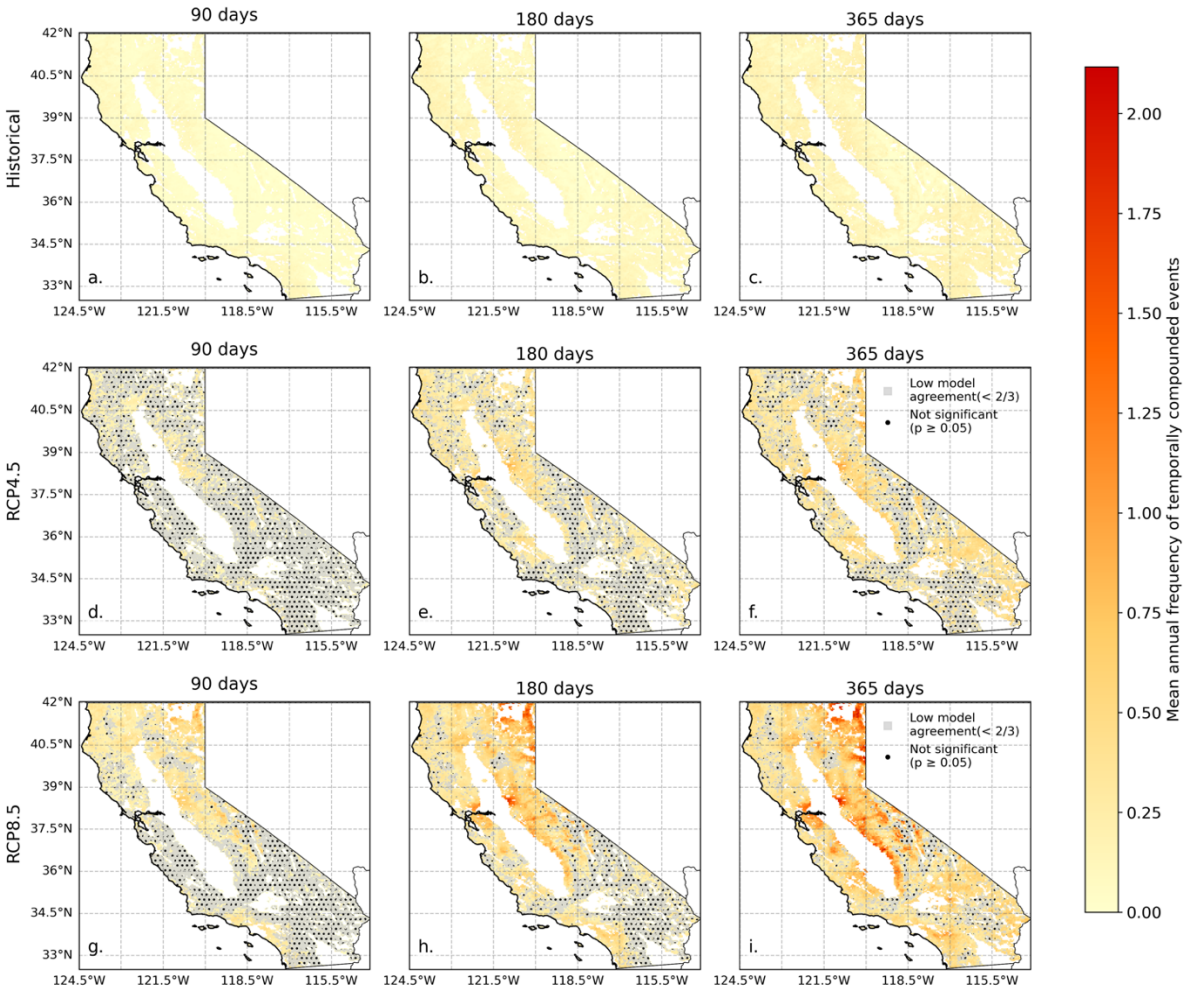


Figure 5.4. Mean annual frequency of temporally compound events across California, defined as an extreme fire-weather event followed by at least one rainfall exceedance within 90- (a.,d.,g.), 180- (b.,e.,h.), and 365-day windows (c.,f.,i.). Columns show the three post-fire search windows, and rows show historical (1990–2004), RCP4.5, and RCP8.5 (2085–2099) conditions. Values represent the multi-model mean across the 16 MACA realizations. Gray shading indicates regions of low model agreement, where fewer than two-thirds of models agree on the sign of change relative to the historical period. Stippling denotes areas where projected changes are not statistically significant based on a Wilcoxon signed-rank test ($p \geq 0.05$).

Under RCP4.5, projected increases are modest and spatially heterogeneous. Frequencies in parts of the Sierra Nevada foothills and Cascades reach approximately 0.5–1 event per year for the 180- and 365-day windows (Figure 5.4f), but large portions of the state show low model agreement and non-significant changes, indicating limited confidence in the spatial

extent of these increases under moderate warming. Under RCP8.5, increases are larger and more spatially coherent, particularly for the 180- and 365-day windows, where multi-model mean frequencies exceed about 1.5 events per year and approach 2 events per year in the Northern Coast Ranges, Sierra Nevada foothills, and parts of the southern Cascades (Figure 5.4h,i). In southern California and Klamath Mountains, increases are generally smaller and accompanied by lower model agreement. Projected changes in frequency are strongly dependent on the length of the post-fire search window. Across both future scenarios, longer windows produce higher frequencies and broader areas of increase, reflecting the greater likelihood that at least one rainfall exceedance occurs following an extreme fire-weather event as the accumulation period expands.

While the frequency of temporally compound events reflects the total number of sequential fire–rainfall events, it does not indicate the likelihood that a given extreme fire-weather event is followed by debris flow-triggering rainfall. To address this, we evaluated the conditional probability that at least one rainfall exceedance occurs within 90-, 180-, and 365-day windows following an extreme fire-weather event (Figure 5.5). Historically, this probability is already relatively high across northern California and the Coast Ranges, particularly for the longer accumulation windows, with values commonly reaching 0.6–0.9 (Figure 5.5c). As expected, probabilities increase systematically with window length, with the 365-day window yielding the highest values across all scenarios.

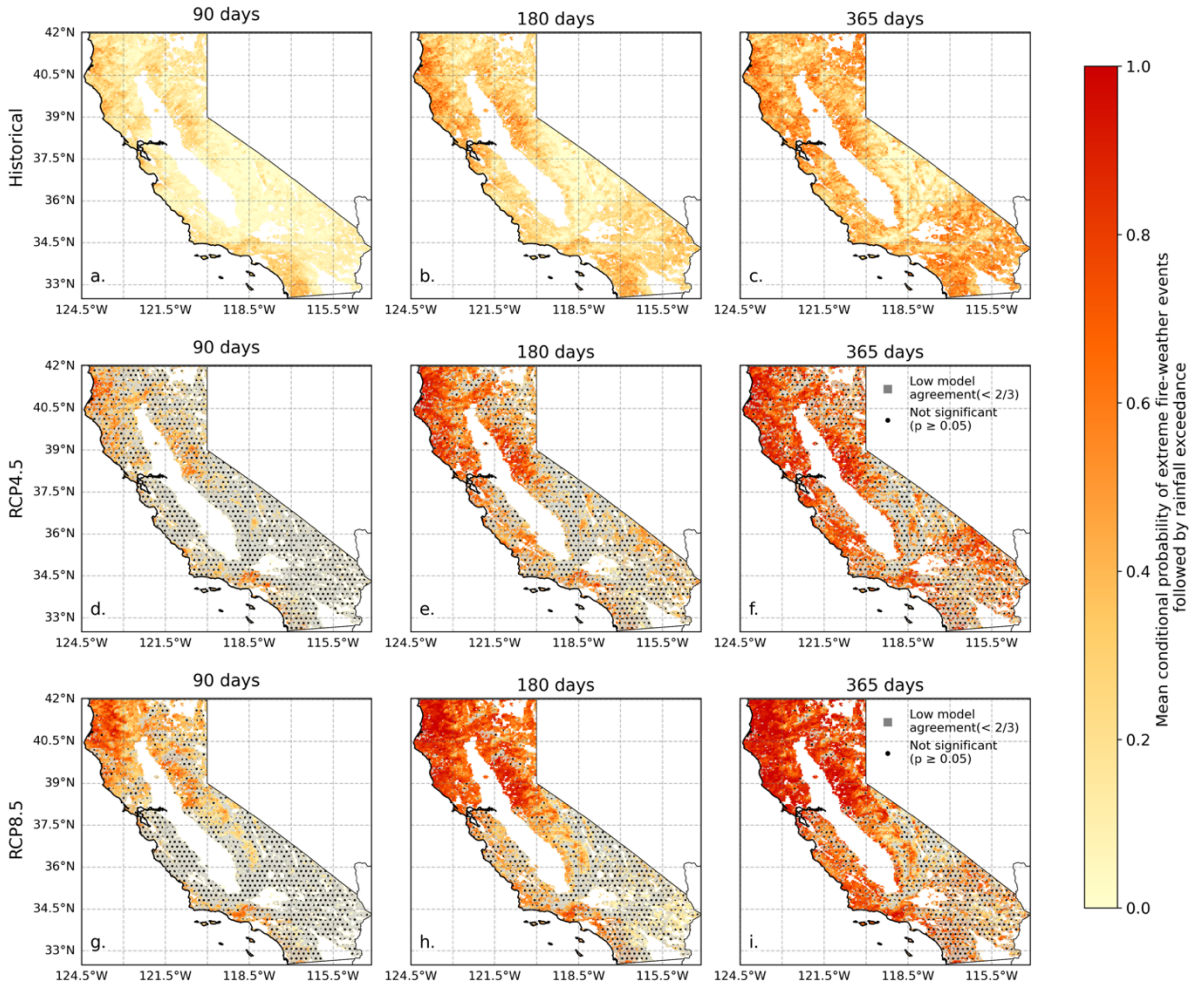


Figure 5.5. Conditional probability that an extreme fire-weather event is followed by at least one rainfall exceedance across California within 90- (a.,d.,g.), 180- (b.,e.,h.), and 365-day windows (c.,f.,i.) for historical (1990–2004), RCP4.5, and RCP8.5 (2085–2099) conditions. Values represent the multi-model mean conditional probability across the 16 MACA realizations. Gray shading indicates low model agreement (<2/3 of models agreeing on the sign of change), and stippling indicates projected changes that are not statistically significant ($p \geq 0.05$; Wilcoxon signed-rank test).

Under RCP4.5, conditional probabilities increase across much of the state, with values approaching 0.9–1.0 in parts of the Klamath Mountains, Sierra Nevada, and portions of southern California (Figure 5.5f). However, low model agreement and non-significant changes remain widespread, indicating limited robustness under moderate warming. Under RCP8.5, the Klamath Mountains, Sierra Nevada, and Northern Coast Ranges, show

conditional probabilities for the 365-day window approaching 1.0, suggesting that nearly every extreme fire-weather event is projected to be followed by at least one rainfall exceedance within a year (Figure 5.5i). Southern California also shows notable increases, especially for the 180- and 365-day windows, although model agreement remains lower than in northern California. Projected increases are also evident for the 90-day window under RCP8.5, particularly in the Klamath Mountains and parts of Southern California (Figure 5.5g).

The monthly distribution of compound events is strongly seasonal, with very low frequencies during late spring and summer and a marked increase beginning in autumn (Figure 5.6). Across all scenarios and search windows, frequencies are highest from October through February, with a clear maximum in November and elevated values persisting through midwinter. The monthly distribution also varies with the length of the post-fire search window. For the 90-day window, compound events are concentrated most strongly in October and November (Figure 5.6a), whereas the 180- and 365-day windows show larger winter frequencies, particularly in January and February (Figure 5.6c). This pattern indicates that shorter search windows emphasize more immediate fire-rainfall succession in autumn, while longer windows include more events extending from late season fire weather into the following wet season.

Under RCP4.5, frequencies increase modestly across most months, with the largest increases occurring from October through January. Under RCP8.5, increases are substantially larger, with the strongest enhancement in October and November, as well as in February, particularly for the 180- and 365-day windows. October also exhibits the strongest relative increase compared with historical conditions. These changes are consistent with a reduced

seasonal separation between extreme fire weather and rainfall exceedance under future warming.

Although absolute frequencies remain low, events also increase modestly in July and August under RCP8.5. This suggests that conditions favorable for sequential fire-rainfall hazard may increasingly arise during the active fire season itself, although such events remain much less frequent than those occurring in autumn and winter.

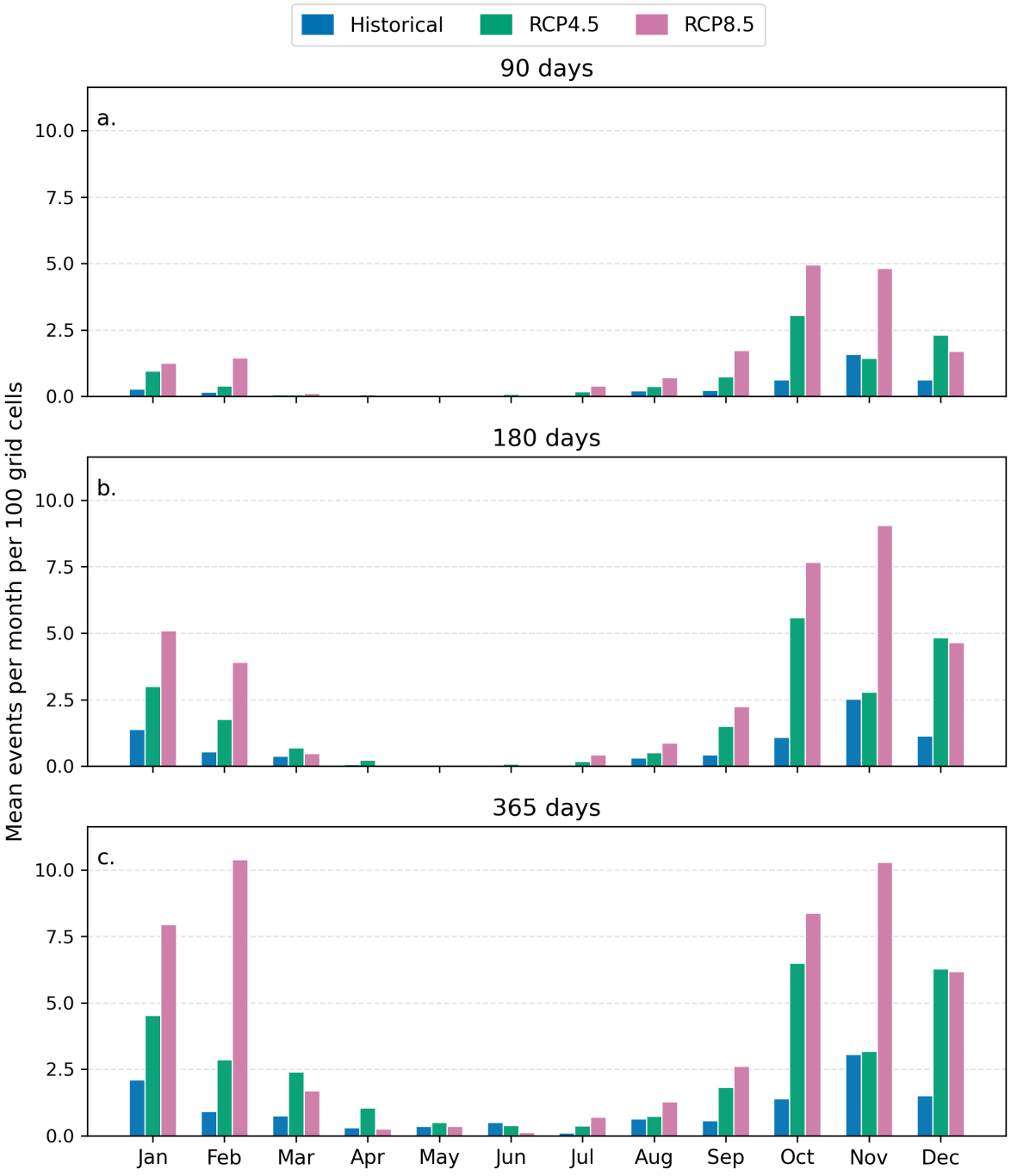


Figure 5.6. Monthly distribution of compound events across California occurring within **a.** 90-, **b.** 180- and **c.** 365-day windows after extreme fire-weather conditions under historical (1990–2004), RCP4.5, and RCP8.5 (2085–2099). Bars show the multi-model mean number of events per month per 100 grid cells (approximately 16,000 km² at model resolution), averaged across all years within each period.

Overall, projected changes under RCP4.5 are modest and largely characterized by low model agreement and statistical non-significance across most metrics, suggesting limited confidence in compound hazard intensification under moderate warming. Under RCP8.5, both individual hazard components and their sequential occurrence increase substantially and robustly across the Cascades, Sierra Nevada foothills, Northern Coast Ranges, the Klamath Mountains, and parts of southern California, with annual event frequencies, conditional probabilities, and seasonal overlap all pointing toward an intensification of post-fire debris flow hazard conditions by end of century.

5.4. Discussion

The projected increases in compound fire-rainfall event frequency identified here are broadly consistent with prior analyses across the western United States. Using large-ensemble climate simulations and LOCA-based projections, Touma et al., (2022) and Moftakhari & AghaKouchak (2019) reported that sequential fire-rainfall events may increase by up to a factor of two by end of century, with the largest increases occurring in northern portions of the domain, including the Cascade Ranges. The present results show a similar spatial pattern, with the strongest increases concentrated in northern mountainous regions of California.

In addition, Touma et al., (2022) reported that approximately two-thirds of extreme fire-weather events may be followed by extreme rainfall within one year under future conditions, while Moftakhari & AghaKouchak (2019) estimated corresponding probabilities of approximately 68% under RCP4.5 and 73% under RCP8.5. However, these comparisons should be interpreted cautiously because event definitions, spatial domains, and temporal windows differ among studies. In particular, prior analyses relied on coarser resolution for precipitation data, whereas the present study defines rainfall exceedance using the statewide

threshold framework of Thomas et al., (2024), providing a representation of rainfall conditions more closely aligned with post-fire debris flow triggering thresholds.

Beyond increases in overall event frequency, the analysis of the seasonal cycle indicates a shift in the temporal relationship between extreme fire-weather conditions and rainfall exceedances that may heighten post-fire debris flow hazard potential. Historically, extreme fire-weather and debris flow triggering rainfall occupy largely distinct seasonal windows, with extreme fire-weather peaking during summer and rainfall exceedances concentrated in the cool season beginning in mid-October. This separation allows several months between the occurrence of fire-conducive conditions and the onset of intense rainfall. Under RCP8.5, however, rainfall exceedances begin to intensify earlier, in September, while extreme fire-weather conditions persist into early autumn, narrowing the interval between the two hazards. This seasonal compression is consistent with projections of a sharper precipitation regime in California under continued warming (Swain, 2021), which could exacerbate wildfire activity and shorten the interval between major fires and the onset of rainfall (Oakley, 2021).

This shortening is important because burned landscapes are typically most susceptible to runoff-driven erosion and debris flow initiation in the months immediately following fire. Vegetation regrowth and soil-hydraulic recovery often require several years, depending on burn severity and antecedent conditions (Ebel et al., 2022; Graber et al., 2023; Santi et al., 2013). As the interval between fire weather and intense rainfall contracts, the chance that rainfall capable of triggering debris flows will occur while burned terrain remains susceptible, increases. This is particularly relevant in settings where late season fire activity already occurs close to the onset of the wet season, such as southern California under Santa Ana winds conditions. The consequences may be amplified by the nonlinear sensitivity of debris flow

response to rainfall intensity as Kean & Staley (2021) showed that an 18% future increase in rainfall intensity could produce a 110% increase in the probability of major debris flows in southern California. In addition to increasing physical susceptibility, a shorter fire-rainfall interval may also constrain post-fire emergency response by reducing the time available for preparedness measures, including debris flow early warning programs, road closure implementation, and evacuation planning, before the arrival of the first intense storms.

The results also suggest that conditions conducive to post-fire debris flow triggering may increasingly extend beyond the traditional cool-season window, as sequential events become more common between July and September under RCP8.5. In California, fall and winter debris flows are commonly associated with landfalling atmospheric rivers and strong orographic precipitation (Oakley et al., 2017), whereas summer events are more often linked to convective storms associated with the North American Monsoon, tropical cyclones, or isolated thunderstorms (Oakley et al., 2025). Although projected summer event frequencies remain low in absolute terms relative to cool-season months, their increase indicates a growing seasonal overlap between extreme fire-weather conditions and rainfall exceedance. This shift may have practical implications because post-fire warning and response systems in California have historically focused on cool-season storm impacts. The occurrence of summer sequential events is also consistent with recent observations of post-fire debris flows during summer in California (Felling et al., 2019; Graber, 2023; McGuire et al., 2018; Thomas et al., 2023). Nevertheless, the future evolution of these summer events remains uncertain. Although global and convection-permitting models suggest declines in mean North American Monsoon precipitation, they also project increases in extreme precipitation intensity (Pascale et al., 2019; Wallace & Minder, 2024). Whether these contrasting changes translate into more

frequent or more significant summer rainfall capable of triggering post-fire debris flows remains an open question and warrants further investigation.

A key limitation of this study is the use of extreme fire-weather conditions, rather than explicit fire occurrence, burned area, or burn severity, as a proxy for wildfire activity. Although the FWI is widely used to characterize atmospheric conditions conducive to fire and has been shown to correlate with wildfire activity in many regions (Abatzoglou et al., 2018; Goss et al., 2020), it does not represent whether ignitions actually occur, how large fires become, what vegetation burns, or the severity of burning. These factors are especially important for post-fire debris flow hazard, which depends strongly on burn severity and its influence on soil hydrophobicity, vegetation loss, runoff generation, and sediment mobilization. Post-fire debris flow occurrence is also controlled by factors not represented in this framework, including sediment availability and soil erodibility (Staley et al., 2017). Accordingly, the metrics for compound events presented here should be interpreted as indicators of conditions favorable for post-fire debris flow hazard, rather than as probabilistic predictions of debris flow occurrence. Incorporating fire occurrence, burned area, and burn severity into future applications of this framework would allow a more physically complete representation of post-fire hazard under climate change.

A second limitation arises from the asymmetry between the fire-weather and rainfall components of the analysis. Fire weather was derived from a 16-model ensemble, which allows some assessment of robustness across climate model realizations, whereas rainfall exceedances were derived from a single convection-permitting WRF-BCC simulation. As a result, uncertainty in projected rainfall exceedances is less fully characterized than uncertainty in projected fire weather, and the rainfall contribution to the sequential hazard signal should

therefore be interpreted more cautiously. In addition, although the 4 km analysis grid represents relatively high spatial resolution for climate-scale hazard assessments, post-fire debris flow processes operate at watershed, channel, and hillslope scales that are often much finer, on the order of tens to hundreds of meters (Kean et al., 2011).This scale mismatch does not diminish the value of the patterns identified in this study, however, the results are more informative for regional hazard assessment than for site-specific triggering conditions. Addressing this limitation will require larger ensembles of convection-permitting simulations and higher-resolution modeling frameworks capable of resolving terrain controls on runoff generation and sediment transport more explicitly.

Finally, an additional source of uncertainty is the relatively short historical baseline used to define thresholds and seasonal climatologies. Because the analysis emphasizes extreme fire-weather conditions (percentile 99.9) and short-duration rainfall extremes, threshold estimates may be sensitive to sampling variability in the historical period. This choice was constrained by the overlap of the available climate datasets, but a longer baseline could yield different local thresholds and event frequencies. Future work could examine the sensitivity of these results to alternative baseline periods and threshold definitions.

5.5. Conclusions

This study introduces a temporally compound event framework to evaluate the historical and projected sequential occurrence of extreme fire-weather conditions and debris flow-triggering rainfall across California. By combining a multi-model ensemble of fire-weather projections with convection-permitting rainfall simulations at sub-hourly resolution, the analysis extends prior compound hazard studies to spatial and temporal scales more relevant to debris flow initiation. Both hazard components intensify substantially under RCP8.5, with

the largest and most robust increases occurring in the Sierra Nevada, and Northern Coast Ranges, Cascades Ranges and Klamath Mountains, where extreme fire-weather events are projected to be followed by debris flow triggering rainfall within a year with very high probability. Under RCP4.5, changes are smaller and generally less robust, highlighting the strong sensitivity of compound hazard to emissions trajectory.

Beyond changes in frequency, the seasonal analysis indicates a progressive shortening of the interval between extreme fire-weather conditions and rainfall exceedance, as cool-season rainfall intensifies earlier while fire-weather conditions persist into autumn. This shift increases the likelihood that intense rainfall will occur while recently burned landscapes remain susceptible, with potential implications for post-fire preparedness and emergency response.

These results suggest that sequences of fire-weather and rainfall conditions conducive to post-fire hazard may become more frequent and more closely timed under continued warming, particularly under high emissions. Although the framework presented here is not a direct forecast of debris flow occurrence, it provides a informed basis for identifying where and when climatic conditions favorable to these sequences may become more common at regional scale, and it offers a foundation for future work aimed at strengthening adaptation and resilience in fire-prone landscapes.

5.6. References

Abatzoglou, J. T., & Brown, T. J. (2012). A comparison of statistical downscaling methods suited for wildfire applications. *International Journal of Climatology*, *32*(5), 772–780. https://doi.org/10.1002/joc.2312

Abatzoglou, J. T., Williams, A. P., Boschetti, L., Zubkova, M., & Kolden, C. A. (2018). Global patterns of interannual climate–fire relationships. *Global Change Biology*, *24*(11), 5164–5175. https://doi.org/10.1111/gcb.14405

Barbero, R., Abatzoglou, J. T., Larkin, N. K., Kolden, C. A., & Stocks, B. (2015). Climate change presents increased potential for very large fires in the contiguous United States. *International Journal of Wildland Fire*, *24*(7), 892–899. https://doi.org/10.1071/WF15083

Bowman, D. M. J. S., Williamson, G. J., Abatzoglou, J. T., Kolden, C. A., Cochrane, M. A., & Smith, A. M. S. (2017). Human exposure and sensitivity to globally extreme wildfire events. *Nature Ecology & Evolution*, *1*(3), 0058. https://doi.org/10.1038/s41559-016-0058

Dong, C., Williams, A. P., Abatzoglou, J. T., Lin, K., Okin, G. S., Gillespie, T. W., Long, D., Lin, Y.-H., Hall, A., & MacDonald, G. M. (2022). The season for large fires in Southern California is projected to lengthen in a changing climate. *Communications Earth & Environment*, *3*(1), 22. https://doi.org/10.1038/s43247-022-00344-6

Dong, L., Leung, L. R., Lu, J., & Song, F. (2019). Mechanisms for an Amplified Precipitation Seasonal Cycle in the U.S. West Coast under Global Warming. *Journal of Climate*, *32*(15), 4681-4698. https://doi.org/10.1175/JCLI-D-19-0093.1

Dunne, T. & Leopold, L.B. (1978). *Water in Environmental Planning*. W.H. Freeman and Company, San Francisco, California

Ebel, B. A., Wagenbrenner, J. W., Kinoshita, A. M., & Bladon, K. D. (2022). Hydrologic recovery after wildfire: A framework of approaches, metrics, criteria, trajectories, and timescales. *Journal of Hydrology and Hydromechanics*, *70*(4), 388–400. https://doi.org/10.2478/johh-2022-0033

Edwards, P. J., Watson, E. A., & Wood, F. (2019). Toward a Better Understanding of Recurrence Intervals, Bankfull, and Their Importance. *Journal of Contemporary Water Research & Education*, *166*(1), 35–45. https://doi.org/10.1111/j.1936-704X.2019.03300.x

Espinoza, V., Waliser, D. E., Guan, B., Lavers, D. A., & Ralph, F. M. (2018). Global Analysis of Climate Change Projection Effects on Atmospheric Rivers. *Geophysical Research Letters*, *45*(9), 4299–4308. https://doi.org/10.1029/2017GL076968

Felling, G., Myers, A., & McCoy, S. W. (2019). *Post-fire debris-flow hazard analysis for Interstate 80, Truckee River Canyon, near the California-Nevada state line, USA.* https://repository.mines.edu/server/api/core/bitstreams/9d5f5165-27bf-44c3-9593-7d1a6a322797/content

Gensini, V. A., Haberlie, A. M., & Ashley, W. S. (2023). Convection-permitting simulations of historical and possible future climate over the contiguous United States. *Climate Dynamics*, *60*(1), 109–126. https://doi.org/10.1007/s00382-022-06306-0

Gershunov, A., Shulgina, T., Clemesha, R. E. S., Guirguis, K., Pierce, D. W., Dettinger, M. D., Lavers, D. A., Cayan, D. R., Polade, S. D., Kalansky, J., & Ralph, F. M. (2019). Precipitation regime change in Western North America: The role of Atmospheric Rivers. *Scientific Reports*, *9*(1), 9944. https://doi.org/10.1038/s41598-019-46169-w

Goss, M., Swain, D. L., Abatzoglou, J. T., Sarhadi, A., Kolden, C. A., Williams, A. P., & Diffenbaugh, N. S. (2020). Climate change is increasing the likelihood of extreme autumn wildfire conditions across California. *Environmental Research Letters*, *15*(9), 094016. https://doi.org/10.1088/1748-9326/ab83a7

Graber, A. P. (2023). *Compilation of runoff-generated debris-flow inventories for 17 fires across Arizona, California, Colorado, New Mexico, and Washington, USA* [Dataset]. U.S. Geological Survey. https://doi.org/10.5066/P98Q4CDH

Graber, A. P., Thomas, M. A., & Kean, J. W. (2023). How Long Do Runoff-Generated Debris-Flow Hazards Persist After Wildfire? *Geophysical Research Letters*, *50*(19), e2023GL105101. https://doi.org/10.1029/2023GL105101

Guzman-Morales, J., Gershunov, A., Theiss, J., Li, H., & Cayan, D. (2016). Santa Ana Winds of Southern California: Their climatology, extremes, and behavior spanning six and a half decades. *Geophysical Research Letters*, *43*(6), 2827–2834. https://doi.org/10.1002/2016GL067887

Huang, X., Swain, D. L., & Hall, A. D. (2020). Future precipitation increase from very high resolution ensemble downscaling of extreme atmospheric river storms in California. *Science Advances*, *6*(29), eaba1323. https://doi.org/10.1126/sciadv.aba1323

Jones, M. W., Abatzoglou, J. T., Veraverbeke, S., Andela, N., Lasslop, G., Forkel, M., Smith, A. J. P., Burton, C., Betts, R. A., van der Werf, G. R., Sitch, S., Canadell, J. G., Santín, C., Kolden, C., Doerr, S. H., & Le Quéré, C. (2022). Global and Regional Trends and Drivers of Fire Under Climate Change. *Reviews of Geophysics*, *60*(3), e2020RG000726. https://doi.org/10.1029/2020RG000726

Kean, J. W., & Staley, D. M. (2021). Forecasting the Frequency and Magnitude of Postfire Debris Flows Across Southern California. *Earth's Future*, *9*(3), e2020EF001735. https://doi.org/10.1029/2020EF001735

Kean, J. W., Staley, D. M., & Cannon, S. H. (2011). In situ measurements of post-fire debris flows in southern California: Comparisons of the timing and magnitude of 24 debris-flow events with rainfall and soil moisture conditions. *Journal of Geophysical Research: Earth Surface*, *116*(F4). https://doi.org/10.1029/2011JF002005

Keeley, J. E., Flannigan, M., Brown, T. J., Rolinski, T., Cayan, D., Syphard, A. D., Guzman-Morales, J., & Gershunov, A. (2024). Climate and weather drivers in southern California Santa Ana Wind and non-Santa Wind fires. *International Journal of Wildland Fire*, *33*(8). https://doi.org/10.1071/WF23190

McGuire, L. A., Rengers, F. K., Kean, J. W., Staley, D. M., & Mirus, B. B. (2018). Incorporating spatially heterogeneous infiltration capacity into hydrologic models with applications for simulating post-wildfire debris flow initiation. *Hydrological Processes*, *32*(9), 1173–1187. https://doi.org/10.1002/hyp.11458

Moftakhari, H., & AghaKouchak, A. (2019). Increasing exposure of energy infrastructure to compound hazards: Cascading wildfires and extreme rainfall. *Environmental Research Letters*, *14*(10), 104018. https://doi.org/10.1088/1748-9326/ab41a6

Oakley, N. S. (2021). A Warming Climate Adds Complexity to Post-Fire Hydrologic Hazard Planning. *Earth's Future*, *9*(7), e2021EF002149. https://doi.org/10.1029/2021EF002149

Oakley, N. S., Cheung, D. J., Lindsay, D. N., & Nash, D. (2025). Insights from a 25-year database of post-fire debris flows in California. *International Journal of Wildland Fire*, *34*(12), WF25136. https://doi.org/10.1071/WF25136

Oakley, N. S., Lancaster, J. T., Kaplan, M. L., & Ralph, F. M. (2017). Synoptic conditions associated with cool season post-fire debris flows in the Transverse Ranges of southern California. *Natural Hazards*, *88*(1), 327–354. https://doi.org/10.1007/s11069-017-2867-6

Pascale, S., Carvalho, L. M. V., Adams, D. K., Castro, C. L., & Cavalcanti, I. F. A. (2019). Current and Future Variations of the Monsoons of the Americas in a Warming Climate. *Current Climate Change Reports*, *5*(3), 125–144. https://doi.org/10.1007/s40641-019-00135-w

Prein, A. F., Rasmussen, R. M., Ikeda, K., Liu, C., Clark, M. P., & Holland, G. J. (2017). The future intensification of hourly precipitation extremes. *Nature Climate Change*, *7*(1), 48–52. https://doi.org/10.1038/nclimate3168

Rengers, F. K., & McGuire, L. A. (2021). Wildfire and earth surface processes. *Earth Surface Processes and Landforms*, *46*(6), 1099–1102. https://doi.org/10.1002/esp.5054

Santi, P., Cannon, S., & DeGraff, J. (2013). 13.16 Wildfire and Landscape Change. In J. F. Shroder (Ed.), *Treatise on Geomorphology* (pp. 262–287). Academic Press. https://doi.org/10.1016/B978-0-12-374739-6.00365-1

Sayre, R. (2022). Global Mountains. GEO Knowledge Hub. https://doi.org/10.60566/9r50z-brw15

Shakesby, R. A., & Doerr, S. H. (2006). Wildfire as a hydrological and geomorphological agent. *Earth-Science Reviews*, *74*(3), 269–307. https://doi.org/10.1016/j.earscirev.2005.10.006

Staley, D. M., Kean, J. W., & Rengers, F. K. (2020). The recurrence interval of post-fire debris-flow generating rainfall in the southwestern United States. *Geomorphology*, *370*, 107392. https://doi.org/10.1016/j.geomorph.2020.107392

Staley, D. M., Negri, J. A., Kean, J. W., Laber, J. L., Tillery, A. C., & Youberg, A. M. (2017). Prediction of spatially explicit rainfall intensity–duration thresholds for post-fire debris-flow generation in the western United States. *Geomorphology*, *278*, 149–162. https://doi.org/10.1016/j.geomorph.2016.10.019

Swain, D. L. (2021). A Shorter, Sharper Rainy Season Amplifies California Wildfire Risk. *Geophysical Research Letters*, *48*(5), e2021GL092843. https://doi.org/10.1029/2021GL092843

Swain, D. L., Langenbrunner, B., Neelin, J. D., & Hall, A. (2018). Increasing precipitation volatility in twenty-first-century California. *Nature Climate Change*, *8*(5), 427–433. https://doi.org/10.1038/s41558-018-0140-y

Thomas, M. A., Lindsay, D. N., Cavagnaro, D. B., Kean, J. W., McCoy, S. W., & Graber, A. P. (2023). The Rainfall Intensity-Duration Control of Debris Flows After Wildfire. *Geophysical Research Letters*, *50*(10), e2023GL103645. https://doi.org/10.1029/2023GL103645

Thomas, M. A., Michaelis, A. C., Oakley, N. S., Kean, J. W., Gensini, V. A., & Ashley, W. S. (2024). Rainfall intensification amplifies exposure of American Southwest to conditions that trigger postfire debris flows. *Npj Natural Hazards*, *1*(1), 14. https://doi.org/10.1038/s44304-024-00017-8

Tilloy, A., Malamud, B. D., Winter, H., & Joly-Laugel, A. (2019). A review of quantification methodologies for multi-hazard interrelationships. *Earth-Science Reviews*, *196*, 102881. https://doi.org/10.1016/j.earscirev.2019.102881

Touma, D., Stevenson, S., Swain, D. L., Singh, D., Kalashnikov, D. A., & Huang, X. (2022). Climate change increases risk of extreme rainfall following wildfire in the western United States. *Science Advances*, *8*(13), eabm0320. https://doi.org/10.1126/sciadv.abm0320

Wagner, C. E. V. (1987). Development and structure of the Canadian Forest Fire Weather Index System. Canadian Forestry Service, Headquarters, Ottawa. Forestry Technical Report 35. 35 p. Retrieved from https://ostr-backend-prod.azure.cloud.nrcan-rncan.gc.ca/server/api/core/bitstreams/5a865686-e097-40df-abc0-65f54c6ff379/content

Wallace, B., & Minder, J. R. (2024). The North American Monsoon precipitation response to climate warming at convection-permitting scales. *Climate Dynamics*, *62*(1), 497–524. https://doi.org/10.1007/s00382-023-06920-6

Williams, A. P., Abatzoglou, J. T., Gershunov, A., Guzman-Morales, J., Bishop, D. A., Balch, J. K., & Lettenmaier, D. P. (2019). Observed Impacts of Anthropogenic Climate Change on Wildfire in California. *Earth's Future*, *7*(8), 892–910. https://doi.org/10.1029/2019EF001210

Williams, A. P., Seager, R., Abatzoglou, J. T., Cook, B. I., Smerdon, J. E., & Cook, E. R. (2015). Contribution of anthropogenic warming to California drought during 2012–2014. *Geophysical Research Letters*, *42*(16), 6819–6828. https://doi.org/10.1002/2015GL064924

Yanites, B. J., Clark, M. K., Roering, J. J., West, A. J., Zekkos, D., Baldwin, J. W., Cerovski-Darriau, C., Gallen, S. F., Horton, D. E., Kirby, E., Leshchinsky, B. A., Mason, H. B., Moon, S., Barnhart, K. R., Booth, A., Czuba, J. A., McCoy, S., McGuire, L., Pfeiffer, A., & Pierce, J. (2025). Cascading land surface hazards as a nexus in the Earth system. *Science*, *388*(6754), eadp9559. https://doi.org/10.1126/science.adp9559

Zscheischler, J., Martius, O., Westra, S., Bevacqua, E., Raymond, C., Horton, R. M., van den Hurk, B., AghaKouchak, A., Jézéquel, A., Mahecha, M. D., Maraun, D., Ramos, A. M., Ridder, N. N., Thiery, W., & Vignotto, E. (2020). A typology of compound weather and climate events. *Nature Reviews Earth & Environment*, *1*(7), 333–347. https://doi.org/10.1038/s43017-020-0060-z

Chapter 6

6. Conclusions

Post-fire debris flows are hazardous landscape responses that occur when rainfall acts on recently burned terrain whose original properties have been fundamentally altered by wildfire. Changes in vegetation cover, reduced infiltration, enhanced runoff, and abundant sediment can make burned areas highly susceptible to rapid debris flow initiation during subsequent storms, mobilizing ash, soil, rock, and organic debris and threatening lives, infrastructure, and downstream communities. Previous research has established that many runoff-generated post-fire debris flows are triggered by short-duration, high-intensity rainfall, with much of this understanding developed from observations in Southern California, where PFDF hazard has been most extensively documented. However, as large wildfires become more widespread across California, post-fire impacts are increasingly being documented in a broader range of climatic and physiographic settings, creating both the need and the opportunity to expand understanding of the rainfall triggering associated with PFDF occurrence.

This dissertation advances knowledge on post-fire debris flow hazard through a more integrated perspective linking atmospheric and rainfall, landscape, and climate controls across multiple spatial and temporal scales represented in the following objectives:

- Characterize the rainfall conditions associated with documented post-fire debris flows in California, including storm duration, rainfall accumulation, short-duration peak intensity, and antecedent rainfall, and evaluate how these vary by region, season, and time since fire.

- Describe the structural properties of precipitation systems associated with PFDFs including direction, speed, area, shape, and radar reflectivity conditions affecting burned areas at peak-short duration rainfall.
- Evaluate the relative importance of rainfall, atmospheric, and surface variables for predicting PFDF occurrence, and assess whether atmospheric drivers improve predictability beyond traditional approaches.
- Examine how the spatial distribution, seasonal timing, annual frequency, and conditional probability of PFDF hazard in California may change under future climate conditions.

6.1. Key results

This dissertation offers an integrated understanding of the rainfall triggering post-fire debris flow hazard in California by moving beyond rain gauges as the primary lens for interpreting hazardous rainfall. Rain station observations remain essential because they identify the immediate trigger and confirm the importance of peak short-duration rainfall intensity across seasons. However, the same short-duration intensity can occur within storms that differ substantially in duration, accumulation, seasonal character, atmospheric forcing, and spatial organization over burned terrain. These differences influence how hazardous rainfall is produced, how it is distributed across burn scars, and how it interacts with landscapes altered by fire to generate debris flow hazard. Conceptually, this work advances PFDF research by showing that debris flow triggering is not a response to rainfall intensity alone, but also the outcome of how storm environments, atmospheric forcing, and susceptible burned terrain interact. By linking rain gauge rainfall metrics with radar-based storm structure, atmospheric predictors and predictive modeling, PFDF hazard is reframed here as an

interdisciplinary, multi-scale process linking meteorology, hydrology, geomorphology, and climate change. This perspective provides a more complete basis for interpreting current PFDF occurrence, complementing existing hazard assessments and early warning efforts, and anticipating how post-fire debris flow hazard may evolve in fire-prone landscapes under future climate conditions.

The first major result of this dissertation is that rainfall conditions associated with documented PFDFs in California vary most clearly in storm duration, cumulative rainfall, and average intensity, whereas peak 15-minute intensity shows substantial overlap across seasonal and post-fire timing groupings. This pattern suggests that rainfall bursts of similar magnitude capable of triggering post-fire debris flows can occur within different broader storm environments. Seasonality emerged as the dominant source of this variability: fall and winter PFDF-producing storms were generally longer and wetter, whereas spring and summer events tended to be shorter and characterized by higher average intensities, consistent with cool-season atmospheric rivers and warm-season convective storms. Regional differences were also evident, although they should be interpreted cautiously because of inventory limitations. Events in Central California and the Coastal Mountains were associated with longer storm durations, greater cumulative rainfall totals, and most persistent antecedent rainfall than Southern California Mountains and the Sierra Nevada, but all events occurred during fall and winter. Overall, this chapter broadens understanding of rainfall triggering PFDF beyond Southern California case studies and highlights the importance of seasonality in shaping storm environments across the state.

Chapter 3 developed and applied a novel method, by adapting a storm-tracking algorithm originally developed for satellite imagery to high temporal resolution radar reflectivity data to

characterize structural properties and reflectivity of precipitation systems linked to PFDFs. Seasonal contrasts were evident: spring and summer systems were generally smaller, slower-moving, and more circular, consistent with localized convective storms, whereas fall and winter systems were larger, faster, and often more elongated, reflecting the influence of broader and more organized cool-season atmospheric phenomena. Radar reflectivity patterns over burned areas also varied seasonally, with cool-season events characterized by more widespread moderate rainfall (25–40 dBZ) and warm-season events showing more localized but frequent bursts of intense rainfall (45–50 dBZ). There was also close temporal correspondence between maximum reflectivity within the burned area and peak 15-minute rainfall intensity recorded by nearby gauges, suggesting that maximum reflectivity in the fire perimeter provides a useful representation of hazardous rainfall conditions over burned terrain. These results show that, when combined with tracking approaches, radar data provide spatial context and situational awareness beyond what rain gauges alone can offer, by identifying how precipitation is organized, how it evolves over burn scars, and when burned landscapes are exposed to rainfall conditions conducive to post-fire debris flows.

A random forest model developed in Chapter 4 allowed to assess the importance of rainfall, atmospheric and surface variables in the occurrence of post-fire debris flows in California. The model demonstrated strong overall predictive skill, with feature importance rankings highlighting reflectivity at the debris flow location, maximum reflectivity within the burned area, peak 15-minute rainfall intensity, integrated water vapor, and low-level wind speed as among the most influential predictors. However, when tested on a case study in the Eaton fire, the model showed that surface factors such as slope, burn severity, and vegetation still played an important role in shaping the spatial distribution of predicted hazard, even if

they ranked lower in global importance. This contrast highlights an important point: while atmospheric and reflectivity variables may dominate statewide model behavior, local interactions between meteorological forcing and surface susceptibility remain critical for interpreting hazard at specific sites. Overall, this chapter illustrates that incorporating atmospheric and storm-scale predictors can improve the interpretation and spatial differentiation of PFDF hazard, while also underscoring ongoing challenges related to class imbalance and the coarse resolution of some atmospheric datasets.

Finally, PFDF hazard was evaluated as a temporally compound event in Chapter 5, defined by the successive occurrence of extreme fire-weather and rainfall exceedances relevant to debris flow triggering. The results showed that these cascading conditions increase under future climate scenarios, with the strongest and most robust changes concentrated in the Sierra Nevada, Northern Coast Ranges, Cascades, and Klamath Mountains under the RCP 8.5 scenario. In addition to increasing annual frequency in some areas up to two events per year, the analysis indicated a shortening of the seasonal interval between extreme fire-weather conditions and rainfall exceedance, as hazardous rainfall begins earlier in the fall while fire-conducive conditions persist later into the year. This seasonal compression increases the likelihood that intense rainfall will affect recently burned landscapes during their period of greatest susceptibility and reduces the time available for post-fire preparedness and recovery. These findings help identify where and when post-fire hazard may intensify under climate change and provide useful context for adaptation and resilience planning in fire-prone landscapes.

6.2. Limitations and future work

This dissertation has several limitations that should be considered when interpreting its findings. First, the compiled PFDF inventory remains limited in size and uneven in geographic and seasonal distribution, with a strong concentration of documented events in both geographic and seasonal distribution in Southern California and events from Central California represented only during the cool season. This pattern may reflect differences in monitoring density, documentation, and reporting practices across the state as much as differences in hazard occurrence, and it constrains the ability to perform robust statistical comparisons. This limitation is especially relevant for the predictive random forest model, where the relatively small number of positive PFDF cases created imbalance between triggering and non-triggering storms, likely contributing to moderate recall and limiting the model's ability to capture all true events. More broadly, global feature-importance rankings may obscure local interactions between storm conditions and surface susceptibility that remain important at specific sites. In addition, consistent information on exact debris flow initiation timing was often unavailable, requiring the use of peak short-duration rainfall as a proxy for initiation timing. As a result, findings presented in this dissertation represent hazardous rainfall conditions when PFDF occur can happen rather than the precise rainfall bursts responsible for initiation.

A second limitation concerns data resolution and preprocessing methods. Radar-based analyses in mountainous terrain are affected by beam blockage, increasing beam height with distance, and other sampling limitations that can influence reflectivity estimates and areal metrics. Even so, radar remains a valuable tool because of the high temporal resolution and spatial context it provides for rainfall conditions associated with post-fire debris flow events.

Similarly, atmospheric predictors derived from reanalysis data in the predictive modeling chapter were relatively coarse in both space and time, limiting their ability to resolve fine-scale convective bursts, localized moisture convergence, and other short-lived processes relevant to characterize processes producing the rainfall known to have triggered PFDF events.

In the climate change analysis, PFDF hazard was represented using extreme fire-weather rather than explicit fire occurrence, burned area, or burn severity, while rainfall exceedances were derived from a single convection-permitting simulation rather than a rainfall ensemble. Consequently, the compound-event framework should be interpreted as identifying weather conditions favorable for wildfire activity and PFDF hazard at regional scales, rather than forecasting debris flow occurrence directly at site scales.

These limitations point to several priorities for future work. Continued expansion of PFDF inventories across California, especially outside Southern California and for later post-fire years, would improve understanding of regional variability and support more robust model development. Future studies should also work toward better constraints on initiation timing through improved monitoring of susceptible watersheds, higher-density rainfall observations, and the integration and publication of compiled events in accessible datasets. Predictive efforts would benefit from larger event and atmospheric datasets better suited to post-fire debris flow hazards, which are often assessed at the watershed scale. Such improvements would help better represent relevant processes and reconcile global model behavior with local hazard expression. Finally, future climate applications should aim to incorporate explicit fire occurrence, in the shaped of burned area or burn severity, while also using larger ensembles

of convection-permitting rainfall simulations that better resolve terrain controls on runoff generation, sediment mobilization, and post-fire recovery.

Appendix A

Chapter 5 Appendix

Table A0.1. CMIP5 models used in the analysis of extreme fire-weather conditions, obtained from the MACAv2-METDATA statistically downscaled dataset.

Model	Country	Modeling Agency	Resolution (Lon × Lat)	Ensemble
bcc-csm1-1	China	Beijing Climate Center, China Meteorological Administration	2.8° × 2.8°	r1i1p1
bcc-csm1-1-m	China	Beijing Climate Center, China Meteorological Administration	1.12° × 1.12°	r1i1p1
BNU-ESM	China	College of Global Change and Earth System Science, Beijing Normal University	2.8° × 2.8°	r1i1p1
CanESM2	Canada	Canadian Centre for Climate Modeling and Analysis	2.8° × 2.8°	r1i1p1
CNRM-CM5	France	National Centre of Meteorological Research	1.4° × 1.4°	r1i1p1
GFDL-ESM2G	United States of America	NOAA Geophysical Fluid Dynamics Laboratory	2.5° × 2.0°	r1i1p1
GFDL-ESM2M	United States of America	NOAA Geophysical Fluid Dynamics Laboratory	2.5° × 2.0°	r1i1p1
HadGEM2-CC365	United Kingdom	Met Office Hadley Centre	1.88° × 1.25°	r1i1p1
HadGEM2-ES365	United Kingdom	Met Office Hadley Centre	1.88° × 1.25°	r1i1p1
IPSL-CM5A-LR	France	Institut Pierre Simon Laplace	3.75° × 1.8°	r1i1p1
IPSL-CM5A-MR	France	Institut Pierre Simon Laplace	2.5° × 1.25°	r1i1p1
IPSL-CM5B-LR	France	Institut Pierre Simon Laplace	2.75° × 1.8°	r1i1p1

MIROC-ESM	Japan	Agency for Marine-Earth Science and Technology, Atmosphere and Ocean Research Institute (The University of Tokyo), and National Institute for Environmental Studies	2.8° × 2.8°	r1i1p1
MIROC-ESM-CHEM	Japan	Agency for Marine-Earth Science and Technology, Atmosphere and Ocean Research Institute (The University of Tokyo), and National Institute for Environmental Studies	2.8° × 2.8°	r1i1p1
MIROC5	Japan	Atmosphere and Ocean Research Institute (The University of Tokyo), National Institute for Environmental Studies, and Agency for Marine-Earth Science and Technology	1.4° × 1.4°	r1i1p1
MRI-CGCM3	Japan	Meteorological Research Institute	1.1° × 1.1°	r1i1p1

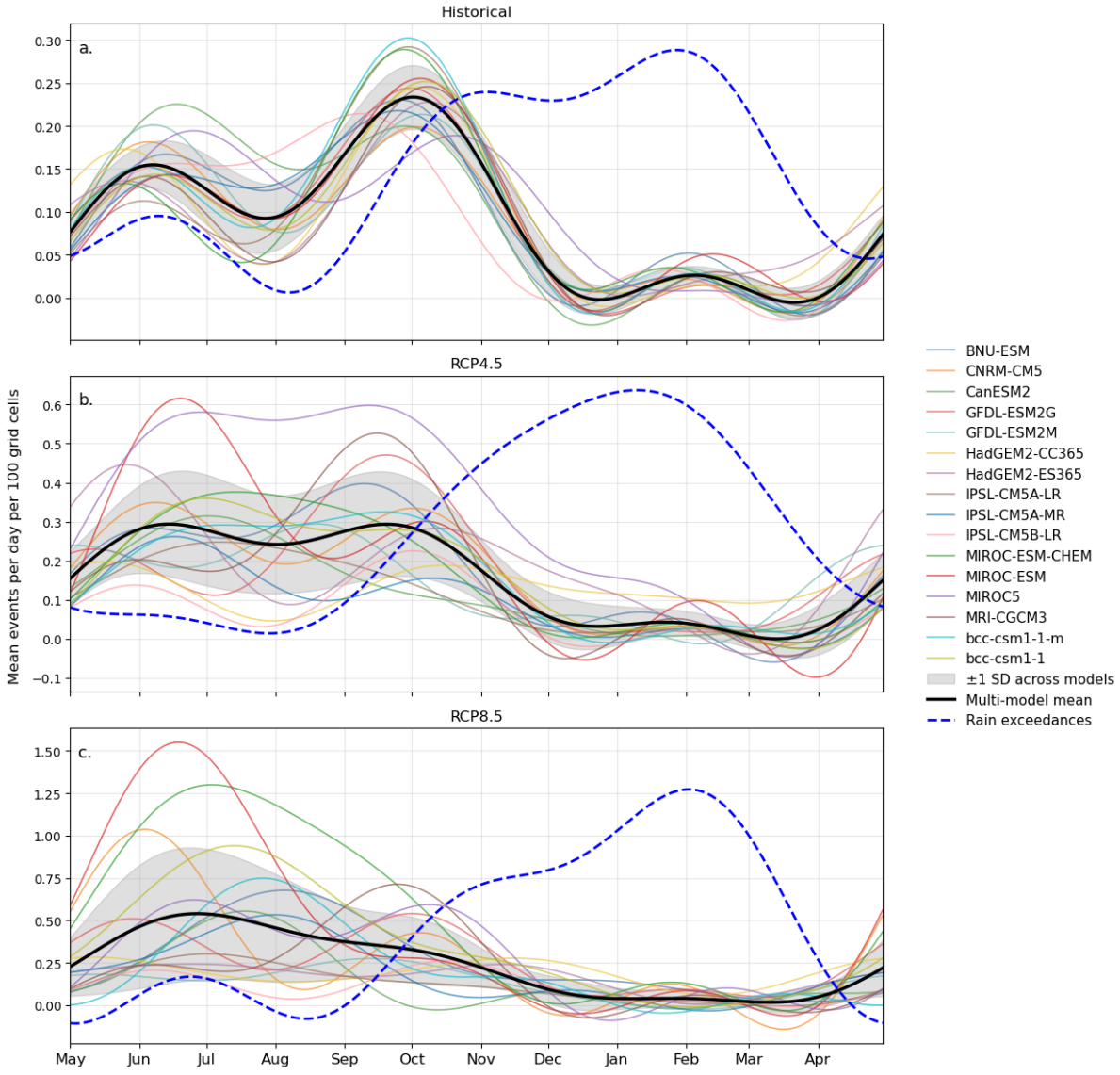


Figure A1. Harmonic seasonal cycle of extreme fire-weather events and rainfall exceedance events under **a.** historical (1990-2004), **b.** RCP4.5, and **c.** RCP8.5 (2085–2099) conditions. Colored lines represent harmonic fits for individual climate models for extreme fire-weather occurrence, the thick black line indicates the multi-model mean, and gray shading shows ±1 standard deviation across models. The blue dashed line represents the harmonic fit for rainfall exceedance events. Values are shown as mean daily occurrence per 100 grid cells (~16,000 km² at model resolution), highlighting the seasonal timing of potential overlap between fire-weather and rainfall exceedance hazards.